DOKUZ EYLÜL UNIVERSITY
GRADUATE SCHOOL OF NATURAL AND APPLIED SCIENCES

AGE AND STRUCTURAL FEATURES OF THE ROCKS OF THE MENDERES MASSIF AROUND ÖZDERE – GÜMÜLDÜR (İZMİR)

by

Hasan Mohammed Ali ALI

September, 2024

İZMİR

AGE AND STRUCTURAL FEATURES OF THE ROCKS OF THE MENDERES MASSIF AROUND ÖZDERE – GÜMÜLDÜR (İZMİR)

A Thesis Submitted to the
Graduate School of Natural and Applied Sciences of Dokuz Eylül University
In Partial Fulfillment of the Requirements for Master of Science in
Department of Geological Engineering, Applied Geology Program

by

Hasan Mohammed Ali ALI

September, 2024

İZMİR

M.Sc THESIS EXAMINATION RESULT FORM

We have read the thesis entitled **"AGE AND STRUCTURAL FEATURES OF THE ROCKS OF THE MENDERES MASSIF AROUND ÖZDERE – GÜMÜLDÜR (İZMİR)"** completed by **HASAN MOHAMMED ALI ALI** under supervision of **PROF.DR. TALİP GÜNGÖR** and we certify that in our opinion it is fully adequate, in scope and in quality, as a thesis for the degree of Master of Science.

Prof.Dr. Talip GÜNGÖR

Supervisor

Dr. Öğr. Üyesi İsmail İŞİNTEK

Jury Member

Prof. Dr. Süha ÖZDEN

Jury Member

Prof. Dr. Okan FISTIKOĞLU

Director

Graduate School of Natural and Applied Sciences

ACKNOWLEDGMENT

I sincerely like to express my gratitude to my esteemed mentor, Prof. Dr. Talip GÜNGÖR, who patiently guided and encouraged me throughout my master's degree timeframe.

I must thank Prof. Dr. Namık AYSAL and Dr. Fatma ŞİŞMAN from İstanbul University – Cerrahpaşa, for their efforts in conducting the geochronological dating for this study.

I would like to extend my endless thanks to my beloved family who always trusted and supported me in every sense they possibly could, especially, i would like to thank my sister Canan KÖRPE and her husband Onur KÖRPE, who contributed to the preparation of this thesis by creating a suitable studying environment with a warm hospitality for me.

Additionally, I feel obliged to thank my dear friend Bahadır DUMAN and his family for their faithful companionship in İzmir.

I would like to thank Geological Engineer Figen GÜNGÖR for her support and pastries in the field studies.

This study was supported by Scientific Research Project unit (project no: FYL-2023-2974) of Dokuz Eylül University. Lastly, I would like to thank Nurdoğan KAYMAZ and Hacer ÖZKAN in this unit for their office help.

Hasan Mohammed Ali ALI

AGE AND STRUCTURAL FEATURES OF THE ROCKS OF THE MENDERES MASSIF AROUND ÖZDERE – GÜMÜLDÜR (İZMİR)

ABSTRACT

The metamorphic rocks of the Özdere – Gümüldür region are investigated to reveal the age and deformation characteristics of the area. The rocks are separated into two tectonic slices by east-dipping Özdere mylonitic shear zone. The footwall block (Özdere Schists) consists of garnet – muscovite schist and the hanging wall block (Zindan Schists) consists of chlorite – biotite – garnet schists at the bottom and quartz – muscovite – chloritoid – kyanite schist at the top intercalated with phyllites and calc-schists. The Kargıcak marbles consisting of metacarbonates such as marbles, metadolomites and dolomitic marbles, tectonically overly the schist units below. The kinematic analysis of the area clearly indicates a top-to-south sense of movement according to the offset of tectonic structures. In addition, the linear fabrics of both tectonic slices indicate a significant north – south trend. According to the petrographic analysis, general mineral assemblage suggest that the metamorphic grade is in Barrovian type greenschist facies yielding chlorite, biotite, and garnet subfacies conditions and both tectonic slices have experienced retrograde metamorphic phases.

The detrital zircons in the Özdere and Zindan schists are radiometrically dated for the first time using U-Pb dating method by LA-MC-ICP-MS. The major age distribution cluster of Özdere Schists peaks at 621 Ma with Neoproterozoic age (%80.2). The youngest coherent $^{206}Pb/^{238}U$ ages yielded weighted mean age of 523 ± 15 Ma. The age distribution of Zindan Schists peaks at 619 Ma with Neoproterozoic age (%63.9). The youngest ages yielded the weighted mean age of 361.5 ± 4.9 Ma.

When considered from the point of detrital zircon distribution, the similarity of zircon population ages between the Menderes Massif and study area implies that the Özdere – Gümüldür region belongs to the Menderes Massif and not to the CBU as it was suggested before in earlier studies.

Keywords: Cycladic Blueschist Unit, Geochronology, Kinematic Analysis, Menderes Massif.

ÖZDERE-GÜMÜLDÜR (İZMİR) ÇEVRESİNDE MENDERES MASİFİ KAYALARININ YAŞI VE YAPISAL ÖZELLİKLERİ

ÖZ

Özdere – Gümüldür yöresinin metamorfik kayaçları, bölgenin yaşını ve deformasyon özelliklerini ortaya çıkarmak amacıyla incelenmiştir. Kayaçlar, doğuya eğimli Özdere mylonitik makaslama zonu tarafından iki tektonik dilime ayrılmıştır. Taban bloğu (Özdere Şistleri) granat-muskovit şistlerden, tavan bloğu (Zindan Şistleri) ise altta klorit-biyotit-granat şistlerden ve üstte fillit ve kalk-şist arakatkılı kuvars-muskovit-kloritoid-kyanit şistlerden oluşmaktadır. Mermerler, metadolomitler ve dolomitik mermerler gibi metakarbonatlardan oluşan Kargıcak mermerleri, alttaki bulunan şist birimlerini tektonik olarak üzerlemektedir. Bölgenin kinematik analizi, tektonik yapıların hareket yönlerine göre güneye doğru bir hareket mekanizması olduğunu açıkça göstermektedir. Her iki tektonik dilimin çizgisel dokusu baskın bir kuzey-güney yönlemin olduğuna işaret etmektedir. Petrografik analize göre, genel mineral topluluğu, metamorfik derecenin klorit, biyotit ve granat alt fasiyes koşullarını veren Barrovian tipi yeşilşist fasiyesinde olduğunu ve her iki tektonik dilimin de retrograd metamorfik fazlar geçirdiğini göstermektedir.

Özdere ve Zindan şistlerindeki kırıntılı zirkonlar ilk kez U-Pb yaşlandırma yöntemi kullanılarak LA-MC-ICP-MS ile yaşlandırılmıştır. Özdere Şistlerinin yaş dağılımı 621 Ma Neoproterozoik (%80.2) ile temsil edilmiştir. En genç uyumlu $^{206}Pb/^{238}U$ yaşlarının ağırlıklı ortalaması 523 ± 15 Ma'dır. Zindan Şistlerinin yaş dağılımı 619 Ma Neoproterozoik (%63.9) olarak zirve yapmaktadır. En genç yaşlar 361.5 ± 4.9 Ma'dır.

Kırıntılı zirkon dağılımı açısından değerlendirildiğinde, MM ve çalışma alanı arasındaki zirkon popülasyon yaşlarının benzerliği, Özdere - Gümüldür bölgesinin daha önceki çalışmalarda önerildiği gibi CBU'ya değil, Menderes Masifine ait olduğunu göstermektedir.

Anahtar kelimeler: Jeokronoloji, Kikladik Mavişist Birimi, Kinematik Analiz, Menderes Masifi.

CONTENTS

Page

M.Sc THESIS EXAMINATION RESULT FORM ii
ACKNOWLEDGMENT iii
ABSTRACT iv
ÖZ v
CONTENTS vi
LIST OF FIGURES viii
LIST OF SYMBOLS xxvii
ABBREVIATIONS xxix

CHAPTER ONE – INTRODUCTION 1

1.1 Brief Research History of the Menderes Massif 1
1.2 Regional Geological Setting 1
1.2.1 Definition of Rock Units in the Menderes Massif 4
1.2.2 Brief Magmatic History of the Menderes Massif 9
1.2.3 Brief Metamorphic History of the Menderes Massif 9
1.2.4 Brief Tectonic History of the Menderes Massif 10
1.2.5 Correlations with Cycladic Blueschist Unit 16
1.3 Study Area 18
1.4 Previous Studies of Gümüldür – Özdere Area 19
1.5 Purpose & Scope 21

CHAPTER TWO – ANALYTICAL METHODS 22

2.1 Field work 22
2.2 Sample Preparation and Laboratory Work 22
2.2.1 Thin Sections 22
2.2.2 Zircon Grain Separation 23

CHAPTER THREE – GEOLOGY OF THE ÖZDERE – GÜMÜLDÜR 25

3.1 Özdere Schists 30

3.1.1 Kinematics of the Özdere Schists 49
3.2 Zindan Schists 52
3.2.1 Quartz-Muscovite-Chloritoid-Kyanite Schists 53
3.2.2 Chlorite-Biotite-Garnet Schists 72
3.2.3 Kinematics of the Zindan Schists 76
3.3 Kargıcak Marbles 79

CHAPTER FOUR – PETROGRAPHY OF SCHIST UNITS 94

4.1 Introduction 94
4.2 Petrography of Özdere Schists 94
4.3 Petrography of Zindan Schists 111
4.3.1 Quartz – Muscovite – Chloritoid – Kyanite Schist 111
4.3.2 Chlorite – Biotite – Garnet Schists 122
4.3.3 Shear Sense Indicators of Zindan Schists 136

CHAPTER FIVE – RADIOMETRIC DATING OF DETRITAL ZIRCONS 138

5.1 U-Pb Zircon Ages of Özdere Schists 138
5.2 U-Pb Zircon Ages of Zindan Schists 142

CHAPTER SIX – RESULTS 149

CHAPTER SEVEN – CONLCUSIONS 151

REFERENCES 152

APPENDICES 159

APPENDIX-1: 159
APPENDIX-2: 171

LIST OF FIGURES

Page

Figure 1.1 Simplified tectonic map of the Aegean region (After Okay., 2001 and Çetinkaplan et al., 2020). The shaded area shows Cycladic Metamorphic Complex corresponding to Cycladic Basement and Cycladic Blueschist Unit..... 2

Figure 1.2 Digital Elevation model showing the topographic properties of the study area and surrounding terrain..... 3

Figure 1.3 The rock units of the Menderes Massif core and cover series (after Bozkurt and Oberhänsli., 2001) 4

Figure 1.4 A) Simplified map showing the major tectonic elements of Aegean region. B) Simplified geological map of the Menderes Massif are showing its subdivisions (Bozkurt and Park, 1994; Bozkurt and Satır, 2000)..... 5

Figure 1.5 A generalized columnar section of the Menderes Massif. The oldest basement unit, comprising paragneisses and mica schists, formed from clastic sediments and are cut by acidic/basic igneous rocks. Cover series consist of metapelites, metacarbonates and metaolistostrome (Dora et al., 2001)..... 8

Figure 1.6 A) Simplified tectonic map showing the geometry of the Hellenic arc. B) Schematic representation in a transverse section of the Hellenic arc (Papanikolaou, 2021) 12

Figure 1.7 Interpretive thrust sequence during formation of the Anatolide Belt (Gessner et al., 2001c). CBU: Cycladic Blueschist Unit; CMT: Cyclades-Menderes Thrust (Gessner et al., 2011) 13

Figure 1.8 Diagram showing distribution of pre-Alpine and Alpine events in the tectonic units of Anatolide belt (Gessner et al., 2001c and references therein) 14

Figure 1.9 Cross section showing the extensional shear zones of the central Menderes Massif (Lips et al., 2001) 15

Figure 1.10 Normalized age distribution diagram showing ages of the samples 5764, 5006, 1468 from shelf sequence of CBU on Andros Island (Bröcker et al., 2016)..... 17

Figure 1.11 The U-Pb ages obtained from the collected sample of CB04 of Naxos Island at the bottom and the CB08 of Ios Island at the top (Zlatkin et al., 2018)..... 18

Figure 2.1 Schematics showing the extraction process steps of common minerals from rock samples..... 24

Figure 3.1 Geological map of the Özdere - Gümüldür area (Modified after Başarır and Konuk 1981)..... 26

Figure 3.2 Explanation of the geological map and the general tectonostratigraphic section..... 27

Figure 3.3 Cross section of X-X"..... 28

Figure 3.4 Cross sections of Y-Y' and Z-Z 29

Figure 3.5 The landscape view of the study area showing the mylonitized shear zone with dashed white line. The area under the line represents the Özdere Schists while the upper part represents the Zindan Schists. The thick grey marbles of Kargıcak are seen resting above the Zindan Schists (coor: UTM-35 S 0510082/4207349) (Personal archive, 2024)..... 30

Figure 3.6 General field view of the Garnet-muscovite Schist unit on an outcrop. Notice the well-developed schistosity (coor: UTM-35 S 0509240/4207383) (Personal archive, 2023) 31

Figure 3.7 The well-developed schistosity of the unit (coor: UTM-35 S 0509148/4207335) (Personal archive, 2023) 31

Figure 3.8 The brownish grey to gray color of the Garnet-muscovite schist unit. Iron oxide coatings are observed as patchy stains (coor: UTM-35 S 0509148/4207335) (Personal archive, 2023) 32

Figure 3.9 The poorly visible porphyroblastic texture of the Garnet-Muscovite schist unit. Some garnets are missing due to the erosion of and weathering of the rock, but the cavities remain (coor: UTM-35 S 0509148/4207335) (Personal archive, 2023)..... 32

Figure 3.10 Oxidized quartz veins exhibiting parallelism with the schistosity of the Garnet-Muscovite schist unit. The stretching lineation trends are measured as 199/12 and the schistosity as 170/14 (coor: UTM-35 S 0509148/4207335) (Personal archive, 2023) 33

Figure 3.11 Some other veins of feldspars are also observed resembling pegmatites (coor: UTM-35 S 0512594/4205045) (Personal archive, 2023) 34

Figure 3.12 Intrafolial folds of the quartz veins are observed in between foliations of the rock unit. The fold axis was measured as 209/11 (coor: UTM-35 S 0509148/4207335) (Personal archive, 2023) 35

Figure 3.13 Recumbent quartz vein folds of approximately 1cm in width and 30 cm in length, developed nearly parallel to the schistosity. The fold axis and stretching lineations were measured as 184/19. The schistosity of the outcrops was measured as 123/25 (coor: UTM-35 S 0512937/4205506) (Personal archive, 2023)..... 36

Figure 3.14 A recumbent quartz vein fold with fold axis of 232/02 within the schistosity of 214/08. Notice the thickness difference between the limbs of fold (coor: UTM-35 S 0509139/4207502) (Personal archive, 2023)..... 37

Figure 3.15 The sheath folds within the unit. Notice how the eroded parts reveal the fold structure (coor: UTM-35 S 0509174/4207469) (Personal archive, 2023)..... 37

Figure 3.16 Kink bands that are faintly visible at a certain direction. Notice the quartz rod above the hammer head with perpendicular linear fabric to the kink band axes. Stretching lineations are 188/07 and the schistosity is 146/07 (coor: UTM-35 S 0509246/4207489) (Personal archive, 2023) 38

Figure 3.17 The quartz rods having similar linear fabric with the mineral stretching lineations of 200/05. The schistosity of the outcrop is measured as 178/04 (coor: UTM-35 S 0509283/4207373) (Personal archive, 2023) 39

Figure 3.18 The typical section for the kinematic analysis of shear sense indicators. The quartz sigmoid is perpendicular to the schistosity and parallel to the stretching lineations. Top-to-south sense of shear was indicated (coor: UTM-35 S 0510141/4207086) (Personal archive, 2024)..... 40

Figure 3.19 Mesoscopic quartz sigmoid with top-to-south sense of shear. Schistosity of the outcrop was 105/19 and the measured stretching lineations were 178/05 (coor: UTM-35 S 0513017/4208895) (Personal archive, 2024) . 40

Figure 3.20 Iron oxide coatings as hematite mineralization observed at the localities rich with quartz veins. The quartz sigmoid exhibits a top-to-south sense of movement. The trend of the schistosity is measured as 178/04 and the stretching lineation as 200/05 (coor: UTM-35 S 0509240/4207383) (Personal archive, 2023)..... 41

Figure 3.21 A quartz sigmoid with top-to-south sense of shear indicator. Stretching lineations are 180/04 and the schistosities are 116/20 in trend (coor: UTM-35 S 0509990/4207423) (Personal archive, 2024) 42

Figure 3.22 Sigmoidal quartz vein with top-to-south sense of shear. Schistosity is measured as 082/23 (coor: UTM-35 S 0512958/4205559) (Personal archive, 2023)..... 42

Figure 3.23 The S-C structures and quartz sigmoids clearly indicate top-to-south sense of shear. Schistosity 087/20. Stretching lineation 359/02 (coor: UTM-35 S 0509991/4207241) (Personal archive, 2024) 43

Figure 3.24 En-echelon quartz vein offset (coor: UTM-35 S 0513165/4209153) (Personal archive, 2024)..... 44

Figure 3.25 The parallel development of the quartz veins and S-C structures. Notice the top-to-south sense of movement indicator of the S-C structure. Schistosity trend is measured as 191/202 (coor: UTM-35 S 0509148/4207335) (Personal archive, 2023) 45

Figure 3.26 The poorly visible S-C structures. Indicates top-to-south sense of shear (coor: UTM-35 S 0509991/4207241) (Personal archive, 2024) 46

Figure 3.27 The contact zone between the Özdere Schists and the overlying Zindan Schist is a mylonitized shear zone. According to the offset of the quartz sigmoids shown in the figure, top-to-south sense of movement was indicated (coor: UTM-35 S 0512995/4205606) (Personal archive, 2023) 47

Figure 3.28 A proximity to the Özdere shear zone has deformed the underlying Özdere Schist unit. Notice the highly deformed quartz veins that are folded (coor: UTM-35 S 0514704/4204386) (Personal archive, 2024)..... 47

Figure 3.29 The shear zone in between the Zindan Schists and the underlying Özdere Schist that is well exposed at the roadcut. Notice the pronounced grey mylonitized contact associated with the shear zone (coor: UTM-35 S 0512611/4204510) (Personal archive, 2024) 48

Figure 3.30 The mylonitized contact of the Özdere Shear Zone. The schistosity of foliations below the shear zone is measured as 181/13 and the mineral lineation are 171/05 in trend (coor: UTM-35 S 0512611/4204510) (Personal archive, 2024)..... 48

Figure 3.31 Stereographic plot showing the orientations of the foliations measured by Başarır and Konuk (1981) on the Özdere Schist unit. Lower hemisphere Schmidt projection (n=45) 49

Figure 3.32 Stereographic plot showing the total foliation orientations of the Özdere Schist unit. Lower hemisphere Schmidt projection (n=83) 50

Figure 3.33 Linear fabrics (mineral stretching lineations) of the Özdere Schist unit. Lower hemisphere Schmidt projection (n=30) 51

Figure 3.34 The fold axes and crenulation cleavage axes of the Özdere Schists. Lower hemisphere Schmidt projection (n=14) 51

Figure 3.35 Rose plot of mineral stretching lineations, crenulation cleavage axes and fold axes of Özdere Schist unit. Dominant linear populations are 10° – 20° (NNE), 180° – 190° (SSW), and 350° – 360° (NNW)..... 52

Figure 3.36 A photograph of Zindan Hill. The point of view is directed towards the south (coor: UTM-35 S 0512720/4204700) (Personal archive, 2023) ... 53

Figure 3.37 General view of the Zindan Schist along the shoreline of the Aegean Sea. The point of view is directed towards the southeast (coor: UTM-35 S 0512583/4204357) (Personal archive, 2024) 53

Figure 3.38 An outcrop of Quartz-Muscovite-Chloritoid-Kyanite Schist unit of Zindan Schists (coor: UTM-35 S 0513379/4209288) (Personal archive, 2024). 54

Figure 3.39 Well exposed foliations of the quartz-muscovite-chloritoid-kyanite schist unit. The trend of schistosity is measured as 100/30 (coor: UTM-35 S 0513139/4204532) (Personal archive, 2024) 54

Figure 3.40 Rectangular joints filled with iron oxide coatings with the approximate trend of 90 and dip of 75 to 80 degrees (coor: UTM-35 S 0512937/4205352) (Personal archive, 2024) 55

Figure 3.41 A recumbent quartz vein fold towards south. Crenulation axis is measured as 173/08 and S1 as 069/34 (coor: UTM-35 S 0513864/4205761) (Personal archive, 2024)..... 55

Figure 3.42 A massive quartz vein fold has been exposed and plunges downward. Notice the parallel development of the schistosity with the fold axial plane

in the core of the antiform (coor: UTM-35 S 0513912/4205780) (Personal archive, 2024)..... 56

Figure 3.43 Some stretching lineations are preserved on the quartz veins that are exposed and measured as 035/12 (coor: UTM-35 S 0513864/4205761) (Personal archive, 2024)..... 56

Figure 3.44 Quartz sigmoid that is observed parallel to the lineations and perpendicular to the schistosity indicating top-to-south sense of shear (coor: UTM-35 S 0513864/4205761) (Personal archive, 2024) 57

Figure 3.45 A well-developed boudinage of a quartz vein in parallel to the schistosity. The trend of the schistosity is measured as 103/34 (coor: UTM-35 S 0513938/4205812) (Personal archive, 2024) 57

Figure 3.46 The schistosity of the outcrop is measured as 031/08 while containing two different stretching lineation trends. SL1: 042/08 and SL2: 001/05. SL1 is the penetrative stretching lineation (coor: UTM-35 S 0513252/4205601) (Personal archive, 2024)..... 58

Figure 3.47 The texture of quartz – muscovite – chloritoid – kyanite schist with the chloritoids visible through naked eye. The schistosity is measured as 083/31 and the contained stretching lineations are 165/12 which is parallel to the crenulation axes (coor: UTM-35 S 0513115/4205593) (Personal archive, 2024)..... 58

Figure 3.48 The stretching lineations are represented by mica minerals and are measured as 185/10 and the schistosity of 099/47 (coor: UTM-35 S 0512942/4205209) (Personal archive, 2024) 59

Figure 3.49 Well visible crenulations that are 152/24 in trend which is also parallel to the stretching lineation. The schistosity is measured as 114/32 (coor: UTM-35 S 0513145/4205588) (Personal archive, 2024)..... 59

Figure 3.50 The trend of mesoscopic crenulation foliations of the outcrop is measured as 151/15 which is also parallel to the stretching lineation of the mica

minerals (coor: UTM-35 S 0513143/4204538) (Personal archive, 2024) 60

Figure 3.51 Another photograph of the well-developed and exposed mesoscopic crenulation foliations of the outcrop (coor: UTM-35 S 0513143/4204538) (Personal archive, 2024)..... 60

Figure 3.52 Some of the outcrops exhibit brittle deformation structures of joints cutting the schistosity (coor: UTM-35 S 0513143/4204538) (Personal archive, 2024)..... 61

Figure 3.53 Phyllite intercalation within quartz-muscovite-chloritoid-kyanite schist (coor: UTM-35 S 0514142/4206760) (Personal archive, 2024) 62

Figure 3.54 Visible crenulations on the foliation surfaces of the unit. The crenulation axes are parallel to the stretching lineations (coor: UTM-35 S 0513041/4205542) (Personal archive, 2023) 62

Figure 3.55 Grey phyllite intercalation (coor: UTM-35 S 0513041/4205542) (Personal archive, 2023)..... 63

Figure 3.56 Grey marble and yellow dolomite intercalations showing lateral facies change during the deposition of the unit. The measured bedding trends vary in between 204/16 and 307/13 at this location (coor: UTM-35 S 0513977/4207063) (Personal archive, 2024) 63

Figure 3.57 This photograph shows the mesoscopic fold with the axis of 181/11 at the schists below the grey marbles. The schistosity is 253/16 at this location (coor: UTM-35 S 0514293/4206942) (Personal archive, 2024) 64

Figure 3.58 Thin calc-schist bands within the gray phyllite of schistosity 094/47. Some bands are folded with the fold axis of 353/11. The shear bands within the outcrop can be used as shear sense indicators that indicate top-to-south sense of shear (coor: UTM-35 S 0513935/4205852) (Personal archive, 2024)..... 64

Figure 3.59 Phyllites with well-developed schistosity and mesoscopic crenulation foliations. This outcrop shows a recumbent fold towards the west. S1: 284/22 and the SL=CCL:011/03 (coor: UTM-35 S 0513688/4206363) (Personal archive, 2024)..... 65

Figure 3.60 Phyllite intercalations are abundant at the proximity of this location with well-developed crenulations trending 193/11 but poorly conserved stretching lineations. Schistosity is measured as 281/22 and which is consistent with the overlying calc-schist (coor: UTM-35 S 0513723/4206303) (Personal archive, 2024) 65

Figure 3.61 The garnet grains with size range in between 1 to 3 mm in phyllite (coor: UTM-35 S 0513723/4206303) (Personal archive, 2024)..... 66

Figure 3.62 The relationship between the tension cracks and the crenulation lineations. The iron oxide material filled tension cracks are developed perpendicular to the 170/11 crenulation axes on the foliations of 091/35 (coor: UTM-35 S 0513038/4205512) (Personal archive, 2024) 66

Figure 3.63 A quartz vein that is deformed into a sigmoid and indicates top-to-south sense of movement (coor: UTM-35 S 0513938/4205812) (Personal archive, 2024)..... 67

Figure 3.64 A quartz sigmoid in the dark grey phyllite intercalation indicating top-to-south sense of shear (coor: UTM-35 S 0513912/4205779) (Personal archive, 2024)..... 68

Figure 3.65 The s-c structure indicates top-to-south sense of movement (coor: UTM-35 S 0513912/4205779) (Personal archive, 2024) 68

Figure 3.66 An s-c structure within the quartz-muscovite-chloritoid-kyanite schist of Zindan Schists indicating top-to-south sense of movement (coor: UTM-35 S 0512781/4205016) (Personal archive, 2024) 69

Figure 3.67 An intercalated and folded outcrop of quartz-muscovite-chloritoid-kyanite schist and calc-schists (coor: UTM-35 S 0513688/4206363) (Personal archive, 2024)..... 70

Figure 3.68 A folded fold. Notice the z-type folds (coor: UTM-35 S 0513857/4206705) (Personal archive, 2024)..... 70

Figure 3.69 The dip-slip fault (coor: UTM-35 S 0512741/4204379) (Personal archive, 2024)..... 71

Figure 3.70 Fault breccia around the fault scraps (coor: UTM-35 S 0512741/4204379) (Personal archive, 2024)..... 71

Figure 3.71 This well exposed outcrop along the coastline reveals numerous folds that have disharmonic fold properties. The fold axis is measured as 170/29 (coor: UTM-35 S 0513686/4204455) (Personal archive, 2024) 72

Figure 3.72 Another photograph of the disharmonic folds found on the coastline outcrop with z-type folds. The stretching lineation at this location are 164/28 in trend (coor: UTM-35 S 0513686/4204455) (Personal archive, 2024)..... 73

Figure 3.73 Disharmonic folds with z-type folds (coor: UTM-35 S 0513686/4204455) (Personal archive, 2024)..... 73

Figure 3.74 The schistosities are measured as 173/33 (coor: UTM-35 S 0513686/4204455) (Personal archive, 2024) 74

Figure 3.75 A folded quartz vein that displays parallelism with schistosity and the fold axial plan of 125/24. The stretching lineations and the crenulation axes at this location are measured as 170/14. Some s-c structures are observed over the upper limb of the fold that indicates top-to-northwest sense of movement which differs from most of the sense of shear indicators (coor: UTM-35 S 0513907/4204461) (Personal archive, 2024)..... 74

Figure 3.76 Grey schists with brown garnet porphyroblasts. The schistosity is 055/27 and the stretching lineation are parallel to the crenulations which are

313/06 in trend (coor: UTM-35 S 0514679/4204365) (Personal archive, 2024)..... 75

Figure 3.77 The schistosity was measured as 035/32 and crenulation axes as 146/06 which was equal to the stretching lineations. Notice the boudins and the intrafolial folds (coor: UTM-35 S 0514679/4204365) (Personal archive, 2024)..... 76

Figure 3.78 Stereographic plot showing the orientations of the foliations measured on the Zindan Schist unit. Lower hemisphere Schmidt projection (n=61) .. 77

Figure 3.79 Linear fabrics (mineral stretching lineations) of the Zindan Schist unit. Lower hemisphere Schmidt projection (n=48) 77

Figure 3.80 The fold axes and crenulation cleavage axes of the Zindan Schists. Lower hemisphere Schmidt projection (n=35)..... 78

Figure 3.81 Rose plot of mineral stretching lineations, crenulation cleavage axes and fold axes of Zindan Schist unit. The dominant linear population is 160° – 180° (SSE)..... 78

Figure 3.82 A landscape view from the field showing the Kargıcak Marbles above the schists of Zindan and Özdere. The point of the view is towards the southeast (coor: UTM-35 S 0512862/4209250) (Personal archive, 2024) 79

Figure 3.83 The yellow dolomite intercalations outcropping under the Kargıcak Marbles (coor: UTM-35 S 0513688/4206363) (Personal archive, 2024)79

Figure 3.84 Grey to white colored and thin laminated marbles including the intercalations (coor: UTM-35 S 0514679/4204365) (Personal archive, 2024)..... 80

Figure 3.85 The Kargıcak marble outcrop contains preserved stretching lineations and folded laminations. The stretching lineations were measured as 031/04 and trend of the laminations were 151/31 (coor: UTM-35 S 0514093/4205943) (Personal archive, 2024)..... 80

Figure 3.86 Folded and recrystallized limestone block (coor: UTM-35 S 0513389/4207162) (Personal archive, 2024) 81

Figure 3.87 Thin laminated limestone outcrop (coor: UTM-35 S 0513389/4207162) (Personal archive, 2024)..... 81

Figure 3.88 The preserved stretching lineations of 209/05 trend in Kargıcak Marble. S1: 130/31 (coor: UTM-35 S 0514093/4205943) (Personal archive, 2024) 82

Figure 3.89 Coarse crystalline white colored marbles with stretching lineations. SL: 180/02 and S1: 086/39 (coor: UTM-35 S 0513443/4207197) (Personal archive, 2024)..... 82

Figure 3.90 Rose diagram of stretching lineation found on the Kargıcak marbles with dominant linear population clustering in 180° - 190° (SSE)..... 83

Figure 3.91 Stereographic plot showing the orientations of the foliations/beddings measured on the Kargıcak marbles. Lower hemisphere Schmidt projection (n=49)..... 83

Figure 3.92 Linear fabrics (mineral stretching lineations) of the Kargıcak marbles. Lower hemisphere Schmidt projection (n=26) 84

Figure 3.93 Marbles containing deformed quartz veins (coor: UTM-35 S 0513349/4207031) (Personal archive, 2024) 85

Figure 3.94 Folded quartz veins within Kargıcak Marbles (coor: UTM-35 S 0513349/4207031) (Personal archive, 2024) 85

Figure 3.95 Sheath folds in Kargıcak marbles (coor: UTM-35 S 0513438/4207318) (Personal archive, 2024)..... 86

Figure 3.96 Sheath folds in Kargıcak marbles (coor: UTM-35 S 0513438/4207318) (Personal archive, 2024)..... 86

Figure 3.97 Pale yellow to crème – colored dolomites. S1: 094/26 (coor: UTM-35 S 0513978/4205873) (Personal archive, 2024) 87

Figure 3.98 Dolomitized limestones of Kargıcak Marbles. Notice the thinly laminated sections around the hammer (coor: UTM-35 S 0513295/4205370) (Personal archive, 2024)..... 87

Figure 3.99 Thinly laminated dolomitic marbles. 280/25 is the trend of the laminations. Stretching lineations are 191/09 (coor: UTM-35 S 0513844/4206905) (Personal archive, 2024)..... 88

Figure 3.100 An old open pit marble mine that has been abandoned (coor: UTM-35 S 0513292/4206973) (Personal archive, 2024) 88

Figure 3.101 The contact between the Kargıcak Marbles and the underlying Zindan Schist. Notice the highly crenulated and foliated texture resembling a ductile shear zone (coor: UTM-35 S 0514679/4204365) (Personal archive, 2024)..... 89

Figure 3.102 The ductile shear zone contact between the dolomites and the underlying schist (coor: UTM-35 S 0513740/4206523) (Personal archive, 2024) ... 89

Figure 3.103 A roadcut showing the relationship between the Kargıcak marbles on top and the underlying Zindan schists (coor: UTM-35 S 0513873/4204484) (Personal archive, 2024)..... 90

Figure 3.104 Schist intercalations in the marbles (coor: UTM-35 S 0513473/4207174) (Personal archive, 2024)..... 90

Figure 3.105 A synform of schist intercalation within marbles. The fold axis is 158/11 (coor: UTM-35 S 0513752/4207151) (Personal archive, 2024) 91

Figure 3.106 A closer photograph of the synform. The trends of the limbs are 239/23 and 110/32 (coor: UTM-35 S 0513752/4207151) (Personal archive, 2024) 91

Figure 3.107 Very thin laminated grey marbles with mica flakes on the laminations. S1: 087/27 (coor: UTM-35 S 0513492/4207354) (Personal archive, 2024) 92

Figure 3.108 Chert imbedded dark grey marble outcrop with very thin laminations. S1: 079/17 (coor: UTM-35 S 0513492/4207354) (Personal archive, 2024) . 92

Figure 3.109 Thin laminated grey marbles (coor: UTM-35 S 0513492/4207354) (Personal archive, 2024) 93

Figure 4.1 A photomicrograph of Muscovite flakes display well-developed parallelism with the foliations. Ms: Muscovite, Qz: Quartz. In the plane polarized light 95

Figure 4.2 Crenulated chlorite foliations coexisting with muscovites in a thin section photomicrograph of Özdere schist. Chlorites are seen as dark green and highly crenulated structures. In the plane polarized light. Plane polarized light 95

Figure 4.3 A photomicrograph of plagioclase poikiloblast containing chlorite inclusions and surrounded by muscovite foliations. Chl: Chlorite – Ms: Muscovite – Pl: Plagioclase. In the plane polarized light 96

Figure 4.4 A photomicrograph of plagioclase poikiloblasts surrounded by chlorite and muscovite. Pl: Plagioclase. A) Under plane polarized light. B) Under cross polarized light 97

Figure 4.5 Plagioclase with a typical twining and surrounded by muscovite flakes. Numerous inclusions can be seen inside the plagioclase poikiloblast. Ms: Muscovite – Pl: Plagioclase. A) Under plane polarized light. B) Under cross polarized light 98

Figure 4.6 Plagioclase porphyroblasts that partially overprinted by muscovite. Pl: Plagioclase. A) Under plane polarized light. B) Under cross polarized light 99

Figure 4.7 Muscovite foliations surrounding quartz and albite minerals. Notice the high level of interference colors of muscovite in cross polarized light. A) Under plane polarized light. B) Under cross polarized light..... 101

Figure 4.8 Albite porphyroblasts within muscovite foliations and quartz. Notice the well-developed alignments of muscovite parallel with the foliations. Ms: Muscovite – Pl: Plagioclase. A) Under plane polarized light. B) Under cross polarized light 102

Figure 4.9 Muscovite foliations surrounding albite. Notice the chloritoid growth over the muscovite flakes. A) Under plane polarized light. B) Under cross polarized light..... 103

Figure 4.10 Anastomosing texture of the muscovite foliations surrounding the quartz crystals. A) Under plane polarized light. B) Under cross polarized light 104

Figure 4.11 Garnet subhedral crystals found as inclusions. Chloritic overprint is noticeable on the muscovite foliations. Chl: Chlorite, Grt: Garnet. Under the plane polarized light 105

Figure 4.12 Another example of chlorite and muscovite together forming the foliations in the schist unit. Notice the tourmaline mineral perfectly dissected perpendicular to the C axis of the crystal. Chl: Chlorite, Ms: Muscovite, and Tur: Tourmaline. A) Under plane polarized light. B) Under cross polarized light..... 106

Figure 4.13 Albite and chlorite minerals. Chl: Chlorite. A) and B) Plane polarized light 107

Figure 4.14 An oriented thin section photomicrograph of Özdere schists showing shear sense indicator of s-c structure. According to the offset of the s-c structure planes, top-to-south sense of movement was indicated 108

Figure 4.15 An oriented thin section photomicrograph of Özdere schists showing shear sense indicator of S-C structure. According to the offset of the S-C structure, top-to-south sense of movement is indicated 109

Figure 4.16 An oriented thin section photomicrograph of Özdere schists showing shear sense indicator of S-C structure. According to the offset of the S-C

structure, top-to-south sense of movement is indicated. A) PPL and, B) XPL 110

Figure 4.17 Poikiloblast grain of Albite with Muscovite and Chloritoid mineralization on the rim. Qz: Quartz – Ab: Albite - Cld: Chloritoid – Ms: Muscovite. A) PPL and B) XPL..... 112

Figure 4.18 Muscovite and Chloritoid minerals align with well-developed foliation. Ab: Albite - Cld: Chloritoid – Ms: Muscovite. A) PPL and B) XPL.... 113

Figure 4.19 Muscovites and Chloritoid minerals showing typical mineralogical features. Cld: Chloritoid – Ms: Muscovite. A) PPL and B) XPL 114

Figure 4.20 A well-developed Chloritoid mineral displaying typical features of high relief and pale green to blue pleochroism. Photomicrograph is in PPL 115

Figure 4.21 A good example of comparative photomicrograph of a thin section including Muscovite flakes and Chloritoid mineralization developed parallel to the foliation. Ms: Muscovite – Cld: Chloritoid. Photomicrograph is in PPL 116

Figure 4.22 Porphyroblastic texture with a garnet crystal porphyroblast surrounded by muscovite and chloritoid minerals. Ms: Muscovite – Cld: Chloritoid – Grt: Garnet. Photomicrograph is in PPL..... 117

Figure 4.23 Garnet porphyroblast in Garnet-Chloritoid schist unit of Özdere tectonic slice. Ms: Muscovite – Cld: Chloritoid – Grt: Garnet. Photomicrograph is in PPL..... 117

Figure 4.24 A garnet porphyroblast being replaced by chloritoid mineral representing retrograd metamorphic phase. Ab: Albite – Cld: Chloritoid – Grt: Garnet. Photomicrographs are in A) PPL and B) XPL 118

Figure 4.25 Subhedral garnet porphyroblast being overprinted by chloritoid. Cld: Chloritoid – Grt: Garnet. Photomicrographs are in A) PPL and B) XPL 119

Figure 4.26 Euhedral and subhedral garnet porphyroblasts surrounded by muscovite flakes at the rims. Notice the Albite development at the pressure shadow of garnet crystals. Ms: Muscovite – Cld: Chloritoid – Grt: Garnet. Photomicrographs are in A) PPL and B) XPL 120

Figure 4.27 A pre-tectonic kyanite crystal coexisting with chloritoid mineral. Notice the deformation and bending of the crystal. Cld: Chloritoid – Ky: Kyanite. Photomicrographs are in A) PPL and B) XPL 121

Figure 4.28 A typical zircon grain enclosed in muscovite foliation. Zrn: Zircon.... 122

Figure 4.29 Fine grained muscovite forming the foliations of the rock unit. Photomicrograph is in XPL..... 123

Figure 4.30 Coexisting of chlorite and muscovite minerals as foliations. Chl: Chlorite – Ms: Muscovite. Photomicrograph is in PPL 124

Figure 4.31 Chlorite and Biotite forming the foliations. Notice the chloritic overprint on the biotite flakes. Chl: Chlorite – Bt: Biotite. Photomicrographs are in A) PPL and B) XPL 125

Figure 4.32 Garnet, chlorite and biotite minerals are coexisting together. Notice the replacement of garnet by chlorite and biotite on the rims of garnet. Photomicrograph is in PPL 126

Figure 4.33 Chloritoid, chlorite and muscovite display well-developed parallelism together forming the foliations. Photomicrographs are in A) PPL and B) XPL 127

Figure 4.34 Albite poikiloblasts containing inclusions of other minerals from the assemblage. Chl: Chlorite – Ms: Muscovite – Ab: Albite. Photomicrographs are in A) PPL and B) XPL 128

Figure 4.35 Albite poikiloblasts containing inclusions of other minerals from the assemblage. Chl: Chlorite – Ms: Muscovite – Ab: Albite. Photomicrographs are in A) PPL and B) XPL 129

Figure 4.36 Albite poikiloblasts containing inclusions of other minerals from the assemblage. Chl: Chlorite – Ms: Muscovite – Ab: Albite - Grt: Garnet. Photomicrographs are in A) PPL and B) XPL 130

Figure 4.37 Garnet rotation porphyroblast rotation. Photomicrographs are in A) PPL and B) XPL..... 131

Figure 4.38 Numerous subhedral garnet grains found as porphyroblasts in the albite and matrix. Biotite and chloritoid are present as foliation forming minerals. Cld: Chloritoid – Bt: Biotite – Grt: Garnet. Photomicrographs are in A) PPL and B) XPL..... 132

Figure 4.39 Garnet porphyroblasts in albite surrounded by muscovite flakes. Grt: Garnet – Ab: Albite – Ms: Muscovite. Photomicrographs are in A) PPL and B) XPL..... 133

Figure 4.40 An albite poikiloblast containing garnet inclusions that have chloritoid mineral development at their pressure shadows. Grt: Garnet – Ab: Albite. Photomicrographs are in A) PPL and B) XPL 134

Figure 4.41 Garnet porphyroblast displaying counterclockwise rotation with respect to the muscovite foliations. Notice the biotite overprint and infiltrate the garnet grain through the right rim indicating a post-tectonic metamorphic process. Grt: Garnet – Bt: Biotite – Ms: Muscovite. Photomicrographs are in A) PPL and B) XPL 135

Figure 4.42 A microphotograph of an oriented thin section showing a garnet grain surrounded by chlorites. Grt: Garnet. A) PPL and B) XPL 136

Figure 4.43 Photomicrograph of Zindan Schists with mica fish. Dextral shear sense indicating top-to-south sense of movement. Under cross polarized light 137

Figure 4.44 Photomicrograph of Zindan Schists with mica fish arranged between C-type shear bands. Dextral shear sense indicating top-to-south sense of movement. Under cross polarized light..... 137

Figure 5.1 The Kernel Density Estimate (KDE) graph of OZD-02 sample collected from garnet – muscovite schist unit of Özdere tectonic slice (n=86). The main age distribution peak is at 621 Ma of Neoproterozoic 139

Figure 5.2 The Concordia diagram graph of OZD-02 sample collected from garnet – muscovite schist unit of Özdere tectonic slice (n=86) 140

Figure 5.3 The youngest coherent $^{206}Pb/^{238}U$ age yielding the weighted mean age of 523 ± 15 Ma that corresponds to the Cambrian period (n=2) 141

Figure 5.4 The age distribution pie chart of the sample OZD_02 of Özdere Schists. The $^{206}Pb/^{238}U$ ages data were used to prepare the chart (n=86)..... 142

Figure 5.5 The Kernel Density Estimate (KDE) graph of OZD-01 sample collected from chlorite – biotite – garnet schist unit of Zindan tectonic slice (n=97). The main age distribution peak is at 619 Ma of Neoproterozoic 143

Figure 5.6 The Concordia diagram graph of OZD-01 sample collected from chlorite – biotite – garnet schist unit of Zindan tectonic slice (n=97)..... 144

Figure 5.7 The youngest coherent $^{206}Pb/^{238}U$ age yielding the weighted mean age of 361.5 ± 4.9 Ma that corresponds to the Devonian period (n=5) 145

Figure 5.8 The age distribution pie chart of the sample OZD_01 of Zindan Schists. The $^{206}Pb/^{238}U$ ages data were used to prepare the chart (n=86)..... 146

Figure 5.9 Menderes Massif Core Schist detrital zircon U-Pb ages. (after Zlatkin et al., 2013)..... 147

Figure 5.10 Kernel Density Estimation (KDE) plots for detrital zircon U-Pb ages compiled from Zindan schists, Özdere schists, Menderes Massif core schists, and CBU cover schists (This study; Zlatkin et al., 2013; Bröcker et al., 2016)..... 148

LIST OF SYMBOLS

The given mineral abbreviations below were used in the thesis according to mineral symbols approved by International Mineralogical Association (IMA).

Ab	: Albite
σ	: Analytical uncertainty (2SE)
~	: Approximately
Ar	: Argon
Bt	: Biotite
Chl	: Chlorite
Cld	: Chloritoid
c.	: Circa (Approximate)
+N	: Cross Polarized Light
rho	: Error correlation coefficient
Grt	: Garnet
Ky	: Kyanite
Pb	: Lead
μm	: Micrometer
Ms	: Muscovite
%	: Percentage
Pl	: Plagioclase

//N	: Plane Polarized Light
±	: Plus-Minus sign
Qz	: Quartz
n	: Sample size
Tur	: Tourmaline
U	: Uranium
Zrn	: Zircon

ABBREVIATIONS

ACCB	: Attic – Cycladic Crystalline Belt
CMT	: Cyclades-Menderes Thrust
CBU	: Cycladic Blueschist Unit
Conc	: Concordance Ratio
CL	: Crenulation Cleavage Axes
XPL	: Cross Polarized Light
ED50	: European Datum – 1950
Ga	: Giga Annum (Billion Years)
HP	: High Pressure
IMA	: International Mineralogical Association
KDE	: Kernel Density Estimate
Kbar	: Kilobar
LA-MC- ICP-MS Mass Spectrometry	: Laser Ablation Multi – Collector Inductively Coupled Plasma
LT	: Low Temperature
MMM	: Main Menderes Metamorphism
Ma	: Mega Annum (Million Years)
MM	: Menderes Massif
PPL	: Plane Polarized Light
P	: Pressure

S1	: Schistosity
SL	: Stretching Lineation
T	: Temperature
UTM	: Universal Transverse Mercator coordinate system

CHAPTER ONE
INTRODUCTION

In this chapter, it is aimed to present the general attributes of the Menderes Massif by mentioning a brief geological research history of the massif and outlining regional geological setting by mentioning magmatic, metamorphic, and tectonic activities concerning the geological evolution of the Menderes Massif. Later, a brief tectonostratigraphic definition of the Cycladic Blueschist Unit is made to elaborate the differences and/or correlations between the two massifs and the study area. Towards the end of this chapter, location of the study area, previous studies, and lastly the purpose and scope of this research is presented.

1.1 Brief Research History of the Menderes Massif

The ancient descriptions of the Menderes Massif (Parèjas, 1940) rocks were carried out by Hamilton (1840) They have approximately localized the NW-SE boundaries of the region but extended the massif to the south of the sea of Marmara at the north. They suggested that the massif consists of micaschists, gneiss, marble, amphibolites, some undefined rocks and granite. In addition, they also point out that similar rocks are present in Cyclades.

Schuiling (1962), made the first systematic geological investigation of the Menderes Massif by the lithostratigraphical sequence and divided the massif into “core and cover” units (Dora, 2011). He indicated that the gneisses of the Menderes Massif are migmatites and the interior of the complex displays a persistent N-S lineations and fold directions that are pre-Variscan orogenic phase and can be correlated with the similarly directed lineation in basement rocks of Western Türkiye and Cyclades.

1.2 Regional Geological Setting

The Menderes Massif has a complicated metamorphic and tectonic history due to its location in the Alpine orogenic belt and covers a large area in western Anatolia (Figure 1). The Menderes Massif tectonically underlays Afyon zone consisting of low-grade metapelite and metacarbonates to the northeast and the shales and carbonates

comprising the Lycian Nappes to the south. To the northwest of the massif, tectonic slices of Cycladic Metamorphic Complex and mélanges of İzmir-Ankara zone including Bornova Flysch Zone of olistostromal character tectonically overlay the Menderes Massif (Şengör and Yılmaz, 1981; Dora et al., 1995; Çetinkaplan et al., 2020).

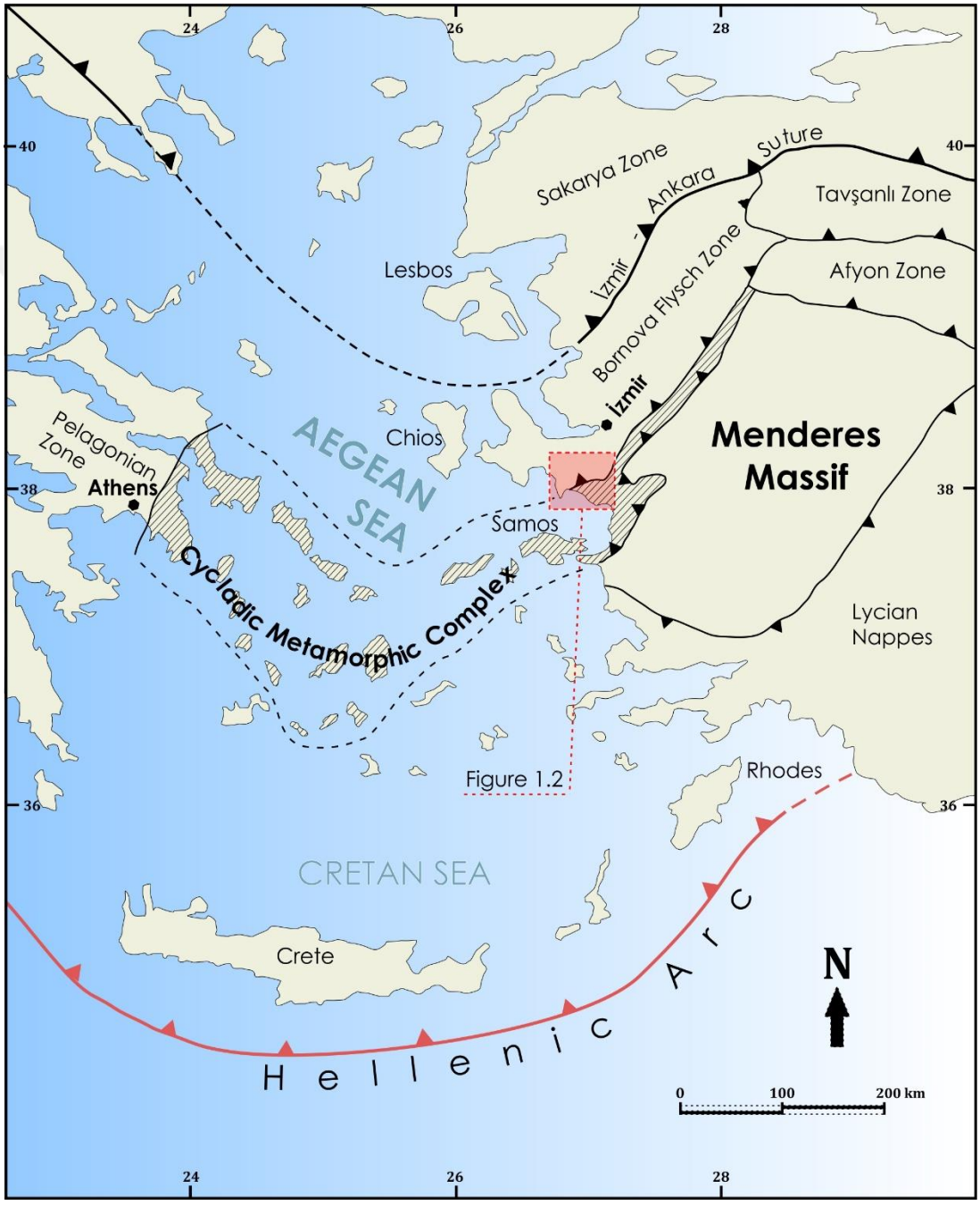


Figure 1.1 Simplified tectonic map of the Aegean region (After Okay., 2001 and Çetinkaplan et al., 2020). The shaded area shows Cycladic Metamorphic Complex corresponding to Cycladic Basement and Cycladic Blueschist Unit

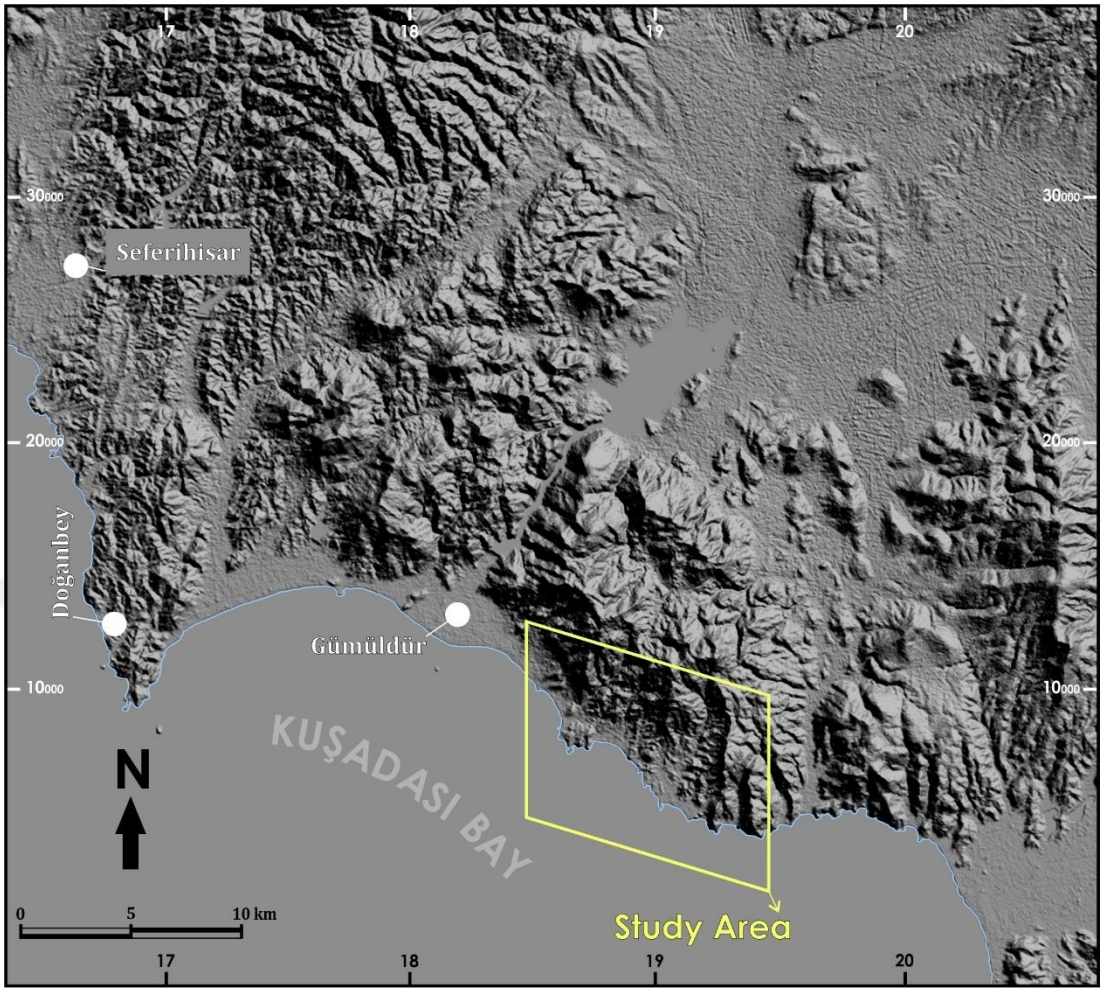


Figure 1.2 Digital Elevation model showing the topographic properties of the study area and surrounding terrain

Metamorphic core complexes form when continental lithosphere extends at high rates and strain within the upper crust becomes localized in detachment faults (Gessner et al., 2001a; 2001b). It is considered that the Menderes Massif is a metamorphic core complex that consists of a central gneiss dome surrounded by a series of metasediments (Dürr, 1975; Şengör and Yılmaz., 1981; Dora et al., 1990; Loose and Reischmann., 1999). This metamorphic complex is bounded by two approximately east-striking, opposite-facing, and low-angle detachment fault systems, the Kuzey (Gediz) Detachment in the north and the Güney (Büyük Menderes) Detachment in the south (Emre and Sözbilir, 1997; Hetzel et al., 1995b; Gessner et al., 2001b; Lips et al., 2001; Gessner et al., 2011).

Due to the Miocene extensional regime in the Western Anatolia, East-West trending Neogene grabens subdivide the massif into Northern, Central, and Southern submassifs (Dora., 1976). This basin and range-type topography is a consequence of Neogene to recent normal and strike-slip faulting (Gessner et al., 2011).

1.2.1 Definition of Rock Units in the Menderes Massif

After decades of research concerning the complex tectonometamorphic history of the Menderes Massif by many researchers, the core structure unit was named as the "Core series", "Gneiss Core", "Precambrian Basement" and "Pan-African Basement" and described as consisting of Augen Gneisses, Metagranites, High grade schists, Paragneisses, and Metagabbros with eclogite relics (Bozkurt and Oberhänsli., 2001). The Augen Gneisses are the most common rock unit in the Precambrian Basement of Menderes Massif exposed in all three submassifs (Candan et al., 2011) (Figure 1.3 – 1.4).

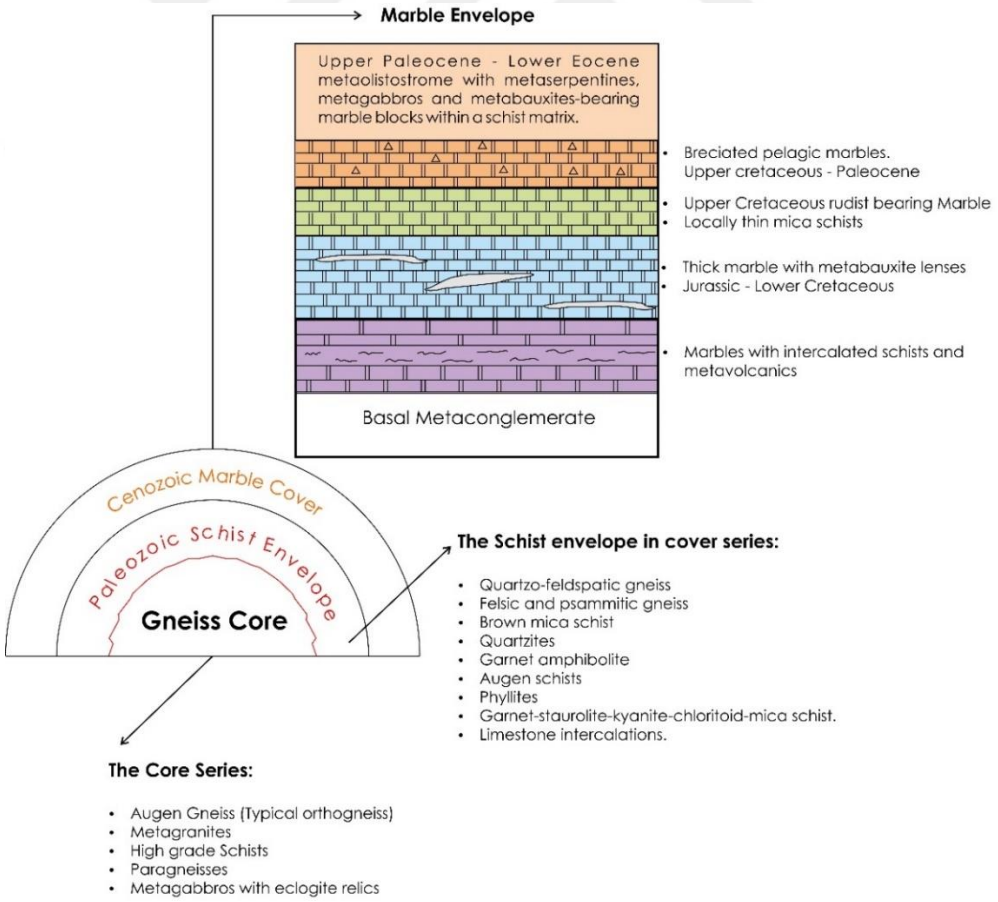


Figure 1.3 The rock units of the Menderes Massif core and cover series (after Bozkurt and Oberhänsli., 2001)

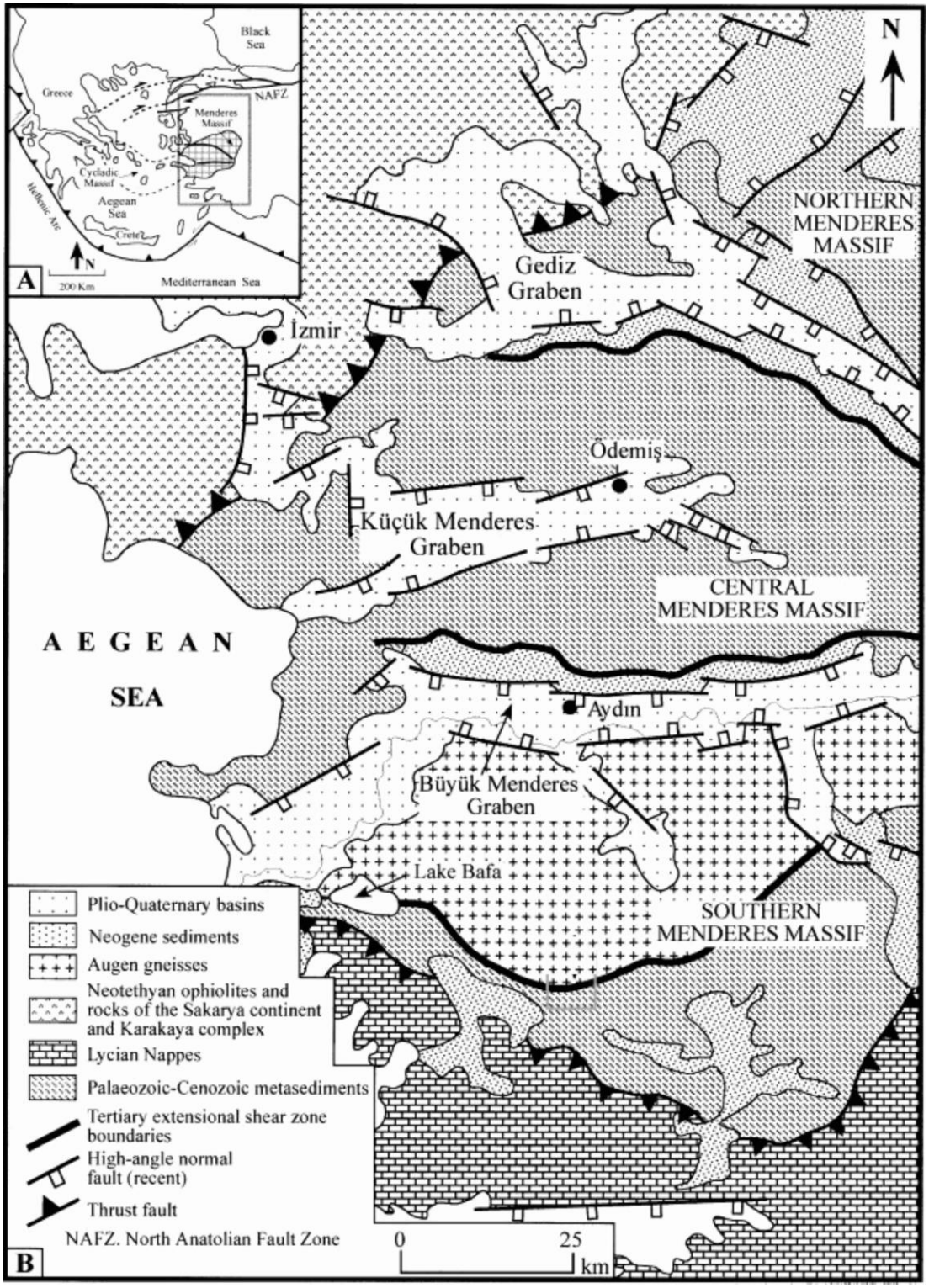


Figure 1.4 A) Simplified map showing the major tectonic elements of Aegean region. B) Simplified geological map of the Menderes Massif are showing its subdivisions (Bozkurt and Park, 1994; Bozkurt and Satır, 2000)

The Gneiss Core consists of a continuous metaclastic sequence with granitoidic intrusions related to the Pan-African orogeny and can be divided into two sub-units of Paragneiss and overlying Schist unit. Due to the Alpine orogenic deformations of thrust faults and the granitoidic intrusions the true thickness of the metaclastic sediments cannot be determined but a minimum of 8 kilometers of true thickness is estimated according to the general stratigraphical and metamorphic properties of tectonic layers. The overlying Schist unit in the Pan-African Basement (Core) is derived from sandstone and mudstone protoliths (Candan et al., 2011).

This "Gneiss Core" is tectonically overlain by "Cover Series" composed of a Paleozoic Schist Envelope and an uppermost Cenozoic Marble cover (Bozkurt and Oberhänsli., 2001). The contact relationship between the core and cover series are regarded as main supra-pan-African unconformity (Şengör et al., 1984).

The Paleozoic cover series consists of a Schist sequence and Göktepe Formation in the Southern submassif. The Schist sequence is made up of garnet-mica schists, micaschists and thick lenses of quartzo-feldspathic schists within micaschists. On the other hand, the Göktepe Formation consists of dark grey – black marble, pale metaquartzites and dark micaschists and phyllite units. The uppermost unit overlying Göktepe Formation is the Cenozoic Milas Marble sequence (Okay., 2001).

To summarize, the basement rocks of the Menderes massif consist of the metasedimentary unit of the paragneisses that are considered as Late Proterozoic in age due to the intruded orthogneisses of 550 Ma age (Dora et al., 2001; Gessner et al., 2004). The protolith of the paragneisses were suggested by Dora et al., (2001) as predominantly clastic sediments of litharenitic composition cratonic provenance with the estimated deposition time of Late Proterozoic. Then, 610 Ma age was obtained for the youngest detrital zircon in this unit using $^{207}Pb/^{206}Pb$ evaporation (Koralay et al., 2003; Zlatkin et al., 2013). The U-Pb zircon ages of the core schist conformably overlying the paragneisses from the Menders massif basement, cluster at an age of 640 – 670 Ma (Candan et al., 2011). The orthogneisses within the basement rocks are intruding the paragneiss and covering schist unit together.

The cover series of the Menders massif consists of Paleozoic age rock units that are mainly quartzite/schist and marble/schist/phyllite.

The lowermost unit above the erosional contact (the "supra pan-African unconformity" termed by Şengör et al., 1984) is yellow-colored metasediments that contain channel fill metaconglomerate with granitic pebbles having identical mineralogy and U-Pb zircon ages with the Neoproterozoic intrusions in the basement, yielding and age of 549.6 ± 3.7 Ma (Candan et al., 2011). Dora et al., (2001) defined the yellow-colored schist as a separate layer by estimating its age as Ordovician – Devonian (Figure 1.5).

The upper section of the cover series is defined as carbonate bearing quartzites yielding 520 Ma of age by youngest detrital zircon providing the lower bound for the time of deposition. The black marbles overlying the quartzites are intercalated towards the bottom and an age of Late Devonian – Early Carboniferous was estimated for the deposition (Loos and Reischmann., 1999; Bozkurt and Oberhänsli., 2001; Zlatkin et al., 2013)

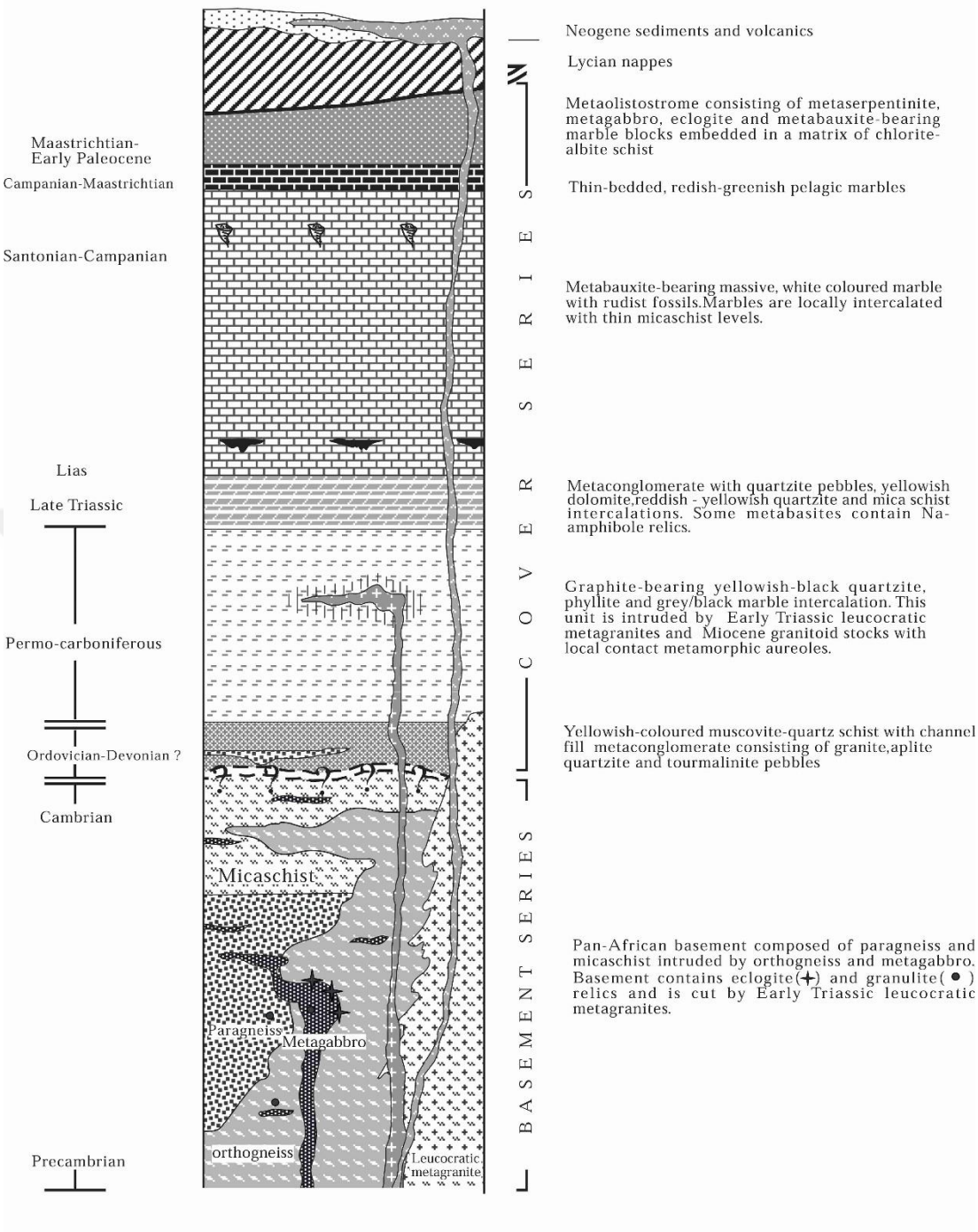


Figure 1.5 A generalized columnar section of the Menderes Massif. The oldest basement unit, comprising paragneisses and mica schists, formed from clastic sediments and are cut by acidic/basic igneous rocks. Cover series consist of metapelites, metacarbonates and metaolistostrome (Dora et al., 2001)

1.2.2 Brief Magmatic History of the Menderes Massif

According to geological and geochronologic evidence, there have been three distinct magmatic activities in the Menderes Massif (Koralay, 2001).

The first magmatic episode is thought to be in Precambrian/Cambrian age. The Precambrian age of 2555-1740 Ma was indicated by $^{207}Pb/^{206}Pb$ single zircon evaporation method and that affected entire Menderes Massif (Reischmann et al. 1991; Bozkurt and Oberhänsli, 2001).

The Cambrian age magmatic activity have been indicated by various ages, $^{207}Pb/^{206}Pb$ single zircon ages of 546.2 ± 1.2 Ma demonstrated that the augen gneisses in the southern Menderes Massif were generated from Pan-African intrusions (Hetzel and Reischmann, 1996). Loose and Reischmann (1999), have indicated that the ages of gneisses range from 520 Ma to 570 Ma with a major event at about 550 Ma according to the single zircon ages.

The second magmatic episode of Triassic age, for the leucogranite orthogneisses, single zircon dating of three samples yielded mean ages of 246 ± 5 Ma, 241 ± 5 and 235 ± 6 Ma that are obtained from $^{207}Pb/^{206}Pb$ evaporation method of single zircon dating (Koralay et al., 2001).

The third magmatic episode occurred in Tertiary, which is unmetamorphosed, yielded 25 to 12 Ma of age (Koralay, 2001). Two granitoids of Turgutlu and Salihli in central Menderes Massif were dated using $^{40}Ar/^{39}Ar$ amphibole isochron method yielded hornblende isochron age of 19.5 ± 1.4 Ma and biotite ages of 13.1 ± 0.2 and 12.2 ± 0.4 Ma (Hetzel et al., 1995a). The U–Pb monazite and allanite ages of Turgutlu and Salihli also yielded 16.1±0.2 Ma and 15.0 ± 0.3 Ma respectively (Glodny and Hetzel, 2007).

1.2.3 Brief Metamorphic History of the Menderes Massif

It has been known for many years that the Menderes Massif has a polyphase metamorphic history. The Precambrian basement rocks of schists, paragneisses, migmatites, orthogneisses, metagranites, charnockites and metagabbros primarily have medium to high-grade metamorphism in three different facies related to the Pan-

African orogeny; i) Granulite, ii) Eclogite, and iii) Amphibolite (Dora, 1995; Oberhänsli et al., 1997; Candan and Dora., 1998; Candan et al., 1998;2001; Koralay, 2001). The charnockites yielded a crystallization age of ~590 Ma for protoliths and they record granulite-facies overprint at ~ 580 Ma (Koralay, 2015). The P-T conditions of the Pan-African high-pressure metamorphism in the eclogites are estimated to be 644 °C with a minimum pressure of approximately 15 kbar (Candan et al., 2001).

$^{40}Ar/^{39}Ar$ phengite ages of cover series from Dilek peninsula determined Tertiary age of 40 Ma for the subduction-related high-pressure metamorphism of 470 °C with minimum pressure conditions of 10 kbar under epidote-blueschist facies (Oberhänsli et al., 1998). The major metamorphic event is called the "Main Menderes Metamorphism" (MMM) that effected the whole massif with high grade amphibolite facies in structurally lower parts, and greenschist grade in the outermost envelope. According to the Rb-Sr isotopic data, it occurred around 35 ± 5 Ma during Latest Eocene time or transition from Eocene to Oligocene (Şengör et al., 1984). Another $^{40}Ar/^{39}Ar$ age was determined by Lips et al. (2001) derived from white mica yielding 36 ± 2 Ma.

The youngest metamorphic event was a Barrovian type medium pressure metamorphism which developed under low-grade greenschist to amphibolite facies of 6 kbar in pressure and 430 – 550 °C in temperature during Oligo-Miocene. This metamorphic process was the effect of the Alpine orogenic events and subsequent extensional regime. The mineral assemblage of garnet, staurolite and kyanite describes the facies that affected only the Dilek nappe and Selçuk mélange, and the overlying Lycian nappes (Ashworth and Evirgen, 1985; Ring et al., 1999a; Jolivet and Brun, 2010; Candan et al., 2011). However, the metamorphic temperature during the alpine orogeny is thought to have not exceeded 540 – 600 °C (Koralay et al., 1998).

1.2.4 Brief Tectonic History of the Menderes Massif

The geodynamic evolution of the Aegean region in eastern Mediterranean started in the Late Cretaceous with the closure of the Tethyan ocean and is still active up to present-day. The exhumation of HP-LT metamorphic rocks, formation of metamorphic core complexes, active rifting in the backarc region, and trench are all

the features of the subduction zone tectonics in the convergent plate regimes. The paleogeographic reconstructions suggest that a northward subduction of the African Plate below the southern margin of the Eurasia from the Late Cretaceous to the present include three-step evolution for HP-LT metamorphic rocks; (1) subduction with the sinking plate, (2) exhumation within subduction channel, and (3) post-orogenic exhumation below low-angle normal faults in extensional metamorphic domes. According to the tomographic models a single subduction zone hypothesis suggests that it has been active through most of the Mesozoic and the entire Cenozoic. The present-day Aegean Sea started to form at least in the Oligocene times above the retreating African slab now still sinking below Crete and the Mediterranean Ridge (Jolivet and Brun., 2010).

The northward subduction of the African plate under the Eurasia on the Vardar Suture Zone resulted in a geological setting resembling subduction zone in the Aegean region. This subduction resulted in the formation of a trench in the forearc basin south of Crete filled with flysch sediments. Crete, Dodecanese, and Peloponnese are the island arc portion of the subduction zone. The Cretan basin to the north of Crete, is formed in the backarc region. Methana, Milos, Santorini, and Nisyros are the resemblance of the volcanic arc (Papanikolaou., 2021) (Figure 1.6).

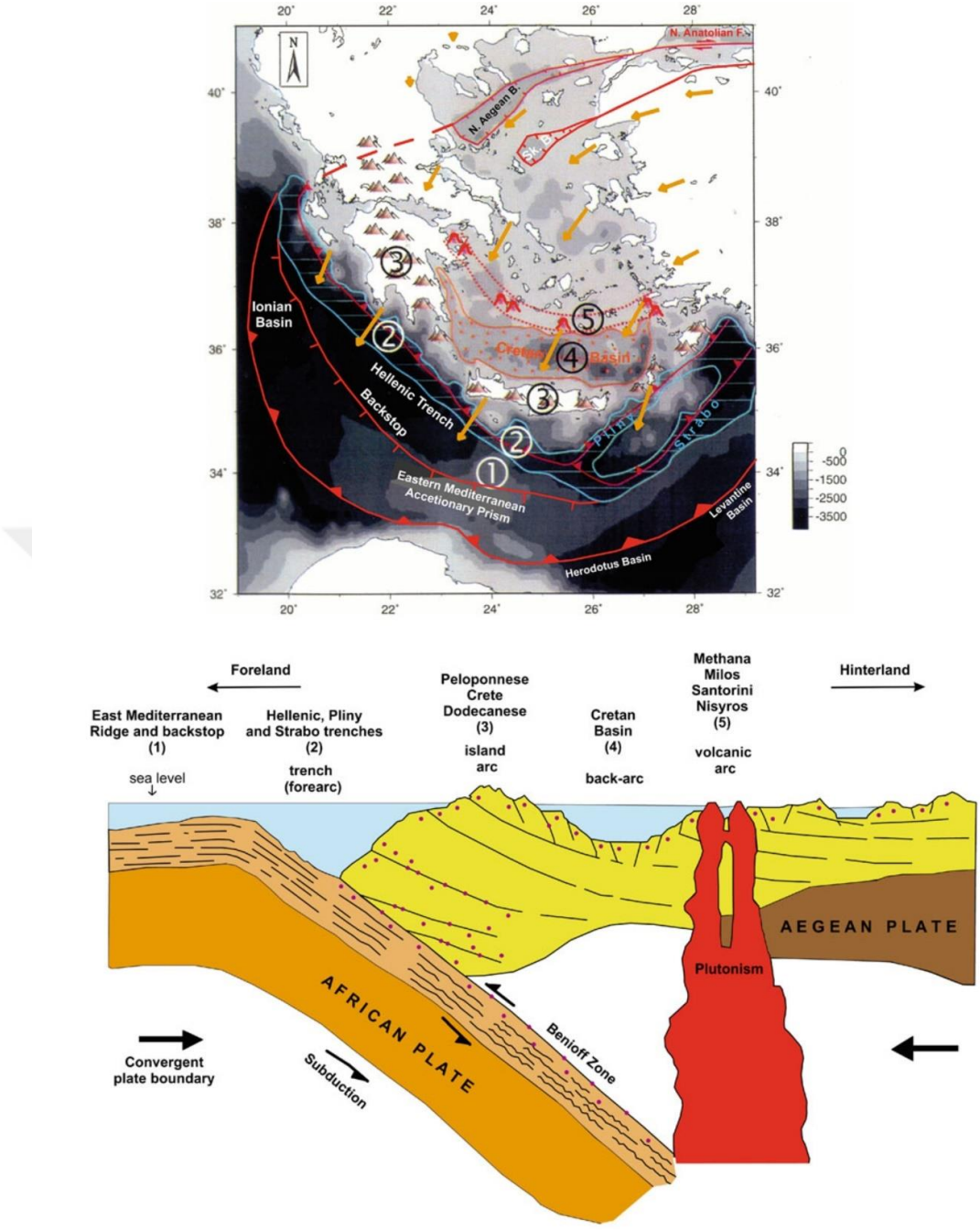


Figure 1.6 A) Simplified tectonic map showing the geometry of the Hellenic arc. B) Schematic representation in a transverse section of the Hellenic arc (Papanikolaou, 2021)

The Menderes Massif consists of four main nappes described and separated by their protoliths and tectono-metamorphic histories as follows in ascending order: Bayındır Nappe, Bozdağ Nappe, Çine Nappe, and Selimiye Nappe (Ring et al., 1999). These nappes make up one of the three major tectonic units in Anatolide Belt; (1) the Lower

Unit or Menderes Nappes (Ring et al., 1999), (2) The Middle Unit comprised of Dilek Nappe and Selçuk Mélange, and (3) The Upper Unit consists of İzmir-Ankara Zone mélanges and Lycian Nappes (Gessner et al., 2011) (Figure 1.7).

The development of Menderes Massif includes a series of orogenic processes such as, Pan-African orogeny, Permo-Triassic Cimmerian event, which is related to closure of remnant basin of Paleotethys, and Alpine orogeny (Şengör et al., 1984).

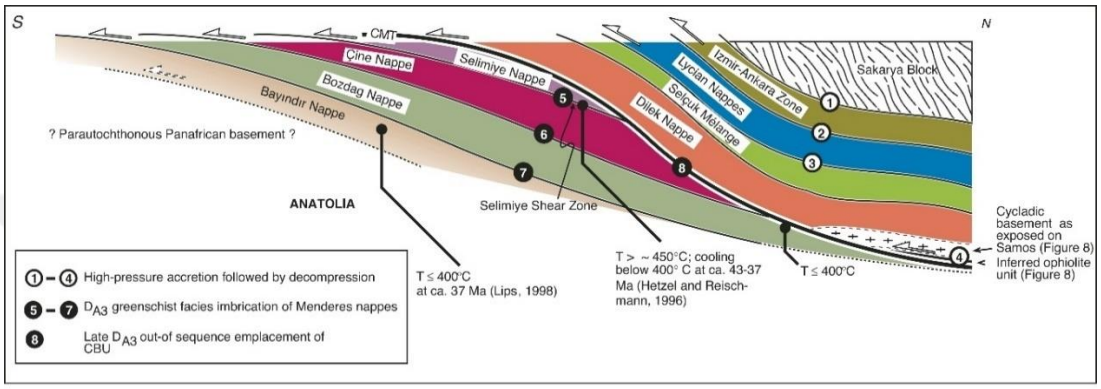


Figure 1.7 Interpretive thrust sequence during formation of the Anatolide Belt (Gessner et al., 2001c). CBU: Cycladic Blueschist Unit; CMT: Cyclades-Menderes Thrust (Gessner et al., 2011)

In Aegean region, the thrusting and HP metamorphism propagates towards the external Hellenides, in contrast, out of sequence thrusting of Dilek nappe/Selçuk Mélange and the Lycian nappes on top of the Menderes Nappes did not cause the HP metamorphism for external Hellenides (Ring et al., 1999a).

The Cycladic Blueschist Unit was assembled on the Menderes nappes by top-to-south thrusting during the greenschist metamorphic facies events in Eocene. The Menderes nappes successfully resisted the subduction. After the thrusting, greenschist events affected both massifs together and the tectonic contact of the Cyclades – Menderes Thrust was formed between the CBU and Menderes nappes during this event. This contact is considered as an out of sequence thrust ramp structure that cuts up-sections of Menderes nappes towards the south (Gessner et al., 2001c) (Figure 1.8).

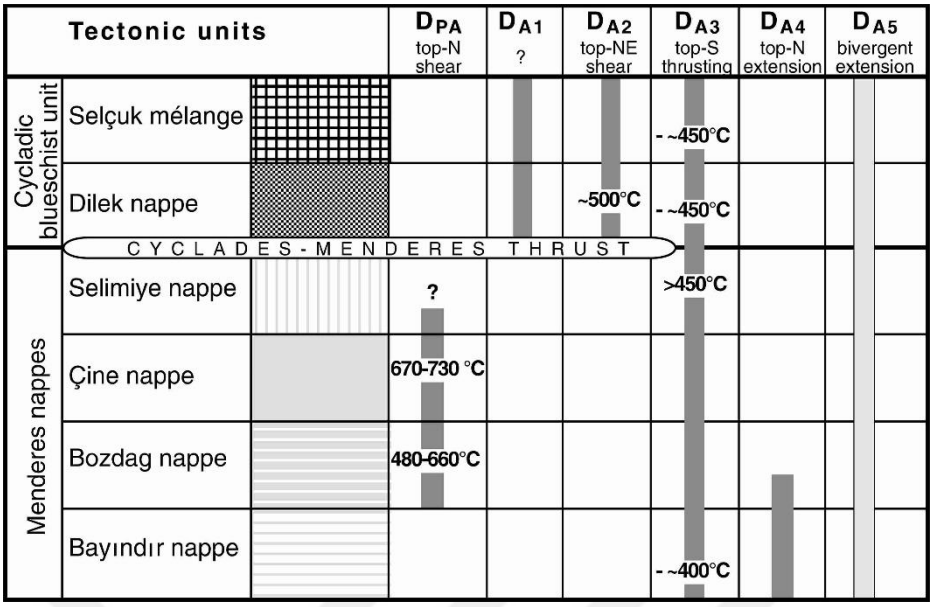


Figure 1.8 Diagram showing distribution of pre-Alpine and Alpine events in the tectonic units of Anatolide belt (Gessner et al., 2001c and references therein)

According to the structural investigations in the central Menderes Massif, the presence of a large-scale low angle extensional shear zone with top-to-N and NE shear sense was indicated. This NNE-directed extensional regime created a high angle normal fault that cuts the detachment fault and marks the southern boundary of the Gediz Graben. The central MM is characterized by N-NE trending stretching lineations in the northern parts and top-to-south shear sense in the southern parts of the submassif. This kinematic data indicated that a "bivergent" extension tectonic regime has been taking place in the Menderes Massif and suggest that a symmetrical collapse of the Alpine Menderes orogenic belt along two extensional shear zones (Hetzel et al., 1995a; 1995b).

During the Oligocene-Miocene, a regional brittle deformation phase of normal faulting dominated the western Türkiye. The exhumation process in the central Menders massif, initiated faulting along the east and west trending Ataşehir and Büyük low-angle detachment faults, and in the Gördes massif a high-angle Simav normal fault (Le Pichon et al., 1982; Bozkurt and Park, 1994; Hetzel et al., 1995a; 1995b). Nearly 150 km of N-S extension occurred in the entire Menderes Massif since Oligocene – Miocene (van Hinsbergen, 2010; Etzel et al., 2020) (Figure 1.9).

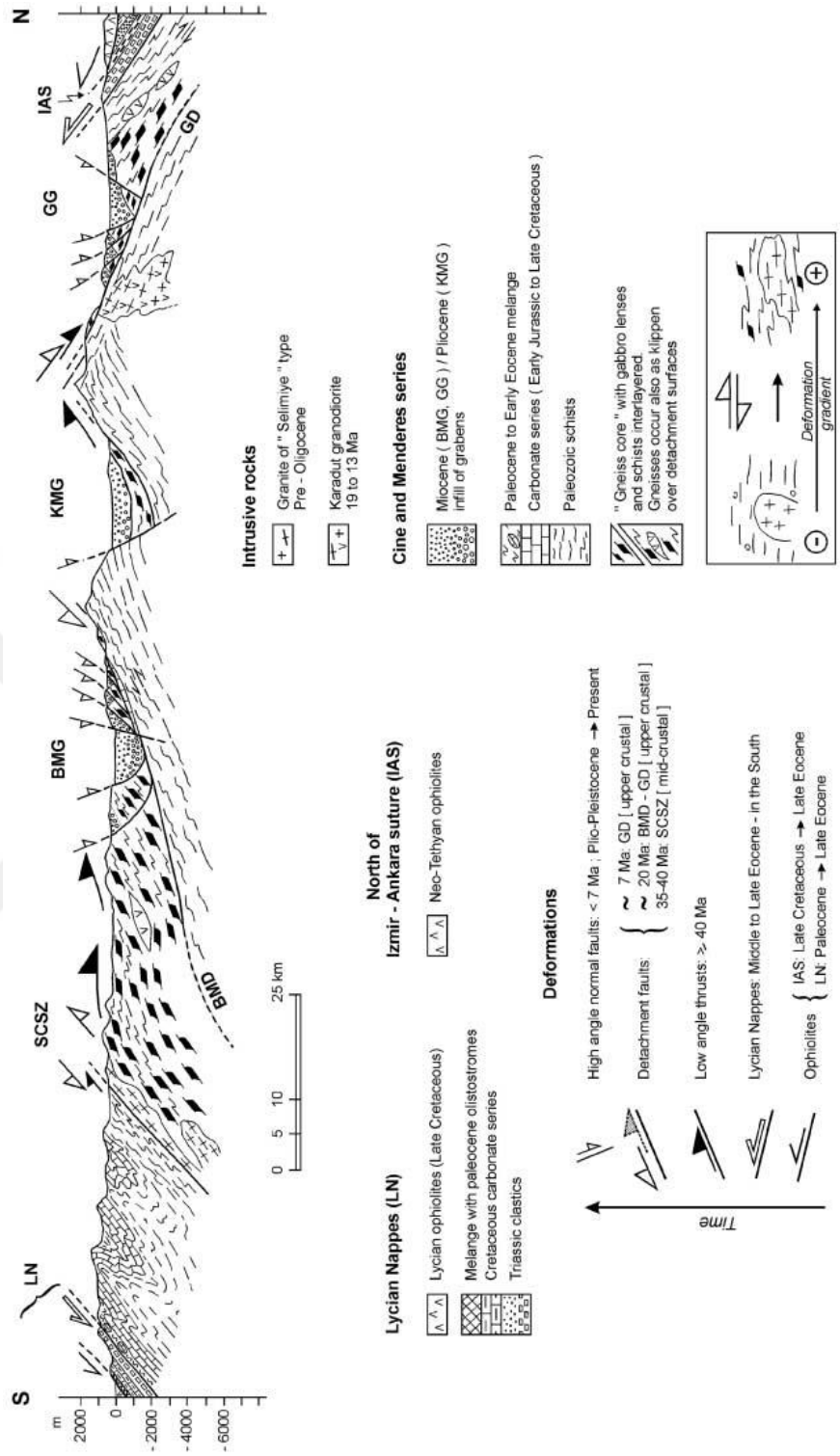


Figure 1.9 Cross section showing the extensional shear zones of the central Menderes Massif (Lips et al., 2001)

1.2.5 Correlations with Cycladic Blueschist Unit

The central Aegean region is represented by the Attic – Cycladic Crystalline Belt (ACCB) that is one of the main tectonostratigraphic units of Hellenic orogen and consists of two subunits, the upper unit of Cycladic nappe which only preserved in small areas of Cycladic islands, are of unmetamorphosed Permian to Mesozoic sedimentary rocks, ophiolites, greenschist to amphibolite-facies rocks and Late Cretaceous granitoids (Dürr et al., 1978; Bröcker et al., 2016).

The complex is divided into three main units according to their depositional age and metamorphic histories. The Upper Cycladic Unit, Cycladic Blueschist Unit (CBU) and the Basal Unit (Dürr et al., 1978; Maar and Jansen., 1983; Altherr et al., 1994; Kotowski et al., 2022).

The lower subunit of the ACCB is called the Cycladic Blueschist Unit (CBU) and it is separated from the upper subunit by a low angle detachment fault called the North Cycladic Detachment System (Jolivet et al., 2010).

The Cycladic Blueschist Unit is composed of a basement rock of schist and orthogneisses with Carboniferous (~360–300 Ma) age, and the overlying a Permo – Triassic passive-margin shelf sequence of marble, metasediments, and volcanics (Dürr et al., 1978; Ring and Layer 2003; Ring et al., 1999b; 2010; Bröcker et al., 2016).

The CBU experienced polyphase Tertiary metamorphisms, the HP/LT eclogite to epidote – blueschist facies metamorphism with pressure and temperature conditions of ~450 – 550 °C and ~12 – 20 kbar occurred mostly at the Eocene (40 – 50 Ma), while the regionally effective greenschist to upper amphibolite facies overprint (Temperature 350 – 520 °C and pressure ~5 – kbar) occurred around Oligocene to Miocene time (16 – 25 Ma) (Bröcker et al., 1993; 2013; 2016; Ring et al., 2010).

The metasediment rock units of the shelf margin in CBU from the Andros Island are dated using U-Pb detrital zircon method and the data obtained are given below. The obtained data from sample 5006 reveals the peak age of 270 – 230 Ma with youngest age of 198 ± 7 Ma, from the sample 1468 the peak age of 240 Ma and youngest age cluster of 205 +8/–4 Ma and finally from the sample 5764, the major

peak of 240 – 190 Ma with the youngest age cluster of 196 +2/–7 Ma (Figure 1.10) (Bröcker et al., 2016).

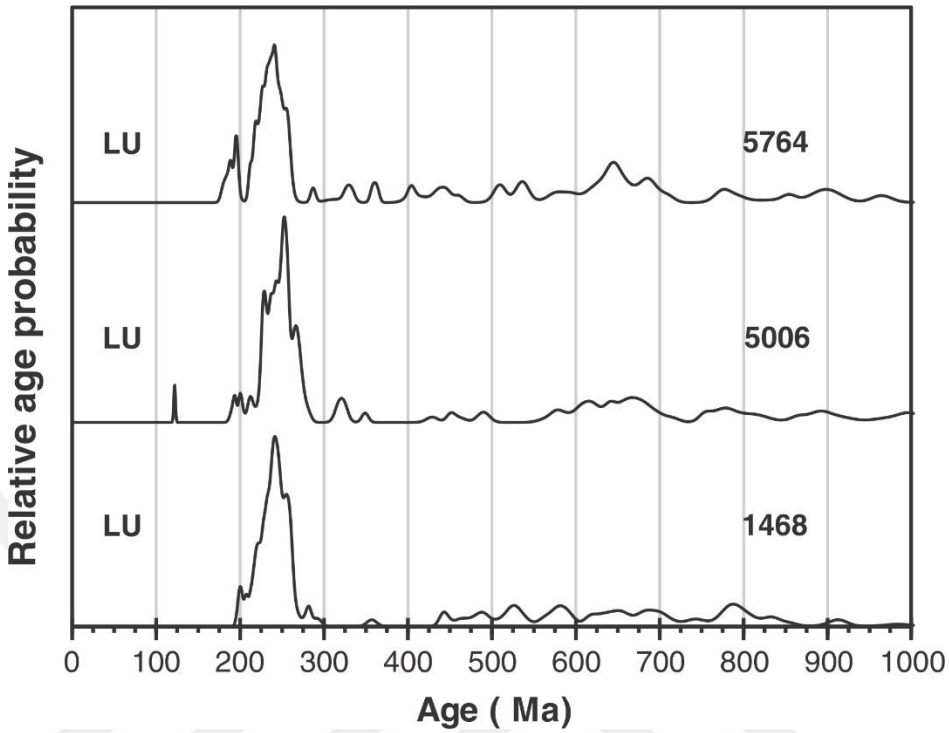


Figure 1.10 Normalized age distribution diagram showing ages of the samples 5764, 5006, 1468 from shelf sequence of CBU on Andros Island (Bröcker et al., 2016)

The basement of the CBU is well exposed in the islands of Ios and Naxos. The metapelite schist sample (CB04) collected from the basement rocks of Naxos yields an age of 400 ± 13 Ma with 101% concordance, while a sample of garnet-bearing microgranite (CB08) located southeast of Ios town yielded a concordia age of 310 ± 3 Ma (Figure 1.11) (Zlatkin et al., 2018).

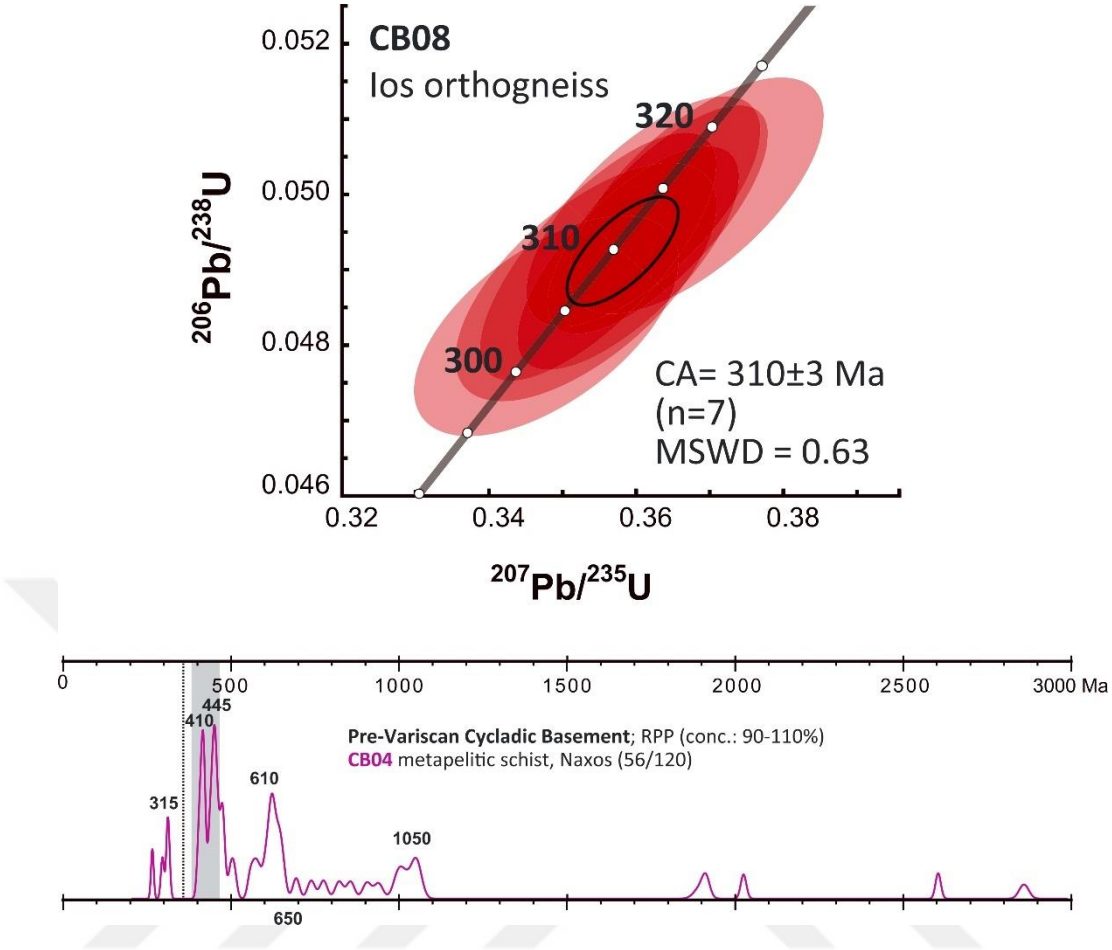


Figure 1.11 The U-Pb ages obtained from the collected sample of CB04 of Naxos Island at the bottom and the CB08 of Ios Island at the top (Zlatkin et al., 2018)

Ring et al., (1999a), indicated that the architecture, age of the basement and the pre-alpine and alpine tectonometamorphic history of both massifs are different from each other, MM consists of remnants of Cycladic massif as an overlying exotic unit on the Menderes nappes. According to Dürr et al., (1978), the basement and cover of both massifs experienced similar tectonic phases, however the Cycladic massif has a tectonic position above the Menderes nappes, the latter represents an exotic unit to the rest of the Menders massif (Ring et al., 1999a).

1.3 Study Area

The Özdere – Gümüldür region is located to the south of İzmir and nearly 32 kilometers to the southeast of Seferihisar. The study area covers nearly an area of 62 square kilometers in between the locations of; zone 35S 505000 - 4213000 northwest

and 515000 - 4203000 southeast according to the UTM-ED84 coordinate system (Figure 1.2 and Figure 3.1).

1.4 Previous Studies of Gümüldür – Özdere Area

The research paper "Crystalline basement and allochthon units of Gümüldür region" by Erol Başarır and Yılmaz T. Konuk is summarized below emphasize some of the key points made in the article and to show the importance of the work to the related topic of this thesis. However, the earliest mapping of the region was carried out by Akartuna (1962) in 1/100000 scale. Due to the scale of the map, some geological details about the region were neglected.

Başarır and Konuk (1981), aimed to describe the relationship between the crystalline basement of the Menderes Massif and the unmetamorphosed rock series above it in Gümüldür – Kesre region, especially in the northwest flank of the Menderes Massif.

Based on the petrological analysis and characteristic mineral assemblages the metamorphic basement rocks of the study area, they concluded that the metasediments of the area have experienced low grade Barrovian type greenschist facies metamorphism within chlorite and biotite sub-facies similar to the Menderes Massif cover series (Başarır and Konuk, 1981).

The fold axes in the study area are consistent with the general fold axes within Menderes Massif with a trend of N20W and plunging to the SE. According to the microtectonic analysis in oriented thin sections, it was observed that the microfolds are also consistent with the Menderes Massif. They also point out that the chloritization of the metasediments are post tectonic with respect to the folds (Başarır and Konuk, 1981).

The Triassic sedimentary rocks were known in the Karaburun Peninsula, however, they are documented according to the calcareous algae fossil records in this study for the first time. The allochthonous units are dated as Triassic-Lower Jurassic based on *Teutloporella tabulata*, *Teutlopotella elongata*, *Palaeodasycladus mediterraneous* and *Taumatoporella parvovesiculifera* (Başarır and Konuk, 1981).

The mentioned carbonate succession was later studied by İnal and İşintek, (2019) indicating the carbonate rocks are represented by neritic limestones, dolomitic limestones and dolostones of different blocks or slices of Bornova Flysch Zone. It was also stated that some blocks were upper Triassic to Lower Jurassic carbonates and some others consist only of Jurassic limestones.

The Triassic and Liassic neritic carbonate sequences of the Menderes-Gümüldür area are similar with those of Karaburun Peninsula, thus the Menderes-Gümüldür carbonates should be deposited in the same paleogeographic zone with the Karaburun-Emet sequences (İnal and İşintek., 2019).

Lastly the age of the thrust was interpreted as Eocene-Oligocene according to the well traceable mylonitized contact between the upper Triassic sequence and the lower metasediments (Başarır and Konuk, 1981).

The research by Çetinkaplan et al., (2020) was a regional study investigating the continuation of Cycladic Blueschist Unit high pressure rocks in western Anatolia. In that study, it was suggested that Eclogite and Blueschist units in western Anatolia are the eastern continuation of Cycladic Blueschist Unit in Türkiye and it was tectonically sandwiched between underlying Menderes Massif and overlying Afyon Zone/Lycian Nappes and the Bornova Flysch Zone.

According to Çetinkaplan et al., (2020), the CBU was characterized as a high-pressure unit and it was attributed to the closure of the Pindos Ocean and consisted of a Triassic to Upper Cretaceous coherent series that derived from passive continental margin sediments and, the tectonically overlying Upper Cretaceous Selçuk mélange with eclogite blocks within pelitic epidote – blueschist matrix.

Based on the conducted $^{40}Ar/^{39}Ar$ white mica and $^{206}Pb/^{238}U$ monazite datings the following ages were presented respectively; The coherent series has undergone epidote – blueschist facies metamorphism in middle Eocene ages of 44 ± 0.3 and 40.1 ± 3.1 Ma, the matrix of the Selçuk mélange has undergone epidote – blueschist facies metamorphism in 57.5 ± 0.3 and 54.5 ± 0.1 Ma, and the eclogite facies metamorphism of the blocks has occurred in Early Eocene 56.2 ± 1.5 Ma dated by U-Pb zircons (Çetinkaplan et al., 2020).

Finally, a retrograde metamorphic event overprints the coherent series that are dated 35.8 ± 0.5 and 34.3 ± 0.1 Ma by $^{40}Ar/^{39}Ar$ white mica and 31.6 ± 6.6 Ma by $^{206}Pb/^{238}U$ allanite dating methods, respectively (Çetinkaplan et al., 2020).

Due to the regional geologic constrains it was considered that the contact between the Cycladic Blueschist Unit and the Menderes Massif originally was a lithosphere-scale transform fault zone that is now defined as a ductile thrust fault. $^{40}Ar/^{39}Ar$ white mica ages from this contact, suggests the time of tectonic juxtaposition of the Cycladic Blueschist Unit and the Menderes Massif as 35.1 ± 0.3 Ma during late Eocene and occurred under greenschist facies conditions (Çetinkaplan et al., 2020).

It was suggested that the Cycladic Blueschist Unit is tectonically overlain by both Bornova Flysch Zone and the Afyon Zone/Lycian nappes. In Gümüldür region (the study area of this study), the Bornova Flysch Zone rests tectonically on the Triassic(?) section of the coherent series consisting of mica schists and conformably overlying metabauxite-bearing platform-type carbonates (Çetinkaplan et al., 2020).

1.5 Purpose & Scope

The ages of the metamorphic rocks in Özdere were based on the correlations. The study of Başarır and Konuk (1981) is outdated, and Çetinkaplan et al., (2020) have included the rocks of the study area to Cycladic Blueschist Unit and there is no radiometric dating from the Özdere area. This study aims to describe the maximum deposition age of metamorphic rocks in Özdere area based on the zircon populations and kinematic analysis of the metamorphic rocks of the Menderes Massif.

CHAPTER TWO
ANALYTICAL METHODS

The thesis writing process started by preparing required literature concerning the study area. Numerous previous study papers were prepared and examined during this step. Field work was planned and carried out accordingly, rock samples from the observation points collected systematically. The sample preparations and laboratory works were conducted and obtained data were analyzed and presented in this research paper.

2.1 Field work

The study area was mapped in the scale of 1/25000. During the process of geological mapping, local topographic map sheets of İzmir L18-D3, L18-D4, and Aydın M18-A2 were used for references. Tectonic and tectonostratigraphic relationships of rock units found in the study area were observed and described. In total, 83 rock samples from the rock units of study area were collected for the purposes of revealing the maximum depositional age, carrying out kinematic analysis, and petrographic examinations.

2.2 Sample Preparation and Laboratory Work

To describe the maximum deposition age of metamorphic rocks in Özdere area based on the zircon populations and tectonostratigraphy by the kinematic analysis, samples were collected from various locations on both tectonic slices of Özdere and Gümüldür. Collected samples were prepared for kinematic analysis as oriented thin sections, for petrographic analysis as thin sections, and for radiometric dating as zircon grain separation from the samples.

2.2.1 Thin Sections

As mentioned before, oriented thin sections and petrographic thin sections were prepared during the laboratory work. The oriented thin sections are required to conduct kinematic analysis by observing shear sense indicators that formed during the deformation of the rock unit. The indicators may include structural elements of rock

fabric such as S-C structures, porphyroblast, porphyroclasts, microfolds, micro faults, sigmoids, shadow pressures, and grain growth or recrystallizations.

The rock samples for oriented thin section purposes must be collected by showing the north direction on the sample and the thin section must be prepared as cutting parallel to the lineations and perpendicular to the schistosity of the rock. Then the north direction is shown on the thin section as a notch. On the other hand, the petrographic thin sections are prepared using standard techniques.

2.2.2 Zircon Grain Separation

Zircon grain separation process was carried out by using standard procedures of jaw crushers, roll mill, sieving (e.g. into 200 micrometers), wet shaking table, magnetic separation (Frantz Isodynamic Separator), heavy liquid separation (Bromoform), and hand picking by using binocular microscope. Collected zircon grains then mounted in epoxy resin and polished. All the procedures were carried out in the sample preparation laboratories of Dokuz Eylül University Geological Engineering Department.

The collected and polished zircon grains then were sent to Geochronology and Geochemistry Laboratory at Istanbul University Cerrahpaşa Faculty of Engineering to carry out the detrital zircon (DZ) U-Pb dating by laser ablation-inductively coupled plasma-mass spectrometry (LA-MC-ICP-MS) method.

Then, the acquired raw U-Pb dates were sent back and reduced on the age distribution feature of AgeCalcML© software to obtain Kernel Density Estimate (KDE) and concordia diagrams.

This open-source data reduction software (AgeCalcML©) is developed by geoscientist Kurt Sundell at the Arizona LaserChron Center, Department of Geosciences, College of Science at the University of Arizona and it is available for any researcher or laboratory to use and/or modify as they wish (github.com/kurtsundell/AgeCalcML) (Sundell et al., 2021).

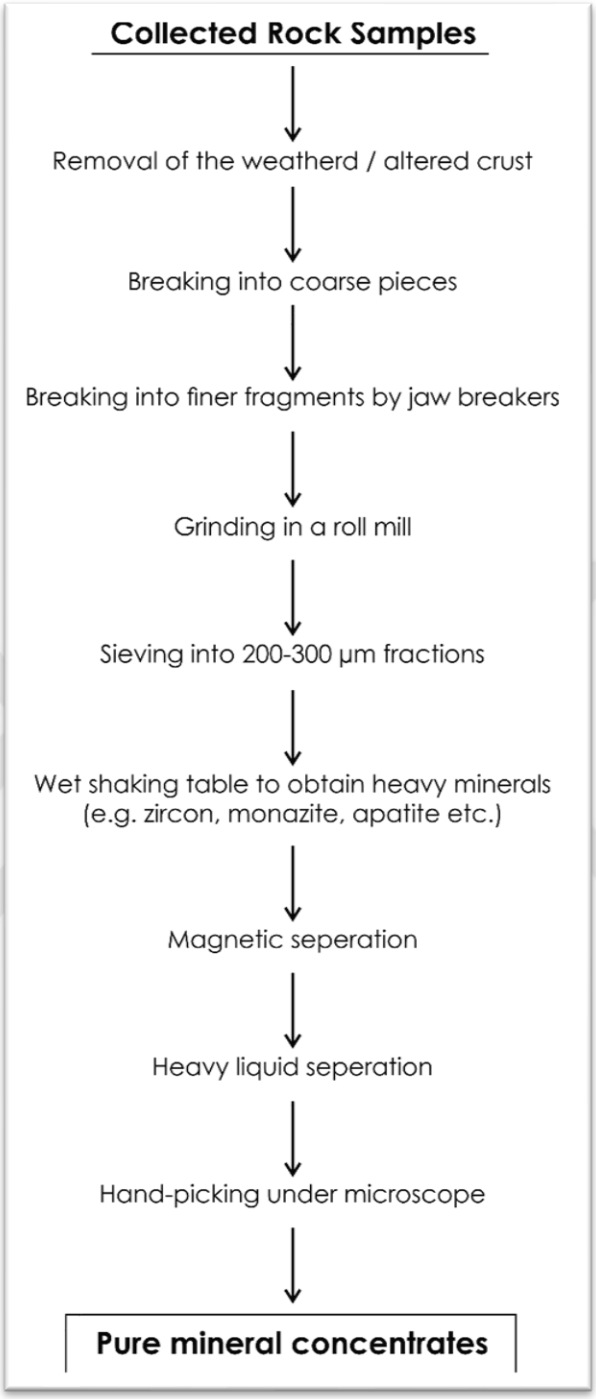


Figure 2.1 Schematics showing the extraction process steps of common minerals from rock samples

CHAPTER THREE
GEOLOGY OF THE ÖZDERE – GÜMÜLDÜR REGION

In this chapter it's aimed to describe and present the local geological and structural features of the rock units found within the study area of Özdere and Gümüldür regions. According to the field observations a geological map was prepared (Figure 3.1 – 3.4) and kinematic analysis was conducted by systematically measured structural data at about 192 observation points. The presented stereonet projections below are prepared by plotting the measured data of fabric elements such as crenulation fold axes, mineral stretching lineations and schistosities.

The Menderes Massif rocks units that are found within the study area are mainly schist units with different mineral assemblages and the overlying metacarbonates (detailed petrographic explanations are made in Chapter Four – Petrography of rock units). The rock units in ascending order are garnet-muscovite schist, quartz-muscovite-chloritoid-kyanite schist, chlorite-biotite-garnet schist, metacarbonates that consist of marbles, metadolomites and dolomitic marbles and lastly the unconformably overlying youngest unit of alluvium.

One of the main structural features of the study area is the mylonitic detachment shear zone located in between two tectonic slices of Özdere Schists to the west and Zindan Schists to the east. The mylonitic shear zone separates the lower tectonic slice of Özdere Schists consisting of garnet-muscovite schist unit and the upper tectonic slice of Zindan Schists consisting of quartz-muscovite-chloritoid-kyanite schist, chlorite-biotite-garnet schist in ascending order. Another ductile shear zone was observed between the Zindan tectonic slice and the overlying metacarbonates of the Kargıcak Marbles separating these units from each other and named Koru Shear zone.

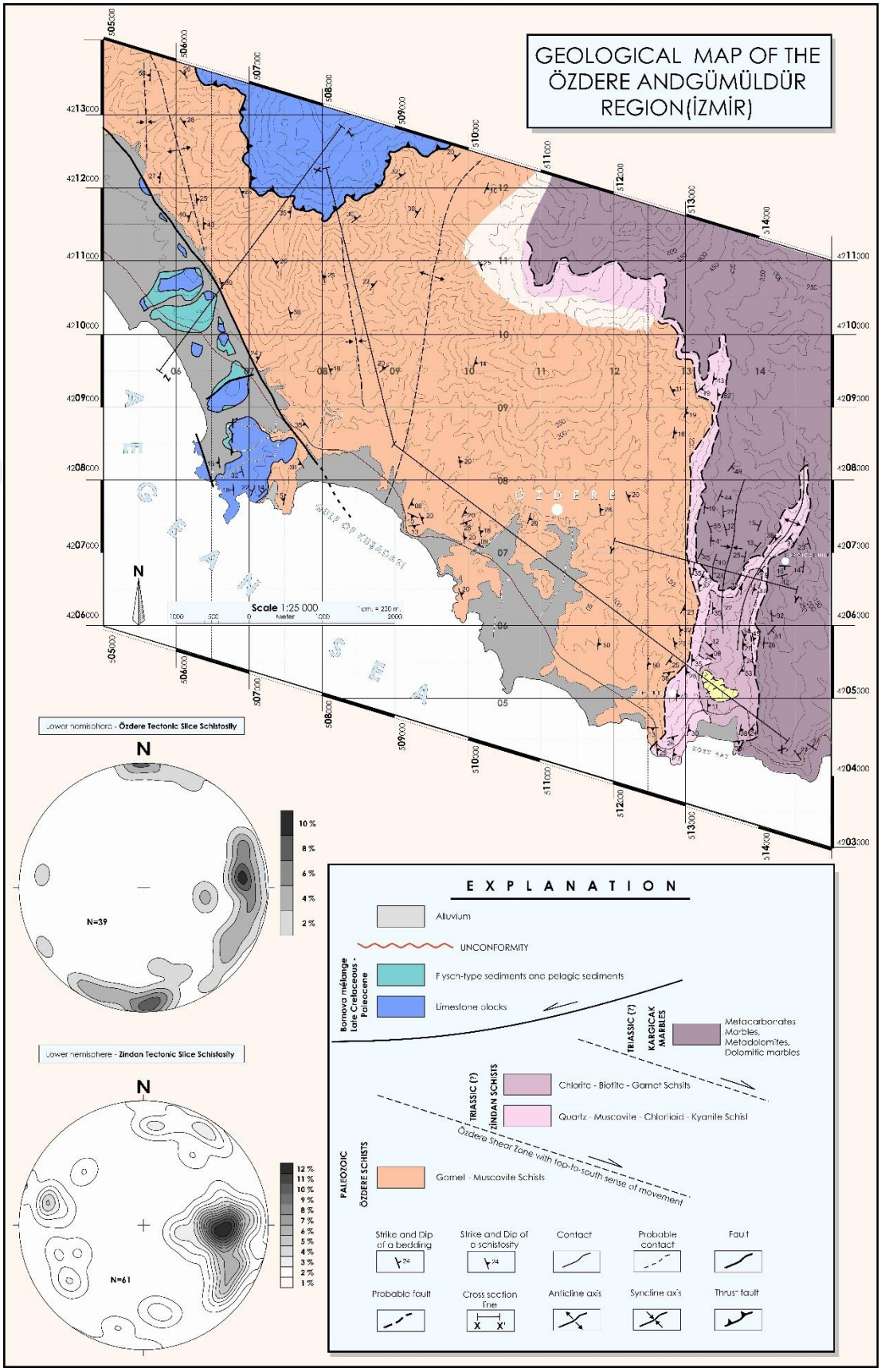


Figure 3.1 Geological map of the Özdere - Gümüldür area (Modified after Başarır and Konuk 1981)

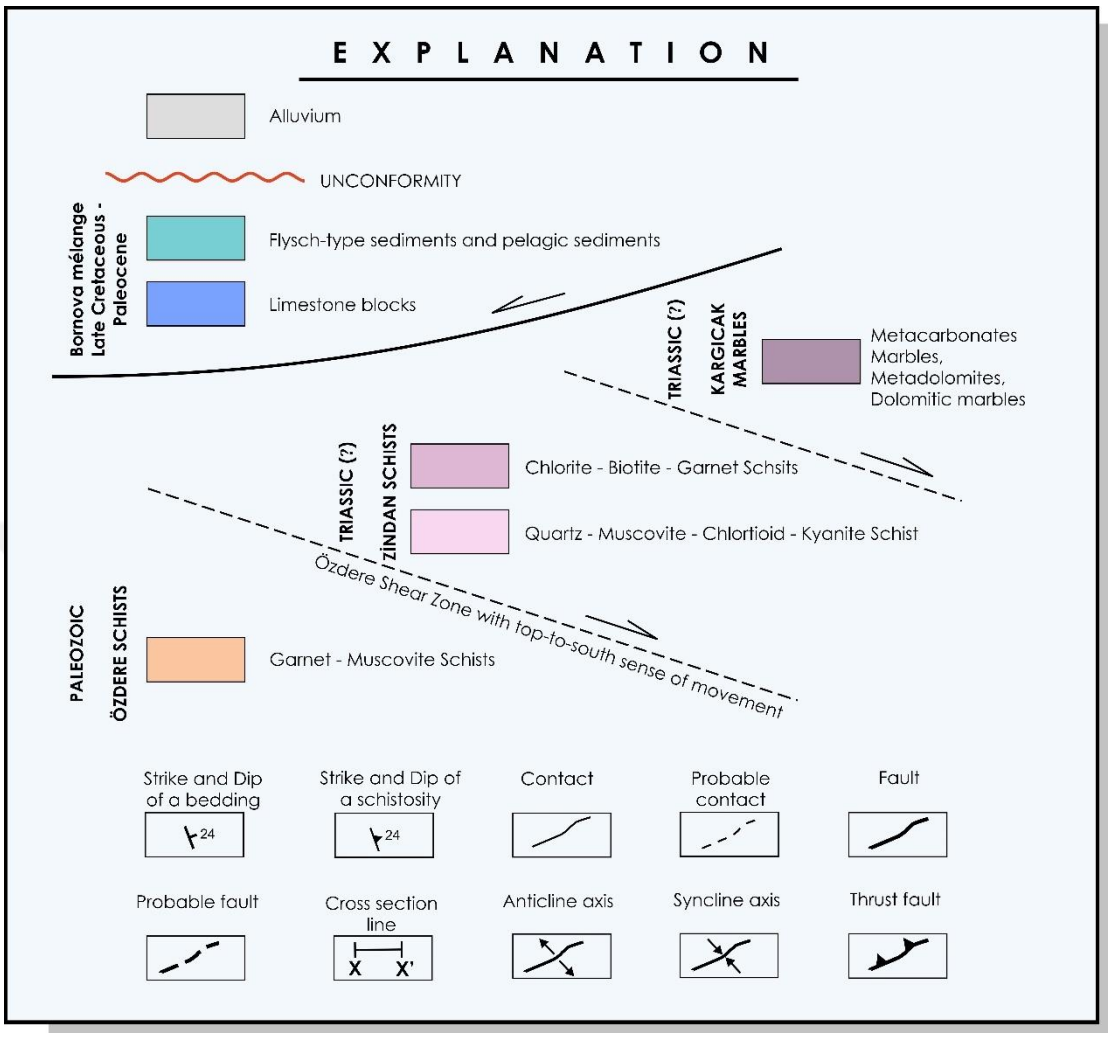


Figure 3.2 Explanation of the geological map and the general tectonostratigraphic section

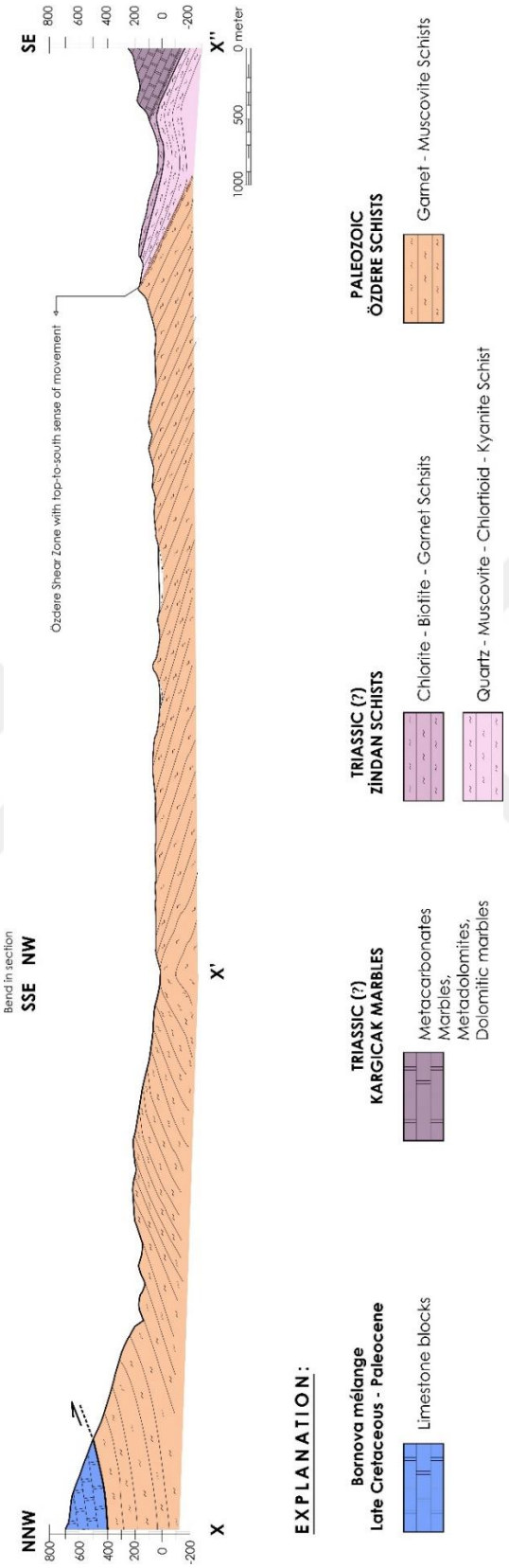


Figure 3.3 Cross section of X-X"

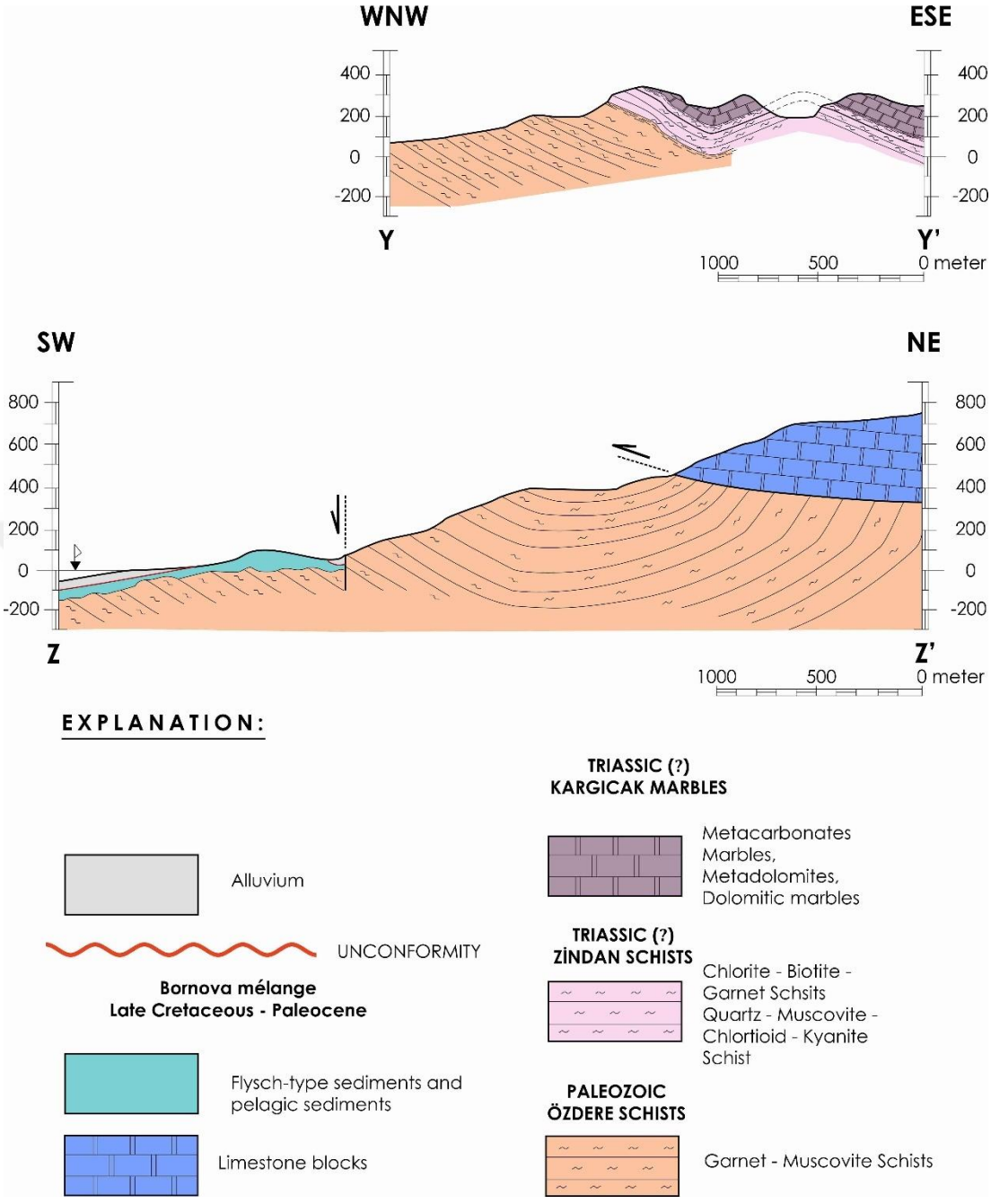


Figure 3.4 Cross sections of Y-Y' and Z-Z

'

3.1 Özdere Schists

The Özdere Schist unit mostly crops out in the western part of the study area by the lithology of garnet-muscovite schist. This unit of schist is observed in greyish – brown to grey colors (Figure 3.5 – 3.7) and generally exhibits well developed stretching lineation over the foliated schistosity which allows conducting kinematic analysis (Figure 3.8). The outcrops also display porphyroblastic-anastomosing texture with garnet porphyroblasts of grain size ranging between 1 mm to 3 mm in diameter (Figure 3.9). The detailed observational notes such as schistosity and stretching lineation trend measurements are made as figure captions below in the following pages of this section.



Figure 3.5 The landscape view of the study area showing the mylonitized shear zone with dashed white line. The area under the line represents the Özdere Schists while the upper part represents the Zindan Schists. The thick grey marbles of Kargıcak are seen resting above the Zindan Schists (coor: UTM-35 S 0510082/4207349) (Personal archive, 2024)

The landscape view of the study area showing the mylonitized shear zone with dashed white line. The area under the line represents the Özdere Schists while the upper part represents the Zindan Schists. The thick grey marbles of Kargıcak are seen resting above the Zindan Schists.



Figure 3.6 General field view of the Garnet-muscovite Schist unit on an outcrop. Notice the well-developed schistosity (coor: UTM-35 S 0509240/4207383) (Personal archive, 2023)



Figure 3.7 The well-developed schistosity of the unit (coor: UTM-35 S 0509148/4207335) (Personal archive, 2023)



Figure 3.8 The brownish grey to gray color of the Garnet-muscovite schist unit. Iron oxide coatings are observed as patchy stains (coor: UTM-35 S 0509148/4207335) (Personal archive, 2023)



Figure 3.9 The poorly visible porphyroblastic texture of the Garnet-Muscovite schist unit. Some garnets are missing due to the erosion of and weathering of the rock, but the cavities remain (coor: UTM-35 S 0509148/4207335) (Personal archive, 2023)

This Özdere Schist unit is also rich with deformed veins that are observed in many locations widespread though the outcropping area. These veins vary in size, shape and

length but generally exhibit parallelism with the schistosity and they are usually coated by iron oxides (Figure 3.10 – 3.11).



Figure 3.10 Oxidized quartz veins exhibiting parallelism with the schistosity of the Garnet-Muscovite schist unit. The stretching lineation trends are measured as 199/12 and the schistosity as 170/14 (coor: UTM-35 S 0509148/4207335) (Personal archive, 2023)

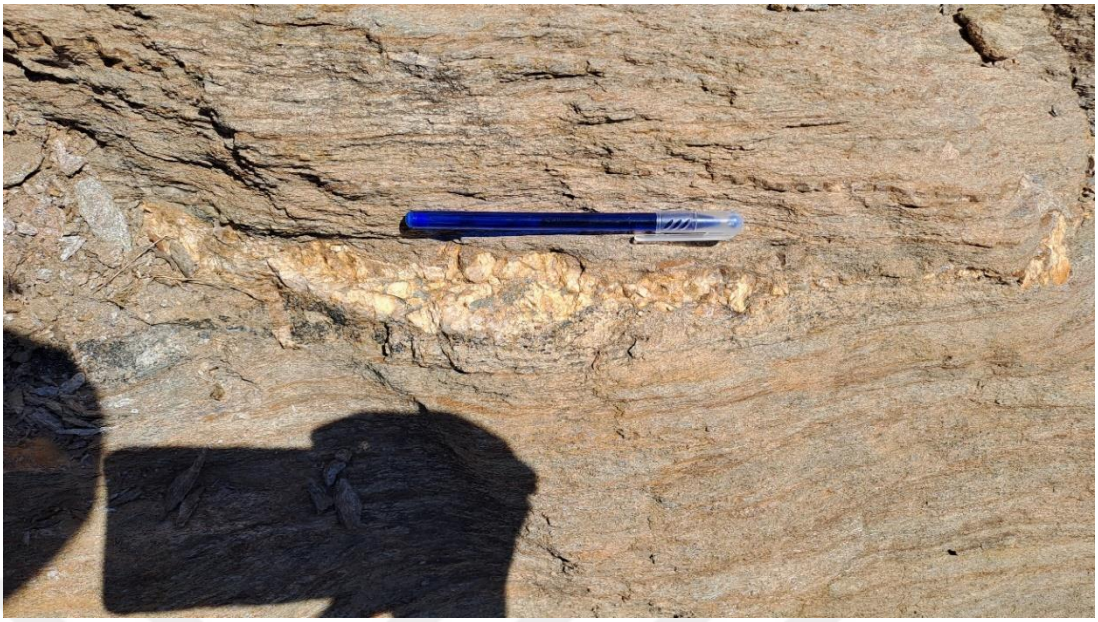


Figure 3.11 Some other veins of feldspars are also observed resembling pegmatites (coor: UTM-35 S 0512594/4205045) (Personal archive, 2023)

The quartz veins are generally observed as deformed structures such as intrafolial, kink, and sheath folds having fold axial plane nearly parallel to the schistosity and sometimes coexisting with quartz rods that are also parallel to the stretching lineations (Figure 3.12 – 3.17).

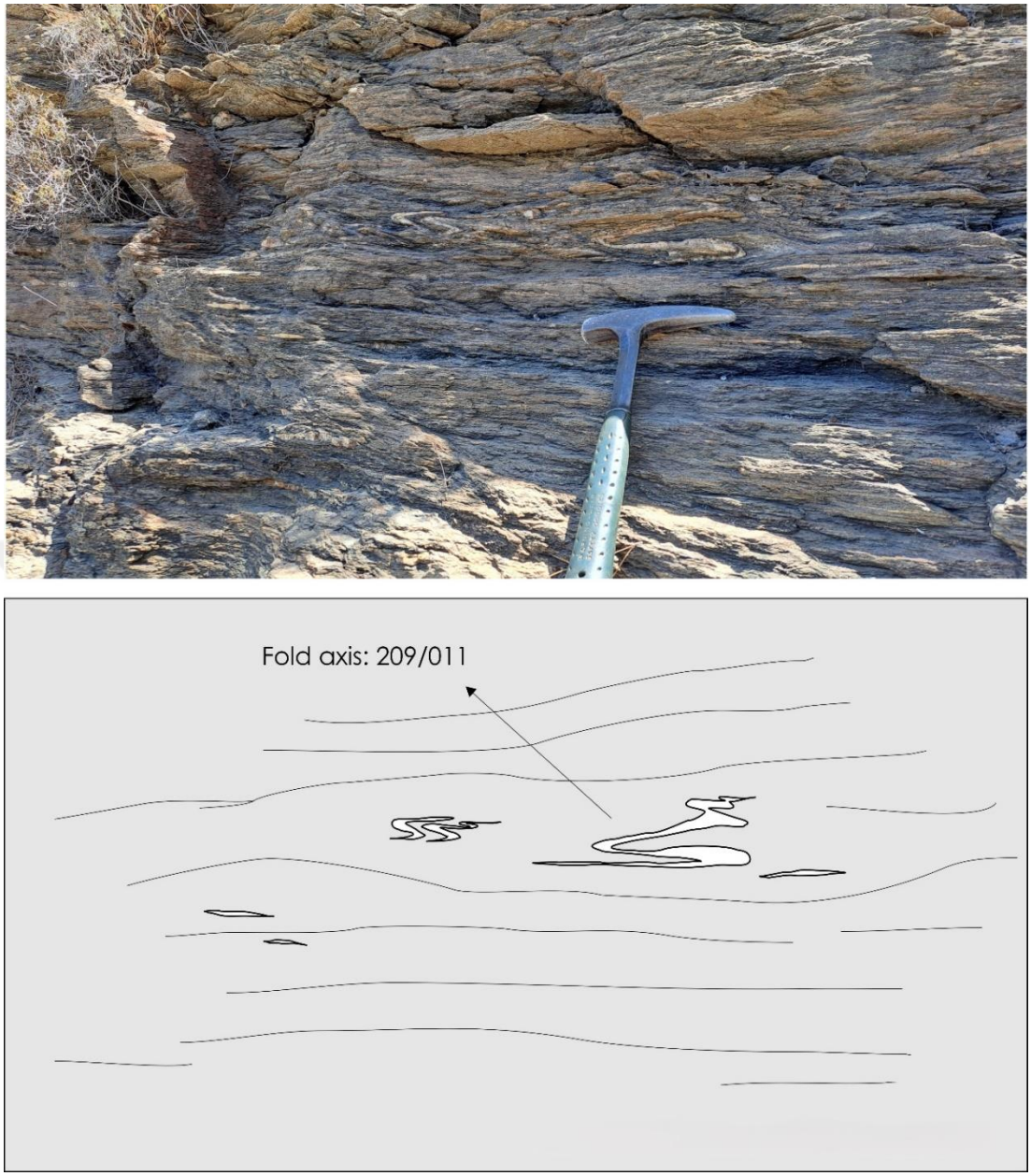


Figure 3.12 Intrafolial folds of the quartz veins are observed in between foliations of the rock unit. The fold axis was measured as 209/11 (coor: UTM-35 S 0509148/4207335) (Personal archive, 2023)

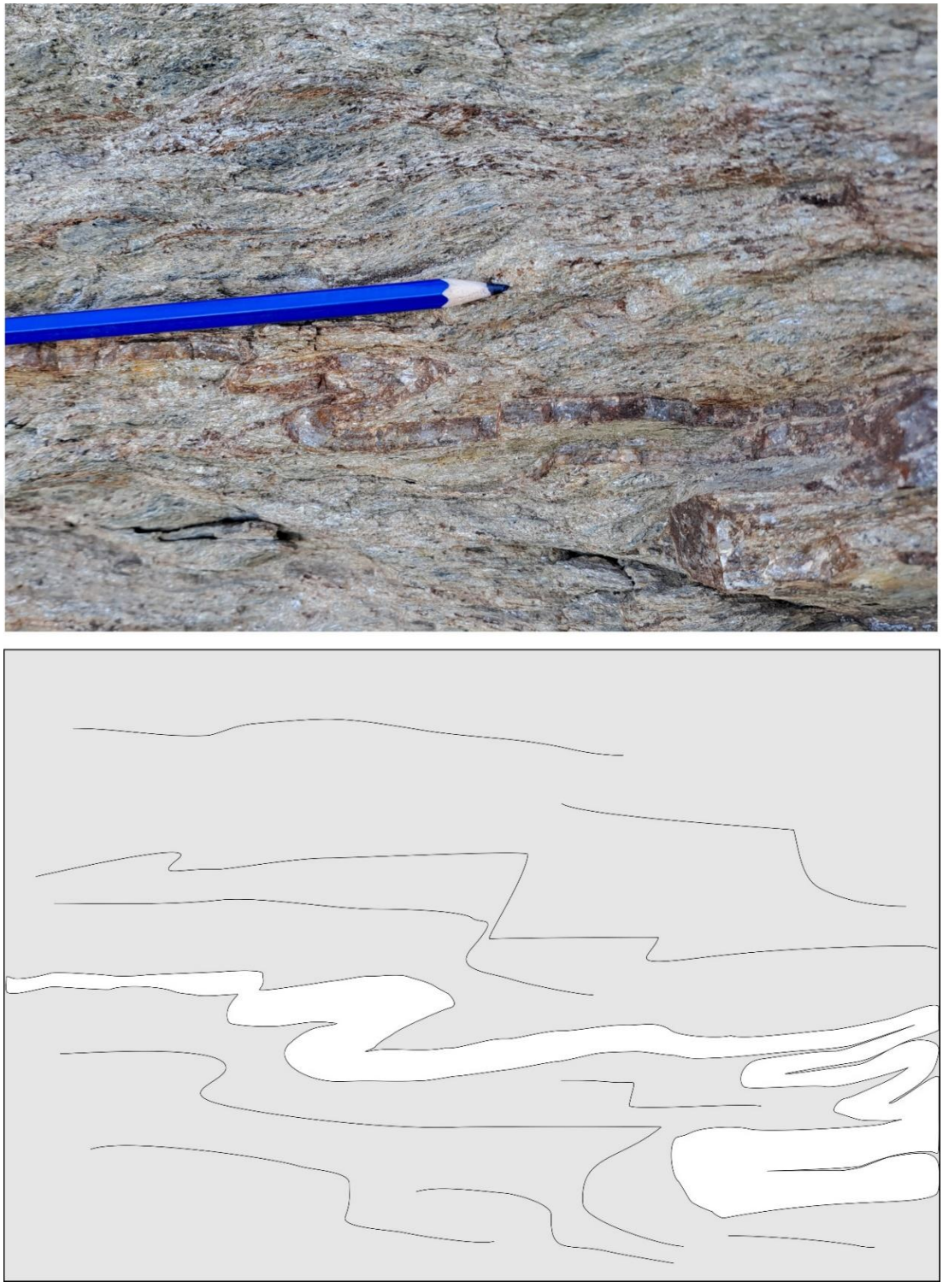


Figure 3.13 Recumbent quartz vein folds of approximately 1cm in width and 30 cm in length, developed nearly parallel to the schistosity. The fold axis and stretching lineations were measured as 184/19. The schistosity of the outcrops was measured as 123/25 (coor: UTM-35 S 0512937/4205506) (Personal archive, 2023)



Figure 3.14 A recumbent quartz vein fold with fold axis of 232/02 within the schistosity of 214/08. Notice the thickness difference between the limbs of fold (coor: UTM-35 S 0509139/4207502) (Personal archive, 2023)



Figure 3.15 The sheath folds within the unit. Notice how the eroded parts reveal the fold structure (coor: UTM-35 S 0509174/4207469) (Personal archive, 2023)

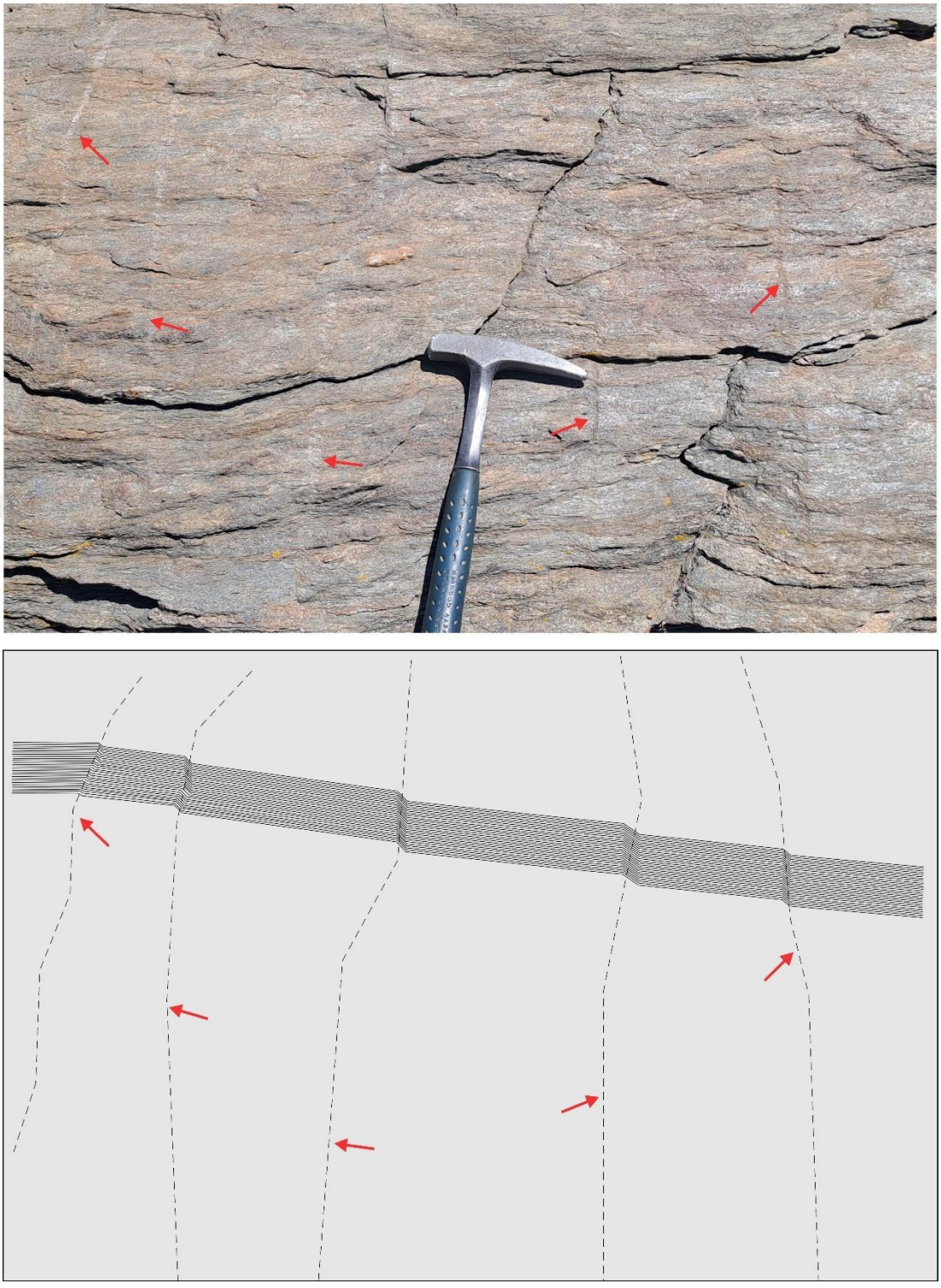


Figure 3.16 Kink bands that are faintly visible at a certain direction. Notice the quartz rod above the hammer head with perpendicular linear fabric to the kink band axes. Stretching lineations are 188/07 and the schistosity is 146/07 (coor: UTM-35 S 0509246/4207489) (Personal archive, 2023)



Figure 3.17 The quartz rods having similar linear fabric with the mineral stretching lineations of 200/05. The schistosity of the outcrop is measured as 178/04 (coor: UTM-35 S 0509283/4207373) (Personal archive, 2023)

The deformed quartz veins within the foliations of the unit also act as shear sense indicators because they are observed in the form of quartz sigmoids. The quartz sigmoids that are developed parallel to the stretching lineations and perpendicular to the schistosity are crucial sense of movement indicators in kinematic analysis (Figure 3.18 – 3.23).



Figure 3.18 The typical section for the kinematic analysis of shear sense indicators. The quartz sigmoid is perpendicular to the schistosity and parallel to the stretching lineations. Top-to-south sense of shear was indicated (coor: UTM-35 S 0510141/4207086) (Personal archive, 2024)



Figure 3.19 Mesoscopic quartz sigmoid with top-to-south sense of shear. Schistosity of the outcrop was 105/19 and the measured stretching lineations were 178/05 (coor: UTM-35 S 0513017/4208895) (Personal archive, 2024)

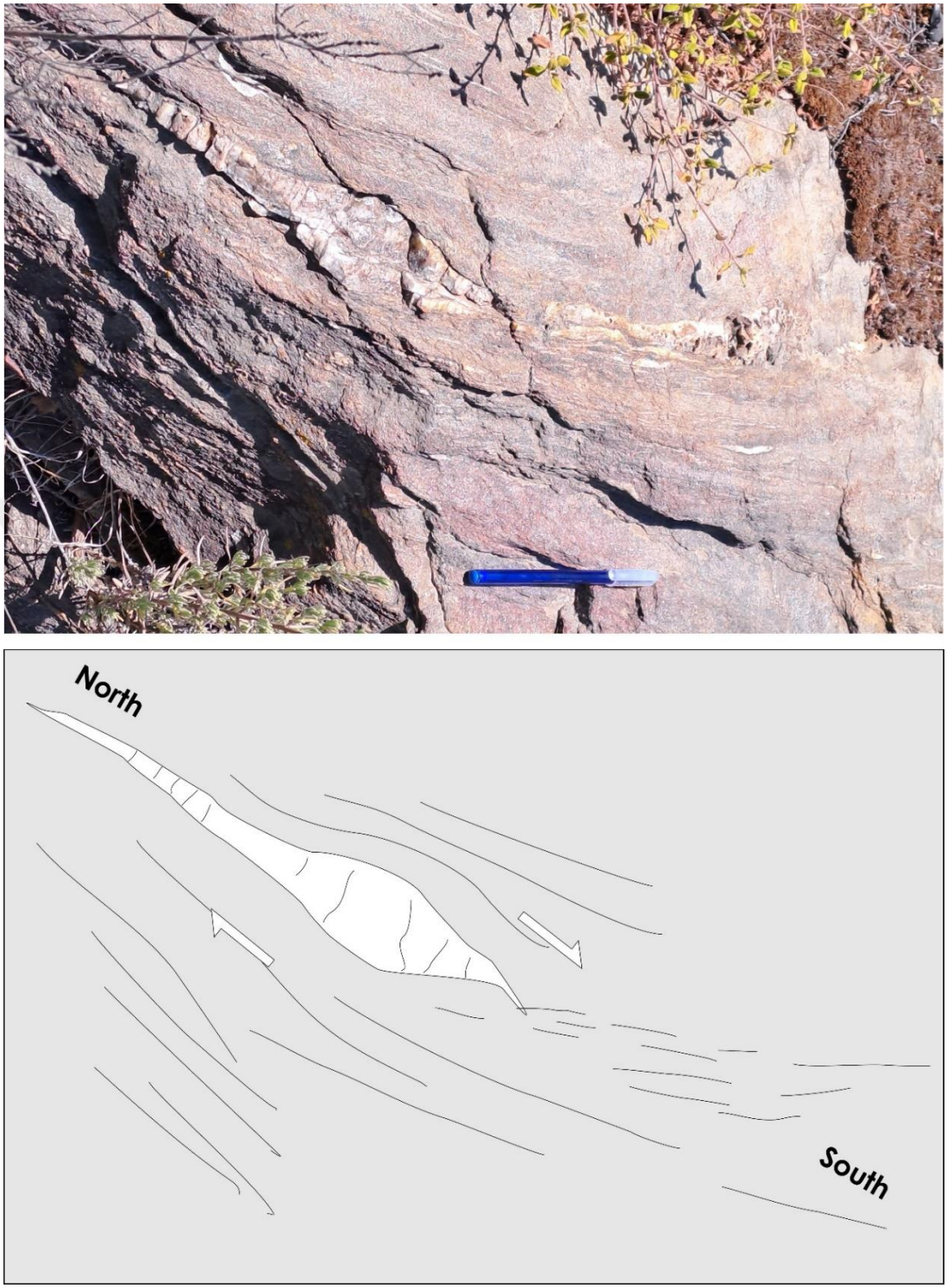


Figure 3.20 Iron oxide coatings as hematite mineralization observed at the localities rich with quartz veins. The quartz sigmoid exhibits a top-to-south sense of movement. The trend of the schistosity is measured as 178/04 and the stretching lineation as 200/05 (coor: UTM-35 S 0509240/4207383) (Personal archive, 2023)



Figure 3.21 A quartz sigmoid with top-to-south sense of shear indicator. Stretching lineations are 180/04 and the schistosities are 116/20 in trend (coor: UTM-35 S 0509990/4207423) (Personal archive, 2024)



Figure 3.22 Sigmoidal quartz vein with top-to-south sense of shear. Schistosity is measured as 082/23 (coor: UTM-35 S 0512958/4205559) (Personal archive, 2023)

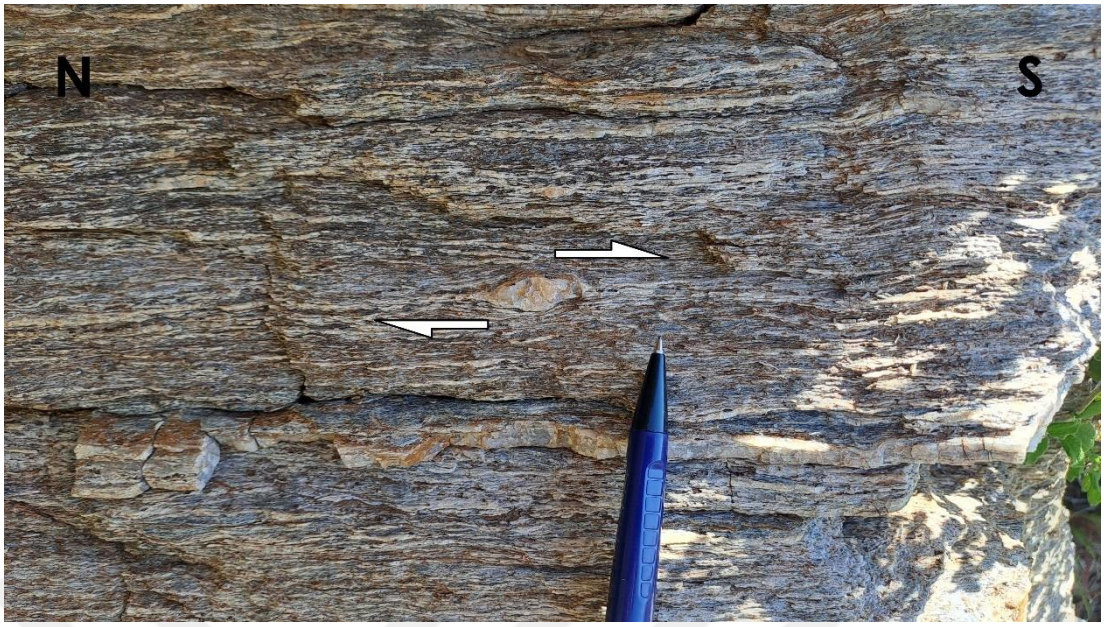


Figure 3.23 The S-C structures and quartz sigmoids clearly indicate top-to-south sense of shear. Schistosity 087/20. Stretching lineation 359/02 (coor: UTM-35 S 0509991/4207241) (Personal archive, 2024)

Some brittle deformation structures such as joints and fractures were also observed during the field work, however they were neglected due to the priorities of the research purposes. An example of brittle deformation can be given as shear sense indicator was en-echelon vein which was parallel to the lineations of 128/09 and perpendicular to the schistosity of 133/18 (Figure 3.24).



Figure 3.24 En-echelon quartz vein offset (coor: UTM-35 S 0513165/4209153) (Personal archive, 2024)

The S-C structures in mesoscopic scale were detected on some outcrops. These structures are tectonic fabrics that are used as shear sense indicators (Figure 3.25 – 3.26). Well-developed microscopic S-C structures were also observed during the petrographic analysis on the oriented thin sections of rock samples.

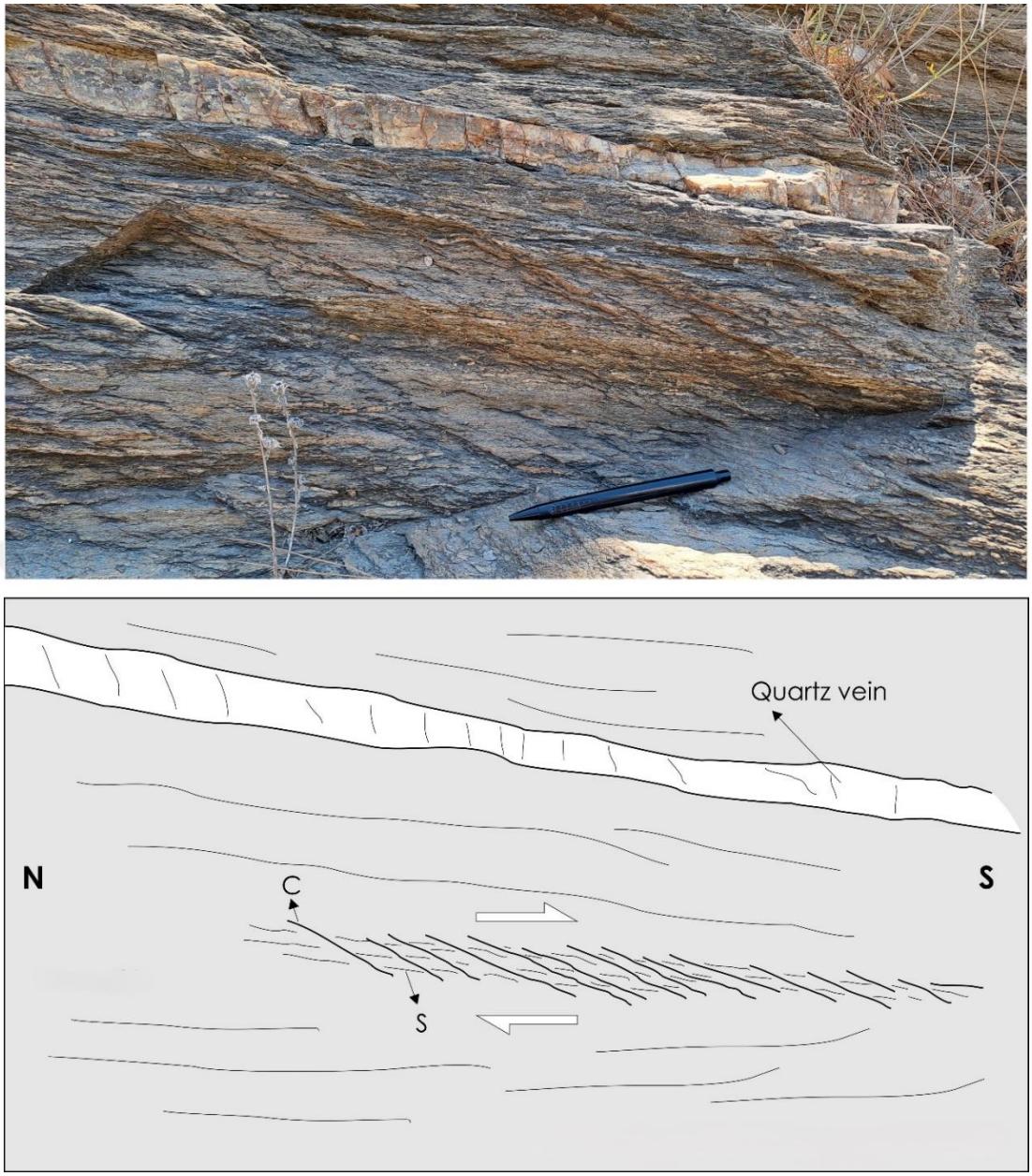


Figure 3.25 The parallel development of the quartz veins and S-C structures. Notice the top-to-south sense of movement indicator of the S-C structure. Schistosity trend is measured as 191/202 (coor: UTM-35 S 0509148/4207335) (Personal archive, 2023)

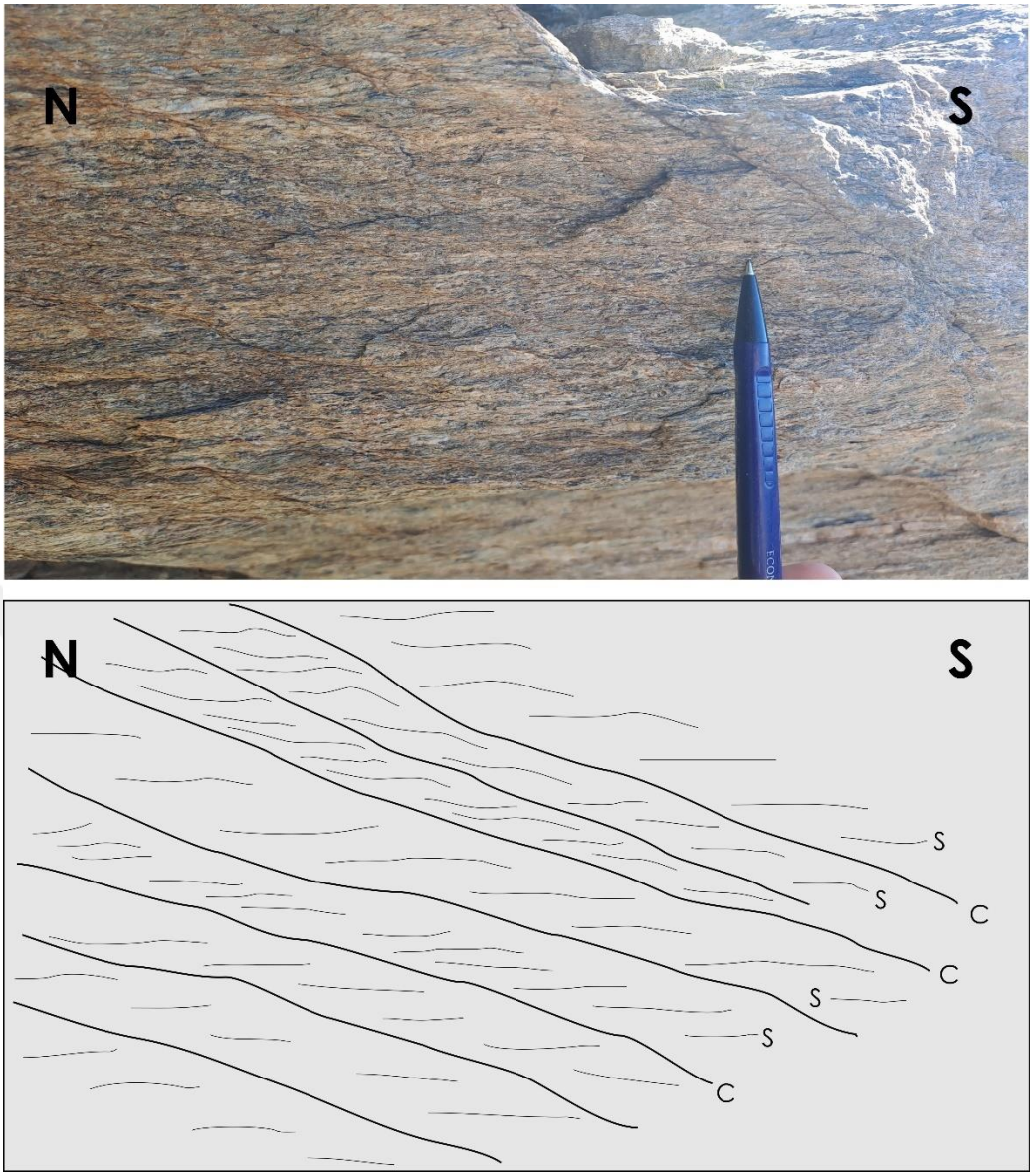


Figure 3.26 The poorly visible S-C structures. Indicates top-to-south sense of shear (coor: UTM-35 S 0509991/4207241) (Personal archive, 2024)

All the observed shear sense indicators of quartz sigmoids, quartz vein folds, and s-c structures of the Özdere Schists indicate top-to-south sense of movement (See Chapter Six – Structural Interpretations for explanation of oriented thin sections). The upper contact of the Garnet-muscovite schist unit of Özdere tectonic slice is described as a mylonitized low angle detachment fault separating the Garnet-muscovite schist and tectonically overlying Quartz-muscovite-chloritoid-kyanite schist unit of Zindan tectonic slice (Figure 3.27 – 3.30).



Figure 3.27 The contact zone between the Özdere Schists and the overlying Zindan Schist is a mylonitized shear zone. According to the offset of the quartz sigmoids shown in the figure, top-to-south sense of movement was indicated (coor: UTM-35 S 0512995/4205606) (Personal archive, 2023)



Figure 3.28 A proximity to the Özdere shear zone has deformed the underlying Özdere Schist unit. Notice the highly deformed quartz veins that are folded (coor: UTM-35 S 0514704/4204386) (Personal archive, 2024)



Figure 3.29 The shear zone in between the Zindan Schists and the underlying Özdere Schist that is well exposed at the roadcut. Notice the pronounced grey mylonitized contact associated with the shear zone (coor: UTM-35 S 0512611/4204510) (Personal archive, 2024)



Figure 3.30 The mylonitized contact of the Özdere Shear Zone. The schistosity of foliations below the shear zone is measured as 181/13 and the mineral lineation are 171/05 in trend (coor: UTM-35 S 0512611/4204510) (Personal archive, 2024)

3.1.1 Kinematics of the Özdere Schists

As mentioned before, Gümüldür region was studied previously by Başarır and Konuk (1981) and the measured 45 foliation orientations of the schist unit were plotted on their map. A prepared stereographic projection of 45 measurements is shown below (Figure 3.31). As seen in the projection, the representative strike and dip of the foliations of Özdere Schist unit in the Gümüldür region chiefly demonstrates a NW-SE strike with a SW dip direction and another less common trend of NE-SW strike with a SE dip direction.

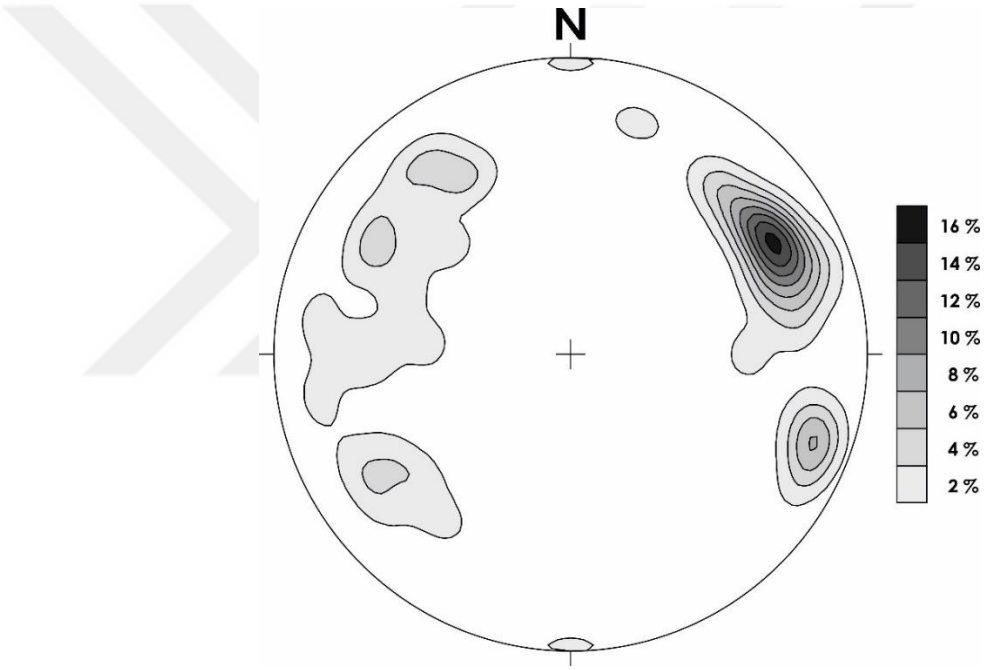


Figure 3.31 Stereographic plot showing the orientations of the foliations measured by Başarır and Konuk (1981) on the Özdere Schist unit. Lower hemisphere Schmidt projection (n=45)

The foliation measurements of Başarır and Konuk (1981) were combined with the Özdere Schist unit data obtained from the measurement during field work of this study and presented below (Figure 3.32). The achieved contour diagram shows that the representative trend of the schistosity is indeed NE-SW directed strike with dip directions of SE.

During the field work, some outcrops preserved good stretching lineations and were detected meanwhile some others poorly preserved mineral lineations or the linear fabrics were absent at all. The detected linear fabrics of Özdere Schist unit were measured and plotted on the stereographic projections. The resulted contour diagram indicates a significant N – S cluster (Figure 3.33 – 3.34).

The total linear structures of crenulation cleavage axes, fold axes, and stretching lineations were also plotted on the stereographic projection to prepare a rose diagram to illustrate the resemblance between them (Figure 3.35).

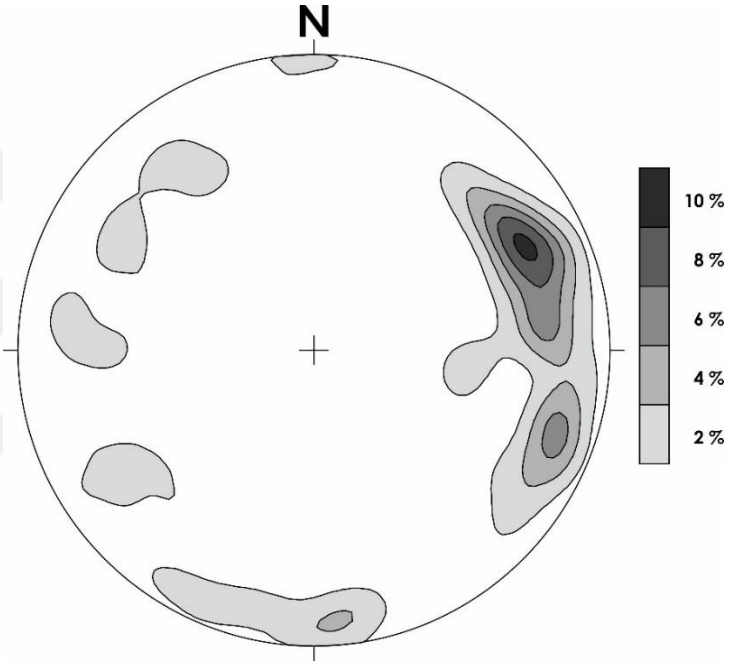


Figure 3.32 Stereographic plot showing the total foliation orientations of the Özdere Schist unit. Lower hemisphere Schmidt projection (n=83)

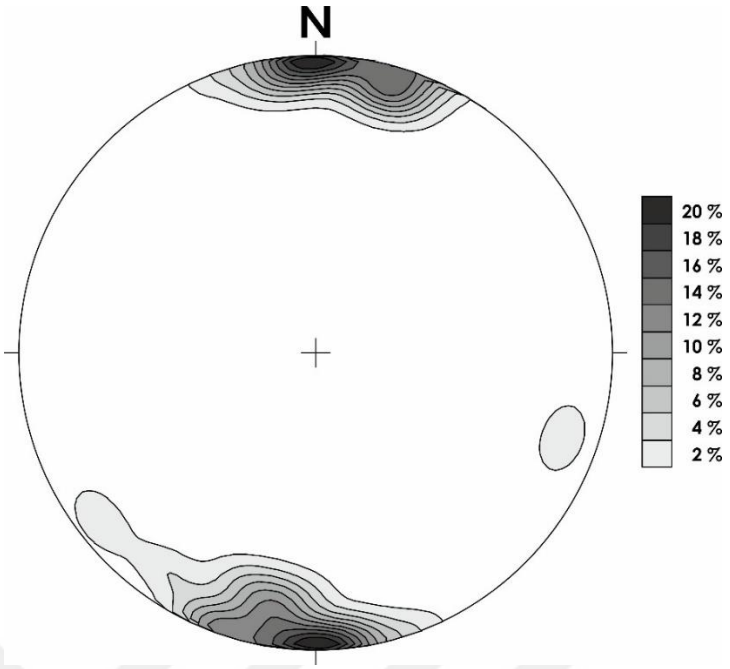


Figure 3.33 Linear fabrics (mineral stretching lineations) of the Özdere Schist unit. Lower hemisphere Schmidt projection (n=30)

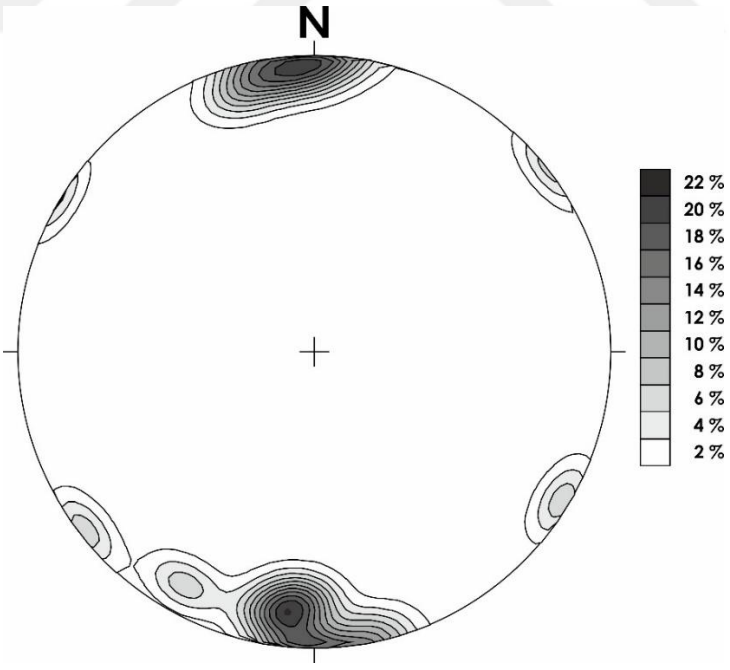


Figure 3.34 The fold axes and crenulation cleavage axes of the Özdere Schists. Lower hemisphere Schmidt projection (n=14)

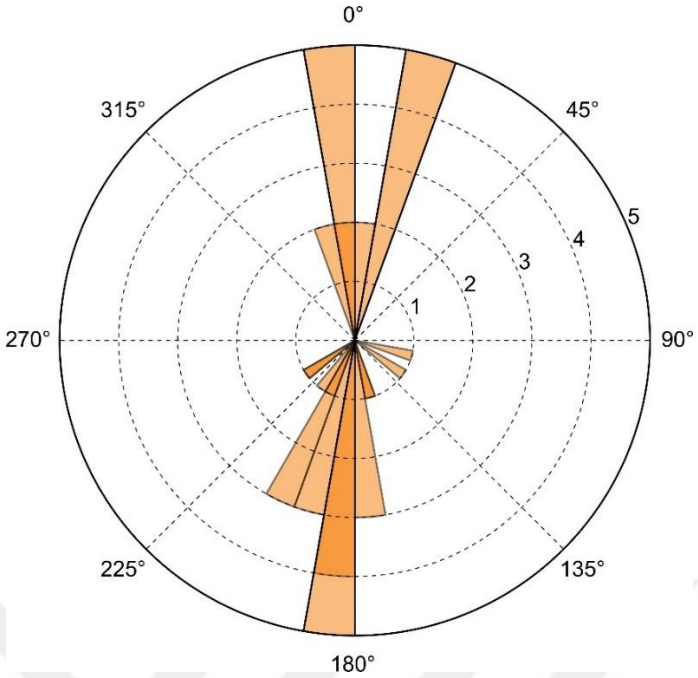


Figure 3.35 Rose plot of mineral stretching lineations, crenulation cleavage axes and fold axes of Özdere Schist unit. Dominant linear populations are 10° – 20° (NNE), 180° – 190° (SSW), and 350° – 360° (NNW)

3.2 Zindan Schists

The Zindan Schists are the metamorphic rock units that consist of Quartz-muscovite-chloritoid-kyanite schists at the bottom and the Chlorite-biotite-garnet schists on top (Figure 3.36 – 3.37). This unit outcrops on the eastern part of the study area and a good locality to observe the unit could be at Zindan Hill which is in zone 35S 512720.00 4204700.00 according to the UTM-ED50 coordinate system.



Figure 3.36 A photograph of Zindan Hill. The point of view is directed towards the south (coor: UTM-35 S 0512720/4204700) (Personal archive, 2023)



Figure 3.37 General view of the Zindan Schist along the shoreline of the Aegean Sea. The point of view is directed towards the southeast (coor: UTM-35 S 0512583/4204357) (Personal archive, 2024)

3.2.1 Quartz-Muscovite-Chloritoid-Kyanite Schists

Quartz-Muscovite-Chloritoid-Kyanite Schist unit has a distinct yellowish – brown to grey color, displaying strongly foliated stratification (Figure 3.38 – 3.39) with mesoscopic scale crenulation folds and iron oxide coatings within rectangular joint fracture cavities at some localities (Figure 3.40).



Figure 3.38 An outcrop of Quartz-Muscovite-Chloritoid-Kyanite Schist unit of Zindan Schists (coor: UTM-35 S 0513379/4209288) (Personal archive, 2024)



Figure 3.39 Well exposed foliations of the quartz-muscovite-chloritoid-kyanite schist unit. The trend of schistosity is measured as 100/30 (coor: UTM-35 S 0513139/4204532) (Personal archive, 2024)



Figure 3.40 Rectangular joints filled with iron oxide coatings with the approximate trend of 90 and dip of 75 to 80 degrees (coor: UTM-35 S 0512937/4205352) (Personal archive, 2024)

The schist unit itself contains numerous amounts of quartz rods, veins, sigmoids, folds, and boudins (Figure 3.41 – 3.48). The well-developed continuous tectonic fabric observed at some localities in the unit allows us to conduct kinematic analysis, the penetrative fabrics on the rock exhibit strong lineation and foliation indicate that they are S/L tectonites.



Figure 3.41 A recumbent quartz vein fold towards south. Crenulation axis is measured as 173/08 and S1 as 069/34 (coor: UTM-35 S 0513864/4205761) (Personal archive, 2024)



Figure 3.42 A massive quartz vein fold has been exposed and plunges downward. Notice the parallel development of the schistosity with the fold axial plane in the core of the antiform (coor: UTM-35 S 0513912/4205780) (Personal archive, 2024)



Figure 3.43 Some stretching lineations are preserved on the quartz veins that are exposed and measured as 035/12 (coor: UTM-35 S 0513864/4205761) (Personal archive, 2024)

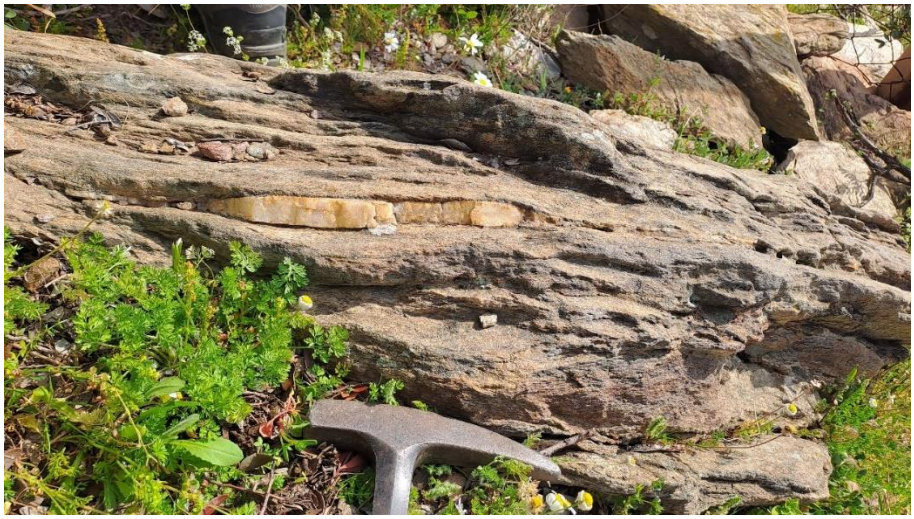


Figure 3.44 Quartz sigmoid that is observed parallel to the lineations and perpendicular to the schistosity indicating top-to-south sense of shear (coor: UTM-35 S 0513864/4205761) (Personal archive, 2024)

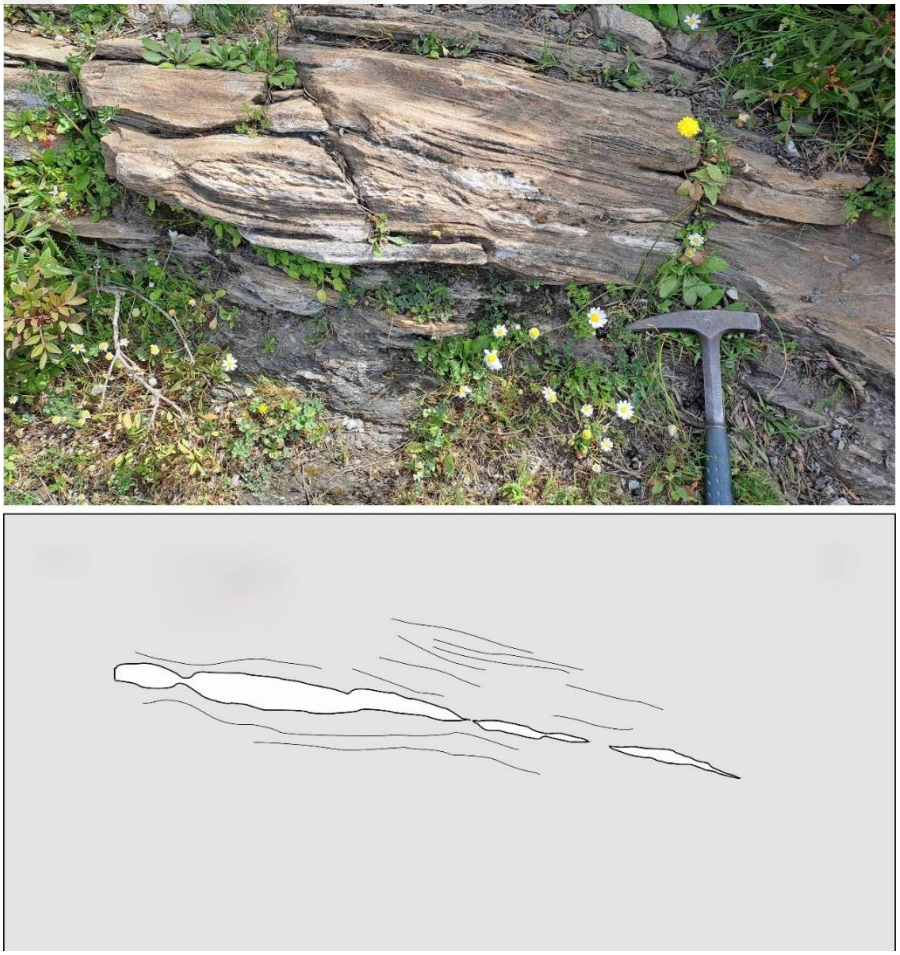


Figure 3.45 A well-developed boudinage of a quartz vein in parallel to the schistosity. The trend of the schistosity is measured as 103/34 (coor: UTM-35 S 0513938/4205812) (Personal archive, 2024)



Figure 3.46 The schistosity of the outcrop is measured as 031/08 while containing two different stretching lineation trends. SL1: 042/08 and SL2: 001/05. SL1 is the penetrative stretching lineation (coor: UTM-35 S 0513252/4205601) (Personal archive, 2024)

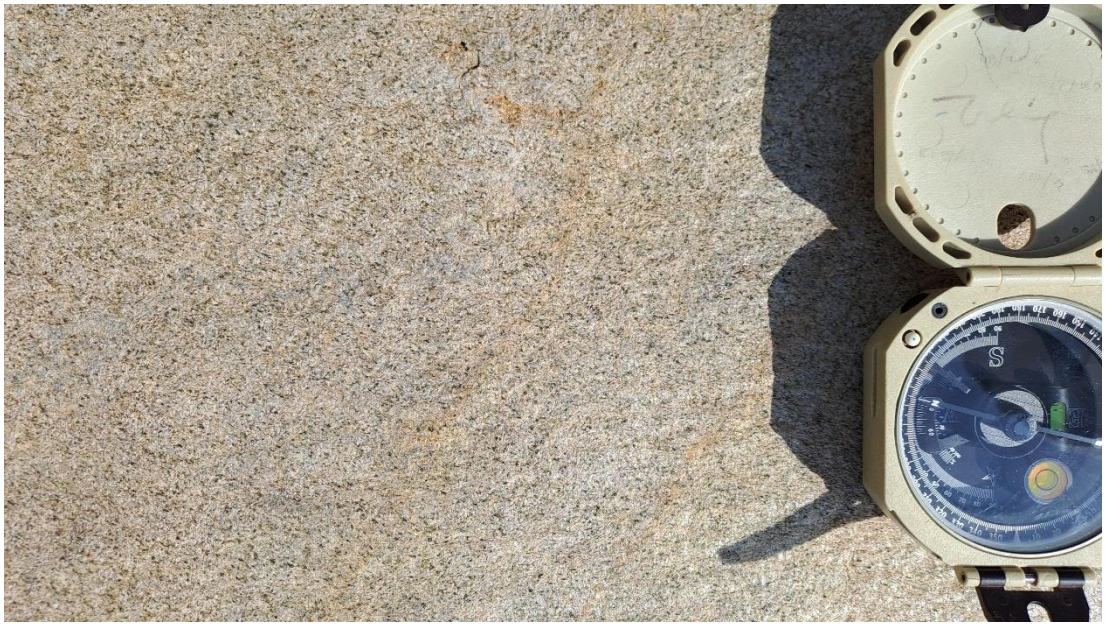


Figure 3.47 The texture of quartz – muscovite – chloritoid – kyanite schist with the chloritoids visible through naked eye. The schistosity is measured as 083/31 and the contained stretching lineations are 165/12 which is parallel to the crenulation axes (coor: UTM-35 S 0513115/4205593) (Personal archive, 2024)



Figure 3.48 The stretching lineations are represented by mica minerals and are measured as 185/10 and the schistosity of 099/47 (coor: UTM-35 S 0512942/4205209) (Personal archive, 2024)

The mica-rich schistosity of the unit indicates low to medium grade metamorphism conditions (greenschist facies). Some outcrops contain symmetric and asymmetric (sigmoidal) crenulation cleavages (Figure 3.49 – 3.52), the axes of the crenulation folds are mainly parallel to the stretching lineations.



Figure 3.49 Well visible crenulations that are 152/24 in trend which is also parallel to the stretching lineation. The schistosity is measured as 114/32 (coor: UTM-35 S 0513145/4205588) (Personal archive, 2024)

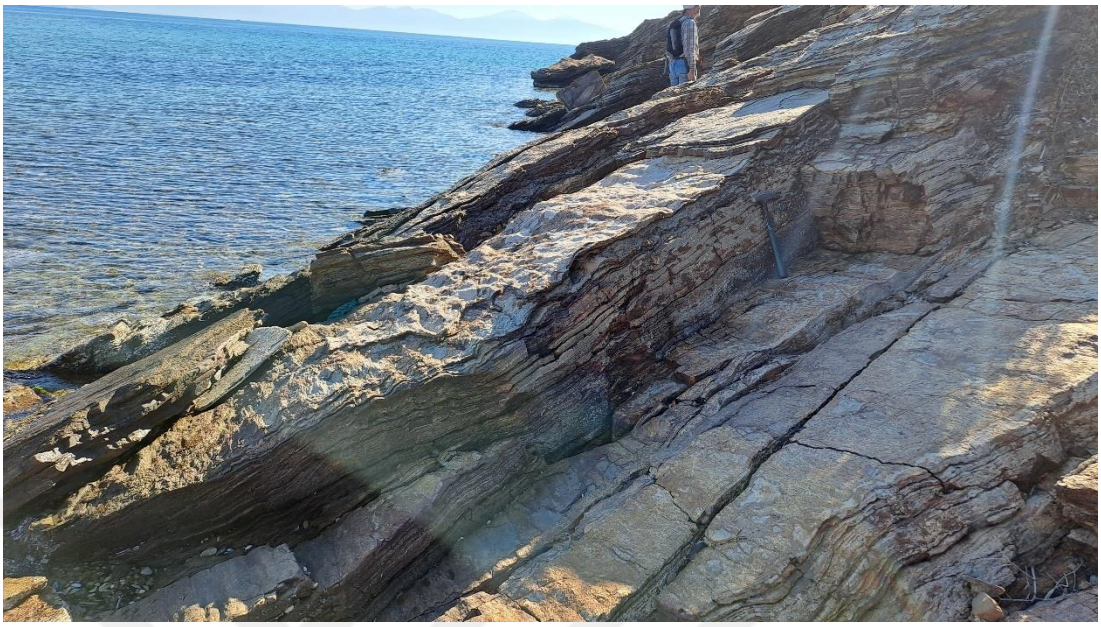


Figure 3.50 The trend of mesoscopic crenulation foliations of the outcrop is measured as 151/15 which is also parallel to the stretching lineation of the mica minerals (coor: UTM-35 S 0513143/4204538) (Personal archive, 2024)



Figure 3.51 Another photograph of the well-developed and exposed mesoscopic crenulation foliations of the outcrop (coor: UTM-35 S 0513143/4204538) (Personal archive, 2024)



Figure 3.52 Some of the outcrops exhibit brittle deformation structures of joints cutting the schistosity (coor: UTM-35 S 0513143/4204538) (Personal archive, 2024)

Overall, this unit exhibits good strength qualities that are differentiated from the phyllite intercalations found in the unit which can break apart easily off the foliation planes (Figure 3.53 – 3.54). Other than phyllites, calc-schist intercalations also can be present at some locations (Figure 3.55 – 3.60).



Figure 3.53 Phyllite intercalation within quartz-muscovite-chloritoid-kyanite schist (coor: UTM-35 S 0514142/4206760) (Personal archive, 2024)



Figure 3.54 Visible crenulations on the foliation surfaces of the unit. The crenulation axes are parallel to the stretching lineations (coor: UTM-35 S 0513041/4205542) (Personal archive, 2023)



Figure 3.55 Grey phyllite intercalation (coor: UTM-35 S 0513041/4205542) (Personal archive, 2023)



Figure 3.56 Grey marble and yellow dolomite intercalations showing lateral facies change during the deposition of the unit. The measured bedding trends vary in between 204/16 and 307/13 at this location (coor: UTM-35 S 0513977/4207063) (Personal archive, 2024)



Figure 3.57 This photograph shows the mesoscopic fold with the axis of 181/11 at the schists below the grey marbles. The schistosity is 253/16 at this location (coor: UTM-35 S 0514293/4206942) (Personal archive, 2024)



Figure 3.58 Thin calc-schist bands within the gray phyllite of schistosity 094/47. Some bands are folded with the fold axis of 353/11. The shear bands within the outcrop can be used as shear sense indicators that indicate top-to-south sense of shear (coor: UTM-35 S 0513935/4205852) (Personal archive, 2024)



Figure 3.59 Phyllites with well-developed schistosity and mesoscopic crenulation foliations. This outcrop shows a recumbent fold towards the west. S1: 284/22 and the SL=CCL:011/03 (coor: UTM-35 S 0513688/4206363) (Personal archive, 2024)



Figure 3.60 Phyllite intercalations are abundant at the proximity of this location with well-developed crenulations trending 193/11 but poorly conserved stretching lineations. Schistosity is measured as 281/22 and which is consistent with the overlying calc-schist (coor: UTM-35 S 0513723/4206303) (Personal archive, 2024)

Phyllite levels are observed as grey to silver colored with fine grained mica flakes that are aligned parallel to the foliation planes. Texturally the phyllite shows

porphyroblastic texture and anastomosing texture containing garnet grains with a size range of approximately 1 to 3 mm that are visible with naked eye (Figure 3.61). Some phyllite levels contain tension fractures that are filled with iron oxide materials (Figure 3.62).



Figure 3.61 The garnet grains with size range in between 1 to 3 mm in phyllite (coor: UTM-35 S 0513723/4206303) (Personal archive, 2024)



Figure 3.62 The relationship between the tension cracks and the crenulation lineations. The iron oxide material filled tension cracks are developed perpendicular to the 170/11 crenulation axes on the foliations of 091/35 (coor: UTM-35 S 0513038/4205512) (Personal archive, 2024)

The quartz sigmoids of the Zindan Schists were used as shear sense indicators. All the detected and observed sigmoids were perpendicular to the schistosity planes and parallel to the lineations. The sigmoidal indicators showed top-to-south sense of movement (Figure 3.63 – 3.64).

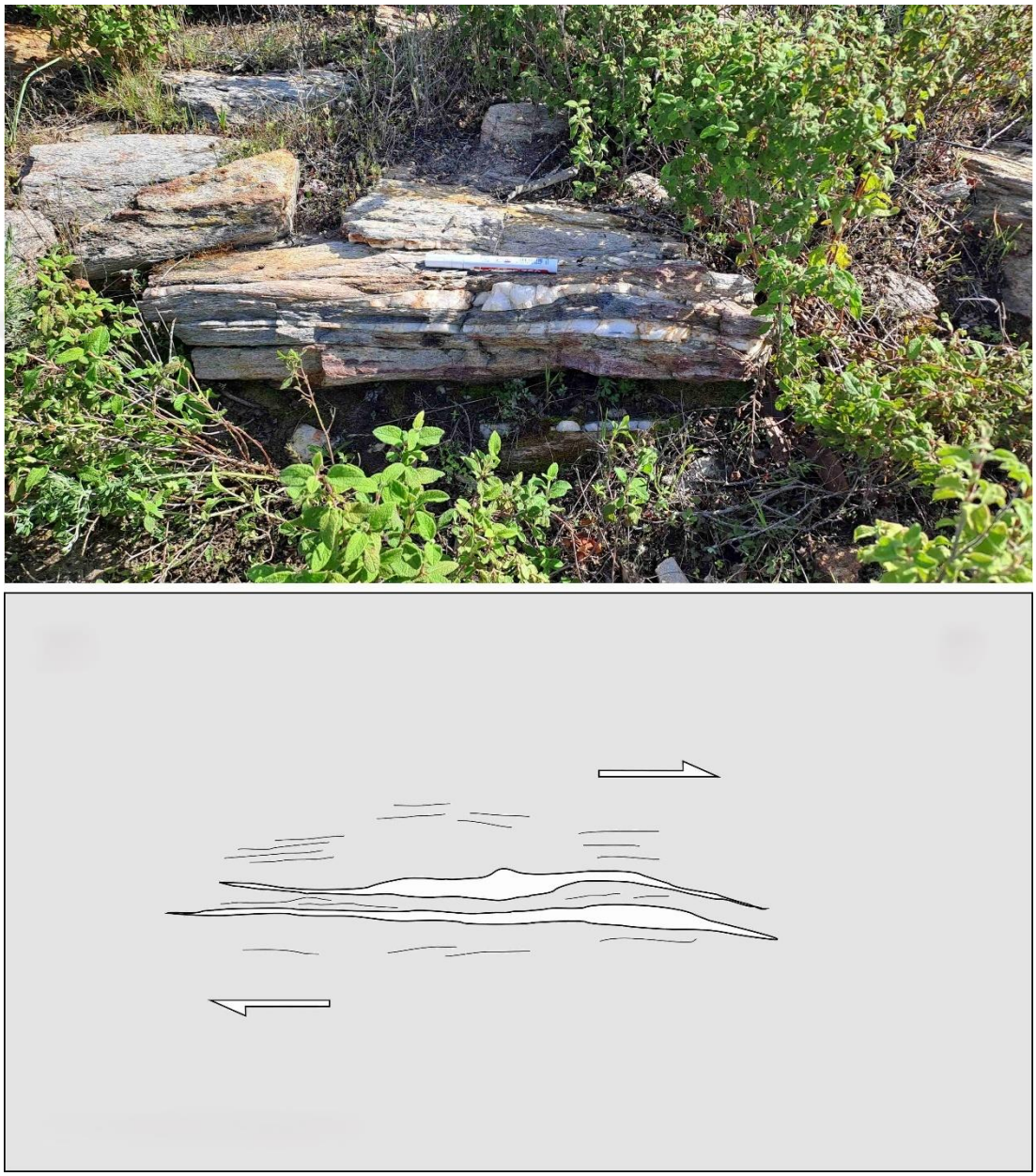


Figure 3.63 A quartz vein that is deformed into a sigmoid and indicates top-to-south sense of movement (coor: UTM-35 S 0513938/4205812) (Personal archive, 2024)



Figure 3.64 A quartz sigmoid in the dark grey phyllite intercalation indicating top-to-south sense of shear (coor: UTM-35 S 0513912/4205779) (Personal archive, 2024)

One of the other shear sense indicators was the s-c structures that were used to conduct kinematic analysis. All the s-c structures indicated a top-to-south sense of movement as well (Figure 3.65 – 3.66).



Figure 3.65 The s-c structure indicates top-to-south sense of movement (coor: UTM-35 S 0513912/4205779) (Personal archive, 2024)

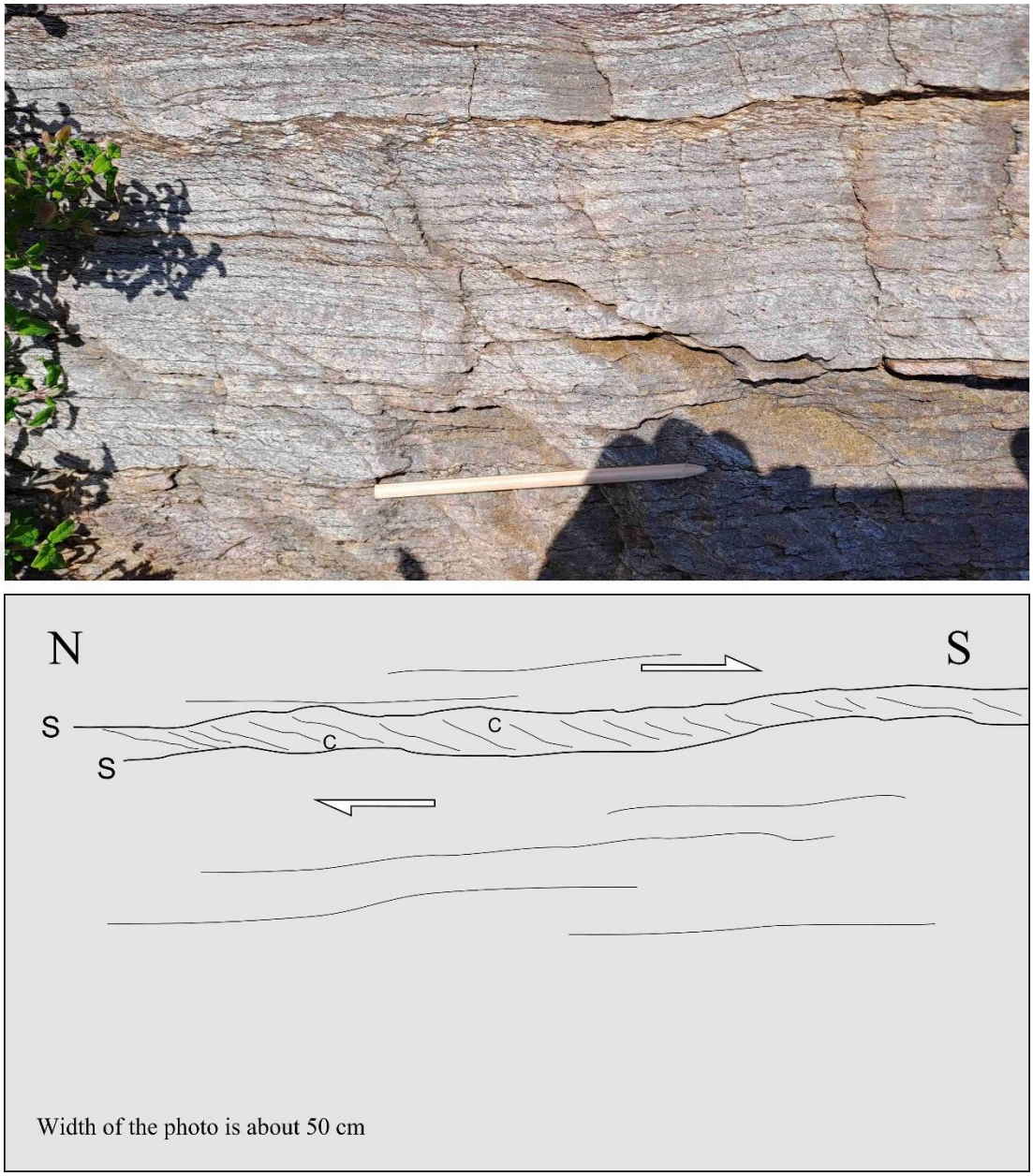


Figure 3.66 An s-c structure within the quartz-muscovite-chloritoid-kyanite schist of Zindan Schists indicating top-to-south sense of movement (coor: UTM-35 S 0512781/4205016) (Personal archive, 2024)

Various sized mesoscopic folds were observed and measured in the quartz-muscovite-chloritoid-kyanite schist unit during the field work. The most significant ones are shown in the figures below (Figure 3.67 – 3.68).



Figure 3.67 An intercalated and folded outcrop of quartz-muscovite-chloritoid-kyanite schist and calc-schists (coor: UTM-35 S 0513688/4206363) (Personal archive, 2024)



Figure 3.68 A folded fold. Notice the z-type folds (coor: UTM-35 S 0513857/4206705) (Personal archive, 2024)

A minor post-metamorphic dip-slip fault has been detected along the roadcut with a fault plane trend of 161/72 and having slickenlines of trend 195/53. The fault has been

cutting the schists units with schistosity of 166/26 and mineral stretching lineations of 176/20 (Figure 3.69 – 3.70).



Figure 3.69 The dip-slip fault (coor: UTM-35 S 0512741/4204379) (Personal archive, 2024)



Figure 3.70 Fault breccia around the fault scraps (coor: UTM-35 S 0512741/4204379) (Personal archive, 2024)

3.2.2 Chlorite-Biotite-Garnet Schists

The Chlorite-Biotite-Garnet Schist unit mainly outcrops to the south-central region of the Zindan schists and can be best observed at the shoreline locality of Koru Bay. The well exposed outcrops mostly display grey tone colors with highly folded and crenulated intercalations (Figure 3.71 – 3.74). This unit also contains great amounts of quartz veins that have experienced ductile deformations in the form of folds and sigmoids (Figure 3.75). The outcrops closer to the shoreline have been altered and eroded due to the sea water exposure.



Figure 3.71 This well exposed outcrop along the coastline reveals numerous folds that have disharmonic fold properties. The fold axis is measured as 170/29 (coor: UTM-35 S 0513686/4204455) (Personal archive, 2024)



Figure 3.72 Another photograph of the disharmonic folds found on the coastline outcrop with z-type folds. The stretching lineation at this location are 164/28 in trend (coor: UTM-35 S 0513686/4204455) (Personal archive, 2024)



Figure 3.73 Disharmonic folds with z-type folds (coor: UTM-35 S 0513686/4204455) (Personal archive, 2024)



Figure 3.74 The schistosities are measured as 173/33 (coor: UTM-35 S 0513686/4204455) (Personal archive, 2024)



Figure 3.75 A folded quartz vein that displays parallelism with schistosity and the fold axial plan of 125/24. The stretching lineations and the crenulation axes at this location are measured as 170/14. Some s-c structures are observed over the upper limb of the fold that indicates top-to-northwest sense of movement which differs from most of the sense of shear indicators (coor: UTM-35 S 0513907/4204461) (Personal archive, 2024)

The well preserved porphyroblastic texture of the phyllite intercalations contain relatively big garnet porphyroblast in good condition (Figure 3.76).



Figure 3.76 Grey schists with brown garnet porphyroblasts. The schistosity is 055/27 and the stretching lineation are parallel to the crenulations which are 313/06 in trend (coor: UTM-35 S 0514679/4204365) (Personal archive, 2024)

Towards the proximity of the Özdere shear zone folds and deformed quartz veins appeared. At this location two different stretching lineations were observed, these stretching lineations were formed on the schistosity of 083/34. The younger stretching lineation of SL2 trend was 002/04 and it was overprinting the older and folded stretching lineation of SL1 with the trend of 082/34. The older stretching lineation of SL1 is observed to be folded and was parallel to the crenulation axis (Figure 3.77).

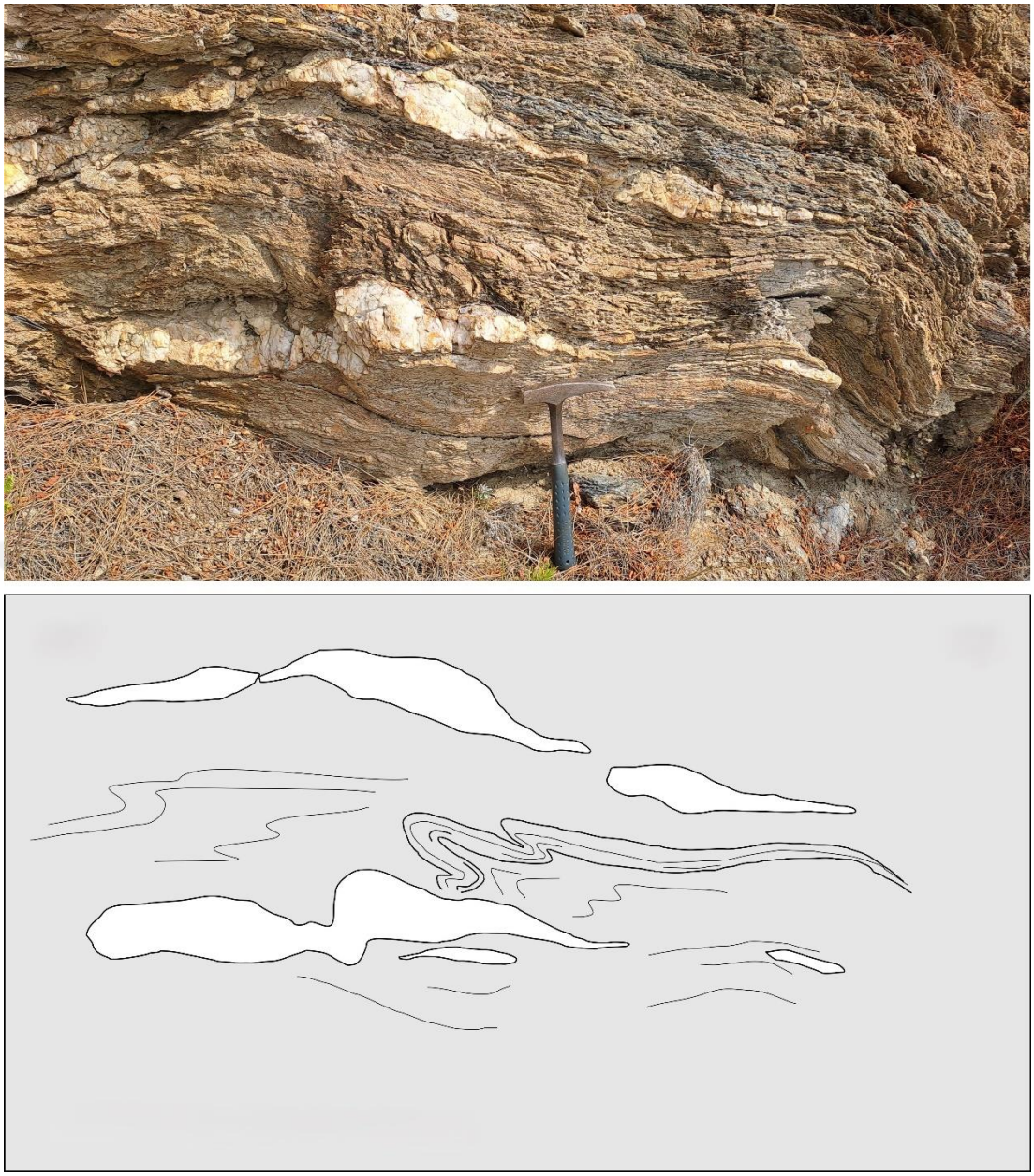


Figure 3.77 The schistosity was measured as 035/32 and crenulation axes as 146/06 which was equal to the stretching lineations. Notice the boudins and the intrafolial folds (coor: UTM-35 S 0514679/4204365) (Personal archive, 2024)

3.2.3 Kinematics of the Zindan Schists

Tectonic fabric elements of the Zindan Schist unit were also measured and plotted on the stereographic projections. Obtained results from the contour diagrams of fabric elements such as mineral stretching lineations, crenulation cleavage axes, and schistosities are presented below (Figure 3.78 – 3.80). In addition, a rose diagram was

prepared to show the combination of mineral stretching lineations, crenulation and fold axes all together (Figure 3.81).

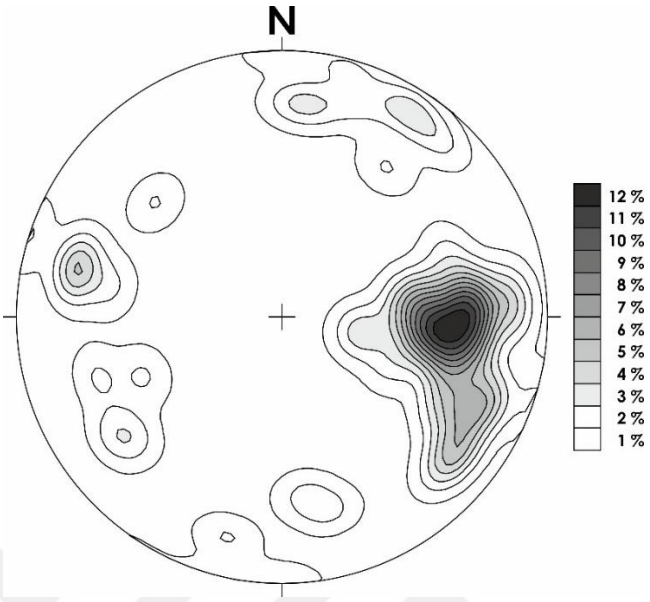


Figure 3.78 Stereographic plot showing the orientations of the foliations measured on the Zindan Schist unit. Lower hemisphere Schmidt projection (n=61)

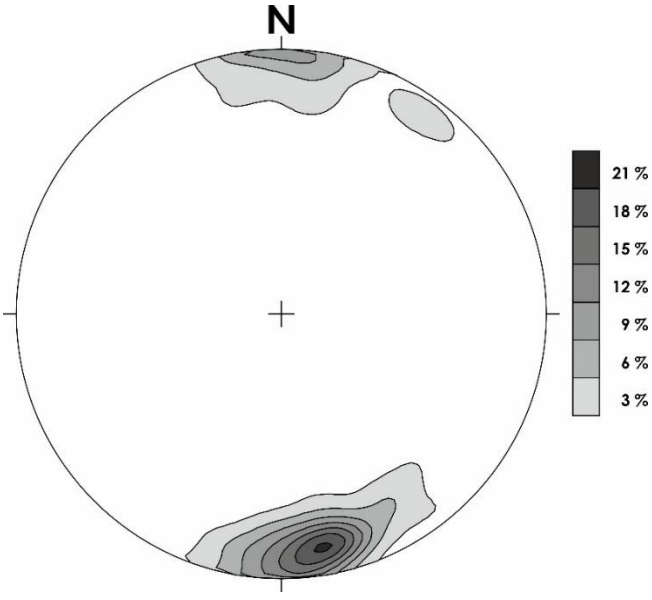


Figure 3.79 Linear fabrics (mineral stretching lineations) of the Zindan Schist unit. Lower hemisphere Schmidt projection (n=48)

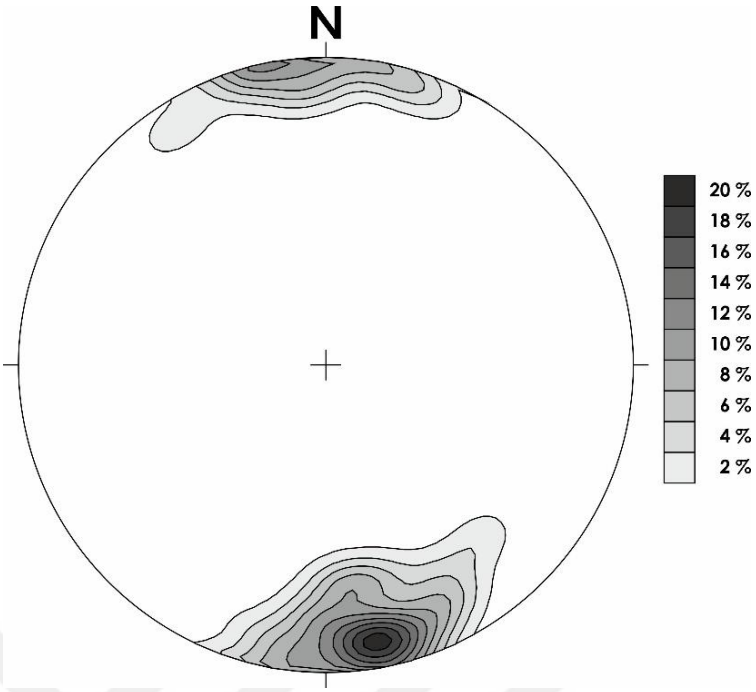


Figure 3.80 The fold axes and crenulation cleavage axes of the Zindan Schists. Lower hemisphere Schmidt projection (n=35)

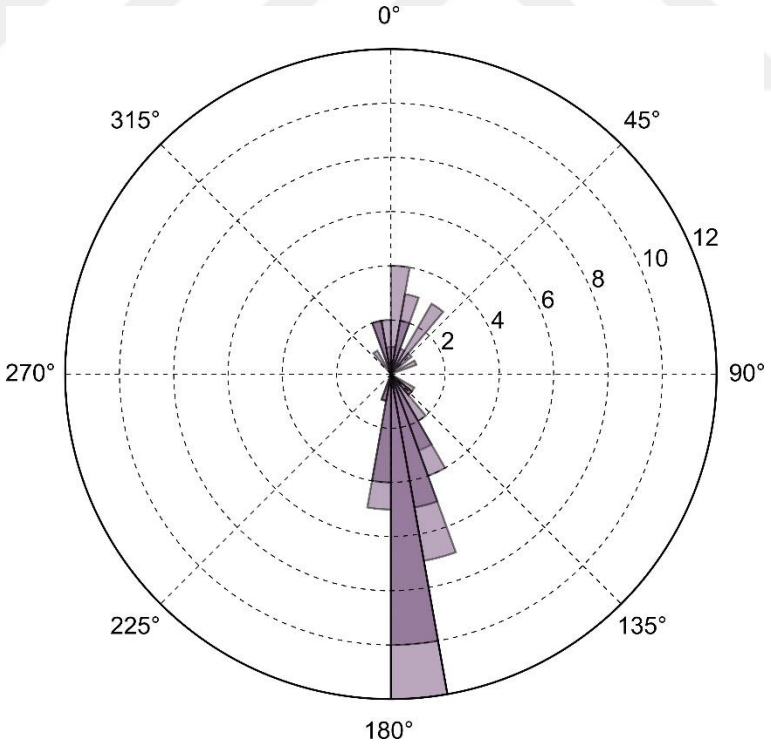


Figure 3.81 Rose plot of mineral stretching lineations, crenulation cleavage axes and fold axes of Zindan Schist unit. The dominant linear population is 160° – 180° (SSE)

3.3 Kargıcak Marbles

The Kargıcak Marbles are best described at the Kargıcak Hill location with the coordinate of zone 35S 514250.00 4206800.00 according to UTM-ED50 (Figure 3.82).

The Kargıcak marbles are the metacarbonate sequence consisting mainly of marbles, metadolomites, and dolomitic marbles. The thick strata of the marble unit are well visible and easily traceable in the field (Figure 3.83).

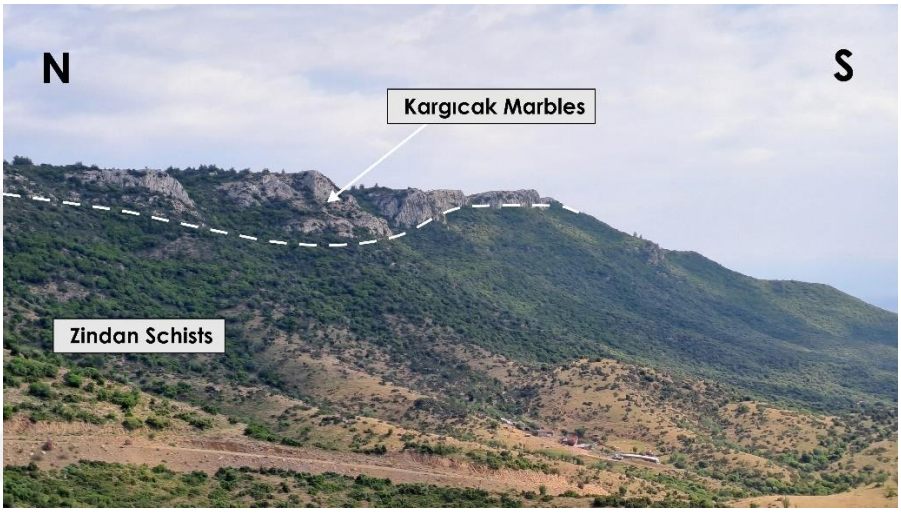


Figure 3.82 A landscape view from the field showing the Kargıcak Marbles above the schists of Zindan and Özdere. The point of the view is towards the southeast (coor: UTM-35 S 0512862/4209250) (Personal archive, 2024)

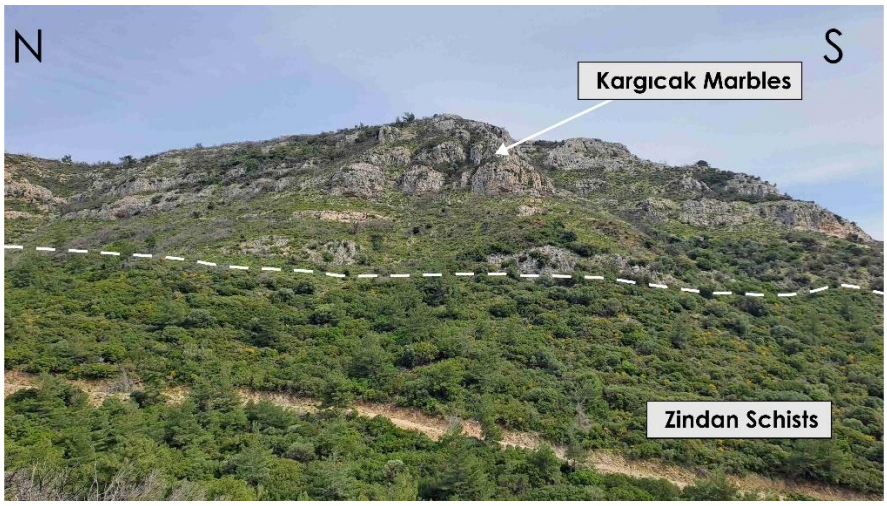


Figure 3.83 The yellow dolomite intercalations outcropping under the Kargıcak Marbles (coor: UTM-35 S 0513688/4206363) (Personal archive, 2024)

The Kargıcak marbles are mainly light grey to yellowish pale brown colored, thick bedded with high strength properties. No fossil traces were found. Some marbles exhibit high recrystallization and contain mineral lineations (Figure 3.84). Some limestone outcrops contained folded laminations and mineral lineations defined by mica flakes (Figure 3.85 – 3.86).



Figure 3.84 Grey to white colored and thin laminated marbles including the intercalations (coor: UTM-35 S 0514679/4204365) (Personal archive, 2024)



Figure 3.85 The Kargıcak marble outcrop contains preserved stretching lineations and folded laminations. The stretching lineations were measured as 031/04 and trend of the laminations were 151/31 (coor: UTM-35 S 0514093/4205943) (Personal archive, 2024)



Figure 3.86 Folded and recrystallized limestone block (coor: UTM-35 S 0513389/4207162) (Personal archive, 2024)

Some limestone outcrops contained stretching lineations such as 165/09 (Figure 3.87 – 3.89)., all observed stretching lineations on the marbles are plotted on the rose diagram that shows dominant linear population clustering in 180° - 190° (SSE) and other significant observation points are shown below (Figure 3.90).



Figure 3.87 Thin laminated limestone outcrop (coor: UTM-35 S 0513389/4207162) (Personal archive, 2024)



Figure 3.88 The preserved stretching lineations of 209/05 trend in Kargıcak Marble. S1: 130/31 (coor: UTM-35 S 0514093/4205943) (Personal archive, 2024)



Figure 3.89 Coarse crystalline white colored marbles with stretching lineations. SL: 180/02 and S1: 086/39 (coor: UTM-35 S 0513443/4207197) (Personal archive, 2024)

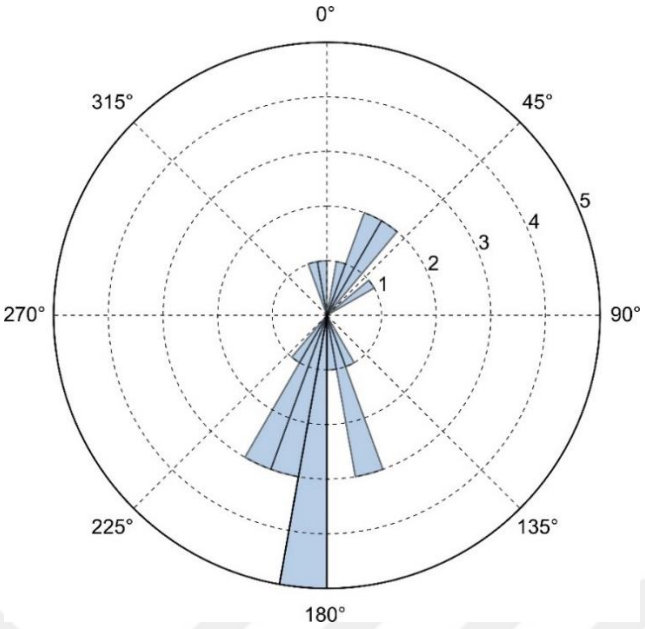


Figure 3.90 Rose diagram of stretching lineation found on the Kargıcak marbles with dominant linear population clustering in 180° - 190° (SSE)

Schistosities, beddings, and stretching lineation that observed on the Kargıcak marbles were measured. The collected measurement data of fabric elements were plotted on stereographic projections to create contour diagrams (Figure 3.91 – 3.92).

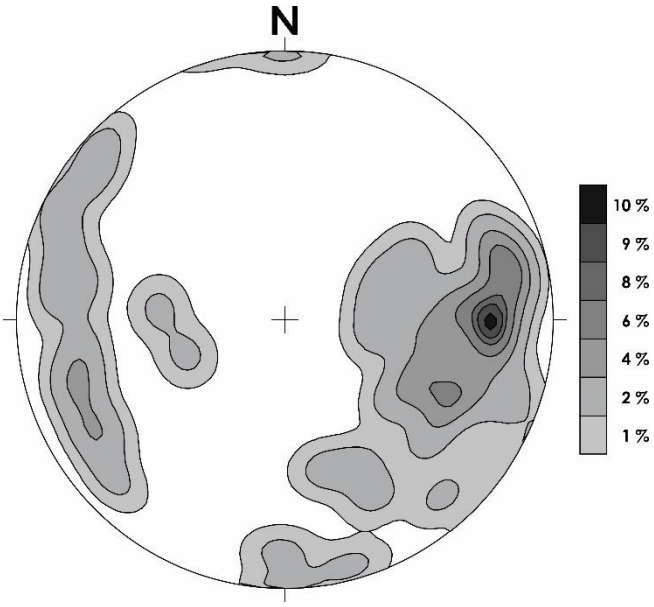


Figure 3.91 Stereographic plot showing the orientations of the foliations/beddings measured on the Kargıcak marbles. Lower hemisphere Schmidt projection (n=49)

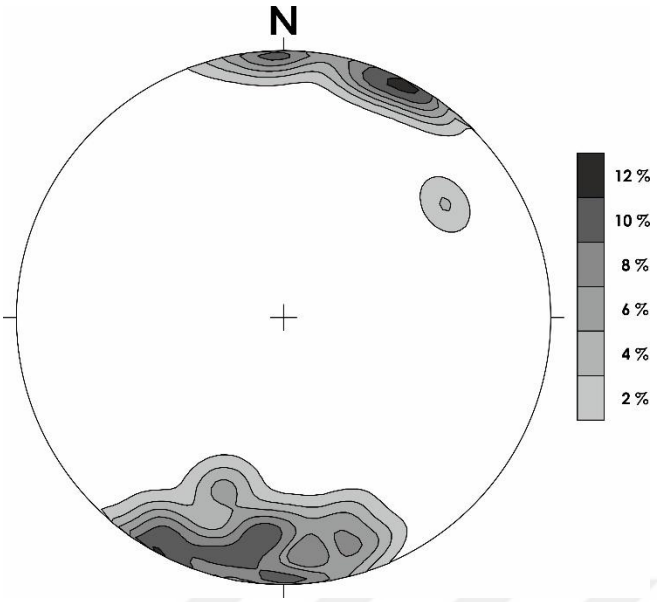


Figure 3.92 Linear fabrics (mineral stretching lineations) of the Kargıcak marbles. Lower hemisphere Schmidt projection (n=26)

The Kargıcak marbles also contain numerous quartz veins that have experienced ductile deformation and form folded structures such as recumbent folds and sheath folds (Figure 3.93 – 3.96). The folded quartz veins generally display north-south lineament parallel to the stretching lineations. The stretching lineations are oriented as 162/24 and 158/11 while schistosity is 064/45.



Figure 3.93 Marbles containing deformed quartz veins (coor: UTM-35 S 0513349/4207031) (Personal archive, 2024)



Figure 3.94 Folded quartz veins within Kargıcak Marbles (coor: UTM-35 S 0513349/4207031) (Personal archive, 2024)



Figure 3.95 Sheath folds in Kargıcak marbles (coor: UTM-35 S 0513438/4207318) (Personal archive, 2024)



Figure 3.96 Sheath folds in Kargıcak marbles (coor: UTM-35 S 0513438/4207318) (Personal archive, 2024)

The outcropping intercalated dolomites mainly show pale crème to white color but sometimes yellow color is also present at some locations. The thin laminated structure of the dolomites are very distinctive features within the outcrops (Figure 3.97 – 3.99).



Figure 3.97 Pale yellow to crème – colored dolomites. S1: 094/26 (coor: UTM-35 S 0513978/4205873) (Personal archive, 2024)



Figure 3.98 Dolomitized limestones of Kargıcak Marbles. Notice the thinly laminated sections around the hammer (coor: UTM-35 S 0513295/4205370) (Personal archive, 2024)



Figure 3.99 Thinly laminated dolomitic marbles. 280/25 is the trend of the laminations. Stretching lineations are 191/09 (coor: UTM-35 S 0513844/4206905) (Personal archive, 2024)

An old, abandoned marble mine was encountered during the field work, the bedding was having trend of 153/27. The marbles were coarsely crystalline and thinly laminated while containing grey colored veins. Some schistosities were observed having muscovite mineralization on the surface (Figure 3.100).



Figure 3.100 An old open pit marble mine that has been abandoned (coor: UTM-35 S 0513292/4206973) (Personal archive, 2024)

The contact relationship between the Kargıcak Marbles and the Zindan Schists is determined to be a ductile shear zone due to the field observations (Figure 3.101 – 3.103).



Figure 3.101 The contact between the Kargıcak Marbles and the underlying Zindan Schist. Notice the highly crenulated and foliated texture resembling a ductile shear zone (coor: UTM-35 S 0514679/4204365) (Personal archive, 2024)



Figure 3.102 The ductile shear zone contact between the dolomites and the underlying schist (coor: UTM-35 S 0513740/4206523) (Personal archive, 2024)



Figure 3.103 A roadcut showing the relationship between the Kargıcak marbles on top and the underlying Zindan schists (coor: UTM-35 S 0513873/4204484) (Personal archive, 2024)

The Kargıcak marbles also contain intercalation of schists and chert rich thin laminated grey marbles showing facies difference according to the color change (Figure 3.104 – 3.106).



Figure 3.104 Schist intercalations in the marbles (coor: UTM-35 S 0513473/4207174) (Personal archive, 2024)



Figure 3.105 A synform of schist intercalation within marbles. The fold axis is 158/11 (coor: UTM-35 S 0513752/4207151) (Personal archive, 2024)



Figure 3.106 A closer photograph of the synform. The trends of the limbs are 239/23 and 110/32 (coor: UTM-35 S 0513752/4207151) (Personal archive, 2024)

Within the Kargıcak marbles grey colored and very thin laminated marbles were observed which included thin layers of chert intercalations (Figure 3.107 – 3.109).



Figure 3.107 Very thin laminated grey marbles with mica flakes on the laminations. S1: 087/27 (coor: UTM-35 S 0513492/4207354) (Personal archive, 2024)



Figure 3.108 Chert imbedded dark grey marble outcrop with very thin laminations. S1: 079/17 (coor: UTM-35 S 0513492/4207354) (Personal archive, 2024)



Figure 3.109 Thin laminated grey marbles (coor: UTM-35 S 0513492/4207354) (Personal archive, 2024)

CHAPTER FOUR
PETROGRAPHY OF SCHIST UNITS

4.1 Introduction

In this chapter, it is aimed to describe the petrographic properties of the schist units of the study area by showing the textural and mineralogical features on thin section photomicrograph obtained from polarized microscope. For petrographic analysis, 74 thin sections were prepared and examined from a total of 83 rock samples collected from the study area. The mineral name abbreviations and photomicrograph properties are shown in the related figures with explanations in their captions below.

4.2 Petrography of Özdere Schists

The Özdere Schists consist of a uniform garnet muscovite schist unit that is the stratigraphically lowest unit mapped in the study area and its majorly exposed in the western part of the region below the Özdere tectonic line.

The general mineral assemblage of this unit is determined to be quartz + albite + muscovite + chlorite + garnet ± chloritoid ± tourmaline ± zircon and in addition some iron oxide coatings observed.

The foliation in the unit is dominantly defined by muscovite minerals (Figure 4.1), however the chloritic overprint with good parallelism occurring around the rims of plagioclase feldspar porphyroblasts are also present (Figure 4.2).

The muscovite mineral flakes display typical optical features of having micaceous colorless crystals under the plane polarized light and display moderate to strong interference colors under the cross polarized light, and a moderate relief. The typical bird’s eye extinction parallel to the foliation is also present.

Quartz is one of the major components found within the schist unit exhibiting anhedral crystals with no pleochroism in plane polarized light while having low interference colors under cross polarized light. Quartz crystals show no relief.

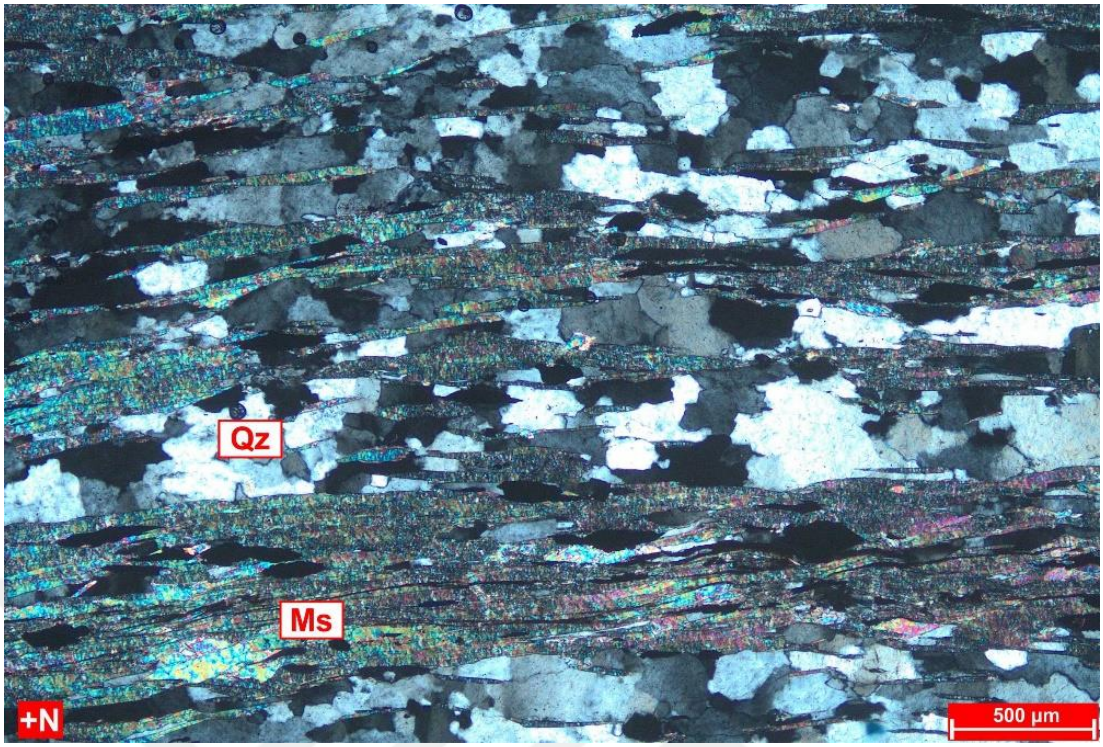


Figure 4.1 A photomicrograph of Muscovite flakes display well-developed parallelism with the foliations. Ms: Muscovite, Qz: Quartz. In the plane polarized light



Figure 4.2 Crenulated chlorite foliations coexisting with muscovites in a thin section photomicrograph of Özdere schist. Chlorites are seen as dark green and highly crenulated structures. In the plane polarized light. Plane polarized light

Albite minerals are abundant in the unit and commonly occur as anhedral crystals with a great number of inclusions in it. The inclusions consist of assemblage minerals especially garnet grains. The garnet crystals were observed as anhedral and subhedral porphyroblasts within the Özdere Schists (Figure 4.3).

Albites have similar relief properties as quartz, they both show low to no relief but albites commonly show twinning and contain inclusions. No pleochroism of albite observed under plane polarized light.

Under cross polarization, the albite crystals have anisotropic properties. The typical gray to white interference colors of order I is observed. The polysynthetic twinning and zoned structure of the albite is not very common in the examined thin sections (Figure 4.4 – 4.6).

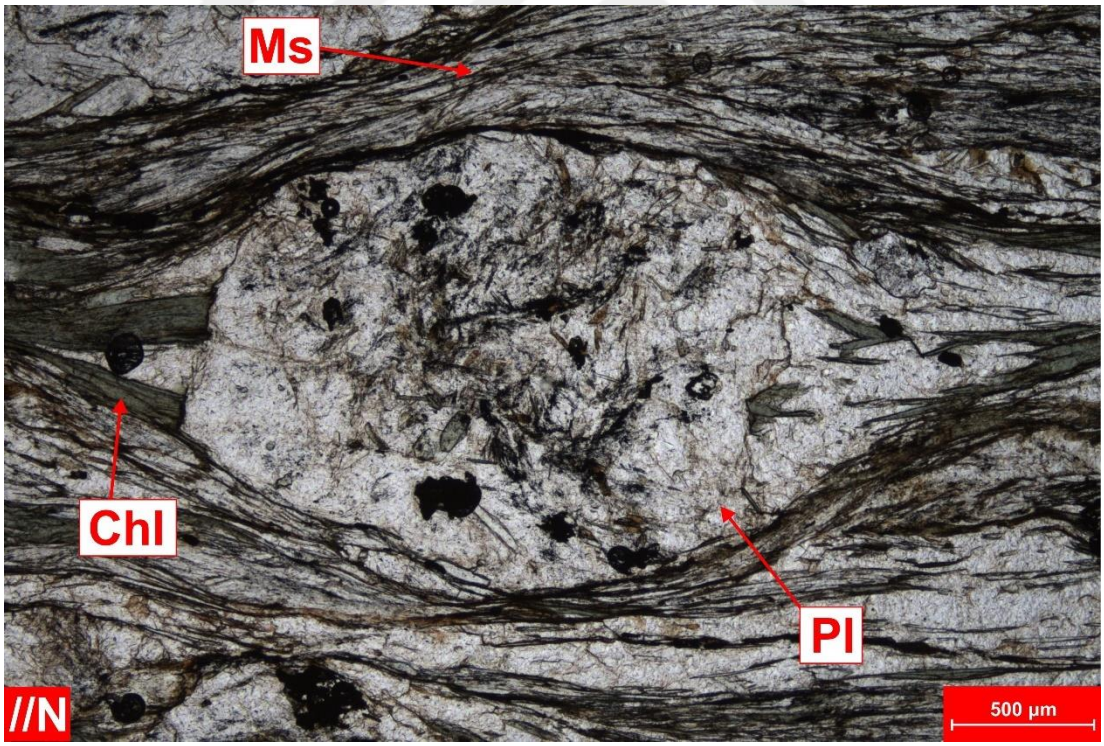


Figure 4.3 A photomicrograph of plagioclase poikiloblast containing chlorite inclusions and surrounded by muscovite foliations. Chl: Chlorite – Ms: Muscovite – Pl: Plagioclase. In the plane polarized light

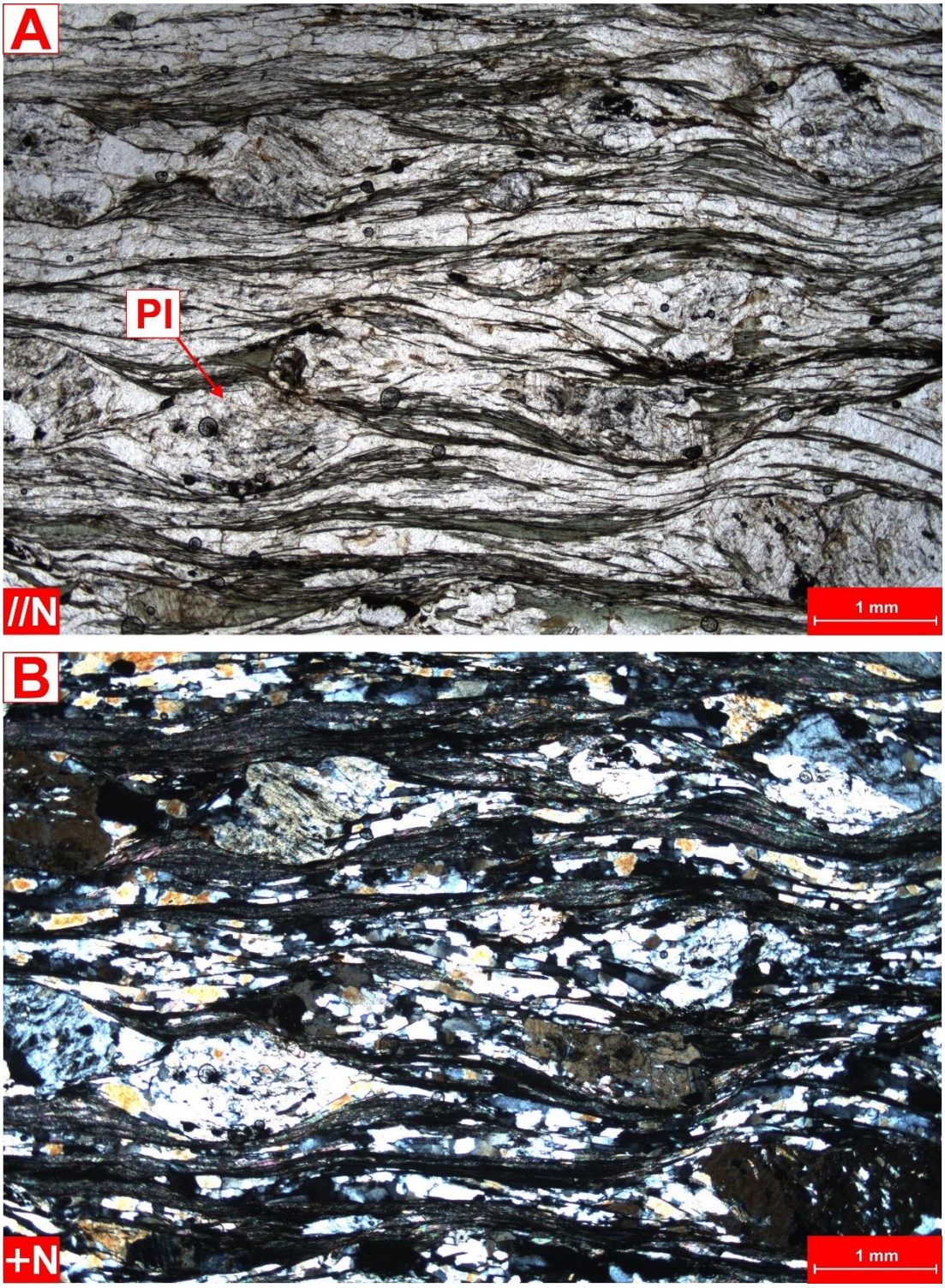


Figure 4.4 A photomicrograph of plagioclase poikiloblasts surrounded by chlorite and muscovite. Pl: Plagioclase. A) Under plane polarized light. B) Under cross polarized light

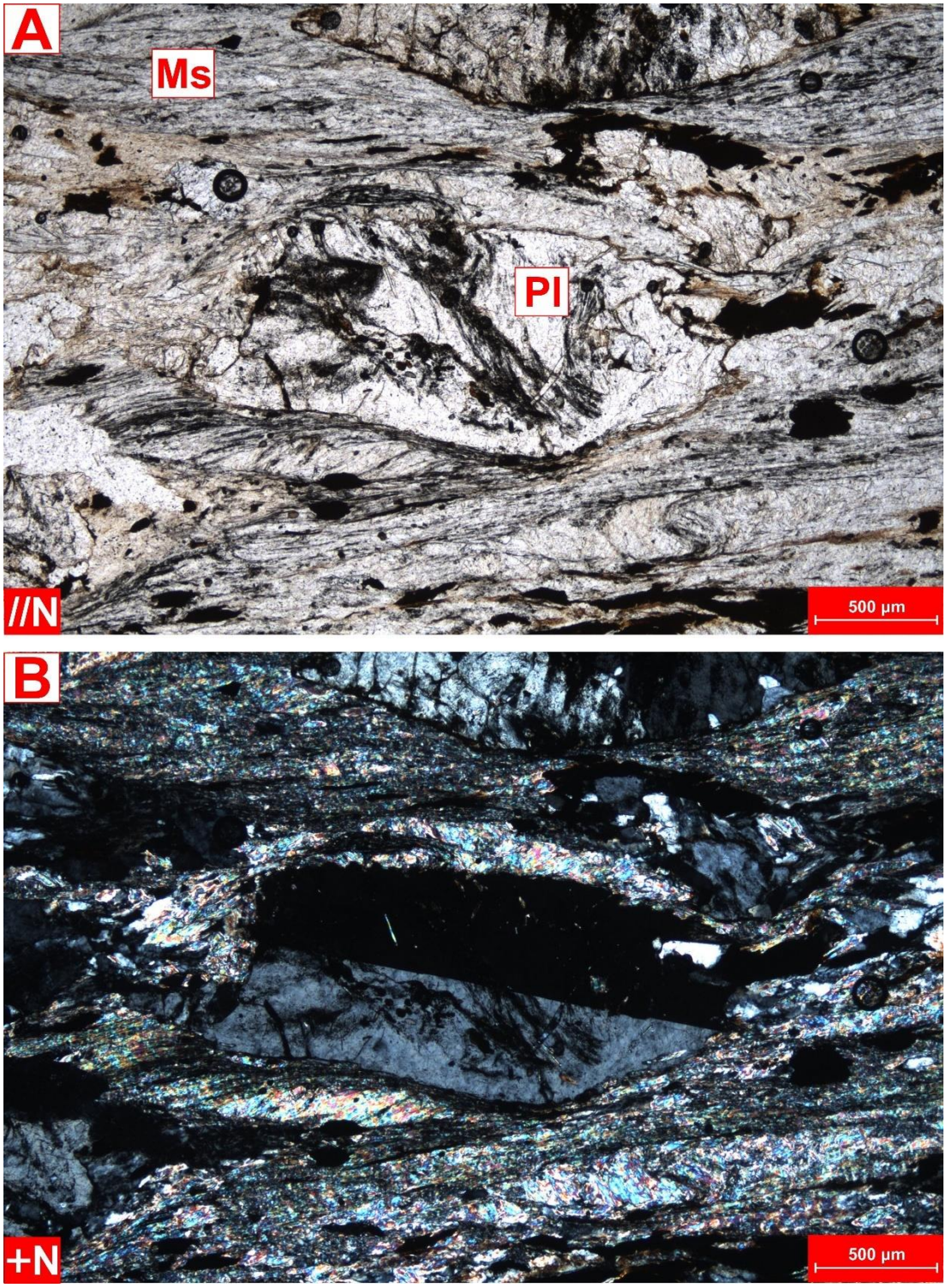


Figure 4.5 Plagioclase with a typical twining and surrounded by muscovite flakes. Numerous inclusions can be seen inside the plagioclase poikiloblast. Ms: Muscovite – Pl: Plagioclase. A) Under plane polarized light. B) Under cross polarized light

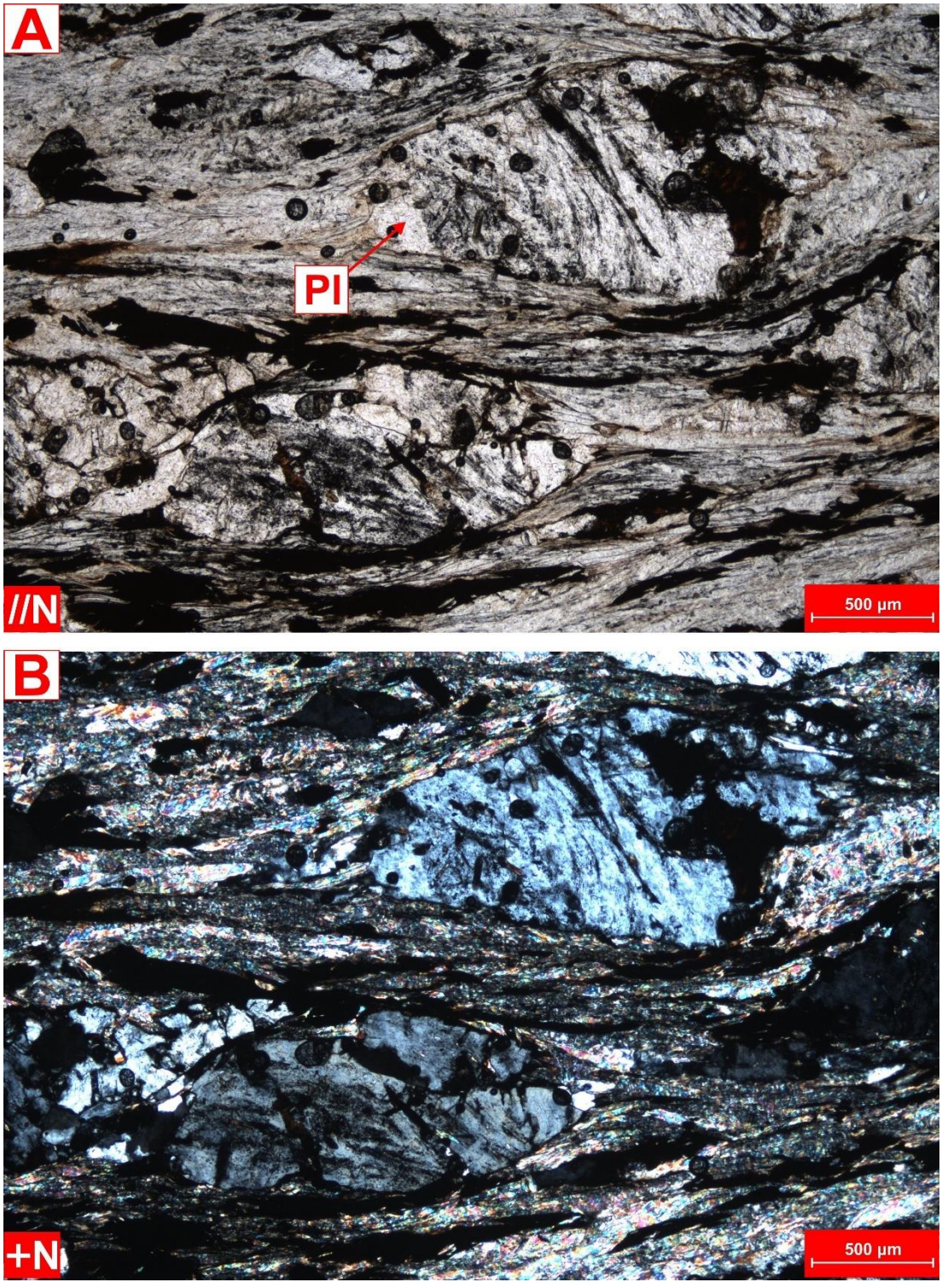


Figure 4.6 Plagioclase porphyroblasts that partially overprinted by muscovite. Pl: Plagioclase. A) Under plane polarized light. B) Under cross polarized light

The muscovite minerals within the Özdere schist unit occur as fine flakes that are significantly parallel with the foliations. The observed muscovite optical properties under the plane polarized light conditions include moderate relief of tabular crystals with irregular outline, no pleochroism to very pale-yellow color. In some thin sections and oriented thin sections, the foliation of muscovite creates crenulation cleavages and can be identified easily. The Özdere Schist unit commonly displays porphyroblastic texture with less common anastomosing texture (Figure 4.7 – 4.10).

Under the cross polarized lights, the muscovites have anisotropic properties that is also very typical with Özdere Schists. The birds eye extinctions and high order interference color is present. No twinning was observed (Figure 4.7 – 4.10).

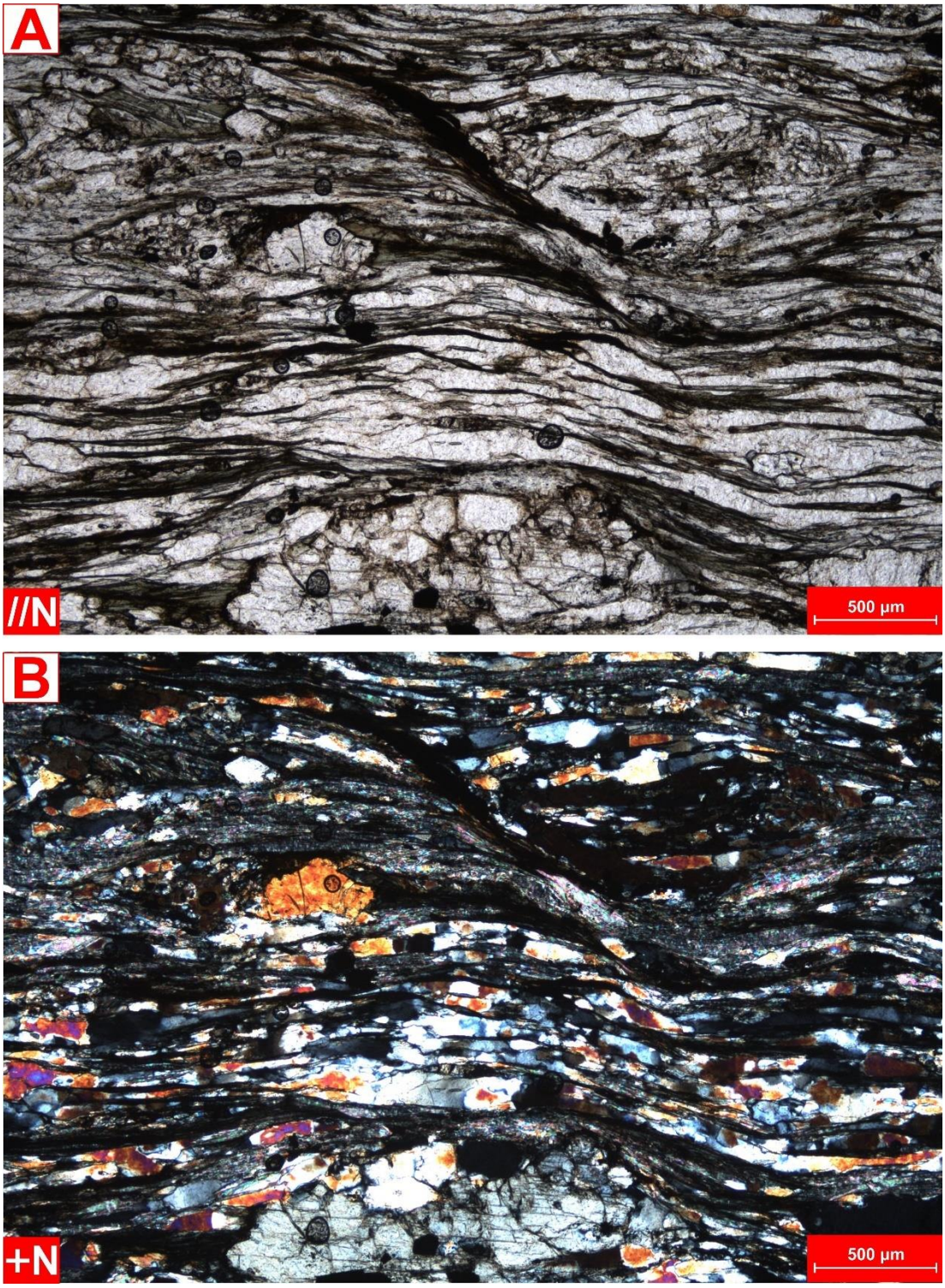


Figure 4.7 Muscovite foliations surrounding quartz and albite minerals. Notice the high level of interference colors of muscovite in cross polarized light. A) Under plane polarized light. B) Under cross polarized light

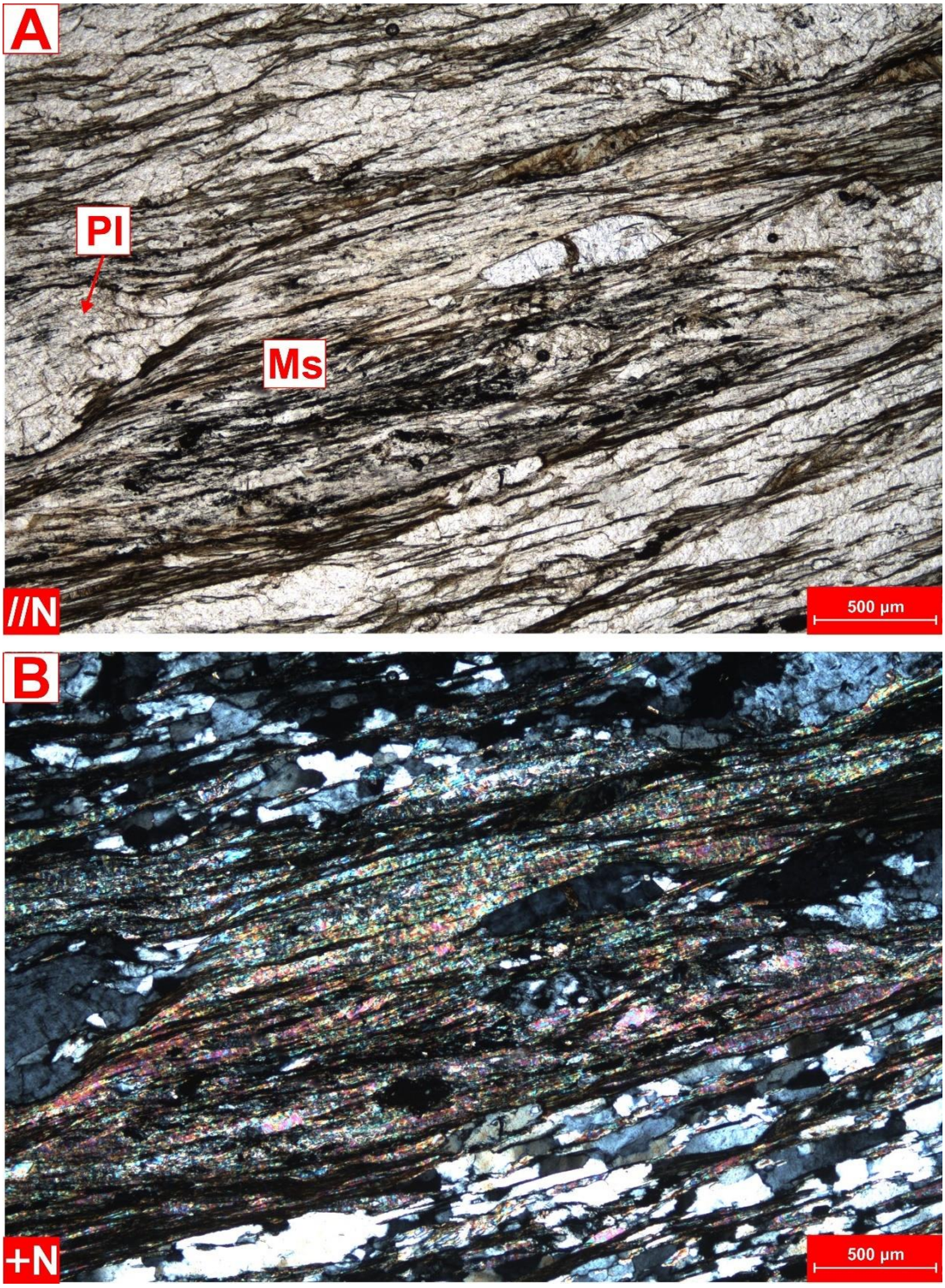


Figure 4.8 Albite porphyroblasts within muscovite foliations and quartz. Notice the well-developed alignments of muscovite parallel with the foliations. Ms: Muscovite – Pl: Plagioclase. A) Under plane polarized light. B) Under cross polarized light

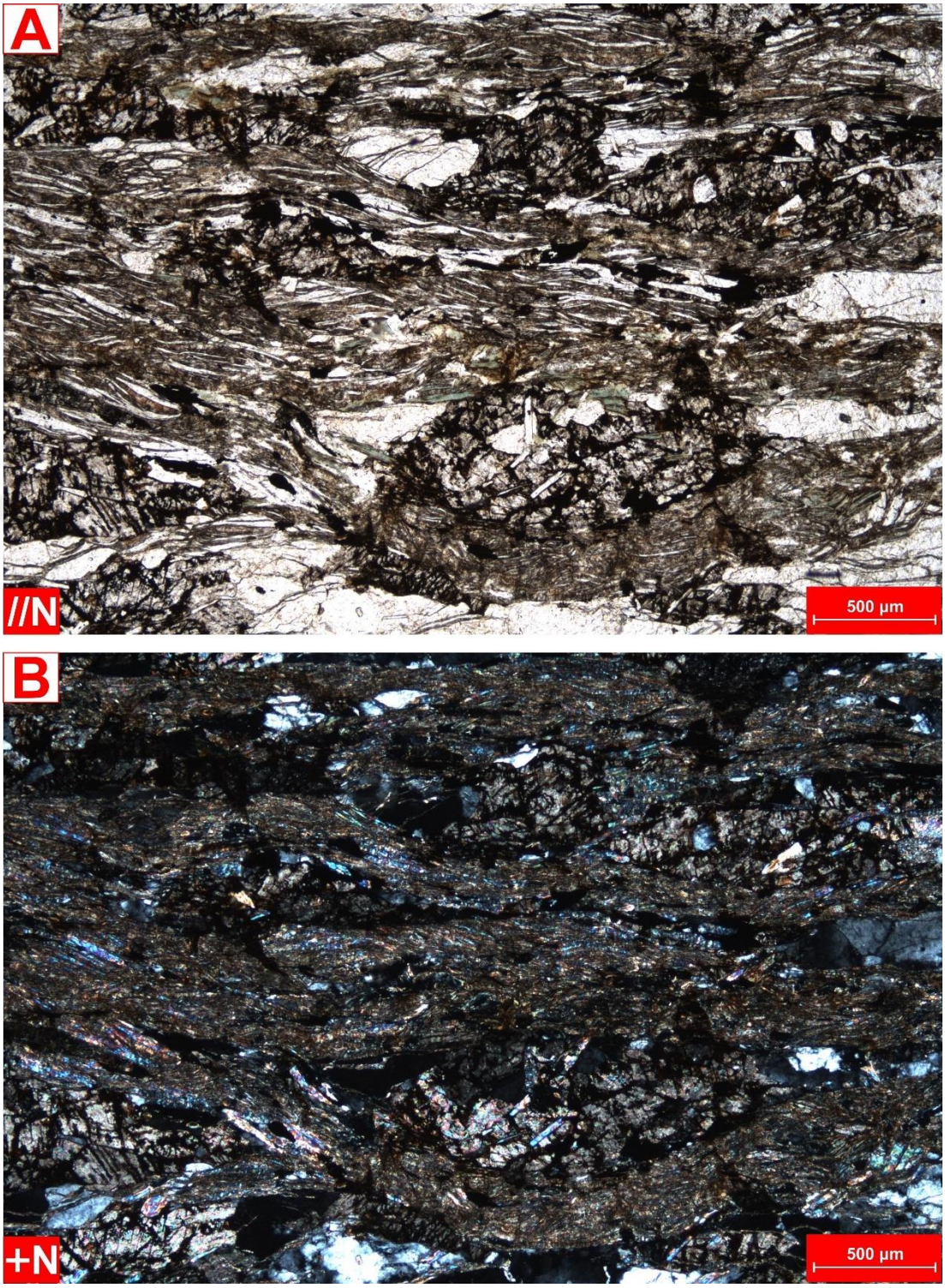


Figure 4.9 Muscovite foliations surrounding albite. Notice the chloritoid growth over the muscovite flakes. A) Under plane polarized light. B) Under cross polarized light

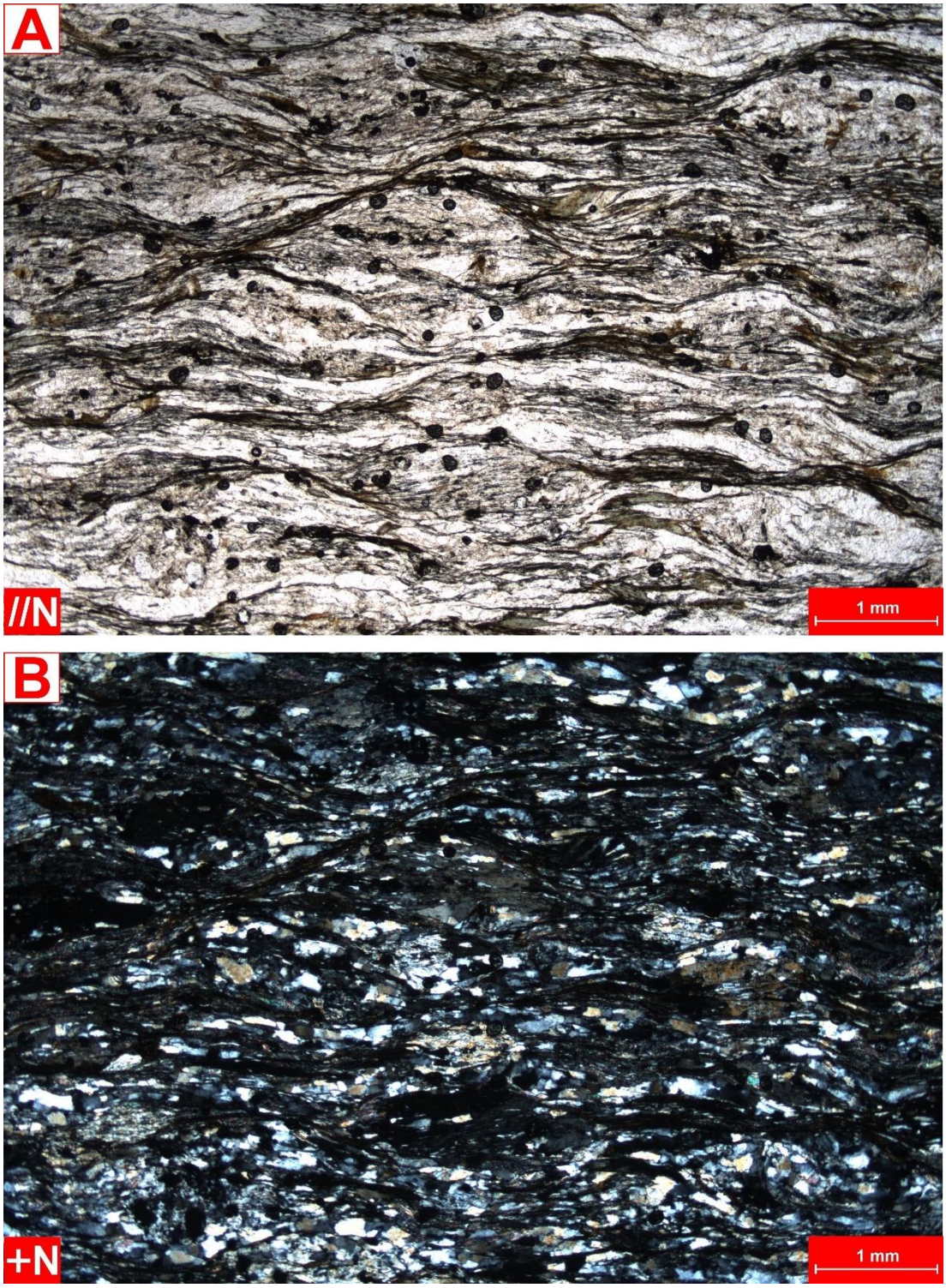


Figure 4.10 Anastomosing texture of the muscovite foliations surrounding the quartz crystals. A) Under plane polarized light. B) Under cross polarized light

The chloritic overprint on the garnet and muscovite minerals, and development of iron oxide coatings coincide with the Zindan schists suggesting that both tectonic slices have experienced retrograde metamorphic phases. Due to the observed rotational deformation marks in the garnets, the chlorite and biotite seem to be grown after the main deformation that caused the foliation (Figure 4.11).

The chlorites found within the Özdere Schists are generally in green, olive green, and pale green color under PPL. As their name derived from Greek word *chlōros* meaning green. They usually exhibit low to moderate relief similar to the muscovite and have moderate pleochroism. The chlorites are anisotropic under XPL conditions and have unusual brownish – green (due to the Mg content) sometimes blue or even purple interference color (Figure 4.12 – 4.13).

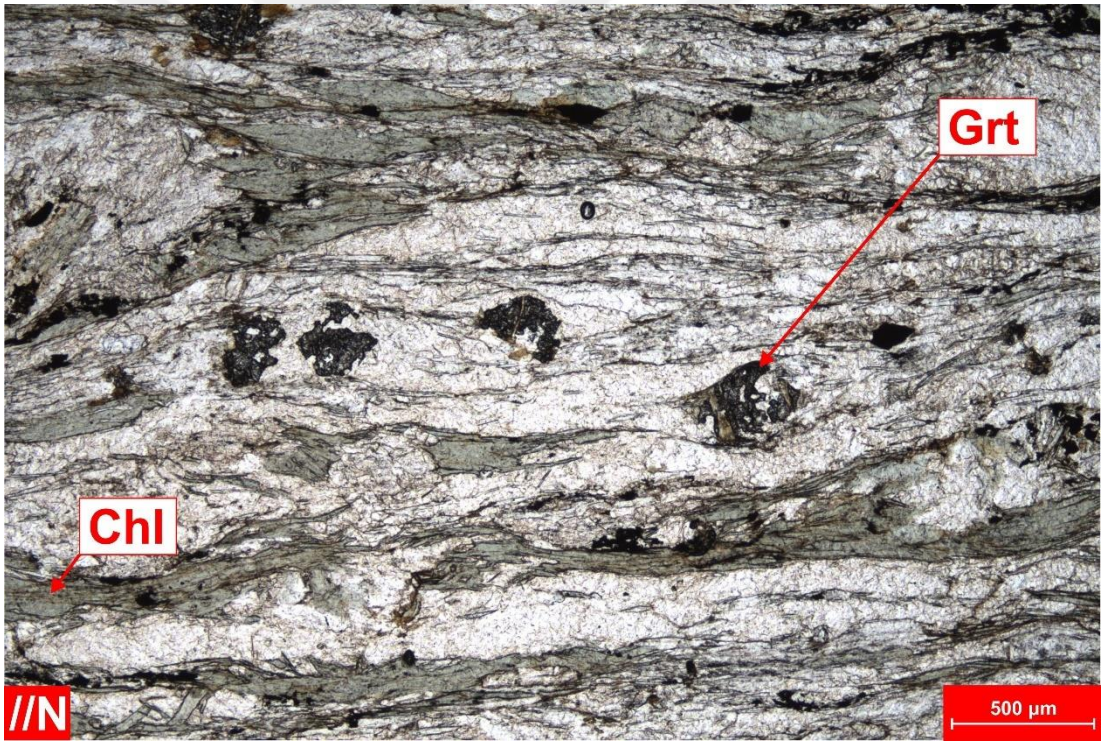


Figure 4.11 Garnet subhedral crystals found as inclusions. Chloritic overprint is noticeable on the muscovite foliations. Chl: Chlorite, Grt: Garnet. Under the plane polarized light

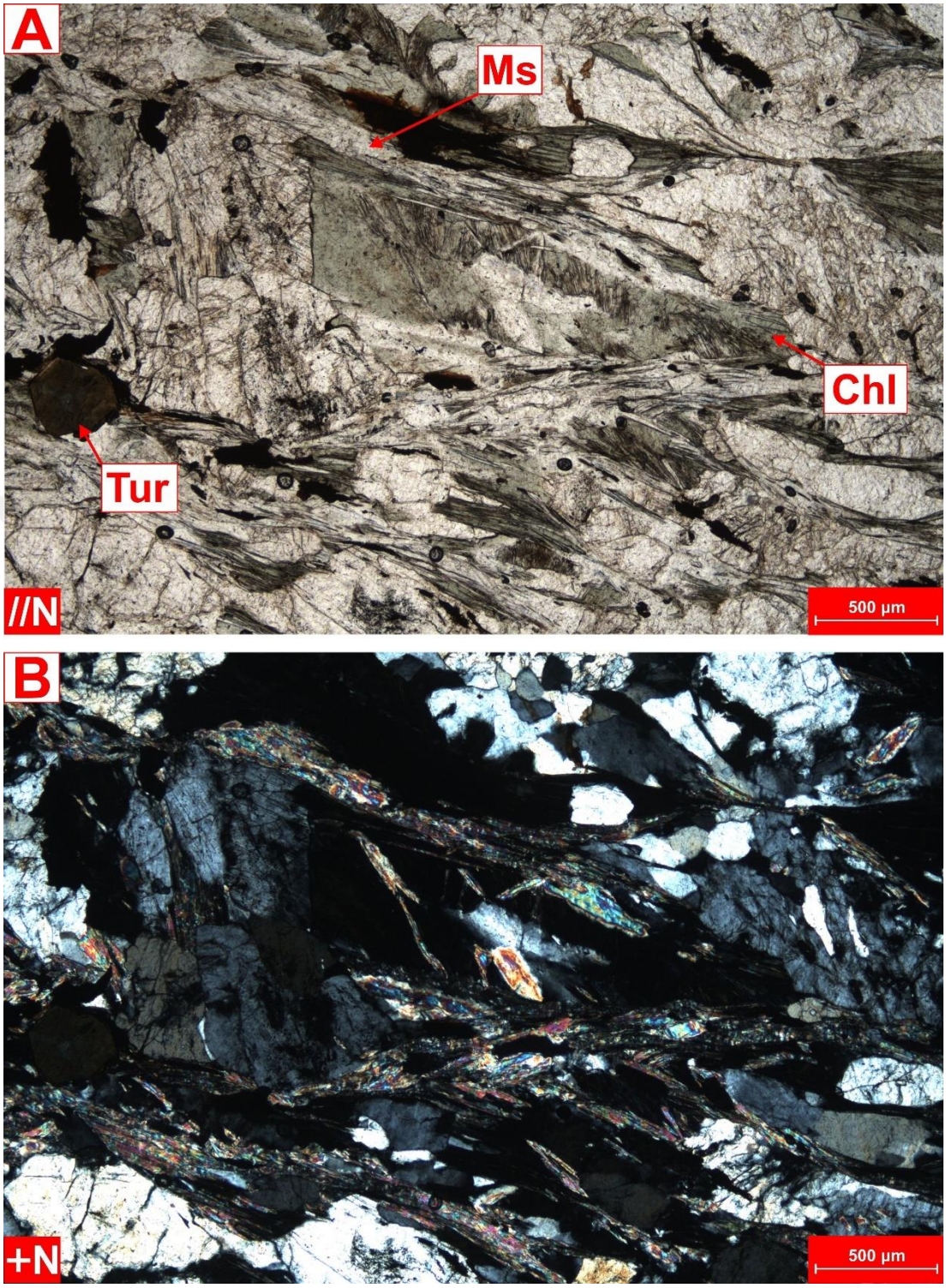


Figure 4.12 Another example of chlorite and muscovite together forming the foliations in the schist unit. Notice the tourmaline mineral perfectly dissected perpendicular to the C axis of the crystal. Chl: Chlorite, Ms: Muscovite, and Tur: Tourmaline. A) Under plane polarized light. B) Under cross polarized light

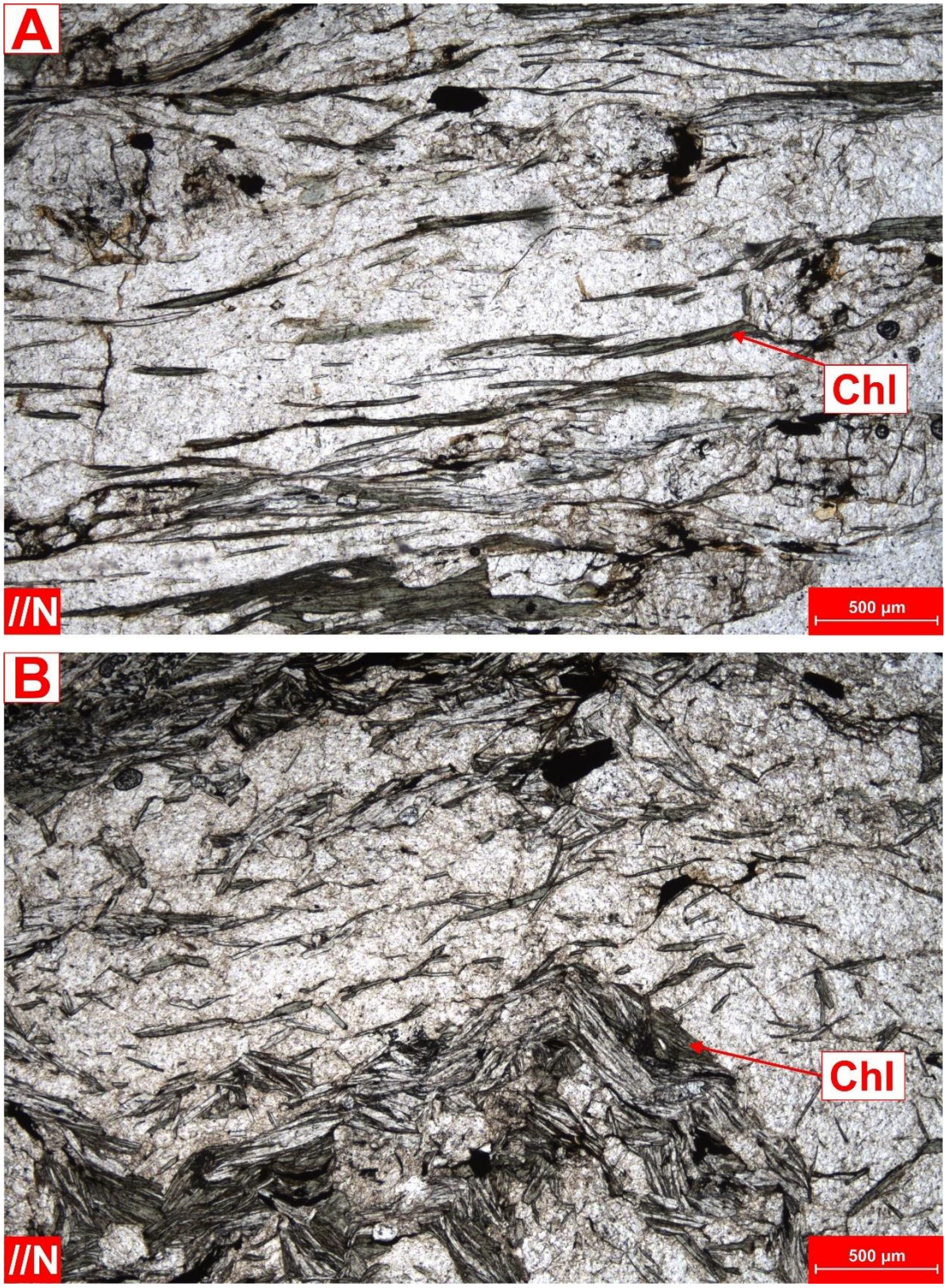


Figure 4.13 Albite and chlorite minerals. Chl: Chlorite. A) and B) Plane polarized light

To indicate the sense of movement and to conduct kinematic analysis upon the Özdere tectonic slice, oriented samples were collected from the field. The oriented thin sections were prepared to serve the orientation, they were sliced parallel to the lineations and perpendicular to the schistosities. The shear sense indicators were identified and are shown in the figures below (Figure 4.14 – 4.16)

To conduct kinematic analysis, shears sense indicator must be observed. The shear sense indicators may include, mica fish, sigmoids of sigma, theta and phi type, s-c structures, shear bands, strain shadows, and porphyroblast rotations.

The Özdere schists, along with the mesoscopic s-c structures as mentioned in Chapter Three, also contains microscopic s-c structures that were observed in prepared oriented thin sections. According to the offset of the c-planes, top-to-south sense of movement was indicated (Figure 4.14 – 4.16). Notice the well-developed shear bands of S and C planes.



Figure 4.14 An oriented thin section photomicrograph of Özdere schists showing shear sense indicator of s-c structure. According to the offset of the s-c structure planes, top-to-south sense of movement was indicated

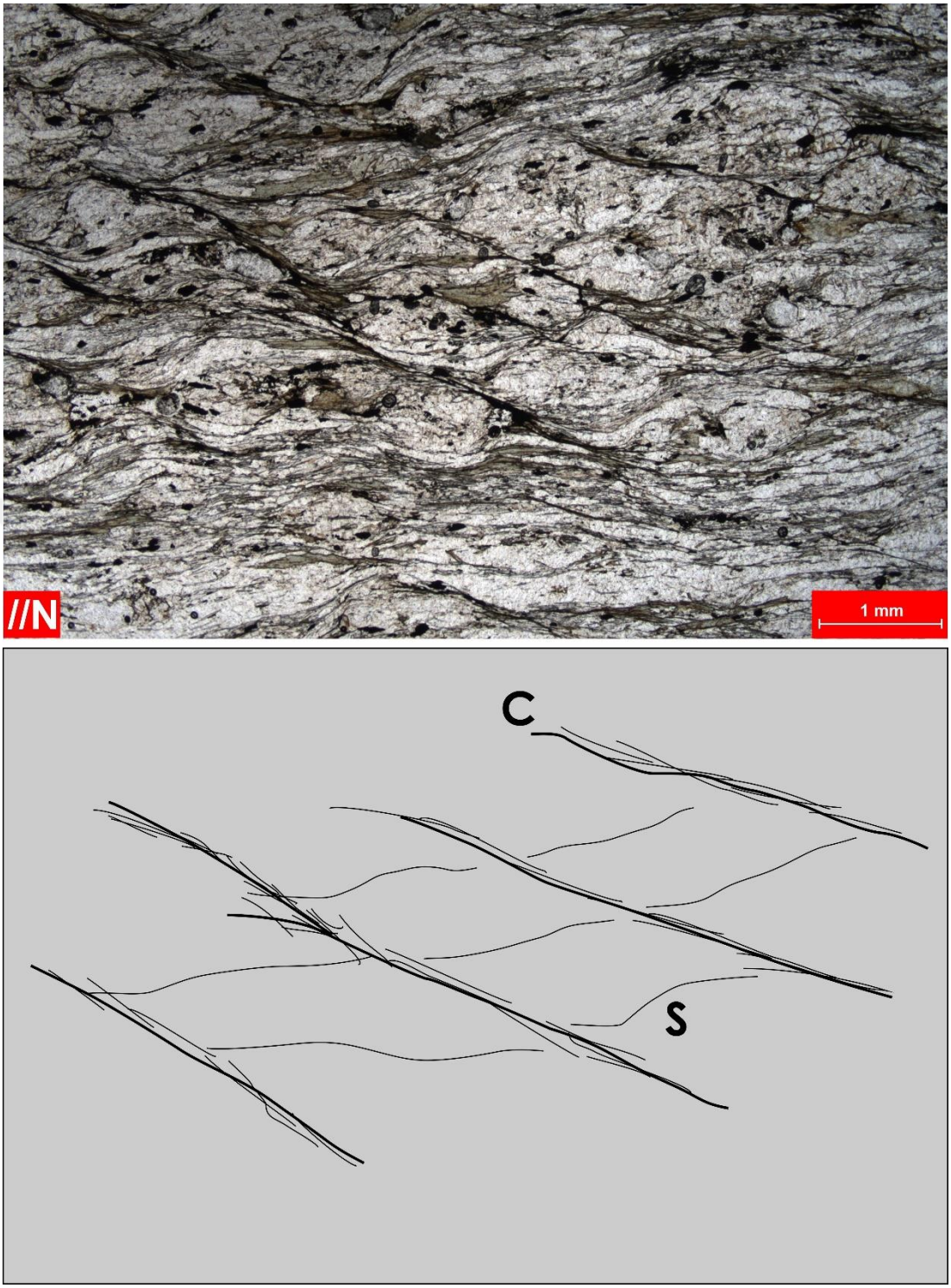


Figure 4.15 An oriented thin section photomicrograph of Özdere schists showing shear sense indicator of S-C structure. According to the offset of the S-C structure, top-to-south sense of movement is indicated

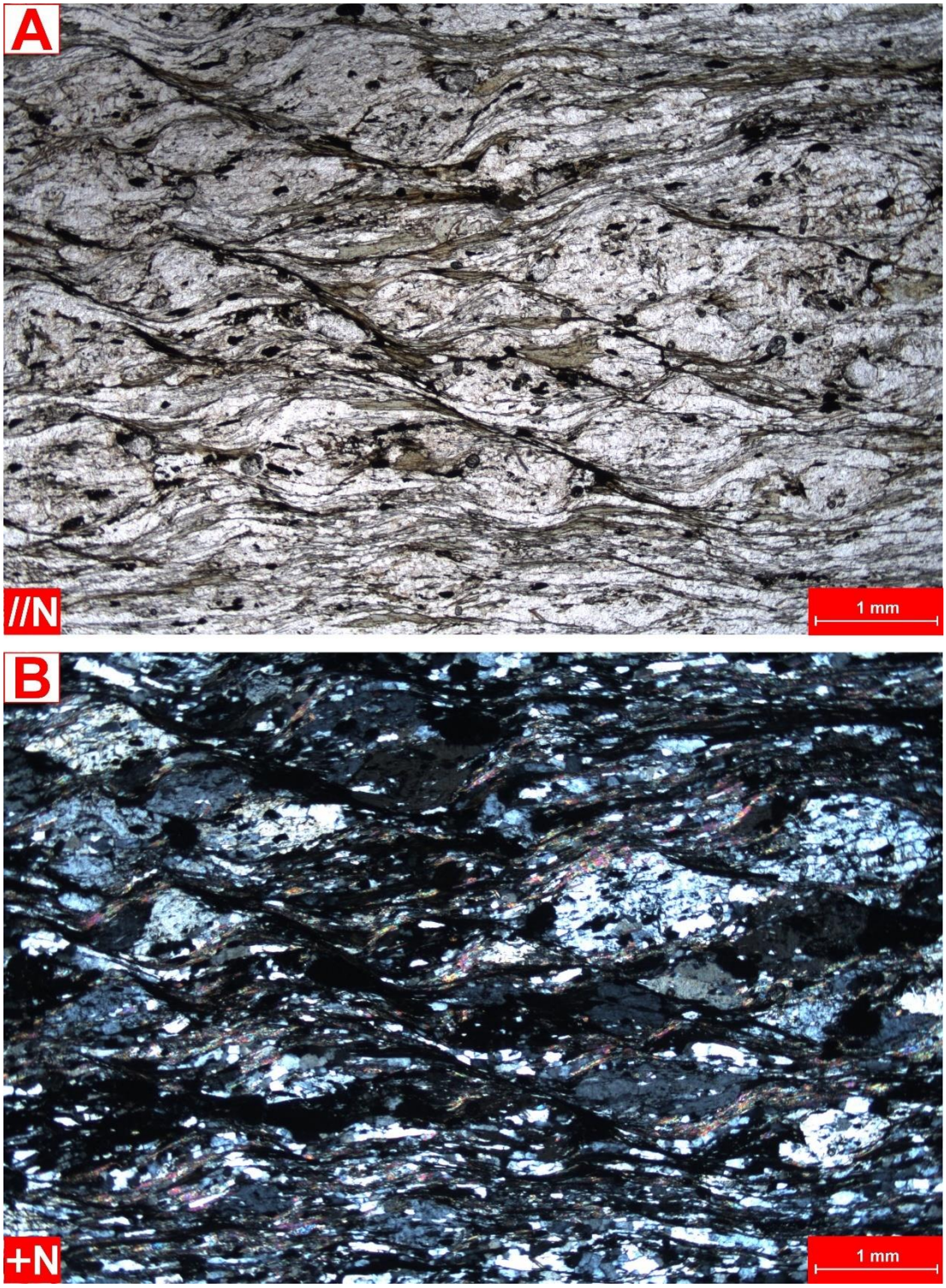


Figure 4.16 An oriented thin section photomicrograph of Özdere schists showing shear sense indicator of S-C structure. According to the offset of the S-C structure, top-to-south sense of movement is indicated. A) PPL and, B) XPL

4.3 Petrography of Zindan Schists

The rock units outcropping in the eastern region of the mapped area are classified as Zindan tectonic slice rock units. The units of the Zindan tectonic slice are in ascending order of schists at the base, phyllites intercalated with calc-schists, and metacarbonates consisting of marbles and dolomites at the top. According to the general mineral assemblage recognized in these units, the index minerals suggest that the metamorphic grade is Barrovian type greenschist facies yielding chlorite, biotite, and garnet subfacies conditions. The schist units in Zindan tectonic slice can be separated into two different schist units according to their mineral assemblages, the stratigraphically lower schist unit of quartz-muscovite-chloritoid-kyanite schist and overlying chlorite-biotite-garnet schist.

4.3.1 Quartz – Muscovite – Chloritoid – Kyanite Schist

The quartz-muscovite-chloritoid-kyanite schist outcrops just above the main detachment mylonitic zone of Özdere ductile shear zone between the two tectonic slices and it is well exposed in a considerably narrow NS trend starting form Zindancık Burnu at the south and extends up to southern mountain foot of Dededağ mountain to the north of the study area. This unit can be distinguished easily by its pale-yellow, yellowish-brown color and is characterized by a common penetrative schistosity of mica flake alignments.

The general mineral assemblage of this unit is determined to be quartz + albite + muscovite + chloritoid + garnet ± kyanite ± zircon and some opaque oxide coatings observed. This unit is generally exhibiting a well-developed lepidoblastic texture - less often displaying anastomosing texture - characterized by a very fine to fine grained muscovite alignments with albite and garnet porphyroblasts/poikiloblasts.

Quartz minerals show anhedral crystal properties in the thin sections and they are one of the most abundant minerals along with the albite found in the assemblage. Albite crystals are sometimes found as matrix forming material and sometimes as porphyroblasts and poikiloblasts containing numerous inclusions of other minerals in the assemblage (Figure4.17 – 4.18).

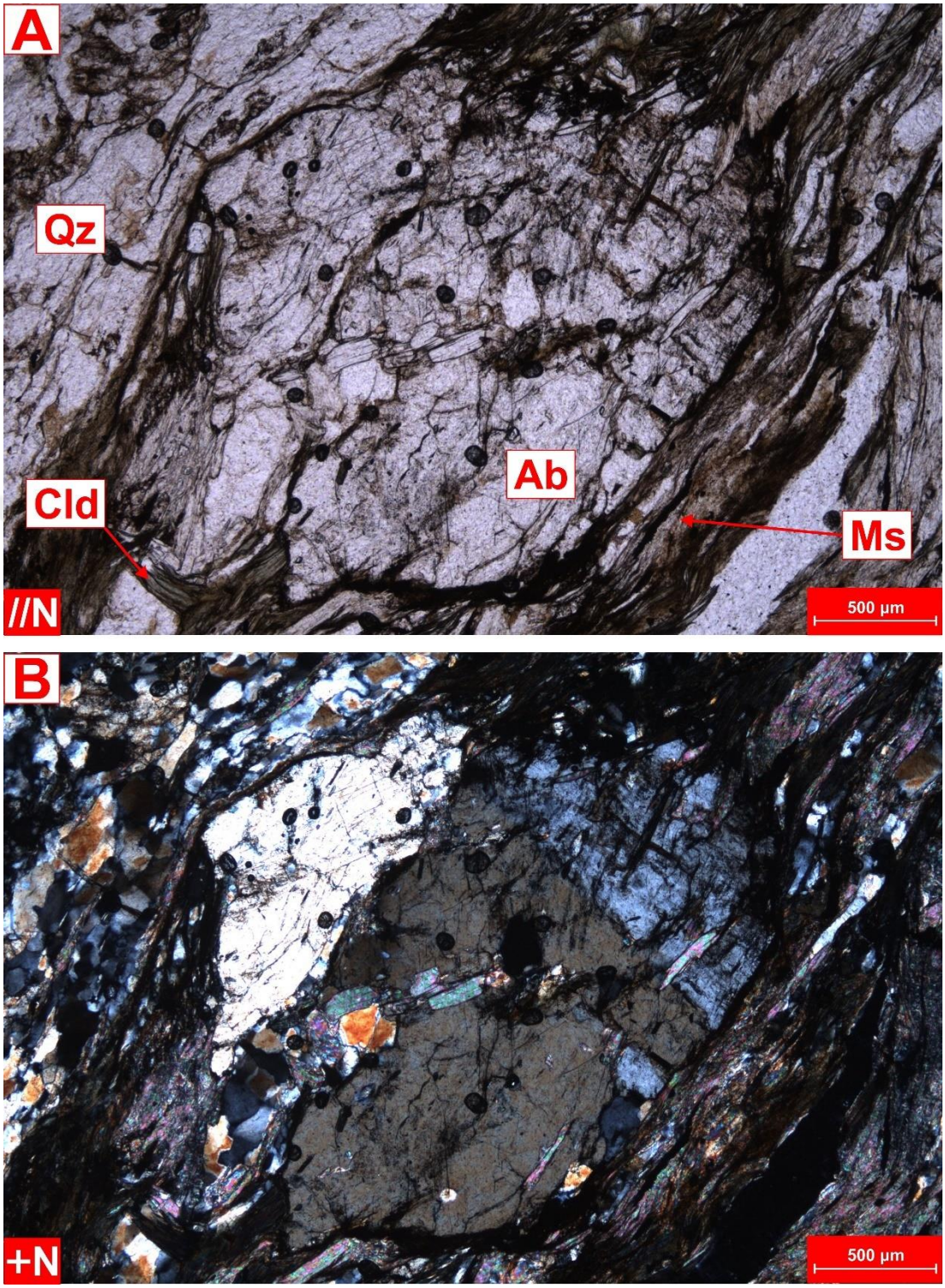


Figure 4.17 Poikiloblast grain of Albite with Muscovite and Chloritoid mineralization on the rim. Qz: Quartz – Ab: Albite - Cld: Chloritoid – Ms: Muscovite. A) PPL and B) XPL

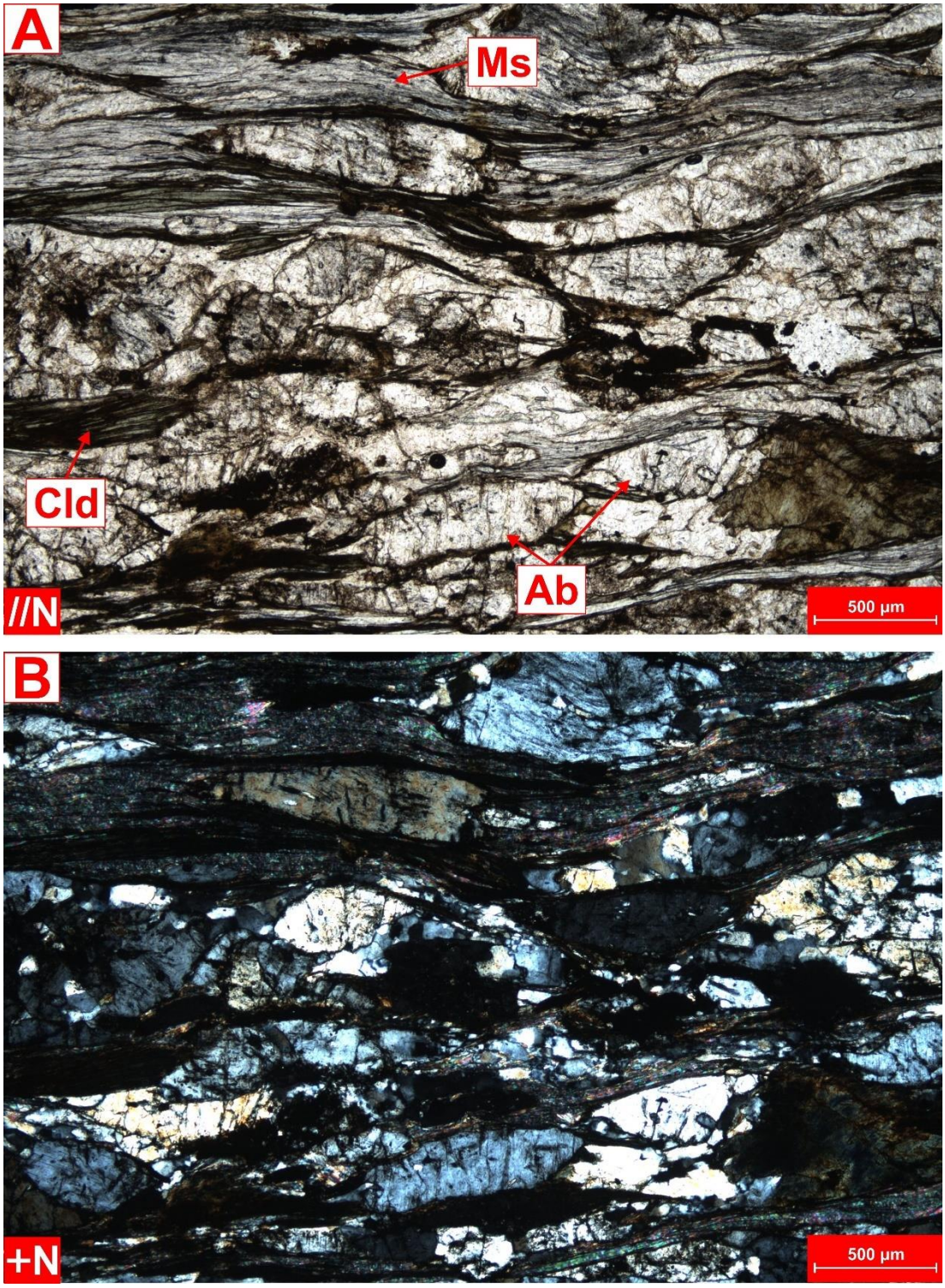


Figure 4.18 Muscovite and Chloritoid minerals align with well-developed foliation. Ab: Albite - Cld: Chloritoid – Ms: Muscovite. A) PPL and B) XPL

Muscovites within the quartz-muscovite-chloritoid-kyanite schist display typical characteristics of low to moderate relief in plane polarized light and show no pleochroism while having a high order interference color and “bird’s eye” extinction in cross polarized light. In addition, muscovite flakes are very dominant in distinctly foliated places (Figure 4.19).

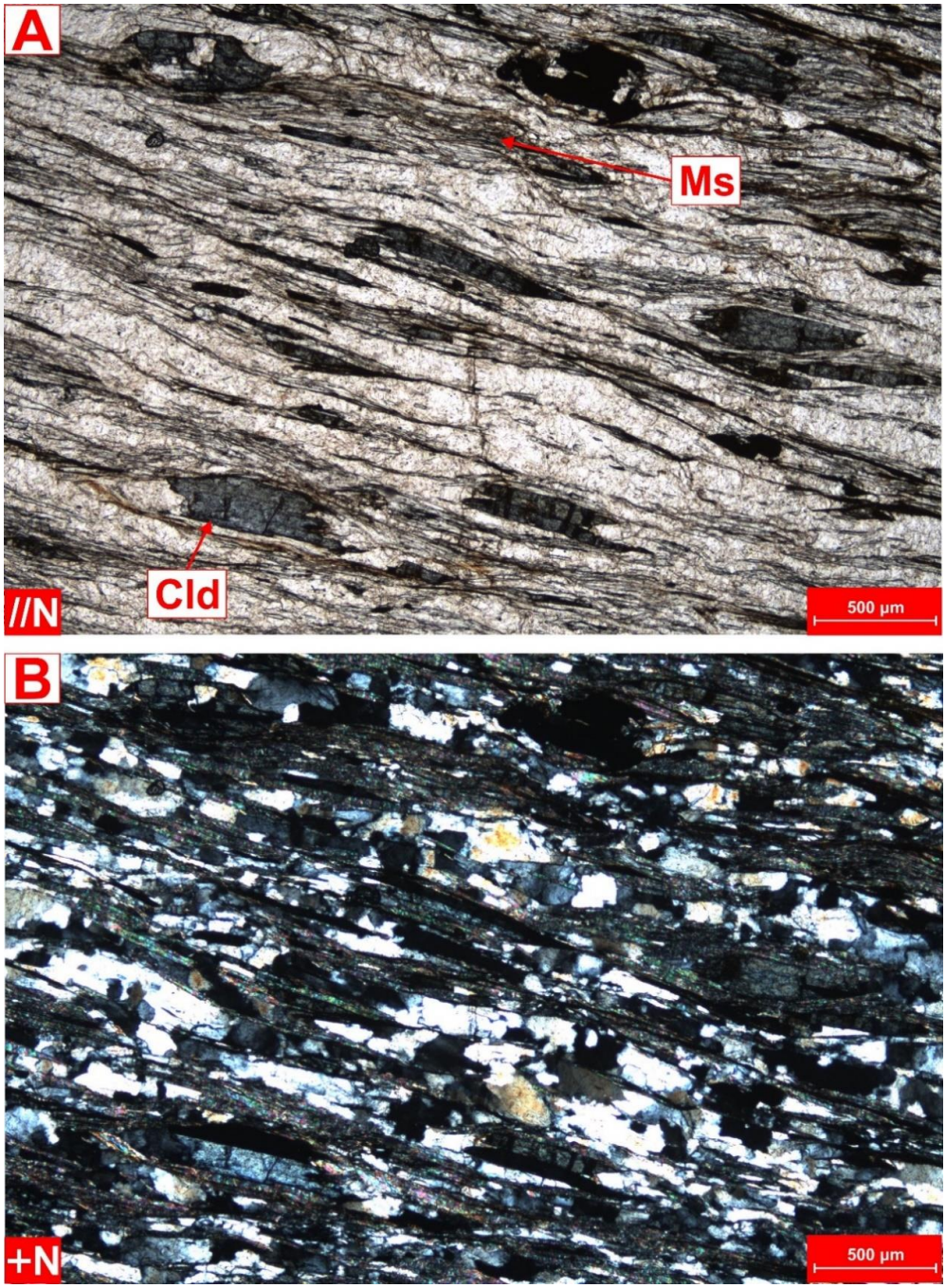


Figure 4.19 Muscovites and Chloritoid minerals showing typical mineralogical features. Cld: Chloritoid – Ms: Muscovite. A) PPL and B) XPL

Chloritoids are very common in the unit and they have been defined as a key mineral in the assemblage. They are showing prominent alignment with muscovite minerals in terms of parallelism in foliations. Common features of high relief and pale green to blue pleochroism is present aside from having dark blue, brown, and purple interference colors (Figure 4.20 – 4.21). Twining in the chloritoid crystals has not been observed.

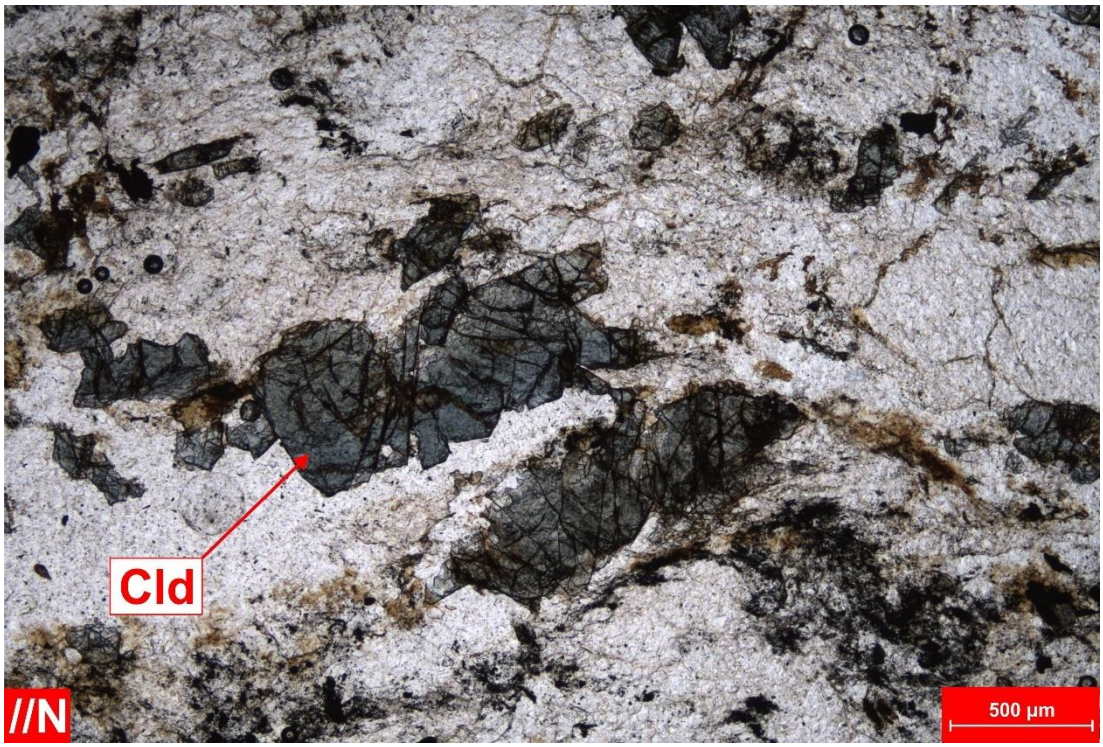


Figure 4.20 A well-developed Chloritoid mineral displaying typical features of high relief and pale green to blue pleochroism. Photomicrograph is in PPL

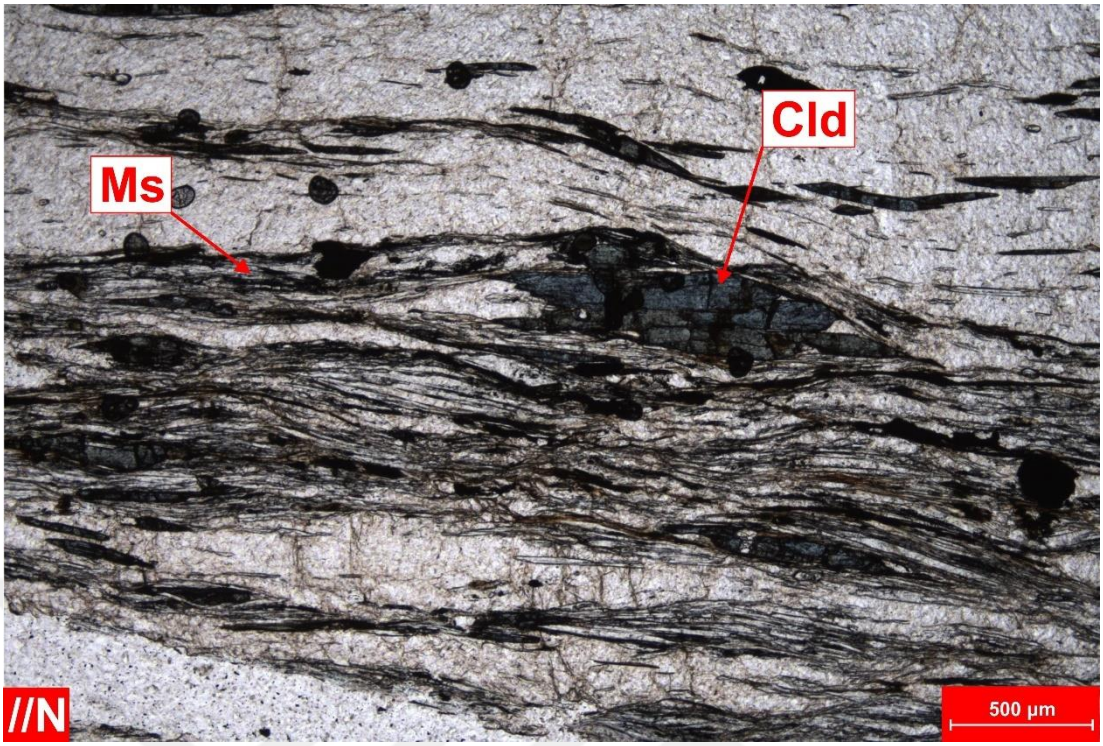


Figure 4.21 A good example of comparative photomicrograph of a thin section including Muscovite flakes and Chloritoid mineralization developed parallel to the foliation. Ms: Muscovite – Cld: Chloritoid. Photomicrograph is in PPL

Aside from the lepidoblastic texture, the unit also shows porphyroblastic texture features with both albite and garnets. The albite porphyroblasts that are usually surrounded by muscovites and chloritoids, have a considerable amount of quartz, garnet and zircon inclusions. The garnet porphyroblasts are usually grown inside the ablites as inclusions. Some garnets crystals are observed to be pseudomorphs and partially replaced by chloritoid minerals. At some localities garnet porphyroblasts are observable in the outcrops with the grain size of garnets changing between 1mm and 3 mm in diameter (Figure 4.22 – 4.26).

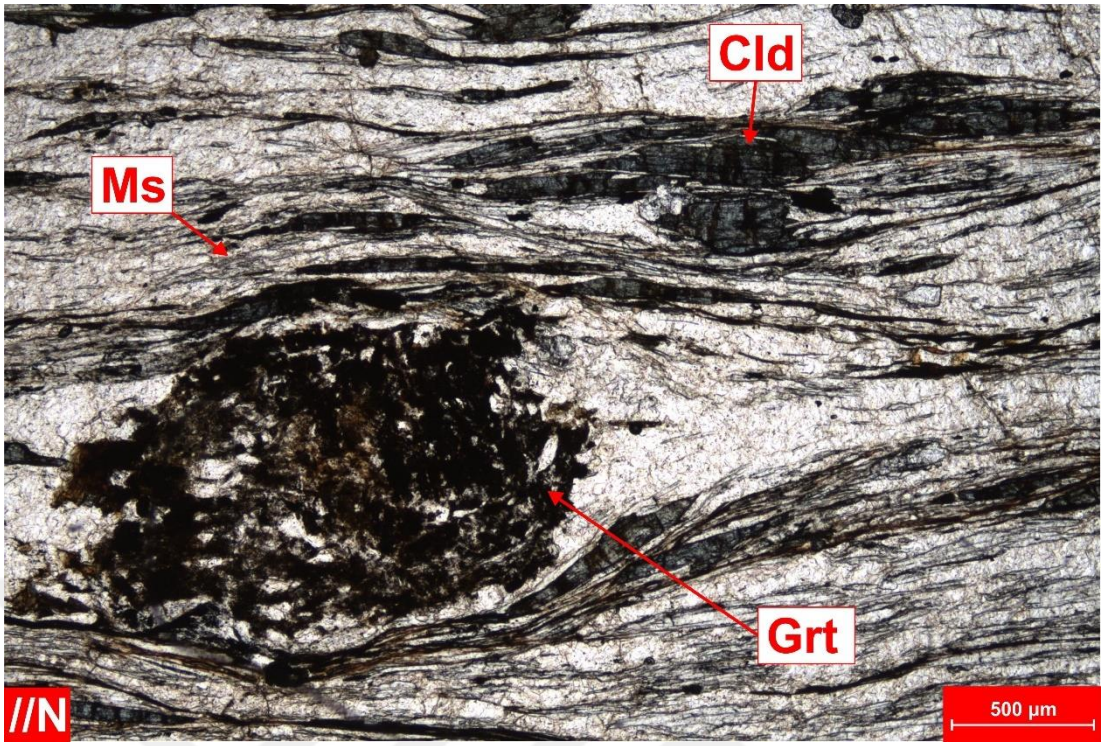


Figure 4.22 Porphyroblastic texture with a garnet crystal porphyroblast surrounded by muscovite and chloritoid minerals. Ms: Muscovite – Cld: Chloritoid – Grt: Garnet. Photomicrograph is in PPL

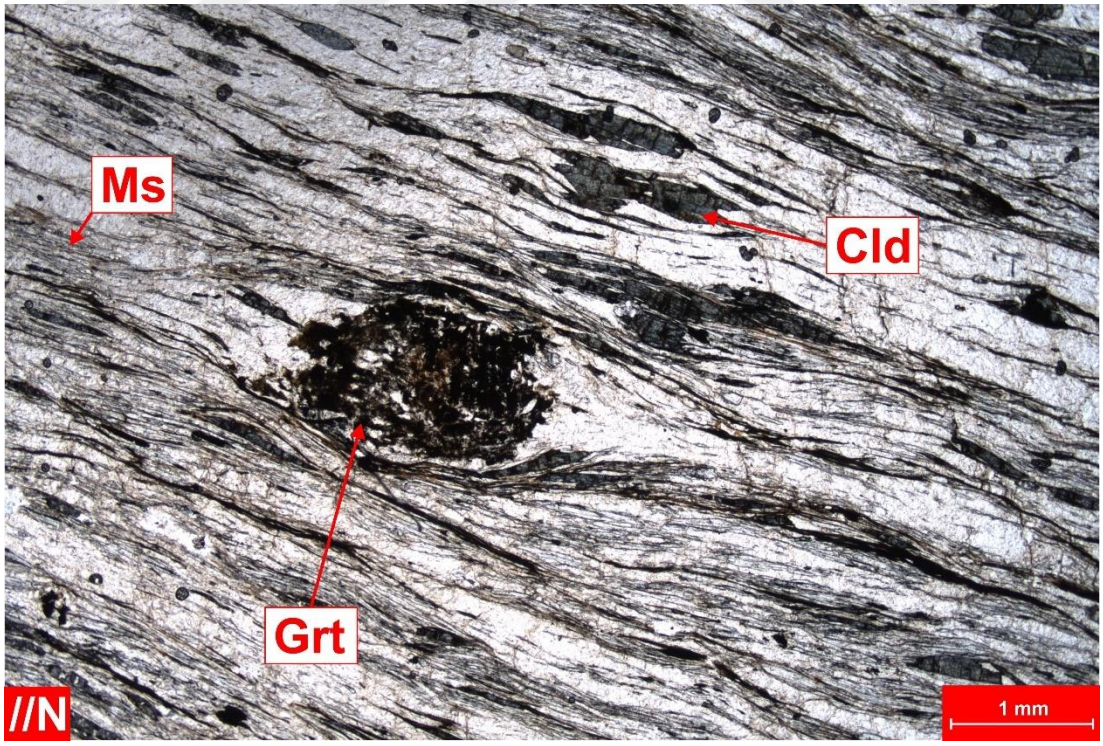


Figure 4.23 Garnet porphyroblast in Garnet-Chloritoid schist unit of Özdere tectonic slice. Ms: Muscovite – Cld: Chloritoid – Grt: Garnet. Photomicrograph is in PPL

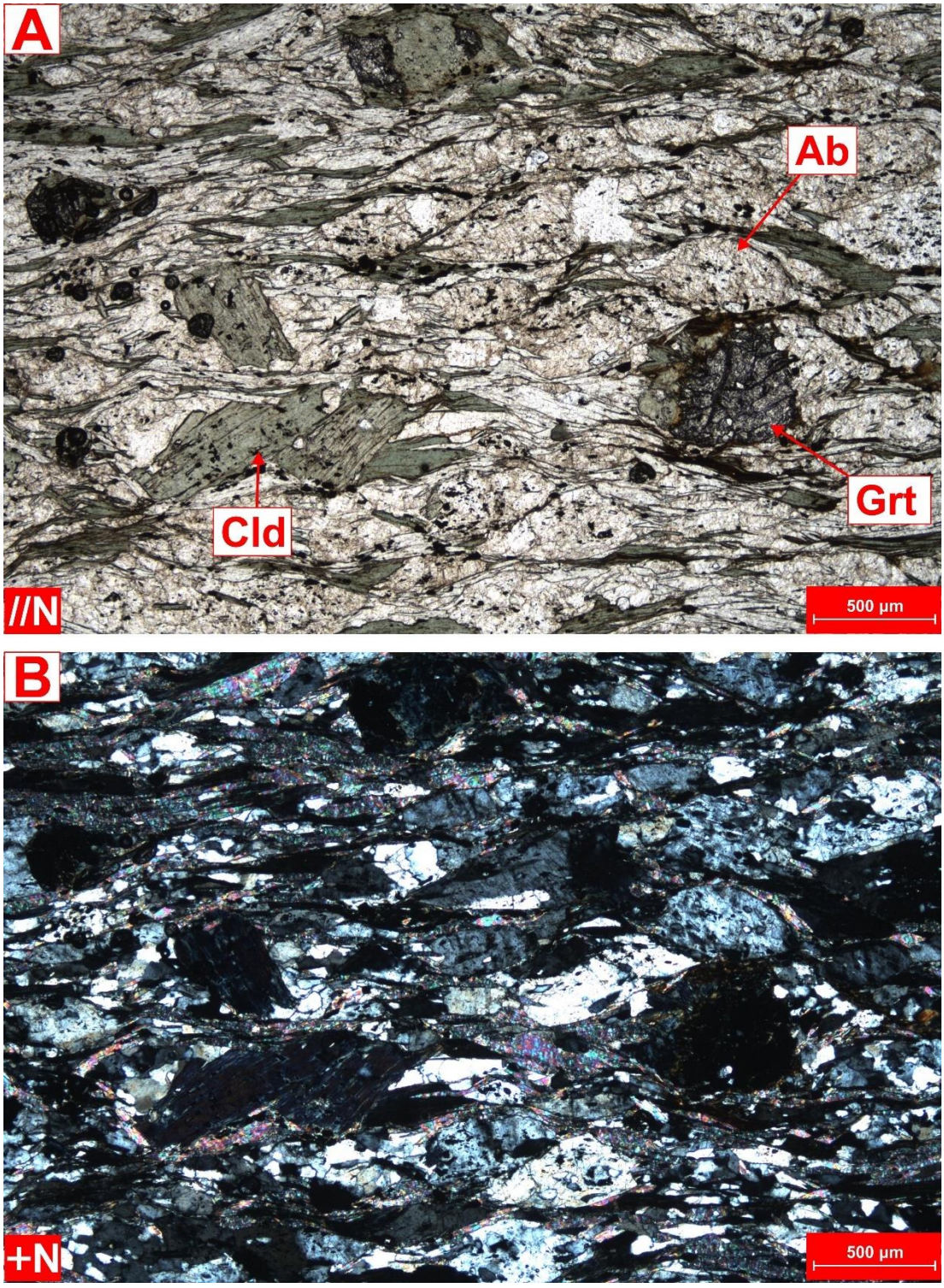


Figure 4.24 A garnet porphyroblast being replaced by chloritoid mineral representing retrograd metamorphic phase. Ab: Albite – Cld: Chloritoid – Grt: Garnet. Photomicrographs are in A) PPL and B) XPL

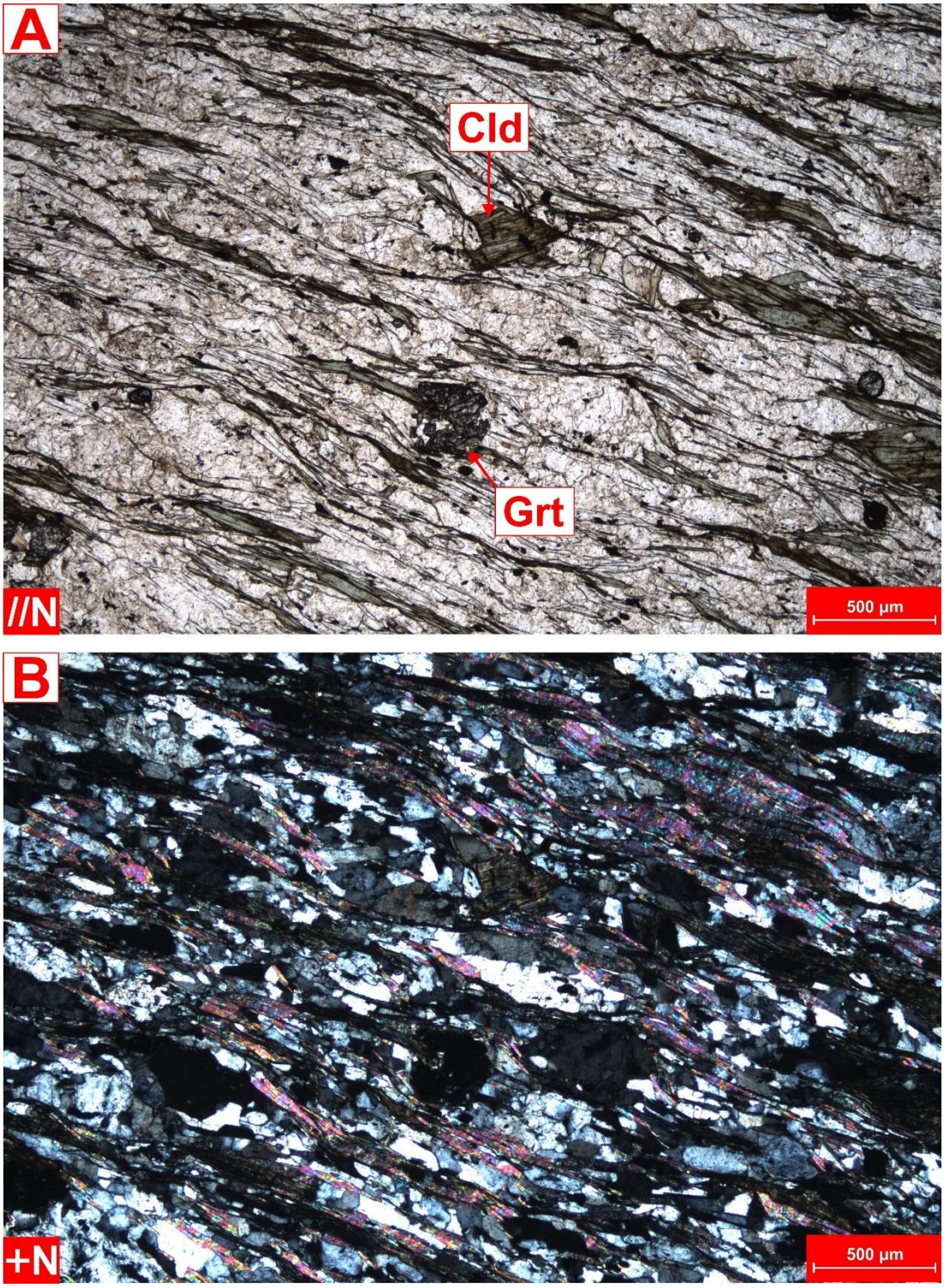


Figure 4.25 Subhedral garnet porphyroblast being overprinted by chloritoid. Cld: Chloritoid – Grt: Garnet. Photomicrographs are in A) PPL and B) XPL

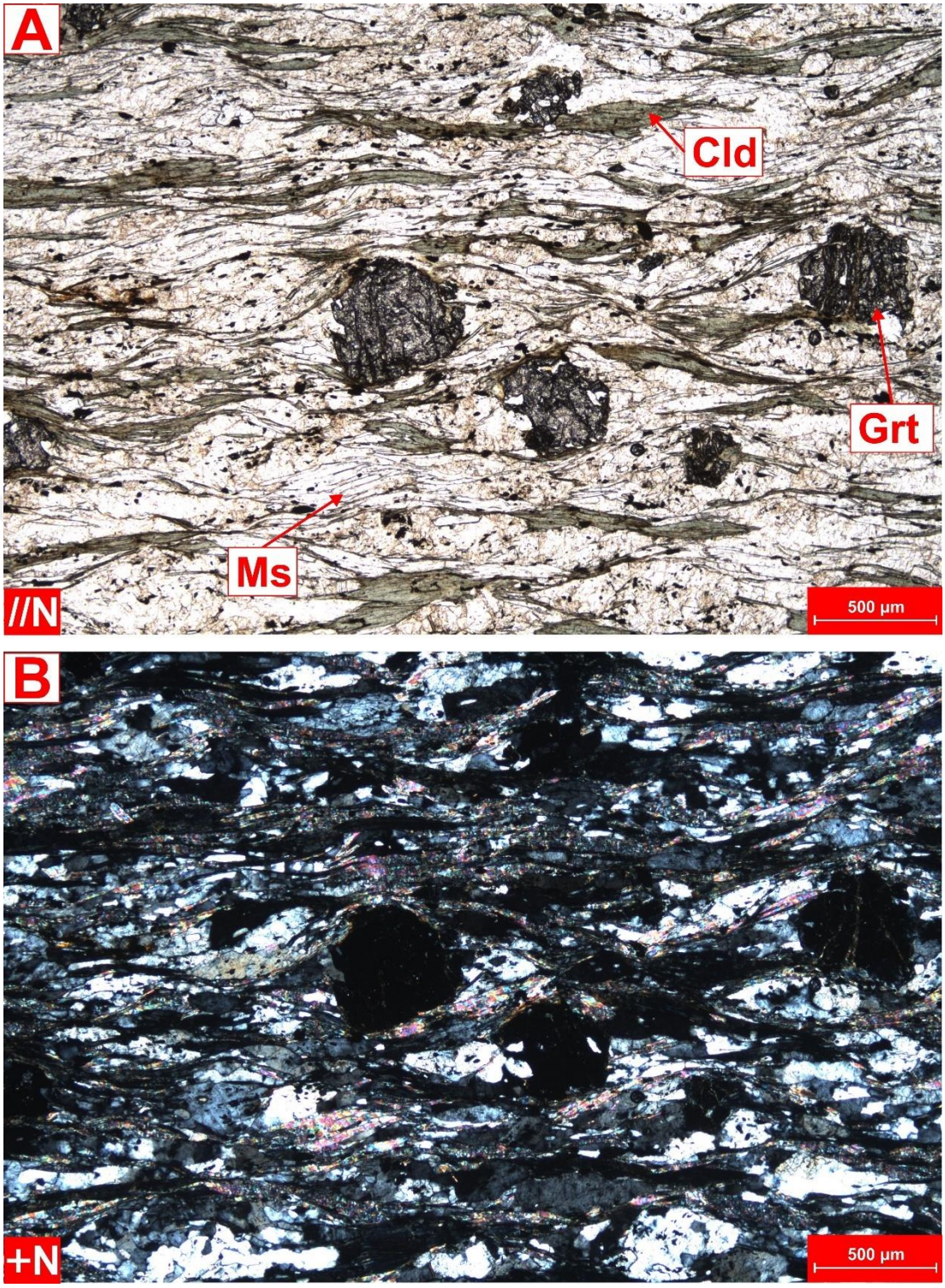


Figure 4.26 Euhedral and subhedral garnet porphyroblasts surrounded by muscovite flakes at the rims. Notice the Albite development at the pressure shadow of garnet crystals. Ms: Muscovite – Cld: Chloritoid – Grt: Garnet. Photomicrographs are in A) PPL and B) XPL

Kyanite mineral was only observed in one thin section obtained from this schist unit as a single crystal bundle in a deformed and bent shape. The crystal displays high relief in plane polarized light (Figure 4.27).

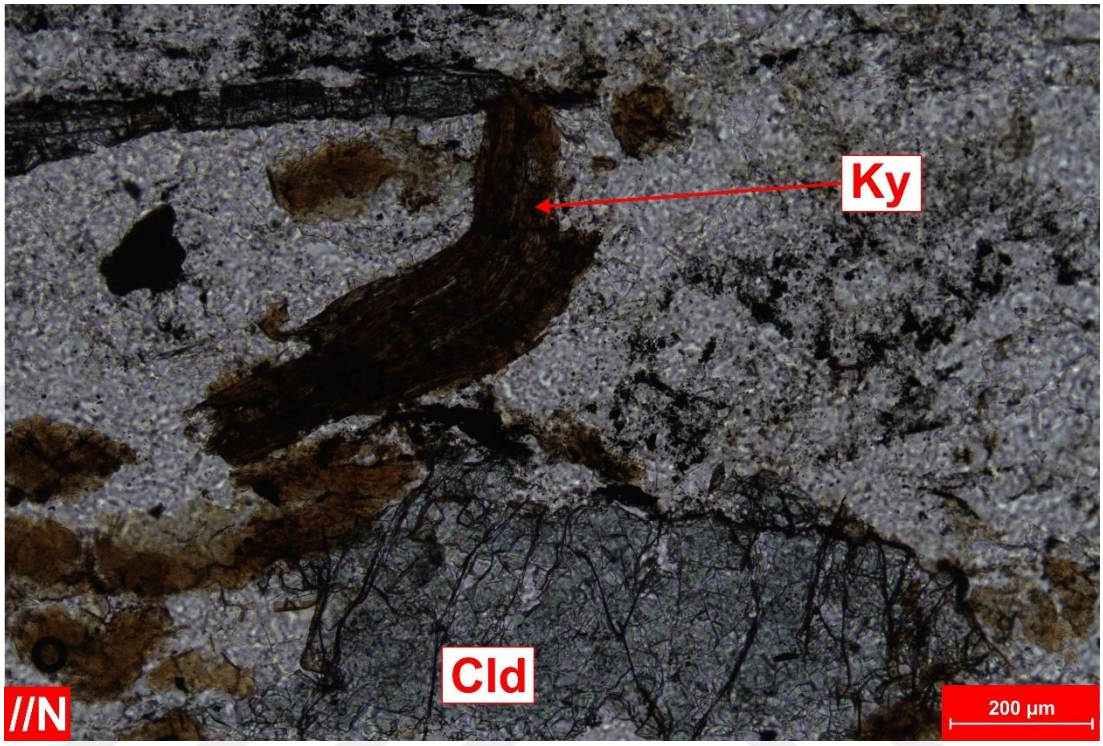


Figure 4.27 A pre-tectonic kyanite crystal coexisting with chloritoid mineral. Notice the deformation and bending of the crystal. Cld: Chloritoid – Ky: Kyanite. Photomicrographs are in A) PPL and B) XPL

Zircon minerals show tetragonal crystal form with colorless and high relief in plane polarized light. It is usually found as inclusions in the albite minerals but also has been observed as enclosed in the muscovite foliations with the same parallelism. In cross polarized light displays strong third and fourth order interference colors (Figure 4.28).

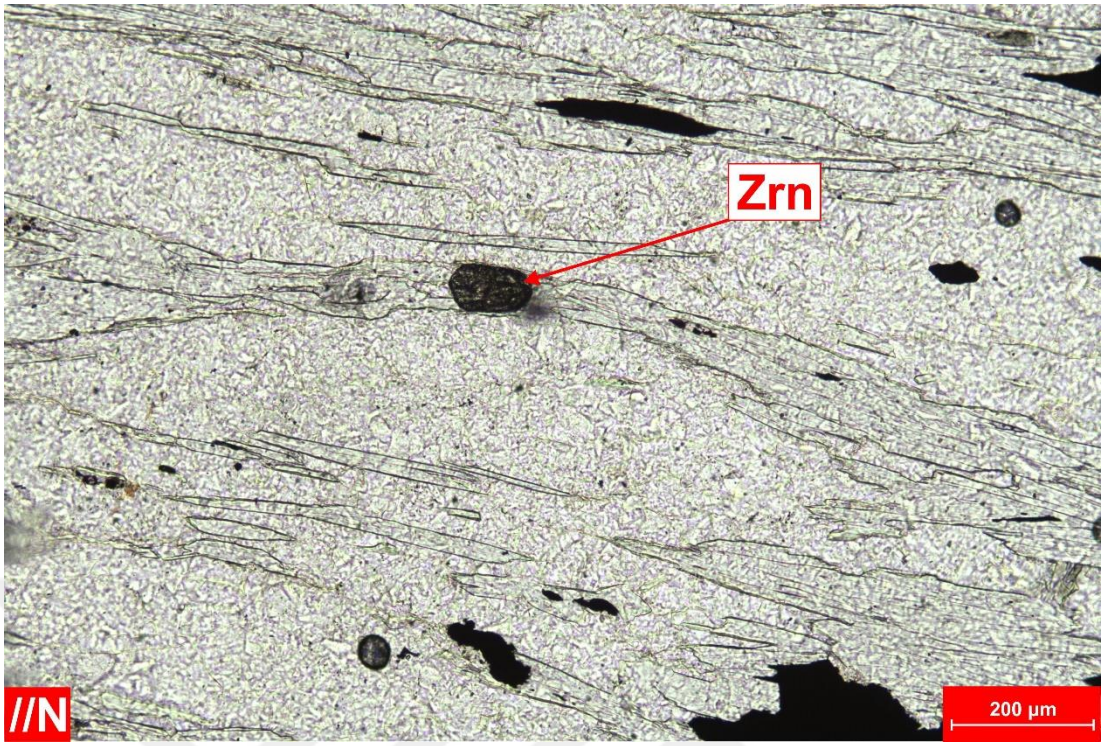


Figure 4.28 A typical zircon grain enclosed in muscovite foliation. Zrn: Zircon

4.3.2 Chlorite – Biotite – Garnet Schists

The chlorite – biotite – garnet schist unit was observed in the south-central part of the Zindan tectonic slice outcropping on a widespread area in between quartz – muscovite – chloritoid – kyanite schist on the bottom and metacarbonates of Kargıcak Marbles on the top. This unit is intercalated with phyllites, calc-schists, and yellow-colored dolomites at some localities close the Koru Shear zone.

The general mineral assemblage of this unit is determined to be quartz + albite + muscovite + chlorite + biotite + garnet ± chloritoid. This unit also exhibits a well-developed lepidoblastic texture characterized by a very fine to fine grained muscovite alignments with albite and garnet porphyroblasts/poikiloblasts. The quartz minerals show anhedral crystal properties and they are one of the most abundant minerals along with the albite and muscovite found in the assemblage (Figure 4.29).

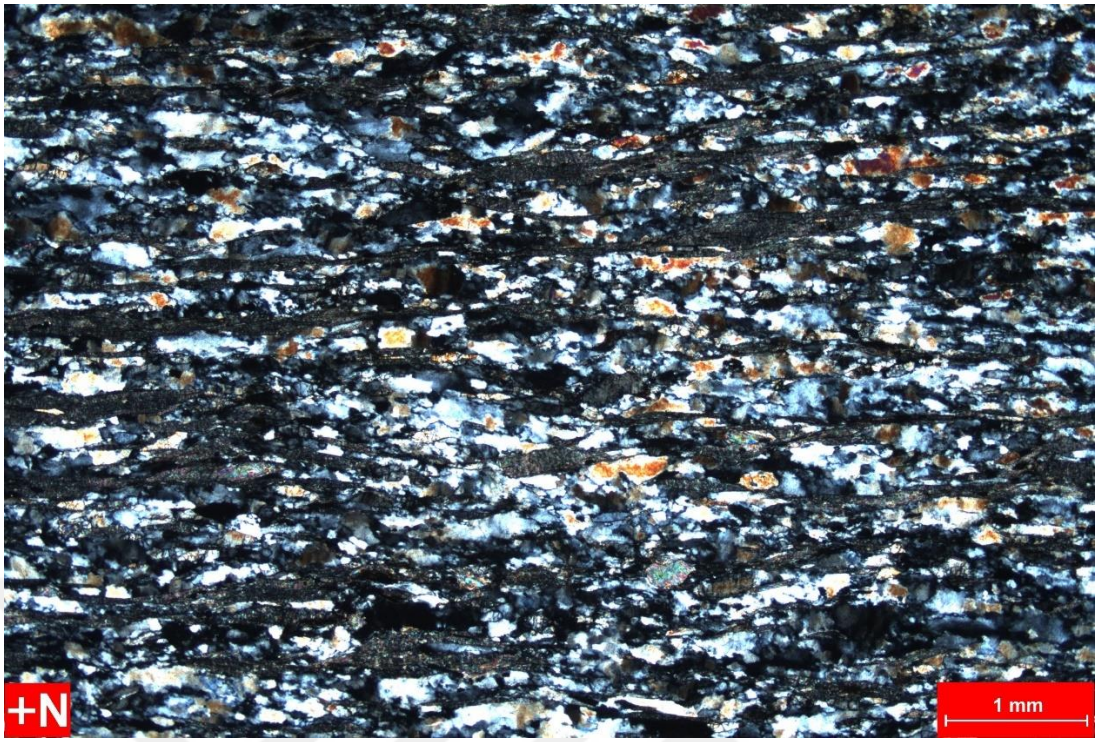


Figure 4.29 Fine grained muscovite forming the foliations of the rock unit. Photomicrograph is in XPL

Muscovite minerals show a good alignment with the foliations and usually they coexist with chlorite and biotite (Figure 4.30 – 4.33). The observed chlorite replacements in the thin sections indicate a common retrogressive metamorphism feature.

The biotite minerals in chlorite – biotite – garnet schist unit display normal pleochroism with E-W orientation in PPL having the darkest color of brown to reddish – brown. Moderate to low relief of biotite minerals were observed. The crystals usually have irregular boundary shapes with general parallelism along the foliations.

The cross polarized light properties of the chlorite – biotite – garnet schist unit include high order interference colors and bird's eye extinction (.

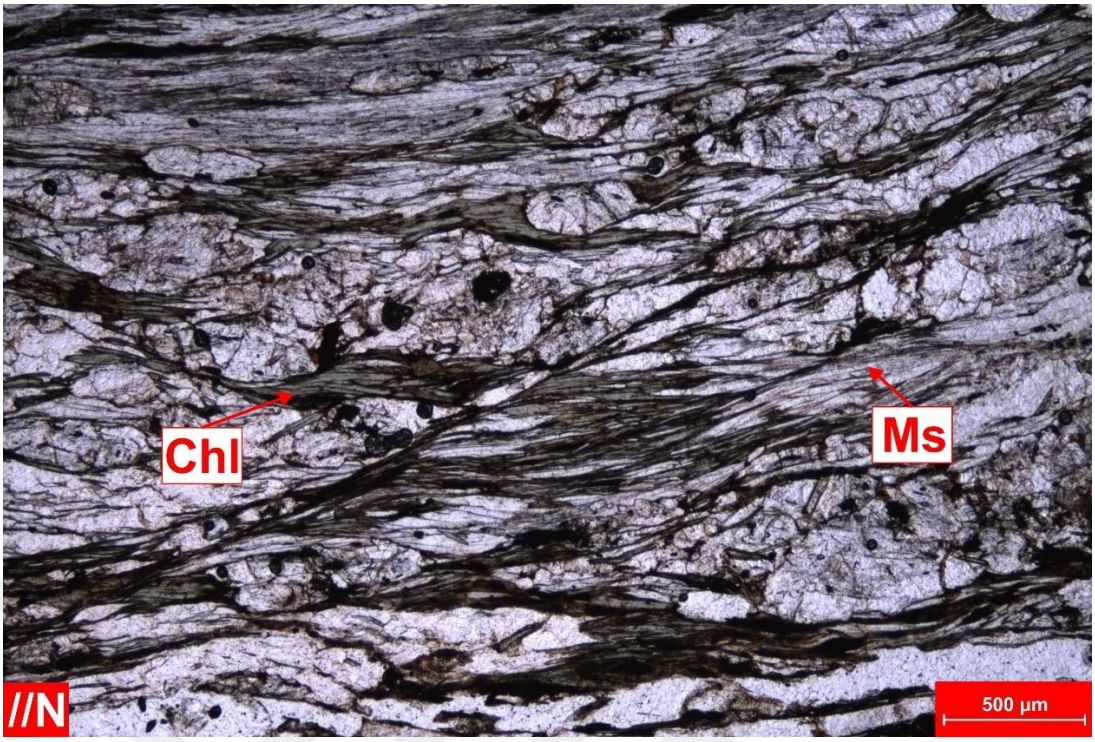


Figure 4.30 Coexisting of chlorite and muscovite minerals as foliations. Chl: Chlorite – Ms: Muscovite. Photomicrograph is in PPL

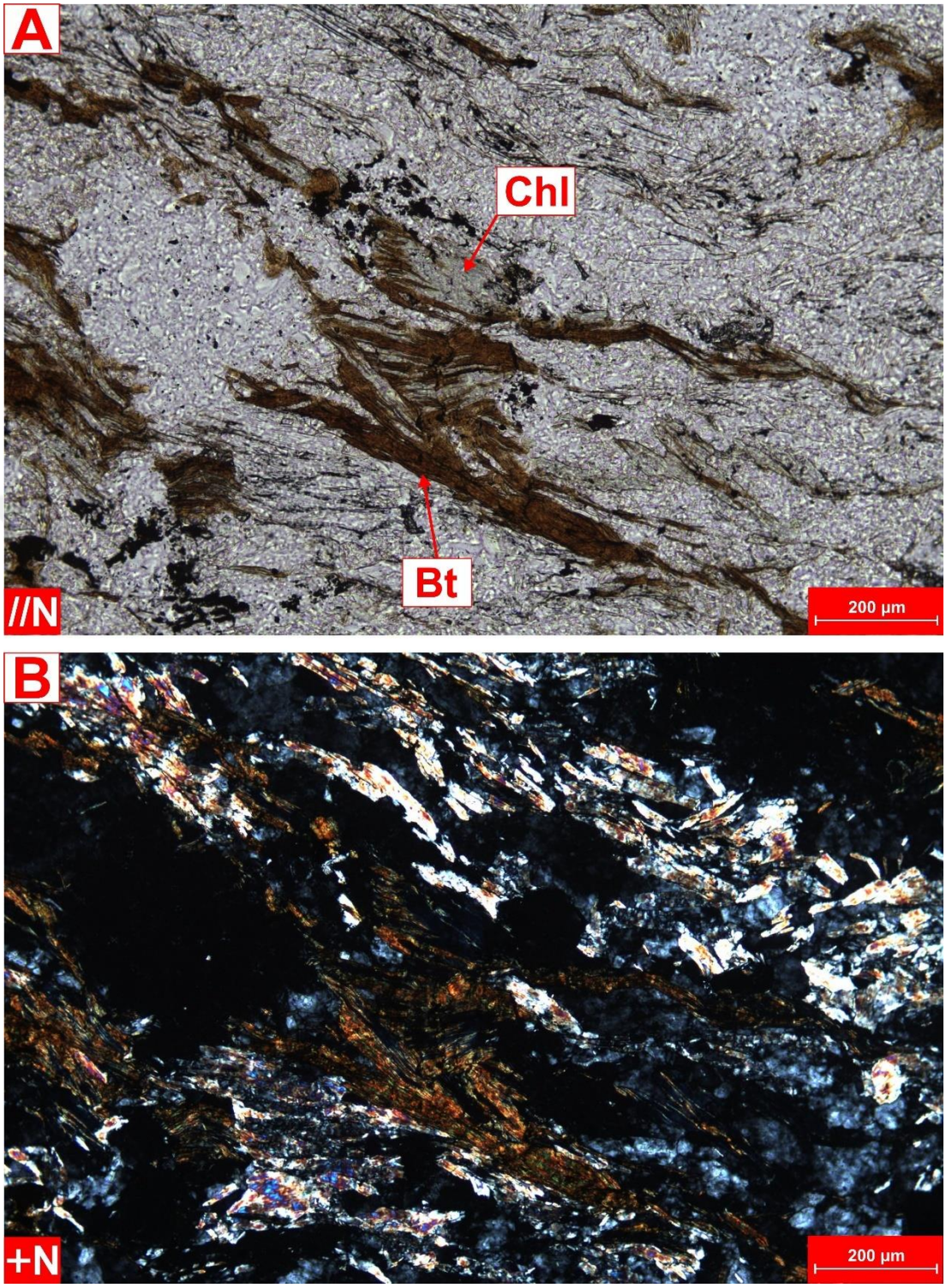


Figure 4.31 Chlorite and Biotite forming the foliations. Notice the chloritic overprint on the biotite flakes. Chl: Chlorite – Bt: Biotite. Photomicrographs are in A) PPL and B) XPL

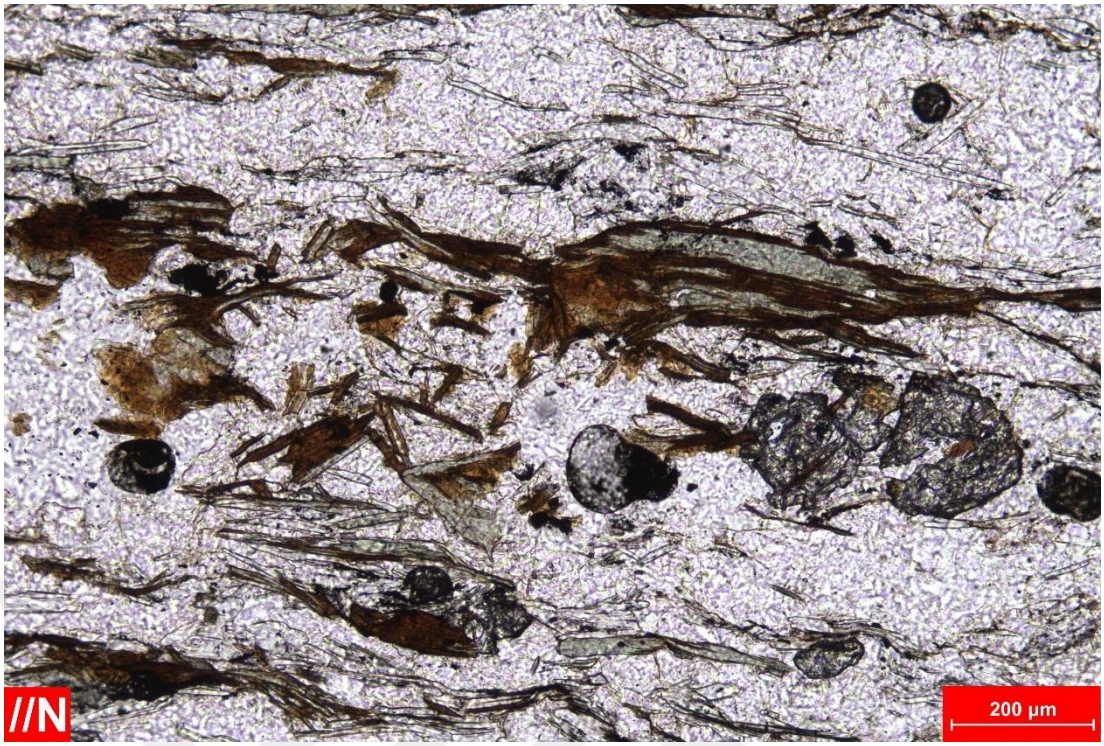


Figure 4.32 Garnet, chlorite and biotite minerals are coexisting together. Notice the replacement of garnet by chlorite and biotite on the rims of garnet. Photomicrograph is in PPL

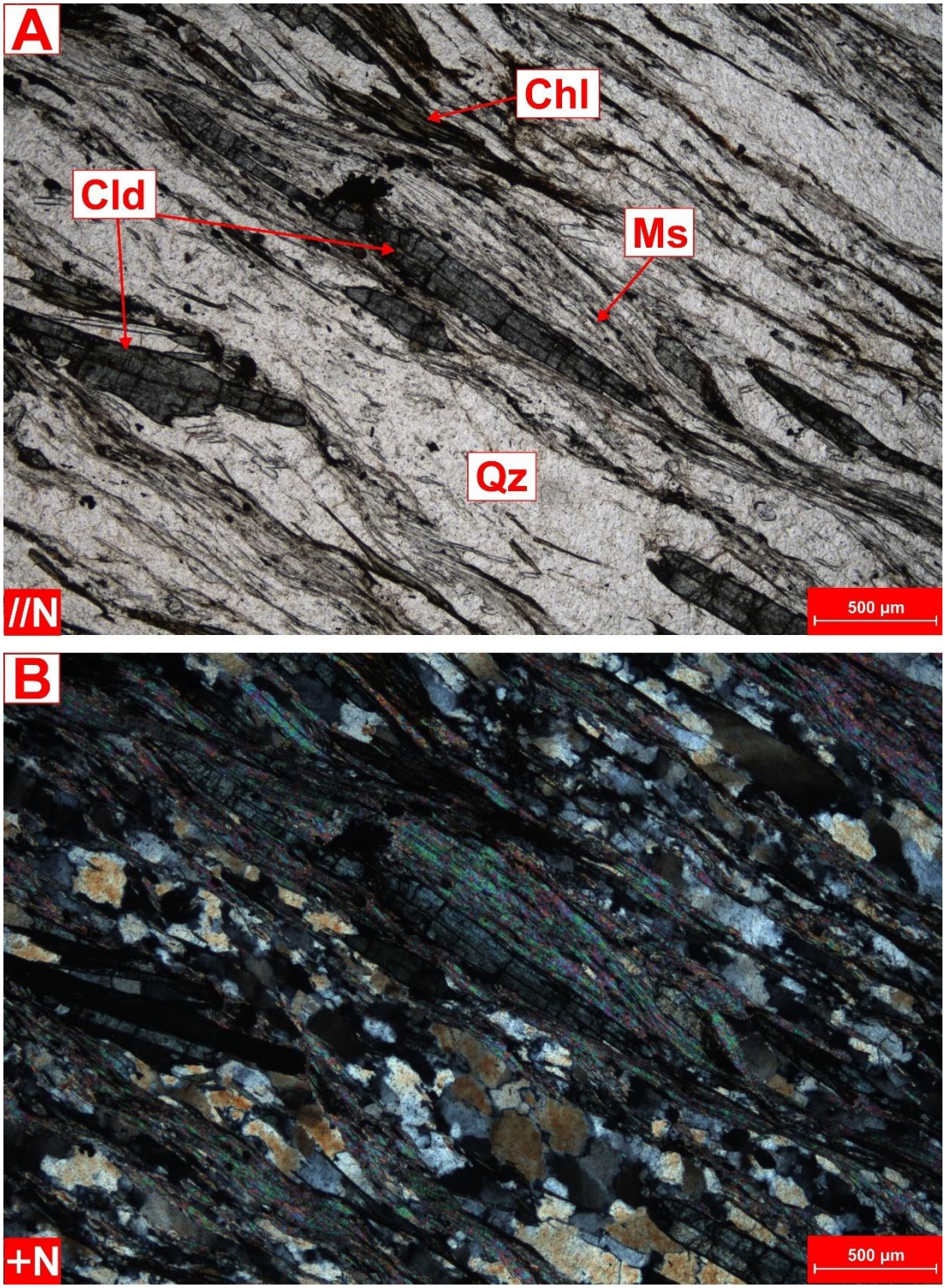


Figure 4.33 Chloritoid, chlorite and muscovite display well-developed parallelism together forming the foliations. Photomicrographs are in A) PPL and B) XPL

Albites are found as poikiloblasts usually with inclusions of garnets and some other minerals found in the assemblage (Figure 4.34 – 4.36).

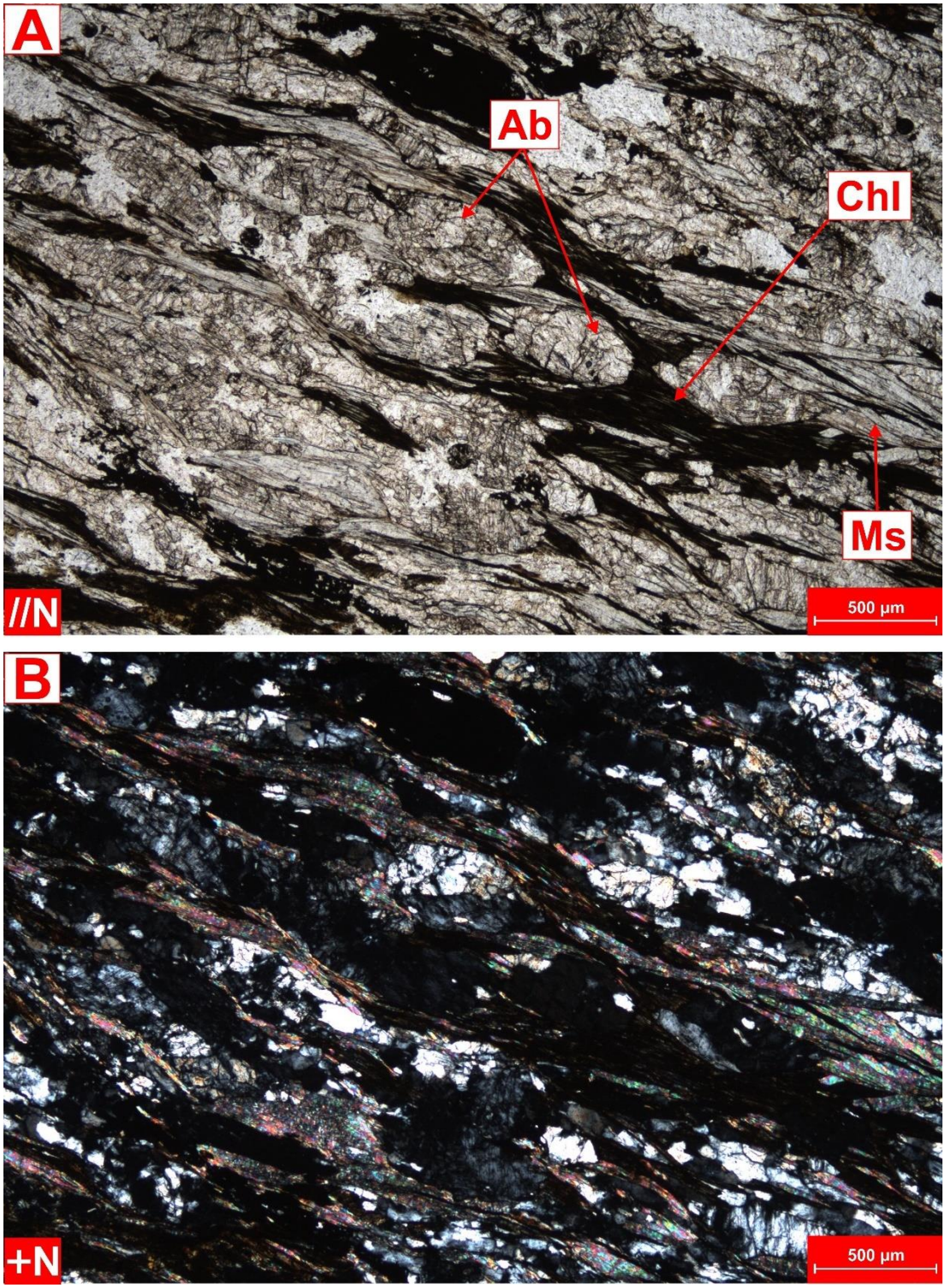


Figure 4.34 Albite poikiloblasts containing inclusions of other minerals from the assemblage. Chl: Chlorite – Ms: Muscovite – Ab: Albite. Photomicrographs are in A) PPL and B) XPL

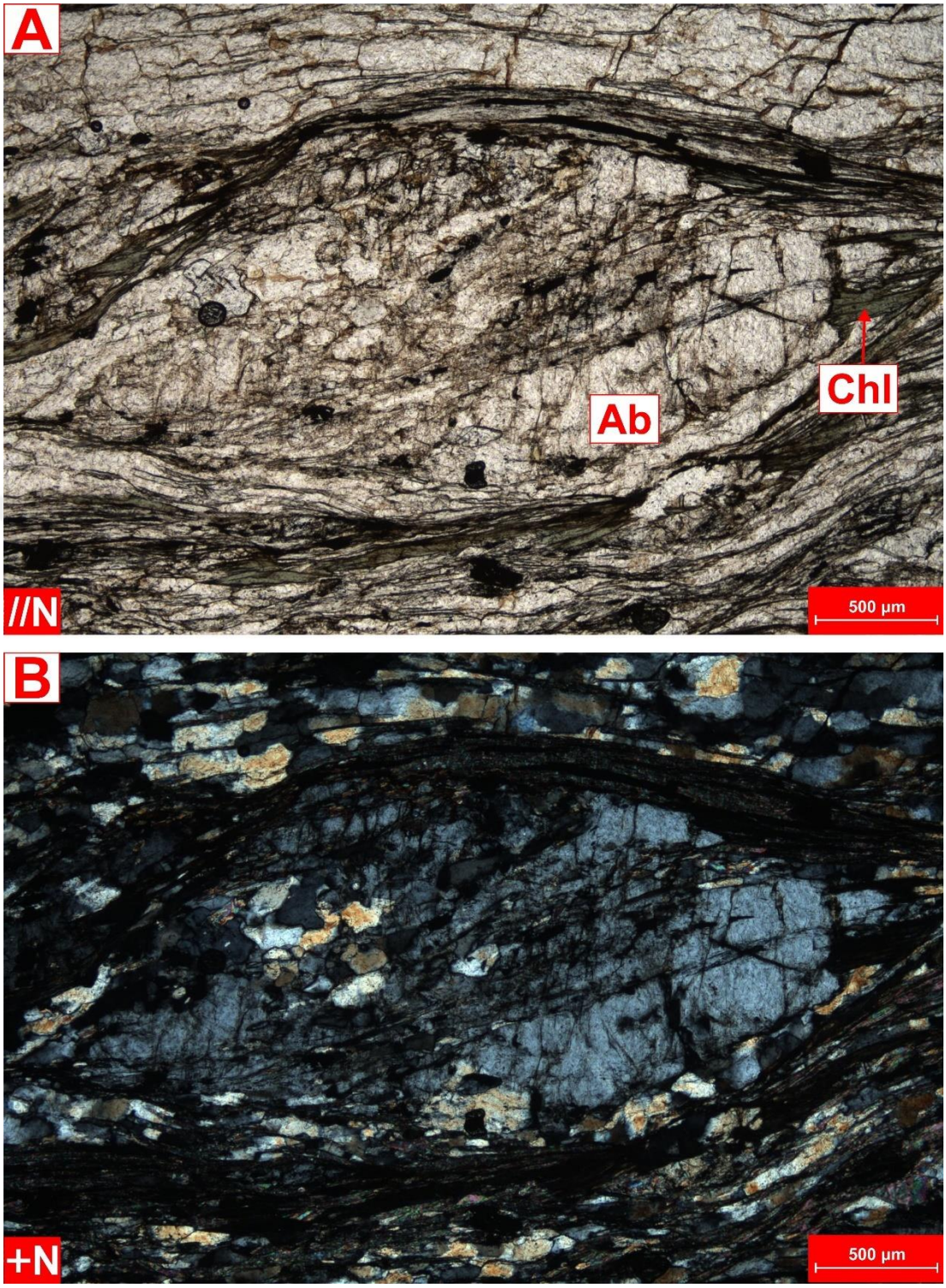


Figure 4.35 Albite poikiloblasts containing inclusions of other minerals from the assemblage. Chl: Chlorite – Ms: Muscovite – Ab: Albite. Photomicrographs are in A) PPL and B) XPL

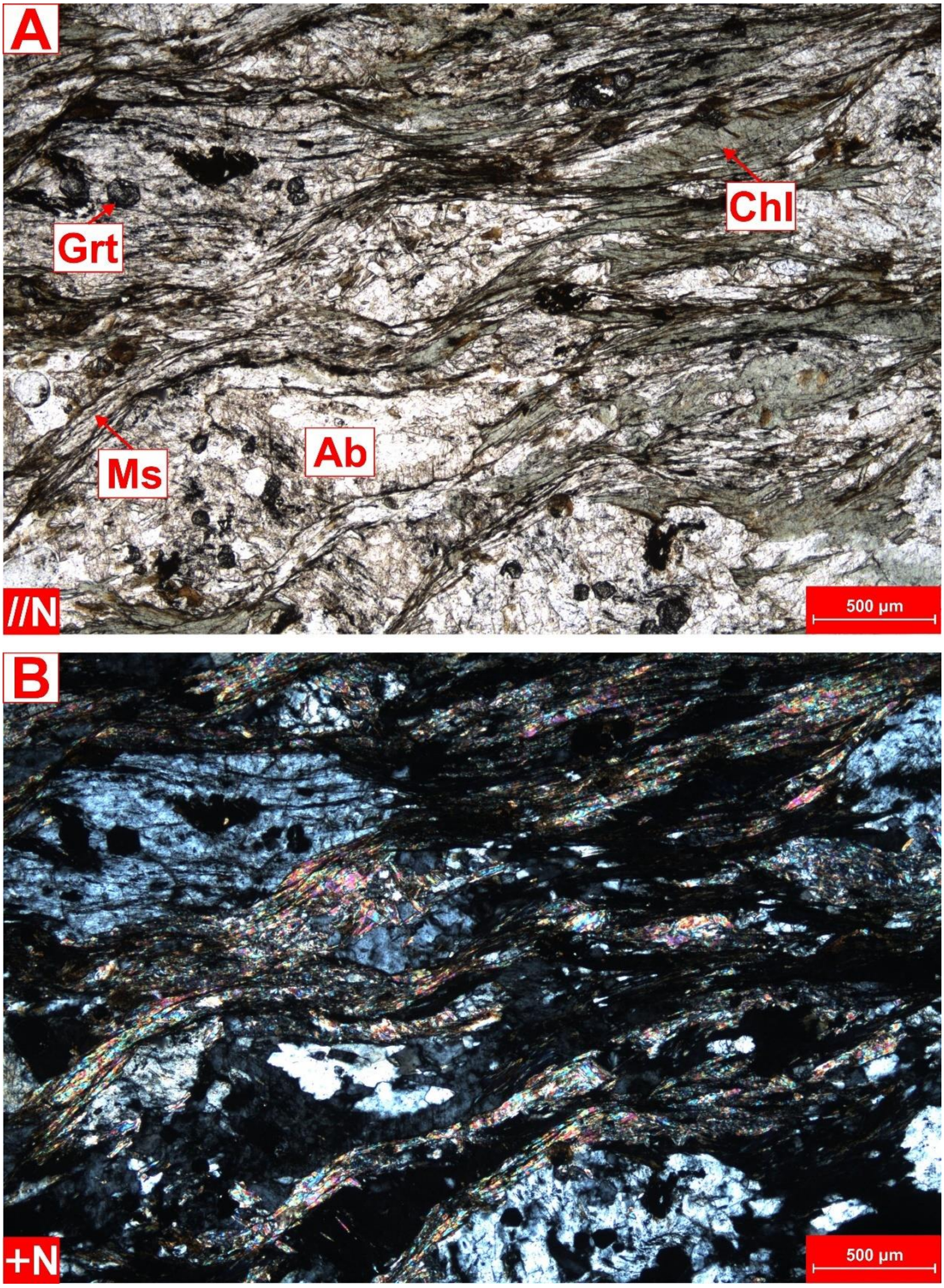


Figure 4.36 Albite poikiloblasts containing inclusions of other minerals from the assemblage. Chl: Chlorite – Ms: Muscovite – Ab: Albite - Grt: Garnet. Photomicrographs are in A) PPL and B) XPL

The observed garnets generally display anhedral and subhedral crystal forms. Garnets and albites occur as porphyroblasts and poikiloblasts. In addition, observed garnet crystals show prominent rotation with respect to the foliation (Figure 4.37 – 4.41).

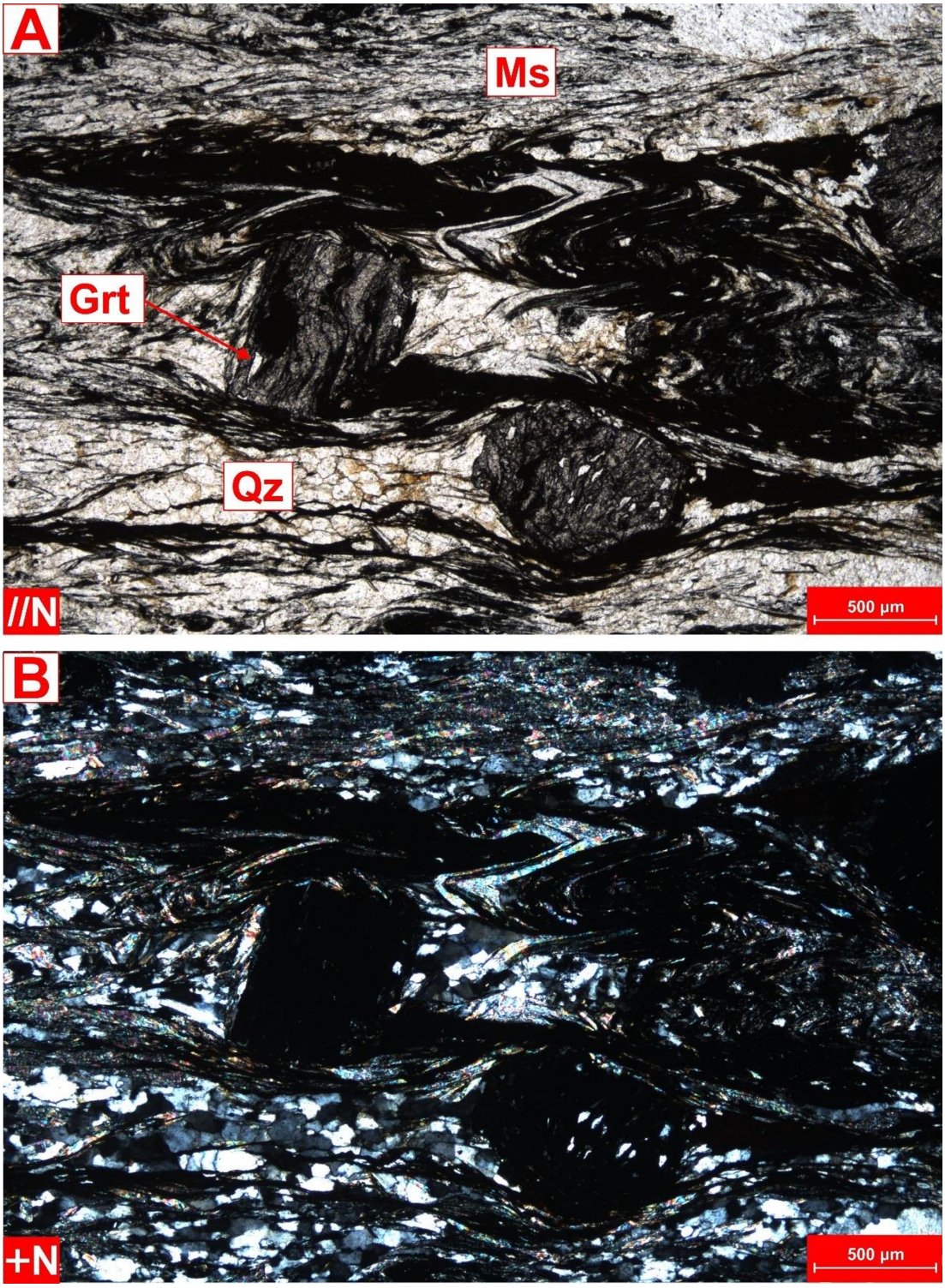


Figure 4.37 Garnet rotation porphyroblast rotation. Photomicrographs are in A) PPL and B) XPL

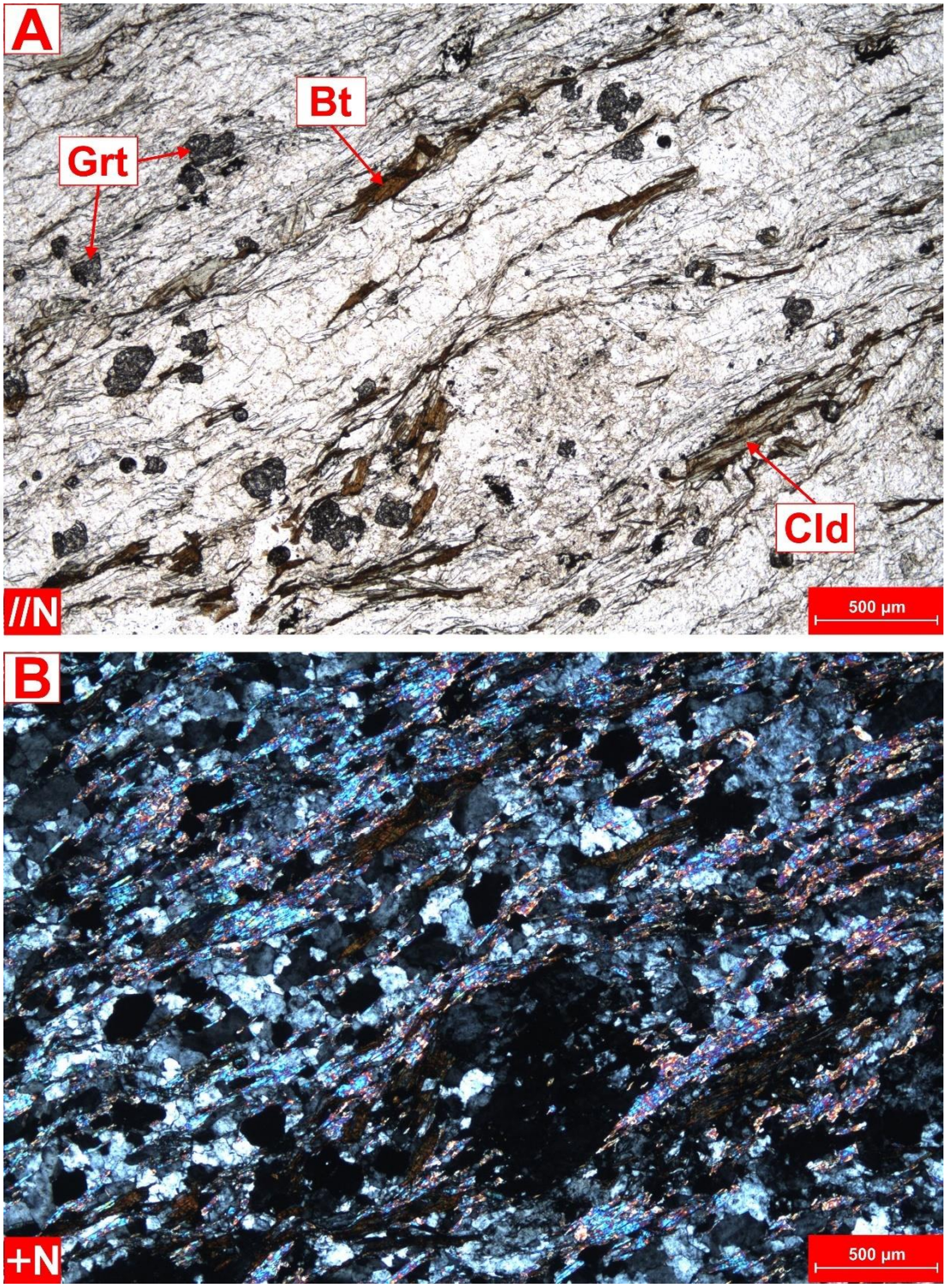


Figure 4.38 Numerous subhedral garnet grains found as porphyroblasts in the albite and matrix. Biotite and chloritoid are present as foliation forming minerals. Cld: Chloritoid – Bt: Biotite – Grt: Garnet. Photomicrographs are in A) PPL and B) XPL

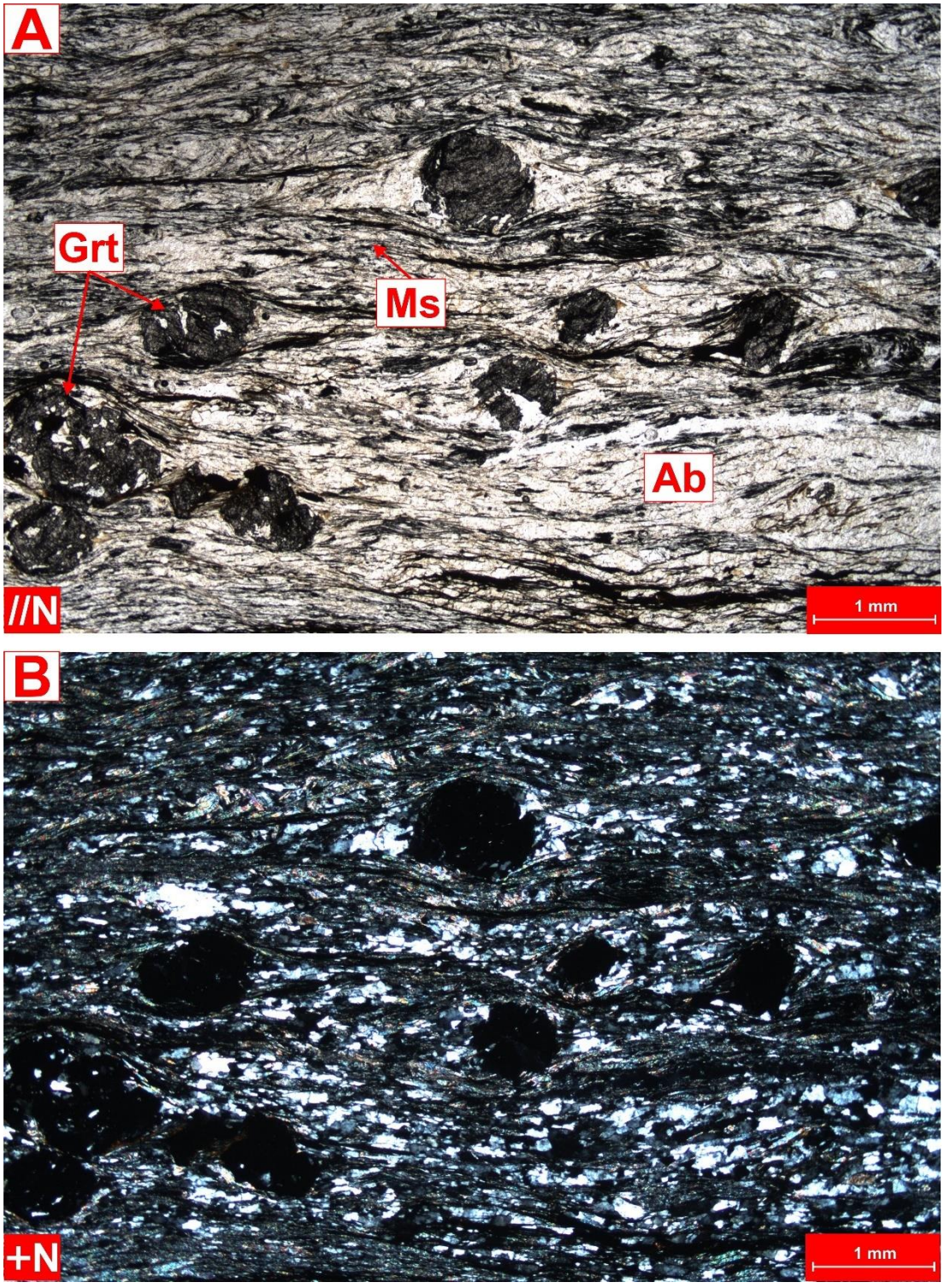


Figure 4.39 Garnet porphyroblasts in albite surrounded by muscovite flakes. Grt: Garnet – Ab: Albite – Ms: Muscovite. Photomicrographs are in A) PPL and B) XPL

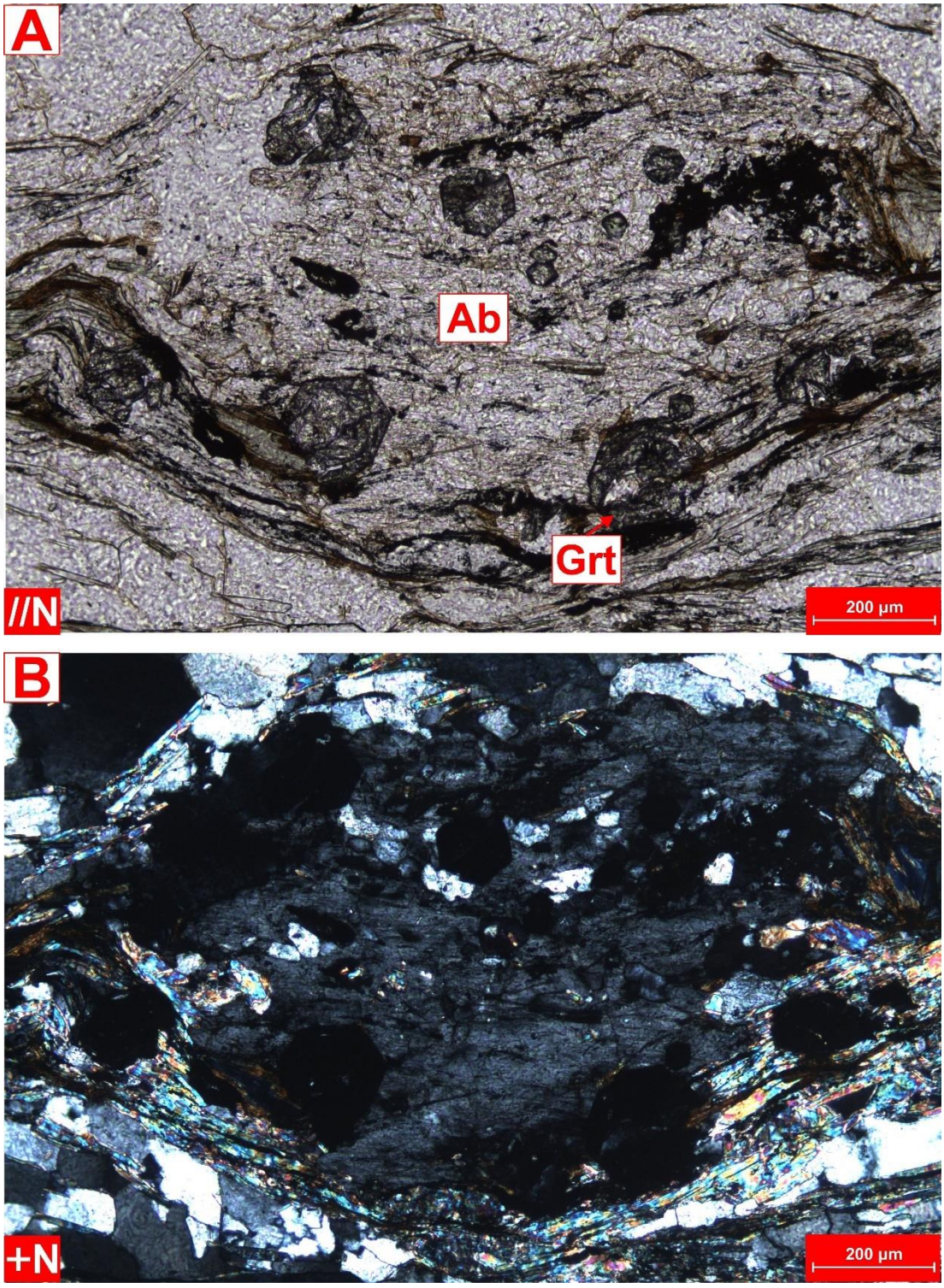


Figure 4.40 An albite poikiloblast containing garnet inclusions that have chloritoid mineral development at their pressure shadows. Grt: Garnet – Ab: Albite. Photomicrographs are in A) PPL and B) XPL

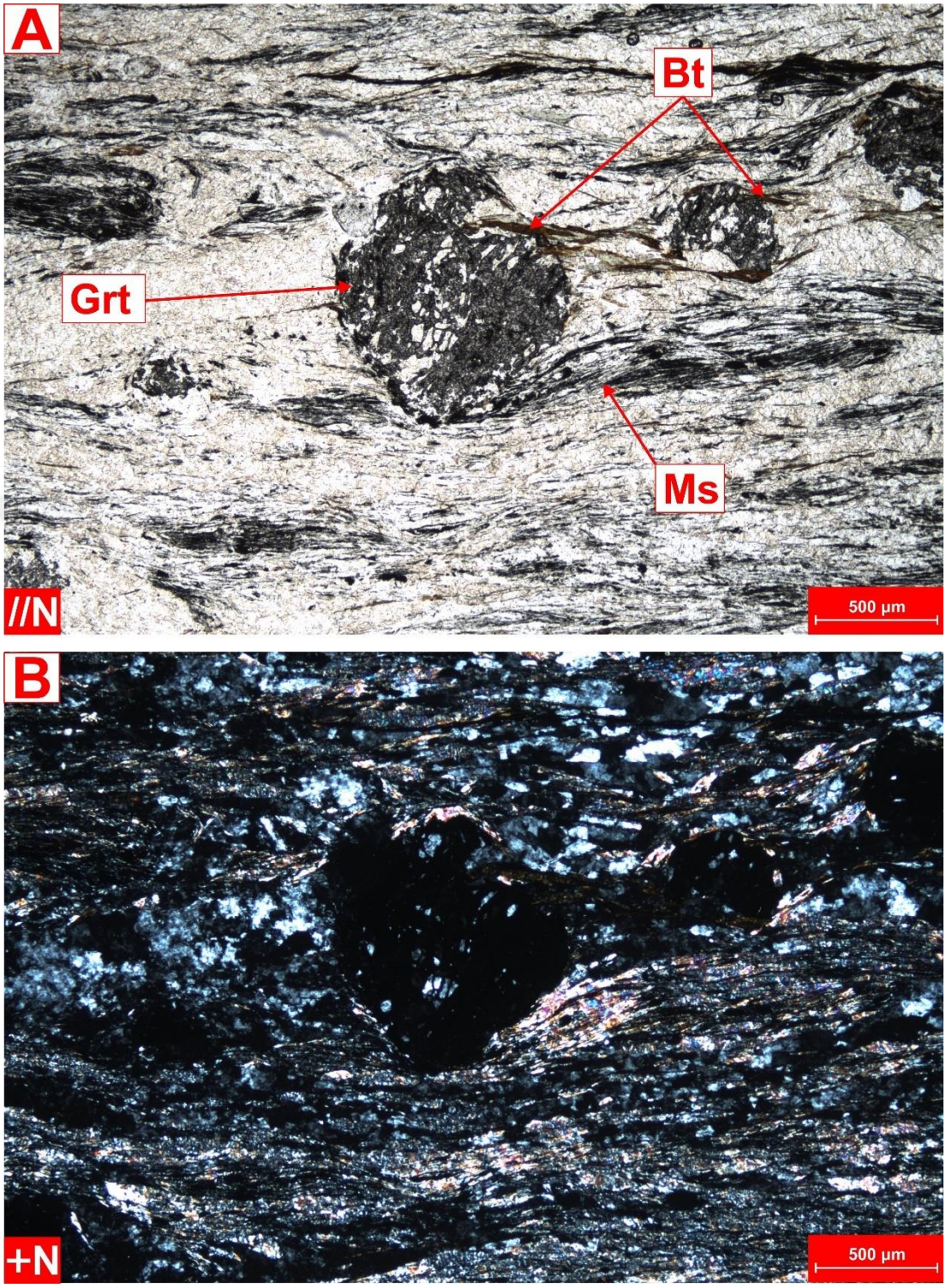


Figure 4.41 Garnet porphyroblast displaying counterclockwise rotation with respect to the muscovite foliations. Notice the biotite overprint and infiltrate the garnet grain through the right rim indicating a post-tectonic metamorphic process. Grt: Garnet – Bt: Biotite – Ms: Muscovite. Photomicrographs are in A) PPL and B) XPL

4.3.3 Shear Sense Indicators of Zindan Schists

The oriented thin sections of Zindan Schists were investigated. According to the kinematic shear sense indicators such as mica fish and garnet porphyroblasts, a significant top-to-south sense of movement was observed (Figure 4.42 – 4.44).

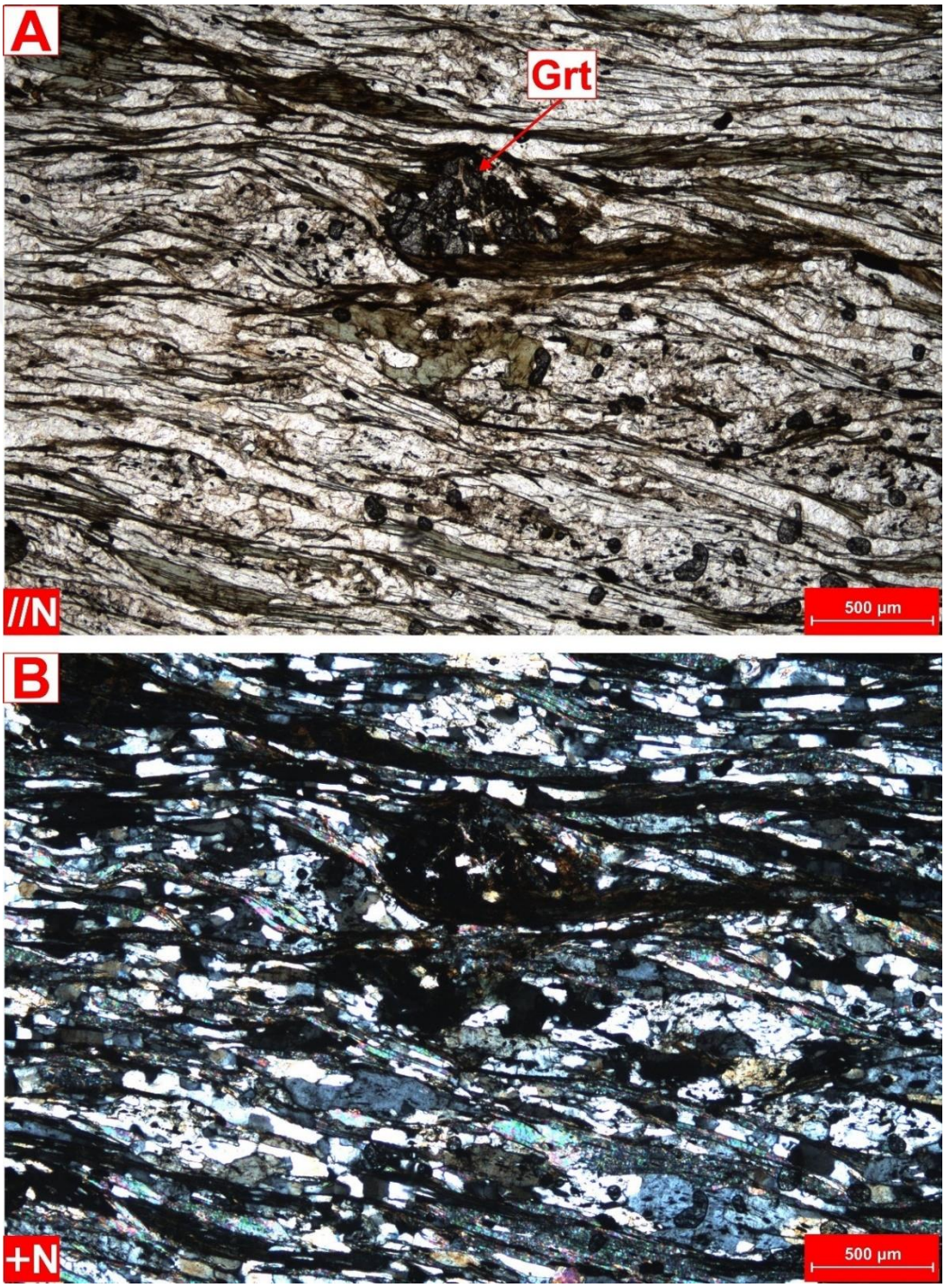


Figure 4.42 A microphotograph of an oriented thin section showing a garnet grain surrounded by chlorites. Grt: Garnet. A) PPL and B) XPL

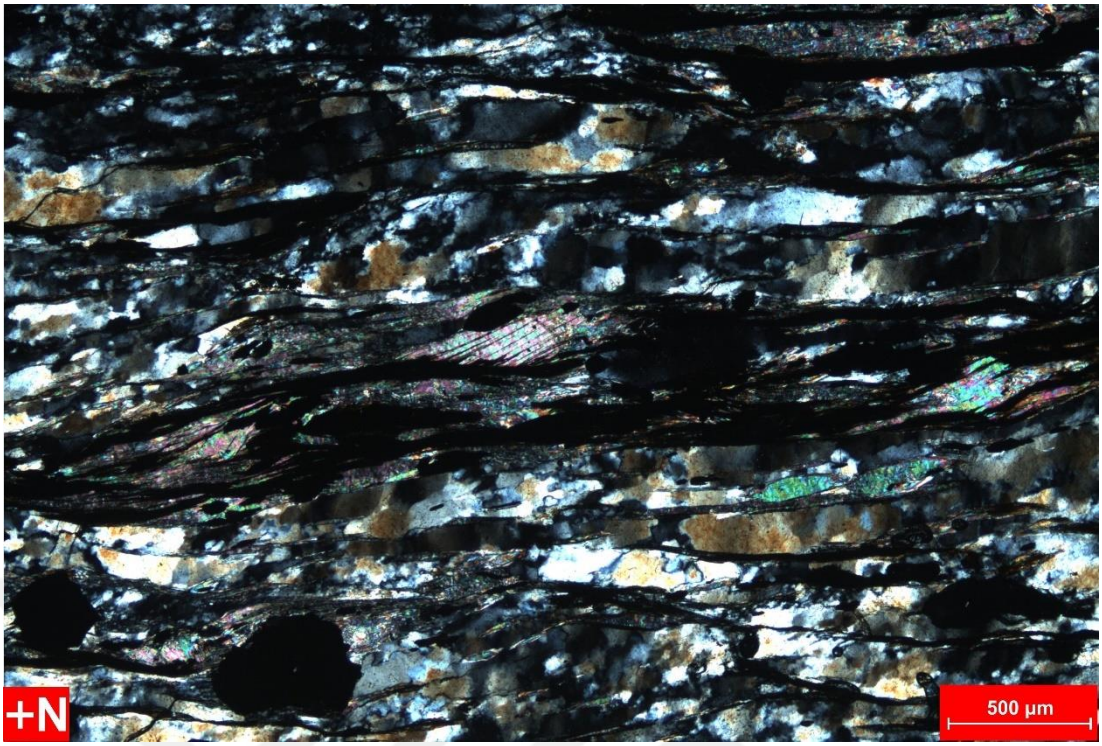


Figure 4.43 Photomicrograph of Zindan Schists with mica fish. Dextral shear sense indicating top-to-south sense of movement. Under cross polarized light

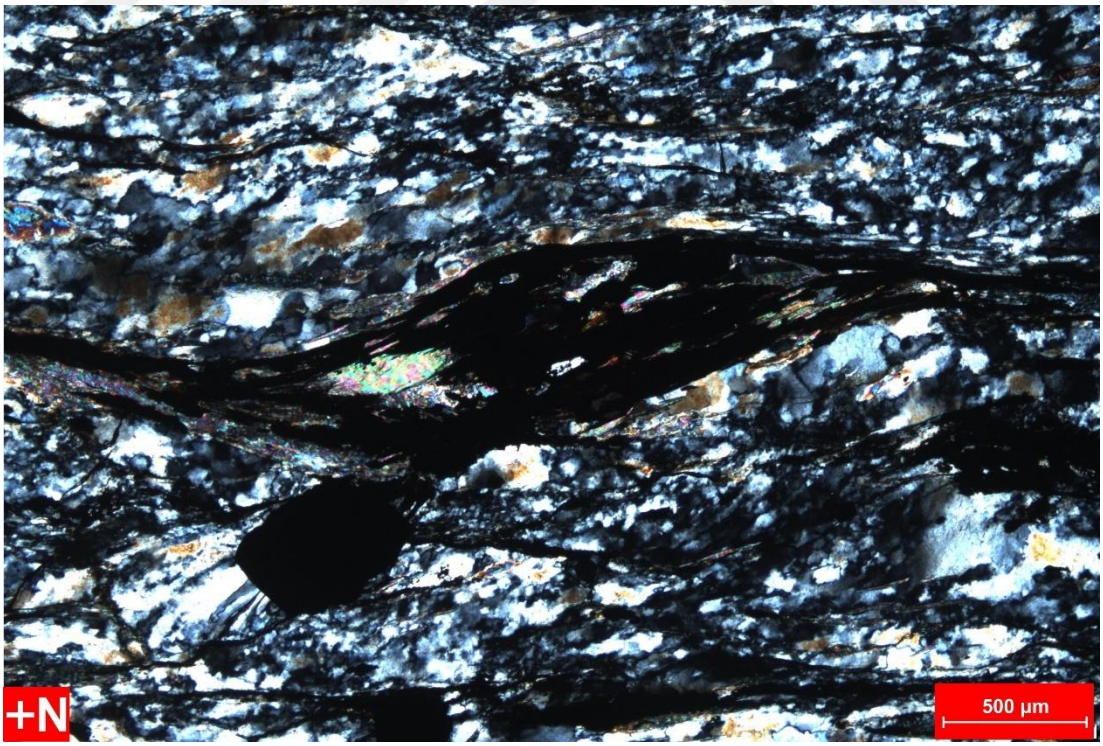


Figure 4.44 Photomicrograph of Zindan Schists with mica fish arranged between C-type shear bands. Dextral shear sense indicating top-to-south sense of movement. Under cross polarized light

CHAPTER FIVE
RADIOMETRIC DATING OF DETRITAL ZIRCONS

Detrital zircons in the metamorphic rock units of the Özdere – Gümüldür area were radiometrically dated for the first time using U-Pb dating method by LA-MC-ICP-MS in the İstanbul University Cerrahpaşa Geochronology and Geochemistry laboratories. The dating analysis of the rocks was conducted on the collected samples during the field work in the study area. Within the collected 83 rock samples, OZD-01 and OZD-02 were most suitable for the zircon grain separation. The mineral separation processes were explained in detail in Chapter Two – Analytical Methods.

These samples were chosen from Özdere tectonic slice and Zindan tectonic slice each representing relationships of deformation and age in the study area. The descriptions, locations, and the results of detrital zircon U-Pb ages of both samples are presented below through the chapter.

5.1 U-Pb Zircon Ages of Özdere Schists

The sample of OZD-02 was collected from garnet – muscovite schist unit of the Özdere tectonic slice, after the zircon mineral separation processes and hand picking of the grains, the polished epoxy resin containing the sample was sent for the U-Pb radiometric dating analysis by LA-ICP-MS.

The obtained age data then were sent back and analyzed using data evaluation software of AgeCalcML©. The U-Pb age distribution of the OZD-02 sample was plotted to create the graphs of Kernel Density Estimate (KDE) and Concordia Diagram which are given below.

The measurement data obtained from zircon grain consists of 104 U-Pb age values that are provided as dataset in Appendix-I, Table A1.1 - The U–Pb Zircon Geochronology Results of OZD-02 (Özdere Schists).

Some of the age measurement data were omitted due to the filtering criteria according to the concordance ratio percentage which was determined to be within the interval of %90 – %110 of concordance. The $^{206}Pb/^{238}U$ and $^{207}Pb/^{235}U$ ages were used

for ages less than 1 Ga and the $^{206}Pb/^{238}U$ and $^{207}Pb/^{206}Pb$ ages were used for ages more than 1 Ga. The omitted 20 data values were falling outside the boundary of determined concordance ratio, so only 84 age measurements were used to create the KDE diagram. All uncertainties are reported at the 2SE level.

The age spectrum of the sample OZD-02 of Özdere Schists ranges from c. 521 Ma to c. 2.7 Ga. The created KDE graph shows a major cluster of age distribution peaking at the Ediacaran period of Neoproterozoic era at 621 Ma and the second closest peak yields an age of 750 Ma corresponding to Tonian period. The other relatively minor peaks indicate ages of 1056 Ma in the Stenian period of the Mesoproterozoic Era, 2012 Ma in the Orosirian period of the Paleoproterozoic Era, and a peak of 2493 Ma, which nearly corresponds to the lower boundary of the Archean Eon (Figure 5.1).

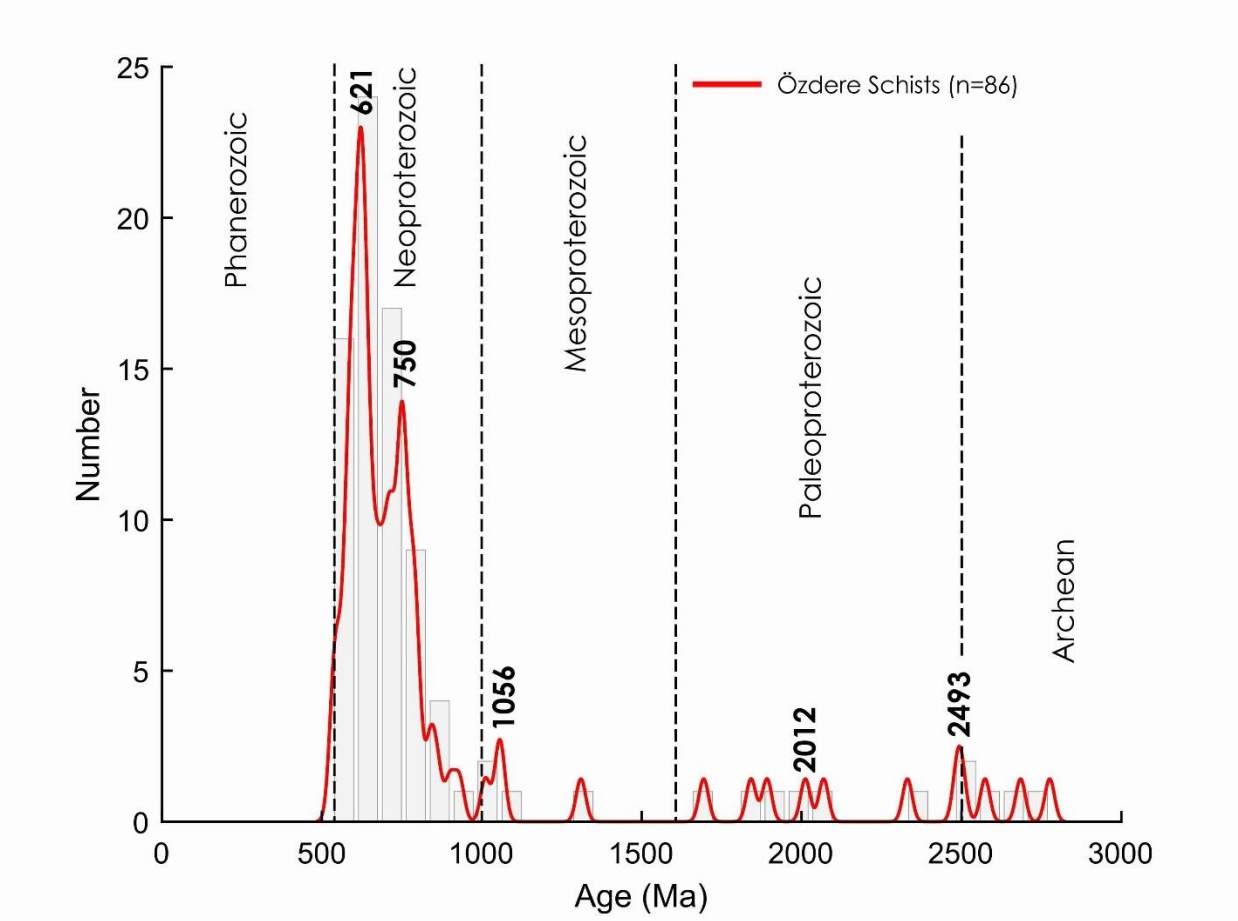


Figure 5.1 The Kernel Density Estimate (KDE) graph of OZD-02 sample collected from garnet – muscovite schist unit of Özdere tectonic slice (n=86). The main age distribution peak is at 621 Ma of Neoproterozoic

The concordia diagram was prepared by using the U-Pb age data and were plotted on the graph of $^{206}Pb/^{238}U$ versus $^{207}Pb/^{235}U$ for OZD-02 of Özdere tectonic slice. The major cluster was concordant between the array of ages 521 Ma and 1040 Ma (Figure 5.2).

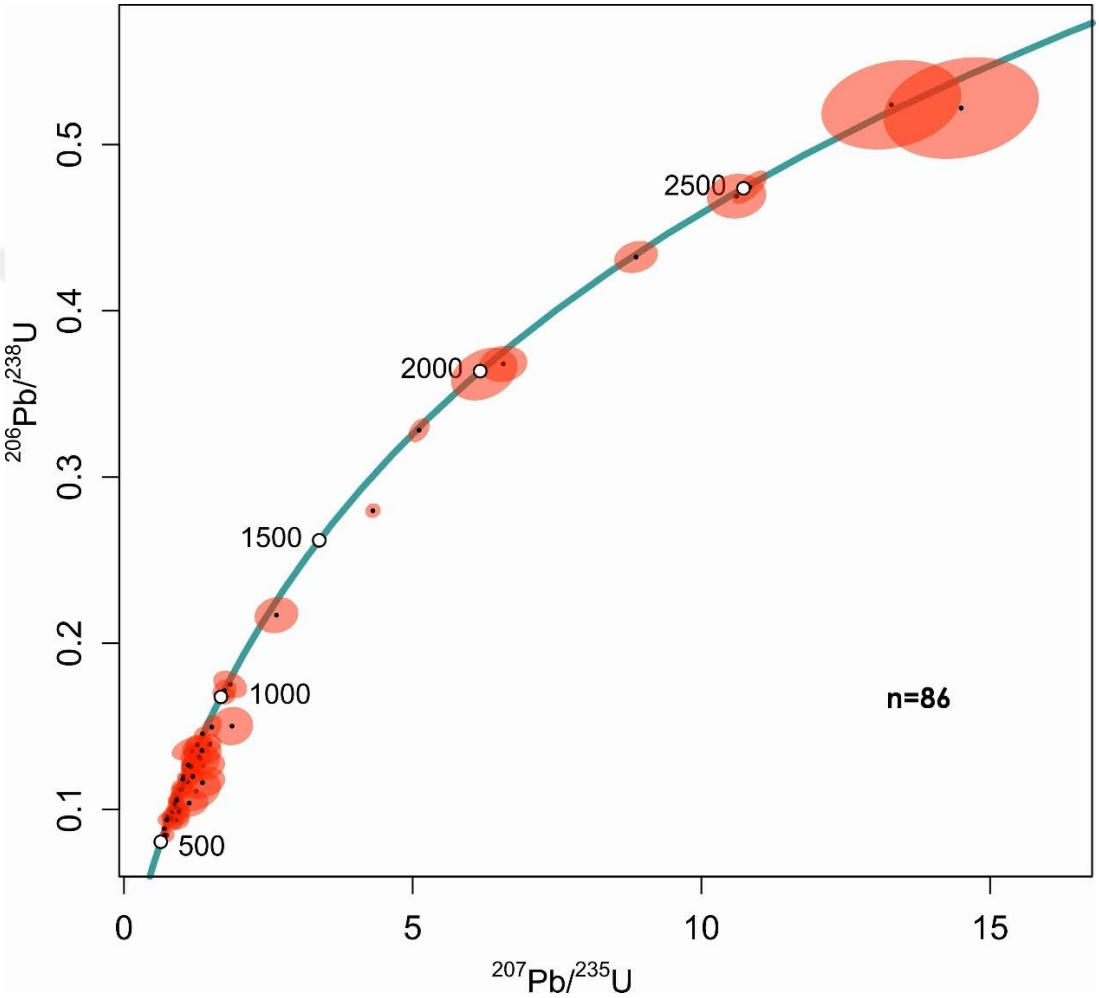


Figure 5.2 The Concordia diagram graph of OZD-02 sample collected from garnet – muscovite schist unit of Özdere tectonic slice (n=86)

The youngest coherent $^{206}Pb/^{238}U$ age group of the sample OZD_02 consisted of two spot measurements of OZD_02_25 and OZD_02_38 yielding the weighted mean age of 523 ± 15 Ma (n=2) that corresponds to the Cambrian period (Figure 5.3).

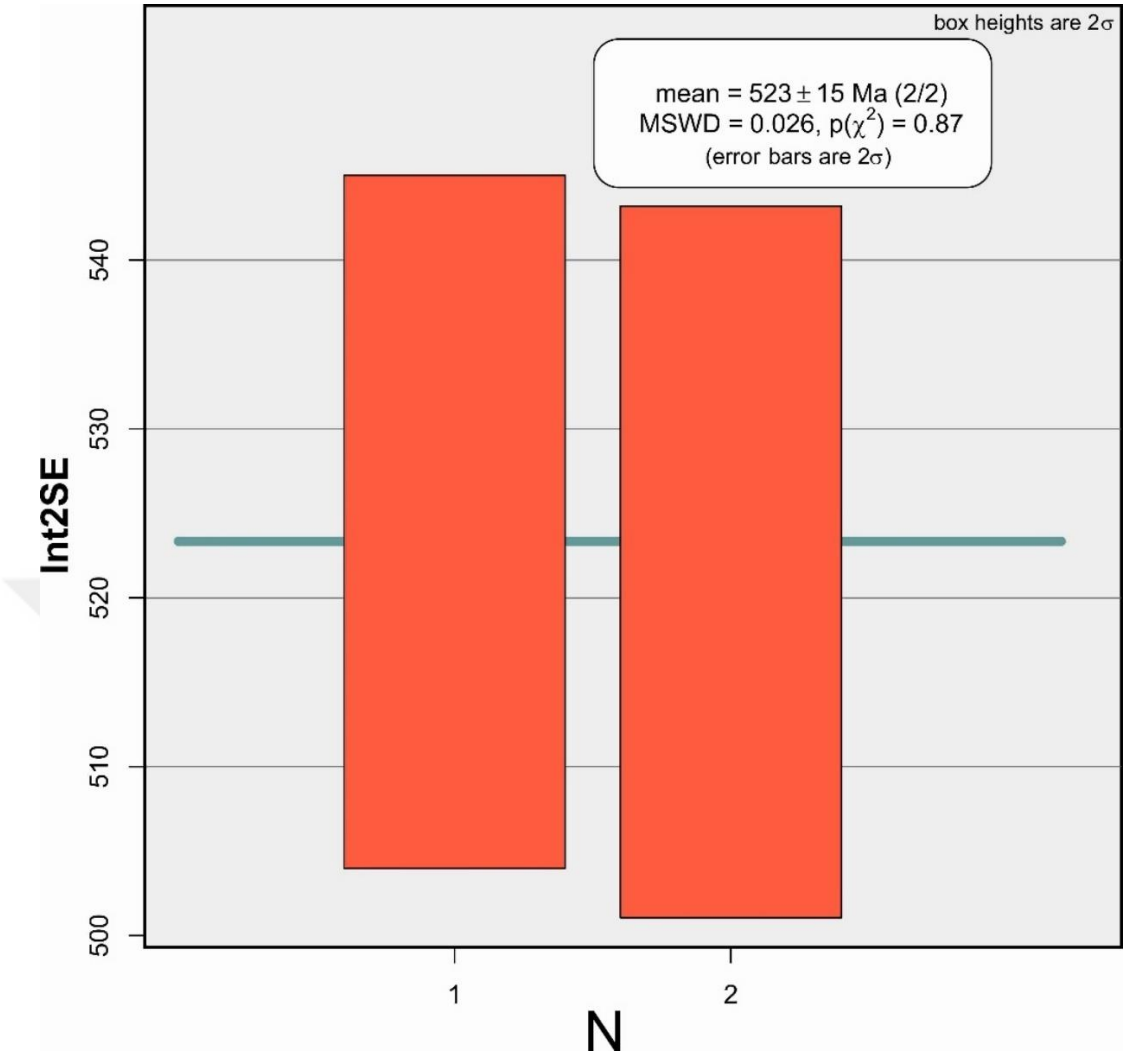


Figure 5.3 The youngest coherent $^{206}Pb/^{238}U$ age yielding the weighted mean age of 523 ± 15 Ma that corresponds to the Cambrian period (n=2)

The $^{206}Pb/^{238}U$ ages of OZD_02 were plotted on a pie chart to illustrate the corresponding age distribution percentages. Out of 86 concordant age distributions the age percentages yielded the following values: Cambrian (%2.3), Neoproterozoic (%80.2), Mesoproterozoic (%5.8), Paleoproterozoic (%9.3), and Archean (%2.3) (Figure 5.4).

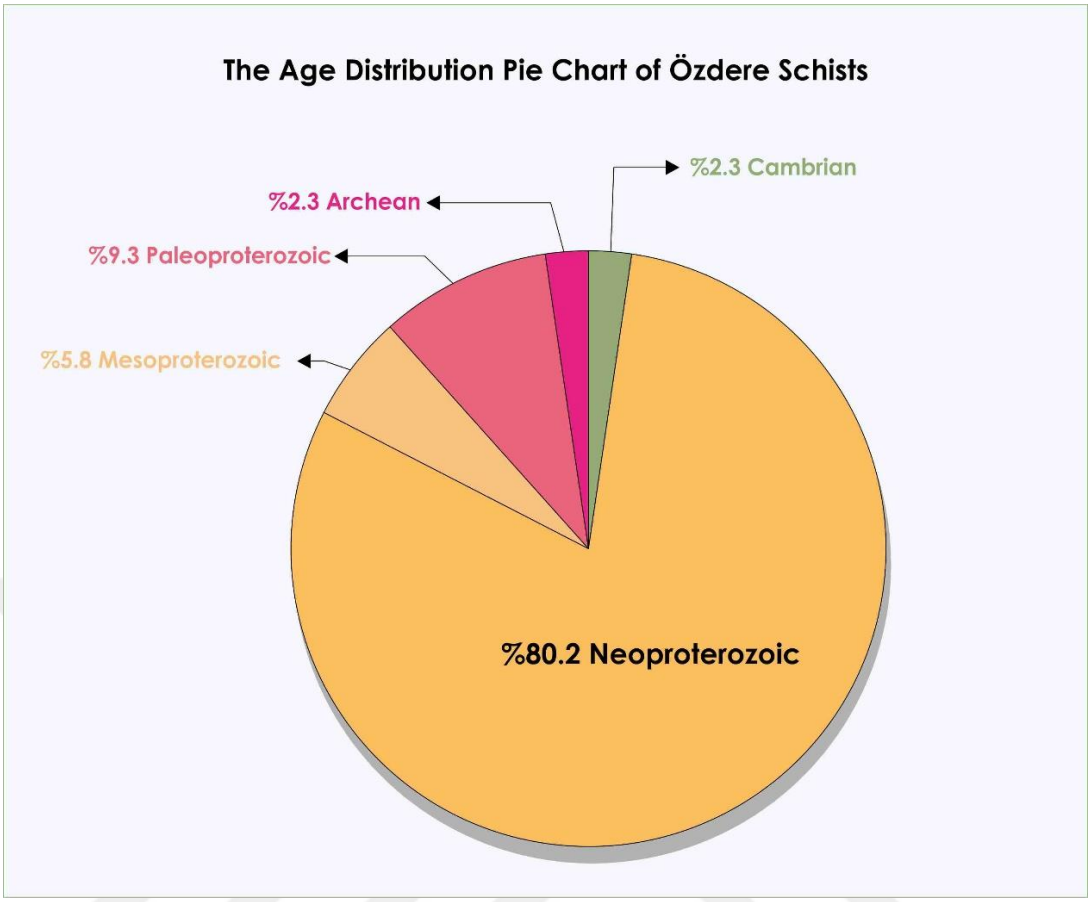


Figure 5.4 The age distribution pie chart of the sample OZD_02 of Özdere Schists. The $^{206}Pb/^{238}U$ ages data were used to prepare the chart (n=86)

5.2 U-Pb Zircon Ages of Zindan Schists

The sample of OZD-01 was collected from chlorite – biotite – garnet schist unit of the Zindan tectonic slice. The U-Pb age distribution of the OZD-01 sample was plotted to create the graphs of Kernel Density Estimate (KDE) and Concordia Diagram which are given below.

The measurement data obtained from zircon grain consists of 104 U-Pb age values that are provided as dataset in Appendix-II, Table A2.1 - The U–Pb Zircon Geochronology Results of OZD-01 (Zindan Schists).

Some of the age measurement data were omitted due to the filtering criteria according to the concordance ratio percentage which was determined to be within the interval of %90 – %110 of concordance. The $^{206}Pb/^{238}U$ and $^{207}Pb/^{235}U$ ages were used

for ages less than 1 Ga and the $^{206}Pb/^{238}U$ and $^{207}Pb/^{206}Pb$ ages were used for ages more than 1 Ga. The omitted 7 data values were falling outside the boundary of determined concordance ratio, so only 97 age measurements were used to create the KDE diagram. All uncertainties are reported at the 2SE level.

The age spectrum of the sample OZD-01 of Zindan Schists ranges from c. 353.8 Ma to c. 2.9 Ga. The created KDE graph shows a major cluster of age distribution peaking at the Ediacaran period of Neoproterozoic era at 619 Ma and the second closest peak yields an age of 980 Ma corresponding to Tonian period. The other relatively minor peaks indicate ages of 1056 Ma in the Stenian period of the Mesoproterozoic Era, 2088 Ma in the Rhyacian period of the Paleoproterozoic Era, and a peak of 2618 Ma, which nearly corresponds to the Neoarchean era of the Archean Eon (Figure 5.5).

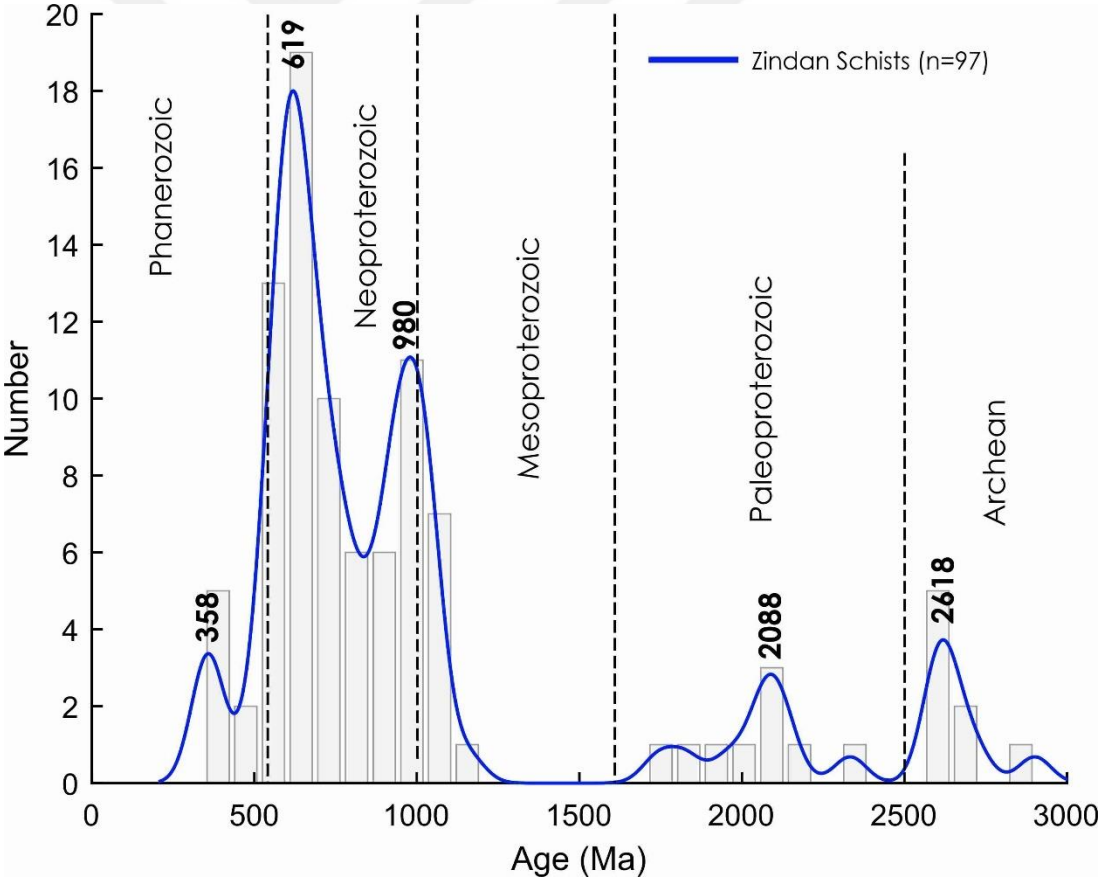


Figure 5.5 The Kernel Density Estimate (KDE) graph of OZD-01 sample collected from chlorite – biotite – garnet schist unit of Zindan tectonic slice (n=97). The main age distribution peak is at 619 Ma of Neoproterozoic

The concordia diagram was prepared by using the U-Pb age data and were plotted on the graph of $^{206}Pb/^{238}U$ versus $^{207}Pb/^{235}U$ for OZD-01 of Zindan tectonic slice. The major cluster was concordant between the array of ages 492 Ma and 1055 Ma (Figure 5.6).

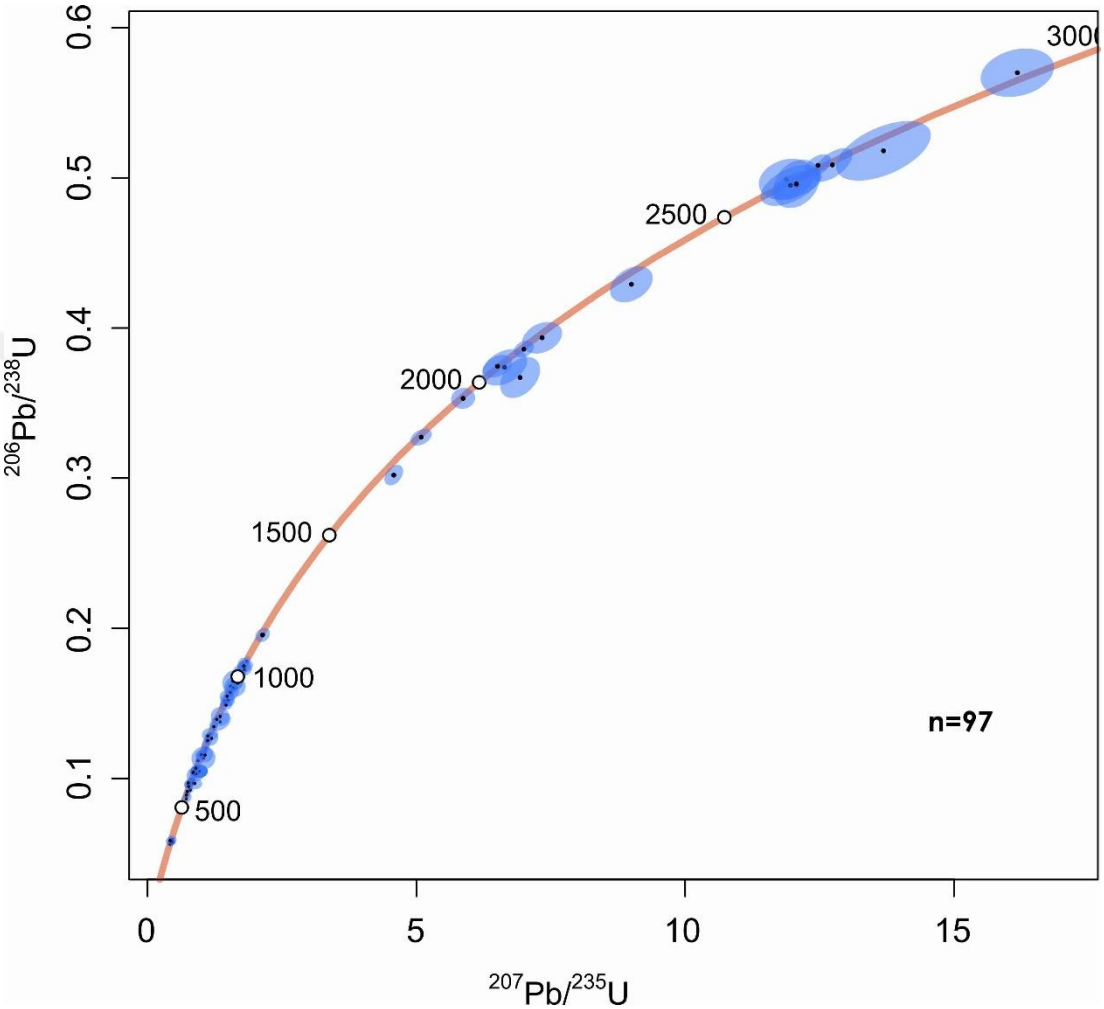


Figure 5.6 The Concordia diagram graph of OZD-01 sample collected from chlorite – biotite – garnet schist unit of Zindan tectonic slice (n=97)

The youngest coherent $^{206}Pb/^{238}U$ age group of the sample OZD_01 consisted of five spot measurements yielding the weighted mean age of 361.5 ± 4.9 Ma (n=5) that corresponds to the Devonian period (Figure 5.7).

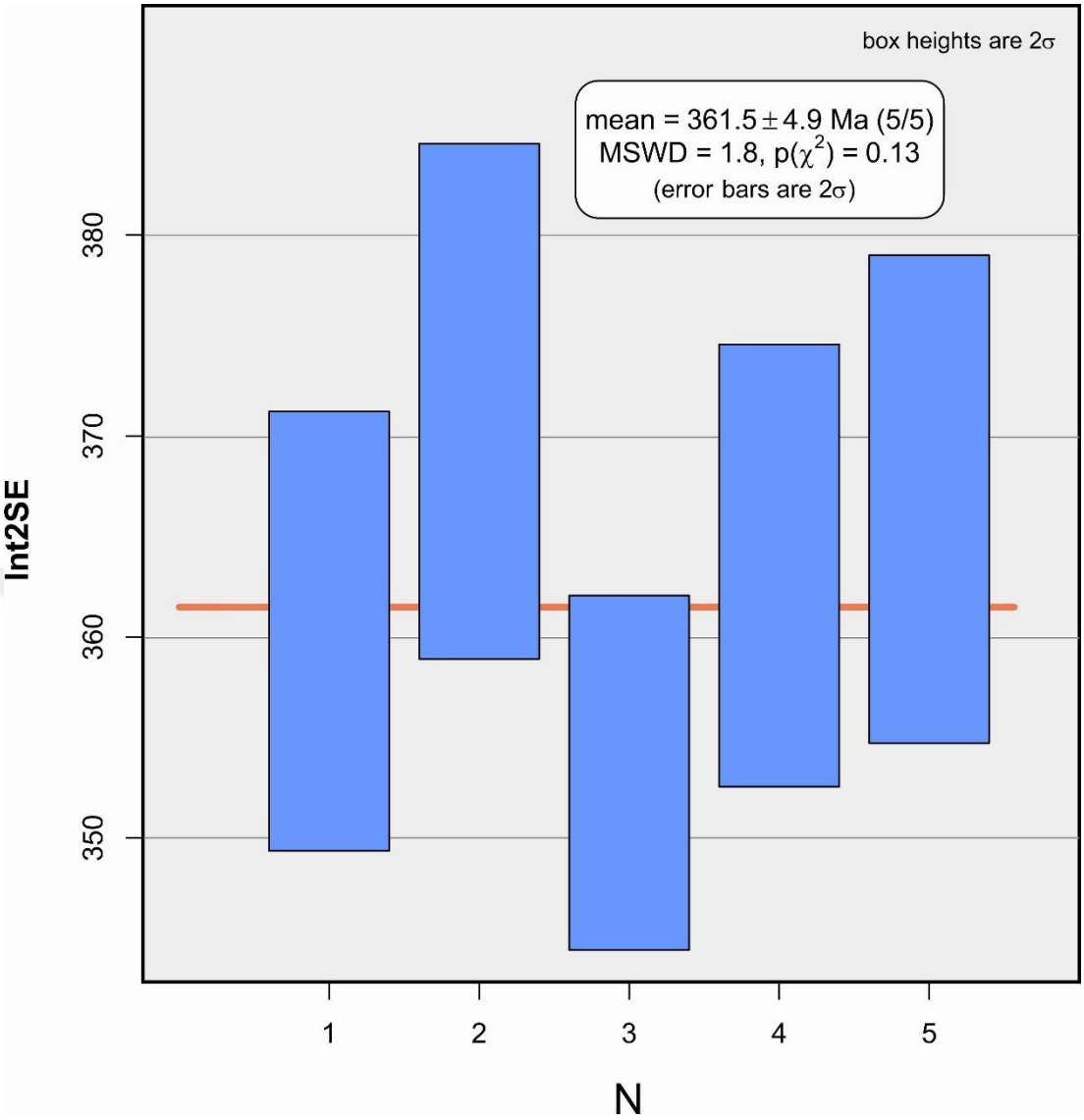


Figure 5.7 The youngest coherent $^{206}Pb/^{238}U$ age yielding the weighted mean age of 361.5 ± 4.9 Ma that corresponds to the Devonian period (n=5)

The $^{206}Pb/^{238}U$ ages of OZD_01 were plotted on a pie chart to illustrate the corresponding age distribution percentages. Out of 97 concordant age distributions the age percentages yielded the following values: Carboniferous (%1.0), Devonian (%4.1), Cambrian (%3.1), Neoproterozoic (%63.9), Mesoproterozoic (%10.3), Paleoproterozoic (%9.3), and Archean (%8.2) (Figure 5.8).

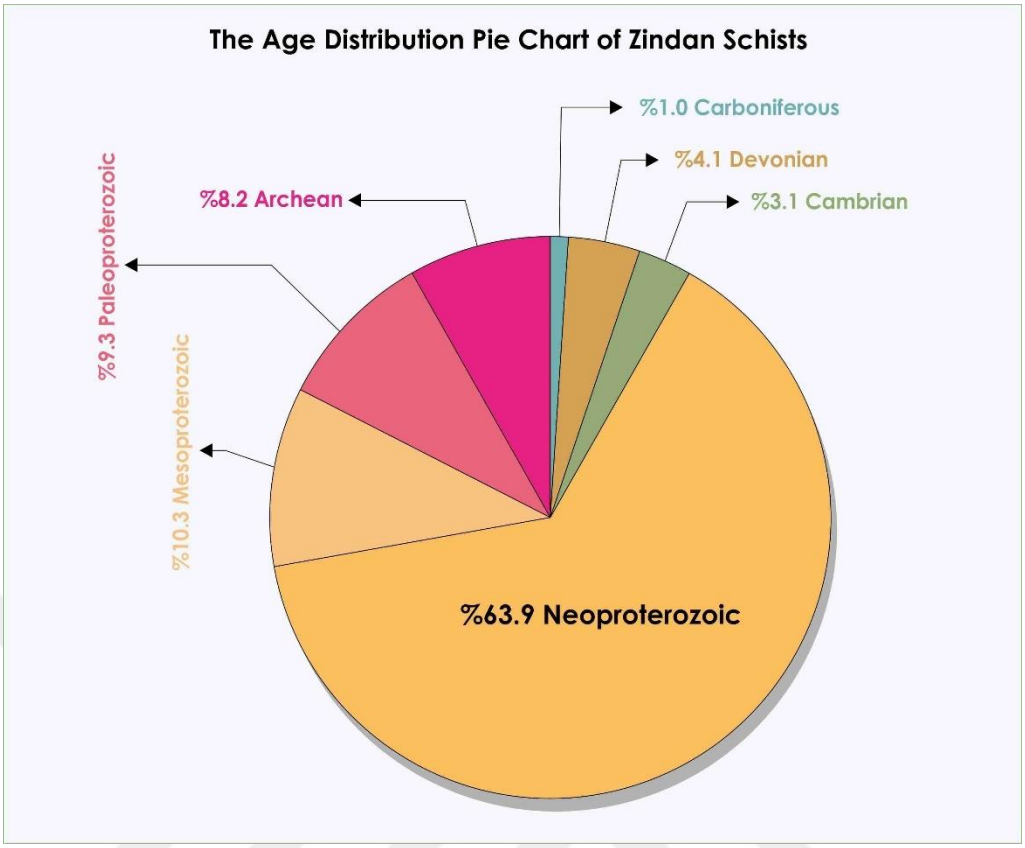


Figure 5.8 The age distribution pie chart of the sample OZD_01 of Zindan Schists. The $^{206}Pb/^{238}U$ ages data were used to prepare the chart (n=86)

Zlatkin et al., (2013), conducted U-Pb detrital zircon geochronology of core schists from the metasedimentary units of the Menderes Massif. The youngest detrital zircon yielded an age of 566 ± 10 Ma. The mean of 6 concordant youngest ages yielded 571 ± 7.1 Ma. The zircon populations are shown %90 Neoproterozoic age. Dominant peak at the graph was approximately 600 Ma (Figure 5.8)

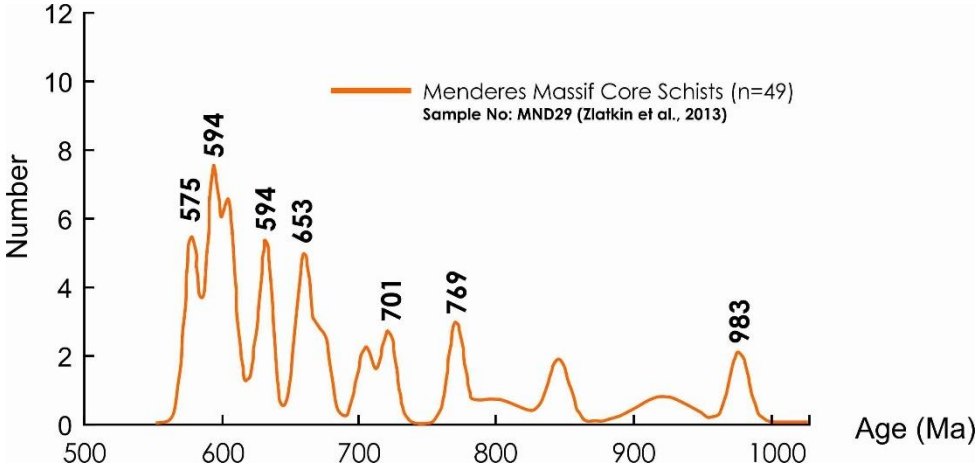


Figure 5.9 Menderes Massif Core Schist detrital zircon U-Pb ages. (after Zlatkin et al., 2013)

The geochronological data presented above are used to plot the Kernel density estimation diagrams of Özdere Schists, Zindan Schists, Menderes Massif Schists and CBU cover schist which are compared below. The similarity of zircon population ages between the Menderes Massif and study area implies that the Özdere – Gümüldür region belongs to the Menderes Massif and not to the CBU, as it was suggested before in earlier studies (Figure 5.10).

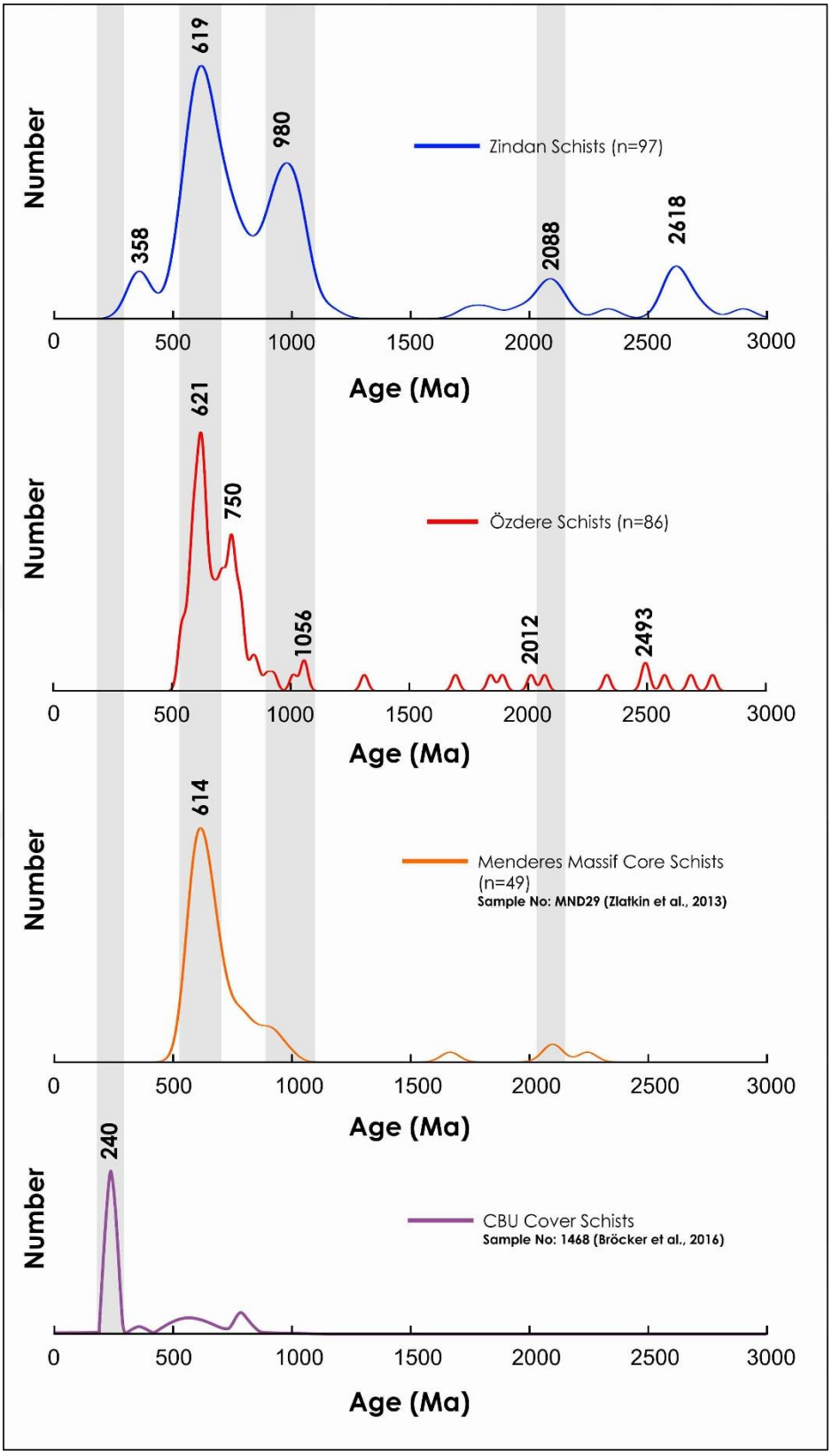


Figure 5.10 Kernel Density Estimation (KDE) plots for detrital zircon U-Pb ages compiled from Zindan schists, Özdere schists, Menderes Massif core schists, and CBU cover schists (This study; Zlatkin et al., 2013; Bröcker et al., 2016)

CHAPTER SIX
RESULTS

According to the field observations, the Özdere – Gümüldür region is geologically mapped and kinematic analysis is conducted by systematically measuring structural and geometrical data at about 192 observation points.

The Özdere – Gümüldür region is located in the southwest part of the İzmir province and consists of Özdere tectonic slice (Özdere Schists), Zindan tectonic slice (Zindan Schists) and the Kargıcak marbles in ascending order. The mentioned tectonic slices are separated by the lower ductile shear zones of Özdere that is a east-dipping mylonitic shear zone (086/22) and the upper ductile shear zone of Koru separating the Kargıcak marbles from the schist units.

The kinematic analysis of the tectonic slices clearly indicates a top-to-south sense of movement according to the offset of numerous observed quartz sigmoids and s-c structures that are located perpendicular to the foliations and parallel to the associated stretching lineations at the outcrops. The mineral stretching lineations, crenulation cleavage axes and fold axes (linear fabrics) of both tectonic slices indicate a significant north – south trend.

Petrographic analysis of schist units was carried out by examining the 74 prepared thin sections out of 83 collected rock samples from various locations of the study area. The outcropping schist units were differentiated by their mineral assemblages of garnet – muscovite schist, quartz – muscovite – chloritoid – kyanite schist, and chlorite – biotite – garnet schist in ascending order.

The recognized general mineral assemblage in these units, the observed chloritic overprint on the garnet and muscovite minerals, and development of iron oxide coatings suggest that the metamorphic grade is in Barrovian type greenschist facies yielding chlorite, biotite, and garnet subfacies conditions and both tectonic slices have experienced retrograde metamorphic phases.

Detrital zircons in the metamorphic rock units of Özdere – Gümüldür area were radiometrically dated for the first time using U-Pb dating method by LA-MC-ICP-MS. Two rock samples were chosen for this purpose, one from each tectonic slice of Özdere and Zindan to represent age and deformation relationships in the study area.

From the evaluated U-Pb age data of the samples, KDE, Concordia, weighted mean, and age distribution chart was created.

The age spectrum of Özdere Schists ranges from c. 521 Ma to c. 2.7 Ga. The major cluster of age distribution peaks at 621 Ma and the second closest peak yields an age of 750 Ma. The youngest coherent $^{206}Pb/^{238}U$ age group yielded the weighted mean age of 523 ± 15 Ma that corresponds to the Cambrian period. The overall age distribution percentages of Özdere Schists are as follows: Cambrian (%2.3), Neoproterozoic (%80.2), Mesoproterozoic (%5.8), Paleoproterozoic (%9.3), and Archean (%2.3).

The age spectrum of Zindan Schists ranges from c. 353.8 Ma to c. 2.9 Ga. The major cluster of age distribution peaks at 619 Ma and the second closest peak yields an age of 980 Ma. The youngest coherent $^{206}Pb/^{238}U$ age group yielded the weighted mean age of 361.5 ± 4.9 Ma that corresponds to the Devonian period. The overall age distribution percentages of Zindan Schists are as follows: Carboniferous (%1.0), Devonian (%4.1), Cambrian (%3.1), Neoproterozoic (%63.9), Mesoproterozoic (%10.3), Paleoproterozoic (%9.3), and Archean (%8.2).

CHAPTER SEVEN
CONCLUSIONS

According to the presented geochronological data concerning the basement and cover series of the Menderes Massif and Cycladic Blueschist Unit, it appears that the two differ from each other in means of both the basement and the cover series age.

The radiometric data obtained from the paragneisses of the Menderes Massif core yield youngest age of ~610 Ma of Late Proterozoic, while the overlying core schists indicate 670 – 640 Ma of Cryogenian Neoproterozoic. The overall Neoproterozoic basement of the Menderes Massif has intrusions of orthogneisses and metabasites of ~550 Ma age. The schist units within cover series of the Menderes Massif indicates ~520 Ma by the youngest detrital zircon age providing the lower bound for the timing of deposition and yields Ordovician – Devonian age. The age of the carbonate sequences overlying the schist unit in cover series of the Menderes Massif was estimated Late Devonian – Early Carboniferous.

The lower nappe unit of the Cycladic Massif is called Cycladic Blueschist Unit and consists of upper cover unit Blueschist Series tectonically overlying the lower unit of basement. The metasediment rock units of the shelf margin in CBU (Blueschist Series), yields a detrital zircon U-Pb age of ~240 Ma Middle Triassic, while the basement of CBU yields an age of 400 ± 13 Ma Devonian.

According to the U-Pb radiometric dating data indicated by this paper, the metamorphic rock units of the study are showing similarities with the geochronological data of the Menderes Massif by yielding ~620 Ma. Hence, the study area of Özdere – Gümüldür region cannot be considered as cover series of Cycladic Blueschist Unit, as it was mapped before in the previous studies.

The obtained U-Pb age data from youngest coherent age groups of Özdere Schists yields 523 ± 15 Ma and Zindan Schist 361.5 ± 4.9 Ma. The youngest detrital zircon age of Zindan Schist suggests that they might have been derived from a region affected by Carboniferous magmatism.

REFERENCES

Akartuna, M. (1962). On the geology of Izmir-Torbali. Seferihisar-Urla district: *MTA Bull, 59* 1 – 18.

Altherr, R., Kreuzer, H., & Lenz, H. (1994). Further Evidence for a Late Cretaceous Low-pressure/high-temperature terrane in the Cyclades, Greece. Petrology and geochronology of crystalline rocks from the islands of Donoussa and Ikaria. *Chem. Erde-Geochem, 54*, 319-328.

Ashworth, J. R., & Evirgen, M. M. (1985). Plagioclase relations in pelites, central Menderes Massif, Turkey. I. The peristerite gap with coexisting kyanite. *Journal of Metamorphic Geology, 3(3)*, 207-218.

Başarır, E., & Konuk, Y. T. (1981). Gümüldür yöresinin kristalin temeli ve allokton birimleri. *Türkiye Jeoloji Kurumu Bülteni, 2*, 1–6, Ankara.

Bozkurt, E., & Oberhänsli, R. (2001). Menderes Massif (western Turkey): structural, metamorphic and magmatic evolution–a synthesis. *International Journal of Earth Sciences, 89(4),* 679-708.

Bozkurt, E., & PARK, L. R. (1994). Southern Menderes Massif: an incipient metamorphic core complex in western Anatolia, Turkey. *Journal of the Geological Society, 151(2),* 213-216.

Bozkurt, E., & Satir, M. (2000). The southern Menderes Massif (western Turkey): geochronology and exhumation history. *Geological Journal, 35(3-4),* 285-296.

Bröcker, M., Huyskens, M., & Berndt, J. (2016). U–Pb dating of detrital zircons from Andros, Greece: constraints for the time of sediment accumulation in the northern part of the Cycladic blueschist belt. *Geological Journal, 51(3),* 354-367.

Candan, O., & Dora, O. Ö. (1998). Granulite, eclogite and blueschist relics in the Menderes Massif: An approach to Pan-African and Tertiary metamorphic evolution. *Geological Bulletin of Turkey, 41(1),* 1-35.

Candan, O., Dora, O., Oberhänsli, R., Çetinkaplan, M., Partzsch, J., Warkus, F., & Dürr, S. (2001). Pan-African high-pressure metamorphism in the Precambrian basement of the Menderes Massif, western Anatolia, Turkey. *International Journal of Earth Sciences, 89*, 793-811.

Candan, O., Koralay, O. E., Akal, C., Kaya, O., Oberhänsli, R., Dora, O. Ö., Konak, N., Chen, F. (2011). Supra-Pan-African unconformity between core and cover series of the Menderes Massif/Turkey and its geological implications. *Precambrian Research, 184(1-4)*, 1-23.

Çetinkaplan, M., Candan, O., Oberhänsli, R., Sudo, M., & Cenki-Tok, B. (2020). P–T–t evolution of the Cycladic Blueschist Unit in Western Anatolia/Turkey: Geodynamic implications for the Aegean region. *Journal of Metamorphic Geology, 38(4)*, 379-419.

Dora, O. O. (1995). New evidence on the geotectonic evolution of the Menderes Massif. *In International Earth Sciences Colloquium on the Eagean Region, Izmir-Turkey*, 1995 (Vol. 1, pp. 53-72).

Dora, O. Ö. (2011). Historical evolution of the geological researches in the Menderes massif. *Bulletin of the Mineral Research and Exploration, 142(142)*, 1-23.

Dora, O. Ö., Candan, O., Kaya, O., Koralay, E., & Dürr, S. (2001). Revision of" Leptite-gneisses" in the Menderes Massif: a supracrustal metasedimentary origin. *International Journal of Earth Sciences, 89*, 836-851.

Dora, O. Ö., Kun, N., & Candan, O. (1990). Metamorphic history and geotectonic evolution of the Menderes Massif. Proc *Int Earth Sci Congr Aegean Regions*, *2*, 102-115.

Dora, O.Ö., (1976). Menderes Masifi'nde alkali feldspatların yapısal durumları ve bunların perojenetik yorumlarda kullanılması. *Türkiye Jeoloji Bülteni, 24*, pp. 91-94.

Dürr, S., 1975. Über Alter und geotektonische Stellung des Menderes-Kristallins/SW-Anatolien und seine Aequivalente in der mittleren Aegaeis. *Habilitations-Schrift, Marburg/Lahn*, 107 pp.

Dürr, S., Altherr, R., Keller, J., OKRliSCH, M., & SEIDEL, E. (1978). The Median Aegean Crystalline Belt: Stratigraphy. Structure, Metamorphism, Magmatism, 455-477.

Emre, T., & Sözbilir, H. (1997). Field evidence for metamorphic core complex, detachment faulting and accommodation faults in the Gediz and Büyük Menderes grabens, western Anatolia. *Iesca Proceedings, 1*, 73-93.

Etzel, T. M., Catlos, E. J., Cemen, I., Ozerdem, C., Oyman, T., & Miggins, D. (2020). Documenting exhumation in the Central and Northern Menderes Massif (Western Turkey): New insights from garnet-based PT estimates and K-feldspar 40Ar/39Ar geochronology. *Lithosphere, 2020(1)*, 8818289.

Gessner, K., Collins, A. S., Ring, U., & Güngör, T. (2004). Structural and thermal history of poly-orogenic basement: U–Pb geochronology of granitoid rocks in the southern Menderes Massif, Western Turkey. *Journal of the Geological Society, 161(1)*, 93-101.

Gessner, K., Piazolo, S., Güngör, T., Ring, U., Kröner, A., & Passchier, C. W. (2001a). Tectonic significance of deformation patterns in granitoid rocks of the Menderes nappes, Anatolide belt, southwest Turkey. *International Journal of Earth Sciences, 89*, 766-780.

Gessner, K., Ring, U., and Güngör, T. (2011). Field guide to Samos and the Menderes Massif: Along-strike variations in the Mediterranean Tethyan Orogen (Vol. 23). *Geological Society of America.*

Gessner, K., Ring, U., Johnson, C., Hetzel, R., Passchier, C. W., & Güngör, T. (2001b). An active bivergent rolling-hinge detachment system: Central Menderes metamorphic core complex in western Turkey. *Geology, 29(7)*, 611-614.

Gessner, K., Ring, U., Passchier, C. W., & Güngör, T. (2001c). How to resist subduction: evidence for large-scale out-of-sequence thrusting during Eocene collision in western Turkey. *Journal of the Geological Society, 158(5)*, 769-784.

Glodny, J., & Hetzel, R. (2007). Precise U–Pb ages of syn-extensional Miocene intrusions in the central Menderes Massif, western Turkey. *Geological Magazine, 144(2)*, 235-246.

Gülmez, F., Damci, E., Ülgen, U. B., & Okay, A. (2019). Deep Structure of Central Menderes Massif: data from deep geothermal wells. *Turkish Journal of Earth Sciences, 28(4)*, 531-543.

Hamilton W. J., & Strickland, H. E. (1841). I.—On the Geology of the Western Part of Asia Minor. *Transactions of the Geological Society of London, 6(1)*, 1-39.

Hetzel, R., & Reischmann, T. (1996). Intrusion age of Pan-African augen gneisses in the southern Menderes Massif and the age of cooling after Alpine ductile extensional deformation. *Geological Magazine, 133(5)*, 565-572.

Hetzel, R., Passchier, C. W., Ring, U., & Dora, O. O. (1995b). Bivergent extension in orogenic belts: the Menderes massif (southwestern Turkey). *Geology, 23(5)*, 455-458.

Hetzel, R., Ring, U., Akal, C., & Troesch, M. (1995a). Miocene NNE-directed extensional unroofing in the Menderes Massif, southwestern Turkey. *Journal of the Geological Society, 152(4)*, 639-654.

İnal, D., & İşintek, İ. (2019). New foraminiferal ages from Mesozoic carbonate blocks between Menderes and Gümüldür (İzmir, western Anatolia): comparison with nearby carbonate sequences. *International Earth Science Colloquium On the Aegean Region (Abstract)*

Jolivet, L., & Brun, J. P. (2010). Cenozoic geodynamic evolution of the Aegean. *International Journal of Earth Sciences, 99*, 109-138.

Jolivet, L., Lecomte, E., Huet, B., Denèle, Y., Lacombe, O., Labrousse, L., ... & Mehl, C. (2010). The north cycladic detachment system. *Earth and Planetary Science Letters, 289(1-2),* 87-104.

Koralay, E., Dora, Ö., Candan, O., Chen, F. ve Satır, M., 2003, Menderes masifindeki paragnaysların ilksel çökelme yaşına tek zirkon Pb/Pb evaporasyon jeokronolojisi yöntemi ile yaklaşım. *56. Türkiye Jeoloji Kurultayı, Bildiri özleri,* 64-65.

Koralay, E., Satir, M., & Dora, O. Ö. (1998). Geochronologic evidence of Triassic and Precambrian magmatism in the Menderes Massif, west Turkey. *In Abstr 3rd Int Turk Geol Symp Ankara* (Vol. 1, p. 285).

Koralay, O. E. (2001). *Geology, geochemistry and geochronology of granitic gneisses and leucocratic orthogneisses at the eastern part of Ödemiş-Kiraz submassif, Menderes Massif: Pan-African and Triassic magmatic activities* (Doctoral dissertation, Dokuz Eylul Universitesi (Turkey)).

Koralay, O. E. (2015). Late Neoproterozoic granulite facies metamorphism in the Menderes Massif, Western Anatolia/Turkey: implication for the assembly of Gondwana. *Geodinamica Acta, 27(4),* 244-266.

Koralay, O. E., Satir, M., & Dora, O. Ö. (2001). Geochemical and geochronological evidence for Early Triassic calc-alkaline magmatism in the Menderes Massif, western Turkey. *International Journal of Earth Sciences, 89,* 822-835.

Kotowski, A. J., Cisneros, M., Behr, W. M., Stockli, D. F., Soukis, K., Barnes, J. D., & Ortega-Arroyo, D. (2022). Subduction, underplating, and return flow recorded in the Cycladic Blueschist Unit exposed on Syros, Greece. *Tectonics, 41(6),* e2020TC006528.

Le Pichon, X., Angelier, J., & Sibuet, J. C. (1982). Plate boundaries and extensional tectonics. *Tectonophysics, 81(3-4),* 239-256.

Lips, A., Cassard, D., Sözbilir, H. et al. (2001). Multistage exhumation of the Menderes Massif, western Anatolia (Turkey). *Int J Earth Sci 89,* 781–792

Loos, S., & Reischmann, T. (1999). The evolution of the southern Menderes Massif in SW Turkey as revealed by zircon dating. *Journal of the Geological Society, 156(5),* 1021-1030.

Oberhänsli, R., Candan, O., Dora, O. Ö., & St H, D. (1997). Eclogites within the Menderes massif/western Turkey. *Lithos, 41(1-3),* 135-150.

Oberhansli, R., Monie, P., Candan, O., Warkus, F. C., Partzsch, J. H., & Dora, O. O. (1998). The age of blueschist metamorphism in the Mesozoic cover series of the Menderes Massif. *Schweizerische Mineralogische und Petrographische Mitteilungen, 78(2).*

Okay, A. I. (2001). Stratigraphic and metamorphic inversions in the central Menderes Massif: a new structural model. *International Journal of Earth Sciences, 89,* 709-727.

Papanikolaou, D. I. (2021). *The geology of Greece.* Springer Nature.

Paréjas, E. (1940). La tectonique transversale de la Turquie. *Istanbul Univ. Fen Fakültesi Mecmuasi.*

Reischmann, T. Kröner A, Todt W, Dürr S, Şengör AMC (1991). Episodes of crustal growth in the Menderes Massif, W Turkey, inferred from zircon dating. *Terra Abstr, 1991,* 3, 34.

Ring, U., & Layer, P. W. (2003). High-pressure metamorphism in the Aegean, eastern Mediterranean: Underplating and exhumation from the Late Cretaceous until the Miocene to Recent above the retreating Hellenic subduction zone. *Tectonics, 22(3).*

Ring, U., Gessner, K., GÜNGÖR, T., & Passchier, C. W. (1999a). The Menderes Massif of western Turkey and the Cycladic Massif in the Aegean—do they really correlate?. *Journal of the Geological Society, 156(1),* 3-6.

Ring, U., Glodny, J., Will, T., & Thomson, S. (2010). The Hellenic subduction system: high-pressure metamorphism, exhumation, normal faulting, and large-scale extension. *Annual Review of Earth and Planetary Sciences, 38(1),* 45-76.

Ring, U., Laws, S., & Bernet, M. (1999b). Structural analysis of a complex nappe sequence and late-orogenic basins from the Aegean Island of Samos, Greece. *Journal of Structural Geology, 21(11),* 1575-1601.

Schuiling, R.D., (1962). On petrology, age and structure of the Menderes migmatite complex (SW - Turkey). *Bulletin Mineral Research Exploration Institute Turkey, 58*, pp.71-84.

Şengör, A. M. C., Satir, M., & Akkök, R. (1984). Timing of tectonic events in the Menderes Massif, western Turkey: Implications for tectonic evolution and evidence for Pan-African basement in Turkey. *Tectonics, 3(7),* 693-707.

Sundell, K. E., Gehrels, G. E., & Pecha, M. E. (2021). Rapid U-Pb geochronology by laser ablation multi-collector ICP-MS. *Geostandards and Geoanalytical Research, 45(1),* 37-57.

Şengör, A. C., & Yilmaz, Y. (1981). Tethyan evolution of Turkey: a plate tectonic approach. *Tectonophysics, 75(3-4),* 181-241.

van der Maar, P. A., & Jansen, J. B. H. (1983). The geology of the polymetamorphic complex of Ios, Cyclades, Greece and its significance for the Cycladic Massif. *Geologische Rundschau, 72*, 283-299.

van Hinsbergen, D. J. (2010). A key extensional metamorphic complex reviewed and restored: the Menderes Massif of western Turkey. *Earth-Science Reviews, 102(1-2),* 60-76.

Zlatkin, O., Avigad, D., & Gerdes, A. (2013). Evolution and provenance of Neoproterozoic basement and Lower Paleozoic siliciclastic cover of the Menderes Massif (western Taurides): coupled U–Pb–Hf zircon isotope geochemistry. *Gondwana Research, 23(2),* 682-700.

Zlatkin, O., Avigad, D., & Gerdes, A. (2018). New detrital zircon geochronology from the Cycladic Basement (Greece): Implications for the Paleozoic accretion of peri-Gondwanan terranes to Laurussia. *Tectonics, 37(12),* 4679-4699.

APPENDICES

APPENDIX-1:

Table A1.1 The U–Pb Zircon Geochronology Results of OZD-02 (Özdere Schists).

Spot	OZD_02_1	OZD_02_2	OZD_02_3	OZD_02_4	OZD_02_5	OZD_02_6	OZD_02_7
$^{207}Pb/^{235}U$	0.89	1.143	1.37	0.68	1.25	0.913	0.84
±2σ (%)	0.23	0.086	0.31	0.32	0.35	0.048	0.25
$^{206}Pb/^{238}U$	0.1052	0.1281	0.1265	0.1016	0.111	0.1048	0.1096
±2σ (%)	0.0047	0.0028	0.0077	0.0076	0.0098	0.0016	0.0059
rho	0.17589	0.020232	0.11918	0.14739	0.26546	0.15057	0.81692
$^{207}Pb/^{235}U$	430	776	770	40	690	654	340
±2σ (Ma)	130	40	140	240	170	26	120
$^{206}Pb/^{238}U$	643	778	766	619	675	642.3	667
±2σ (Ma)	28	16	44	44	57	9.2	34
$^{207}Pb/^{206}Pb$	60	740	660	-1100	470	690	-230
±2σ (Ma)	430	160	440	650	550	110	400
Conc (68/75) (%)	150	100	99	1548	98	98	196
Conc (68/76) (%)							

Tablo A1.1 continues

OZD_02_16	OZD_02_15	OZD_02_14	OZD_02_13	OZD_02_12	OZD_02_11	OZD_02_10	OZD_02_9	OZD_02_8
10.61	1.106	0.937	0.73	0.866	6.57	0.85	0.86	0.845
0.42	0.079	0.069	0.24	0.046	0.34	0.076	0.15	0.053
0.469	0.1239	0.1079	0.0949	0.1006	0.3681	0.1054	0.0978	0.1043
0.011	0.0032	0.0021	0.0062	0.0016	0.0089	0.0026	0.0046	0.0018
0.076084	0.10289	-0.14494	0.057702	-0.055821	0.10234	-0.17868	0.01563	0.048943
2486	759	677	270	635	2069	628	515	620
38	38	34	160	25	48	40	94	29
2475	753	660	581	618.9	2021	647	602	639
46	18	12	36	9.2	43	15	27	10
2462	770	730	-370	700	2158	600	340	550
75	150	150	540	120	97	180	340	130
	99	97	215	97		103	117	103
101					94			

Tablo A1.1 continues

OZD_02_25	OZD_02_24	OZD_02_23	OZD_02_22	OZD_02_21	OZD_02_20	OZD_02_19	OZD_02_18	OZD_02_17
0.74	5.11	1.23	0.805	0.838	1.19	0.825	8.87	10.84
0.11	0.15	0.11	0.033	0.046	0.13	0.079	0.31	0.25
0.0844	0.3282	0.1292	0.0978	0.1002	0.1278	0.0999	0.4324	0.4744
0.0035	0.0059	0.0034	0.0014	0.0016	0.0047	0.0026	0.0079	0.0082
0.14039	0.40505	0.73763	0.27025	0.35549	-0.055416	-0.05102	0.20236	0.6663
532	1842	786	604	614	797	591	2331	2501
65	27	49	19	25	61	43	31	20
521	1828	782	602.8	615.6	774	614	2318	2500
21	28	20	8.3	9.4	27	15	35	36
540	1895	800	585	630	870	500	2361	2523
280	54	160	84	110	230	200	61	29
98		99	100	100	97	104		
	96						98	99

Tablo A1.1 continues

OZD_02_34	OZD_02_33	OZD_02_32	OZD_02_31	OZD_02_30	OZD_02_29	OZD_02_28	OZD_02_27	OZD_02_26
0.85	0.805	0.803	0.752	0.99	0.951	0.79	0.863	1.072
0.15	0.072	0.081	0.067	0.23	0.046	0.22	0.083	0.073
0.0924	0.0983	0.0952	0.0946	0.1138	0.1122	0.0987	0.1042	0.1239
0.0042	0.0027	0.0026	0.0027	0.0065	0.0018	0.0066	0.0027	0.0024
0.1188	0.15896	-0.13463	0.24243	-0.096739	0.11201	0.016366	-0.069827	0.0872
589	620	589	570	500	672	530	633	748
85	39	44	41	130	24	130	44	36
569	604	586	582	703	686	605	638	752
25	16	15	16	38	10	39	16	14
770	610	510	510	130	700	320	480	720
390	160	200	200	420	100	500	200	140
97	97	99	102	141	102	114	101	101

Tablo A1.1 continues

OZD_02_43	OZD_02_42	OZD_02_41	OZD_02_40	OZD_02_39	OZD_02_38	OZD_02_37	OZD_02_36	OZD_02_35
0.94	0.995	0.9	1.21	1.087	0.7	0.902	1.21	0.778
0.17	0.08	0.12	0.19	0.048	0.086	0.055	0.17	0.043
0.0978	0.1111	0.1027	0.1319	0.1198	0.0846	0.1067	0.1278	0.0932
0.0056	0.0025	0.0036	0.0054	0.002	0.0036	0.0023	0.0053	0.0018
-0.020652	0.034652	0.18457	0.074912	0.14334	0.56509	0.084556	0.12875	-0.019668
592	695	611	710	747	543	644	716	585
96	42	63	100	24	53	31	87	25
599	678	629	796	729	524	653	773	575
33	15	21	31	11	21	13	30	11
490	750	540	560	820	630	600	640	620
360	170	240	310	98	200	130	290	130
101	98	103	112	98	97	101	108	98

Tablo A1.1 continues

OZD_02_52	OZD_02_51	OZD_02_50	OZD_02_49	OZD_02_48	OZD_02_47	OZD_02_46	OZD_02_45	OZD_02_44
1.165	1.18	0.99	1.32	0.897	0.77	1.18	1.87	13.29
0.097	0.1	0.15	0.28	0.081	0.1	0.29	0.3	0.99
0.126	0.1283	0.1117	0.1305	0.1087	0.0952	0.137	0.1502	0.524
0.003	0.0035	0.004	0.0083	0.0028	0.0032	0.0061	0.0094	0.022
-0.0062771	-0.0020117	0.087511	-0.011659	0.21085	-0.11755	0.41517	0.054858	0.2088
785	801	683	750	663	592	790	900	2685
45	45	76	140	43	55	140	120	72
764	777	682	787	665	586	827	906	2696
17	20	23	47	16	19	35	52	95
800	850	670	600	620	560	610	840	2740
180	170	300	440	170	260	460	350	140
97	97	100	105	100	99	105	101	
								98

Tablo A1.1 continues

OZD_02_61	OZD_02_60	OZD_02_59	OZD_02_58	OZD_02_57	OZD_02_56	OZD_02_55	OZD_02_54	OZD_02_53
0.84	1.29	1.48	1.58	1.76	1.41	1.84	0.928	0.86
0.15	0.19	0.17	0.27	0.14	0.15	0.24	0.075	0.18
0.0953	0.1323	0.1394	0.1118	0.1681	0.125	0.1753	0.1078	0.1011
0.0053	0.0054	0.005	0.006	0.004	0.0037	0.0067	0.0026	0.0043
-0.039114	-0.12529	0.094767	0.13002	0.11668	0.039438	-0.32054	0.11369	0.13017
616	751	845	800	1011	852	1061	643	550
93	99	80	120	52	71	89	40	110
595	799	839	684	1000	760	1040	660	620
29	31	28	34	22	21	37	15	25
560	600	790	920	1010	990	1040	540	280
360	320	250	370	160	230	310	160	390
97	106	99	86		89		103	113
				99		100		

Tablo A1.1 continues

OZD_02_70	OZD_02_69	OZD_02_68	OZD_02_67	OZD_02_66	OZD_02_65	OZD_02_64	OZD_02_63	OZD_02_62
1.36	1.3	5.42	1.52	1.027	0.813	11.7	0.9	1.02
0.32	0.43	0.13	0.14	0.089	0.098	0.28	0.19	0.16
0.1162	0.126	0.3156	0.1496	0.1157	0.0946	0.4499	0.0938	0.1134
0.0079	0.014	0.0039	0.0058	0.0027	0.0034	0.0061	0.0049	0.0041
0.20858	-0.11654	0.23889	0.23175	0.17274	0.14721	0.37021	0.049097	-0.039027
700	670	1892	930	720	594	2574	570	631
140	190	21	57	45	57	23	110	87
704	761	1767	903	707	582	2401	577	691
46	81	19	32	15	20	27	28	24
540	370	1977	990	610	640	2708	420	380
450	620	45	200	160	240	40	390	290
101	114		97	98	98		101	110
		89				89		

Tablo A1.1 continues

OZD_02_79	OZD_02_78	OZD_02_77	OZD_02_76	OZD_02_75	OZD_02_74	OZD_02_73	OZD_02_72	OZD_02_71
1.18	1.36	1.1	0.9	0.942	14.5	1.16	1.07	6.24
0.12	0.12	0.12	0.13	0.085	1.1	0.14	0.46	0.47
0.1349	0.1455	0.1167	0.1114	0.1003	0.522	0.1256	0.116	0.362
0.0041	0.0037	0.0034	0.004	0.0025	0.025	0.0044	0.013	0.013
0.096375	0.20538	0.044154	-0.058199	-0.072504	0.19375	-0.043229	0.8535	0.29731
751	862	713	589	671	2776	747	190	2012
66	51	67	72	43	80	76	250	66
818	874	711	682	617	2700	761	700	2000
23	21	20	23	14	110	25	74	65
500	710	620	340	730	2760	640	-500	2080
210	170	230	260	180	160	250	710	130
109	101	100	116	92		102	368	
					98			96

Tablo A1.1 continues

OZD_02_88	OZD_02_87	OZD_02_86	OZD_02_85	OZD_02_84	OZD_02_83	OZD_02_82	OZD_02_81	OZD_02_80
0.895	1.27	0.95	0.757	1.22	1.74	0.81	0.819	0.836
0.066	0.17	0.15	0.041	0.43	0.17	0.4	0.049	0.062
0.1047	0.1389	0.099	0.0957	0.086	0.1715	0.1	0.0952	0.0987
0.0022	0.005	0.0051	0.0014	0.014	0.0055	0.012	0.0016	0.0024
0.22289	0.022779	0.14317	0.066266	0.286	0.18715	0.27312	0.20515	-0.053049
631	833	621	569	720	1052	260	597	612
36	69	82	24	230	62	210	27	34
641	837	611	589.1	526	1018	608	586.2	606
13	29	30	8.3	85	30	70	9.4	14
540	540	510	430	900	960	-590	540	550
150	260	300	110	820	180	730	120	160
102	100	98	104	73		234	98	99
					106			

Tablo A1.1 continues

OZD_02_97	OZD_02_96	OZD_02_95	OZD_02_94	OZD_02_93	OZD_02_92	OZD_02_91	OZD_02_90	OZD_02_89
0.82	1.022	1.13	0.69	4.31	0.91	0.891	1.35	1.19
0.19	0.085	0.27	0.13	0.11	0.1	0.064	0.28	0.15
0.1009	0.1201	0.1039	0.0921	0.2798	0.1068	0.1019	0.1355	0.1199
0.0066	0.0024	0.0069	0.0044	0.0036	0.0037	0.0024	0.0069	0.0041
0.0068516	0.11497	0.10307	0.17353	0.09786	0.10104	0.081172	-0.034325	0.095522
480	708	620	438	1694	626	648	760	728
100	42	130	78	21	61	34	130	77
616	731	635	569	1591	653	625	817	731
39	14	40	25	18	22	14	39	24
50	490	380	0	1652	310	490	340	580
380	160	440	290	53	220	150	370	250
128	103	102	130		104	96	108	100
				96				

Tablo A1.1 continues

OZD_02_104	OZD_02_103	OZD_02_102	OZD_02_101	OZD_02_100	OZD_02_99	OZD_02_98
1.017	0.74	0.699	0.915	1.11	2.64	0.879
0.079	0.13	0.045	0.094	0.1	0.31	0.071
0.1183	0.0938	0.0886	0.1057	0.1268	0.217	0.1037
0.003	0.0036	0.0023	0.0026	0.0044	0.0089	0.0023
0.10343	-0.011802	-0.056968	0.02763	0.15927	0.10394	0.17315
715	545	543	620	739	1310	645
38	73	26	52	49	90	38
720	578	547	647	768	1264	636
17	21	14	15	25	47	14
580	360	370	450	570	1280	510
160	340	120	200	200	250	150
101	106	101	104	104		99
					99	

APPENDIX-2:

Table A2.1 The U–Pb Zircon Geochronology Results of OZD-01 (Zindan Schists).

Spot	OZD_01_1	OZD_01_2	OZD_01_3	OZD_01_4	OZD_01_5	OZD_01_6	OZD_01_7
$^{207}Pb/^{235}U$	0.96	1.8	12.74	11.88	1.16	1.444	0.826
±2σ (%)	0.13	0.17	0.3	0.41	0.12	0.076	0.059
$^{206}Pb/^{238}U$	0.1047	0.1283	0.5086	0.499	0.1293	0.15	0.097
±2σ (%)	0.0036	0.006	0.009	0.011	0.0035	0.0022	0.002
rho	0.040431	0.36234	0.59517	0.21757	0.083065	0.21865	0.19021
$^{207}Pb/^{235}U$	630	1035	2662	2590	800	904	629
±2σ (Ma)	69	62	23	33	51	31	31
$^{206}Pb/^{238}U$	641	777	2649	2608	785	901	598
±2σ (Ma)	21	34	38	46	20	12	12
$^{207}Pb/^{206}Pb$	620	1660	2677	2567	580	890	700
±2σ (Ma)	280	180	33	60	200	100	130
Conc (68/75) (%)	102	75			98	100	95
Conc (68/76) (%)			99	102			

Tablo A2.1 continues

OZD_01_16	OZD_01_15	OZD_01_14	OZD_01_13	OZD_01_12	OZD_01_11	OZD_01_10	OZD_01_9	OZD_01_8
1.35	0.936	1.696	1.683	1.041	1.035	0.453	1.49	1.56
0.16	0.035	0.086	0.058	0.036	0.043	0.056	0.11	0.11
0.1376	0.1079	0.1713	0.166	0.1168	0.1157	0.0574	0.1521	0.1568
0.0049	0.0016	0.0032	0.0027	0.0016	0.0018	0.0018	0.0035	0.0041
0.37346	0.15824	0.12839	-0.0046396	0.09884	0.16166	0.18683	0.032104	0.26302
842	671	999	999	723	720	372	929	966
67	19	33	22	18	22	40	46	41
830	660.1	1018	991	711.7	706	360	912	939
27	9.1	18	15	9	11	11	20	23
690	620	940	987	732	795	390	930	1040
230	80	110	77	73	94	230	150	130
99	98		99	98	98	97	98	97
		108						

Tablo A2.1 continues

OZD_01_25	OZD_01_24	OZD_01_23	OZD_01_22	OZD_01_21	OZD_01_20	OZD_01_19	OZD_01_18	OZD_01_17
6.64	0.723	0.795	0.732	1.64	0.833	0.721	0.776	1.233
0.34	0.048	0.055	0.039	0.15	0.048	0.079	0.031	0.058
0.3738	0.0889	0.0984	0.0906	0.1605	0.0995	0.0865	0.0951	0.1344
0.0098	0.0019	0.0019	0.0018	0.0051	0.002	0.0027	0.0013	0.0023
0.36849	0.0099306	0.11078	0.088513	0.12	0.36995	0.34774	0.076657	0.15048
2066	545	596	555	967	613	565	580	809
44	29	33	22	57	26	45	18	27
2045	549	604	559	958	611	534	585.3	814
46	11	11	10	28	11	16	7.4	13
2019	470	500	480	890	640	600	504	750
86	140	140	120	190	130	220	85	100
	101	101	101	99	100	95	101	
101								101

Tablo A2.1 continues

OZD_01_34	OZD_01_33	OZD_01_32	OZD_01_31	OZD_01_30	OZD_01_29	OZD_01_28	OZD_01_27	OZD_01_26
0.777	1.59	1.286	1.061	0.645	0.93	5.87	12.07	1.35
0.037	0.067	0.042	0.044	0.038	0.049	0.18	0.38	0.14
0.0948	0.16	0.1393	0.118	0.0794	0.1073	0.3531	0.4953	0.1412
0.0014	0.003	0.0018	0.0016	0.0019	0.0015	0.0056	0.008	0.005
0.21353	0.18855	0.22326	0.19226	0.18514	0.22972	0.067077	0.55155	-0.043547
585	964	842	738	501	664	1958	2607	856
22	25	19	21	24	26	27	30	69
584.6	956	840	718.7	492	656.8	1950	2592	850
8.3	17	10	9.2	11	8.8	27	34	28
543	988	823	725	480	660	1932	2588	710
97	88	69	84	130	110	61	44	230
100	99	100	97	98	99			99
						101	100	

Tablo A2.1 continues

OZD_01_43	OZD_01_42	OZD_01_41	OZD_01_40	OZD_01_39	OZD_01_38	OZD_01_37	OZD_01_36	OZD_01_35
0.819	0.458	12.47	7.34	5.53	1.779	0.99	6.51	0.656
0.055	0.066	0.2	0.3	0.13	0.074	0.074	0.22	0.02
0.0981	0.0592	0.5083	0.3935	0.3098	0.1765	0.1151	0.3745	0.0828
0.002	0.0022	0.006	0.0085	0.0041	0.0031	0.0024	0.0061	0.0012
0.078342	-0.013219	0.44614	0.30145	0.36544	0.064471	0.23471	0.36398	0.28958
602	348	2639	2143	1906	1035	704	2049	512
32	44	15	39	21	27	36	30	12
604	370	2650	2136	1739	1047	702	2048	513.1
12	13	26	39	20	17	14	29	6.9
570	170	2658	2160	2105	978	680	2060	489
140	240	25	75	42	93	150	55	63
100	106					100		100
		100	99	83	107		99	

Tablo A2.1 continues

OZD_01_52	OZD_01_51	OZD_01_50	OZD_01_49	OZD_01_48	OZD_01_47	OZD_01_46	OZD_01_45	OZD_01_44
0.457	0.815	1.674	0.9	0.941	0.872	0.419	0.845	0.837
0.052	0.045	0.082	0.14	0.047	0.022	0.047	0.047	0.042
0.0577	0.0966	0.1632	0.1031	0.1074	0.10266	0.0563	0.0977	0.0979
0.0019	0.0016	0.0028	0.0045	0.0014	0.0009	0.0015	0.002	0.0016
-0.014832	0.10739	0.083946	0.24428	0.039159	0.052503	-0.0080535	-0.070847	0.11276
363	604	996	598	676	636	346	623	609
37	25	33	79	25	12	35	27	23
361	595.2	974	634	657.7	629.9	353.8	600	601.9
11	9.3	16	26	8.3	5.3	8.9	12	9.2
390	640	1040	450	720	674	310	720	600
220	120	110	280	110	55	210	140	100
99	99	98	106	97	99	102	96	99

Tablo A2.1 continues

OZD_01_61	OZD_01_60	OZD_01_59	OZD_01_58	OZD_01_57	OZD_01_56	OZD_01_55	OZD_01_54	OZD_01_53
1.719	1.843	1.775	4.58	0.905	0.752	13.69	0.905	4.598
0.063	0.053	0.055	0.14	0.041	0.06	0.71	0.048	0.075
0.1681	0.1779	0.1744	0.302	0.1073	0.0963	0.518	0.1068	0.2864
0.003	0.0027	0.0022	0.0055	0.0013	0.0021	0.016	0.0019	0.0038
0.54049	0.30789	0.06654	0.37941	0.24691	0.18758	0.5263	0.19679	0.48883
1014	1055	1031	1743	649	559	2723	656	1749
23	19	20	25	22	35	50	25	14
1001	1055	1037	1701	656.7	592	2690	654	1623
17	15	13	27	7.7	13	70	11	19
1019	1054	1016	1789	619	440	2790	630	1924
60	53	68	55	90	170	68	110	26
				101	106		100	
98	100	102	95			96		84

Tablo A2.1 continues

OZD_01_70	OZD_01_69	OZD_01_68	OZD_01_67	OZD_01_66	OZD_01_65	OZD_01_64	OZD_01_63	OZD_01_62
1.81	15.8	1.433	0.94	1.751	0.88	0.795	1.085	8.19
0.12	0.54	0.043	0.047	0.074	0.11	0.048	0.06	0.2
0.1747	0.47	0.1514	0.1118	0.1703	0.0966	0.0923	0.12	0.3618
0.0034	0.0094	0.0021	0.0017	0.0024	0.003	0.0017	0.0021	0.0044
0.17023	0.31507	0.19143	0.19856	0.19808	-0.054987	0.12749	0.10608	0.1671
1044	2861	905	671	1028	597	597	739	2252
42	33	17	25	27	60	27	29	22
1037	2483	909	682.8	1015	594	570	730	1990
18	41	12	9.7	13	18	10	12	21
1030	3138	873	550	1016	520	630	710	2467
130	50	60	110	83	240	120	120	41
		100	102		99	95	99	
101	79			100				81

Tablo A2.1 continues

OZD_01_79	OZD_01_78	OZD_01_77	OZD_01_76	OZD_01_75	OZD_01_74	OZD_01_73	OZD_01_72	OZD_01_71
0.758	7	10.73	0.763	1.542	2.14	1.04	0.741	1.8
0.056	0.15	0.23	0.061	0.099	0.11	0.18	0.027	0.11
0.097	0.3859	0.4353	0.0947	0.1614	0.1955	0.1135	0.0913	0.1725
0.0018	0.0045	0.0052	0.0022	0.0047	0.0038	0.0062	0.0014	0.0034
0.16204	0.26775	0.41283	-0.041034	0.26074	0.21753	0.049632	0.23485	0.15773
569	2106	2500	569	956	1159	647	560	1035
31	18	19	34	40	36	94	16	40
597	2104	2328	584	964	1150	695	563.3	1025
11	21	23	13	26	20	36	8.1	19
440	2071	2615	460	920	1160	480	543	1080
150	36	31	160	130	100	330	80	120
105			103	101		107	101	
	102	89			99			95

Tablo A2.1 continues

OZD_01_88	OZD_01_87	OZD_01_86	OZD_01_85	OZD_01_84	OZD_01_83	OZD_01_82	OZD_01_81	OZD_01_80
0.89	11.96	0.902	1.461	1.501	1.71	6.93	1.108	1.79
0.064	0.45	0.03	0.096	0.083	0.14	0.3	0.081	0.1
0.1062	0.495	0.1069	0.1488	0.1519	0.1408	0.367	0.1245	0.1749
0.0023	0.011	0.0013	0.0026	0.0031	0.0049	0.011	0.0046	0.0031
0.061432	0.52286	0.277	0.14716	0.16948	0.37603	0.38461	0.50844	0.17073
643	2599	650	906	923	1000	2096	744	1050
33	34	16	39	35	52	39	36	39
653	2600	654.6	894	911	848	2012	755	1038
13	46	7.4	15	17	28	51	26	17
550	2564	616	800	890	1340	2124	650	1020
150	57	70	140	120	150	78	110	120
102		101	99	99	85		101	
	101					95		102

OZD_01_97	OZD_01_96	OZD_01_95	OZD_01_94	OZD_01_93	OZD_01_92	OZD_01_91	OZD_01_90	OZD_01_89
12.07	1.07	1.48	0.996	1.537	1.59	0.418	5.09	1.59
0.35	0.12	0.11	0.087	0.061	0.16	0.065	0.16	0.047
0.496	0.1155	0.1547	0.1159	0.1573	0.1647	0.0586	0.3273	0.1603
0.013	0.004	0.0035	0.0024	0.0031	0.006	0.002	0.0045	0.0018
0.27112	0.11921	0.05467	0.12045	0.41458	0.17136	0.19221	0.38138	0.24315
2614	696	922	698	943	979	360	1828	965
29	61	42	45	25	65	50	27	18
2602	703	926	708	941	985	367	1824	959.1
54	23	19	14	17	34	12	22	9.9
2617	620	880	570	1004	940	330	1871	946
56	210	150	170	78	210	290	57	58
	101	100	101	100	101	102		99
99							97	

Tablo A2.1 continues

Tablo A2.1 continues

OZD_01_104	OZD_01_103	OZD_01_102	OZD_01_101	OZD_01_100	OZD_01_99	OZD_01_98
9	16.18	0.845	1.12	0.857	1.119	1.19
0.32	0.55	0.053	0.043	0.044	0.047	0.1
0.4291	0.57	0.1039	0.1282	0.1043	0.1253	0.1266
0.0097	0.013	0.002	0.0019	0.0021	0.0022	0.0038
0.35098	0.22897	0.066182	0.13501	0.070028	0.30419	0.11384
2333	2901	615	765	627	760	783
33	33	29	21	25	23	48
2300	2905	637	779	639	761	771
44	54	12	11	12	12	22
2373	2900	490	702	550	750	840
58	64	140	86	120	90	170
		104	102	102	100	98
97	100					